NASA

Turbine Vane External Heat Transfer

Volume I.
Analytical and Experimental Evaluation
of Surface Heat Transfer Distributions
with Leading Edge Showerhead Film Cooling

By: E. R. Turner
M. D. Wilson
L. D. Hylton
R. M. Kaufman

Allison Gas Turbine Division
General Motors Corporation
Indianapolis, Indiana 46206-0420

Final Report

prepared for

National Aeronautics and Space Administration
NASA-Lewis Research Center
Cleveland, Ohio 44135
Contract No. NAS3-23695

NASA

Turbine Vane External Heat Transfer

Volume I.
Analytical and Experimental Evaluation of Surface Heat Transfer Distributions with Leading Edge Showerhead Film Cooling

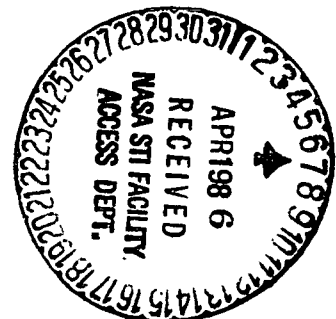By: E. R. Turner
M. D. Wilson
L. D. Hylton
R. M. Kaufman

Allison Gas Turbine Division
General Motors Corporation
Indianapolis, Indiana 46206-0420

Final Report
July 1985

TABLE OF CONTENTS

LIST OF ILLUSTRATIONS

LIST OF ILLUSTRATIONS (CONT)

LIST OF TABLES

I. SUMMARY

This two-volume report addresses the progress of contract NAS3-23695 to improve the predictive design capabilities for external heat transfer to turbine vanes including the effects of leading edge showerhead film cooling. Volume I describes the analytical and experimental program conducted at Allison Gas Turbines to examine the effect of leading edge showerhead film cooling on downstream heat transfer. The experimental study was performed in a two-dimensional (2-D) linear cascade previously used to obtain vane surface heat transfer distributions on nonfilm-cooled airfoils under NAS3-22761.

The experimental program provided a data base for leading edge showerhead film-cooled turbine vanes to use in developing and evaluating new analytical models.

The analytical effort described in Volume I consists of modifications to the 2-D boundary layer model previously developed under NAS3-22761. The effort resulted in the formulation and test of an effective viscosity model capable of predicting heat transfer phenomena downstream of the leading edge film-cooling array on both the suction and pressure surfaces, with and without mass injection. Comparisons of heat transfer calculations made with the model with data taken during the program are presented and indicate good agreement.

Volume II describes work performed under subcontract by Scientific Research Associates. This analytical effort examined the application of the time-dependent ensemble-averaged Navier-Stokes equations to transonic turbine cascade flow fields. In particular, efforts focused on an assessment of the procedure in conjunction with a suitable turbulence model to calculate steady turbine flow fields using an O-type coordinate system. Three cascade configurations were considered.

Comparisons were made between the predicted and measured surface pressures and heat transfer distributions wherever available. In general, the pressure predictions were in good agreement with data. The computed heat transfer results also showed good agreement with data when an empirical transition model was used. However, further work in the development of laminar-turbulent

transitional models is indicated. The calculations showed most of the known features associated with turbine cascade flow fields. These results indicate the ability of the Navier-Stokes analysis to predict, in reasonable amounts of computation time, the surface pressure distribution, heat transfer rates, and viscous flow development for turbine cascades operating at realistic flow conditions.

II. INTRODUCTION

The thermal design of contemporary high-pressure turbine nozzle guide vanes clearly represents one of the more difficult engineering tasks in the design of any modern aircraft gas turbine. Aerodynamic and thermal analysis procedures currently available to turbine designers have deficiencies that do not permit a priori designs that achieve design goals without expensive experimental development iterations.

This study is the second part of a combined analytical and experimental program initiated to address one particular aspect of the overall design problem; namely, the prediction of external convective heat transfer. In the first program, Hylton et al (Ref 1) reported results of a study that emphasised the development of a more reliable procedure for determining convective heat transfer loads to nonfilm-cooled airfoil geometries. The purpose of this study was to examine the problem of convective heat transfer prediction for leading edge film-cooled airfoil geometries.

In terms of developing an overall procedure for predicting convective heat transfer phenomena on any arbitrary, discrete site, film-cooled airfoil geometry, it could be argued that the special case of leading edge injection is perhaps the most difficult to model using conventional turbine design system methodology. If conventional methodology is taken to be synonymous with boundary layer theory, discrete jet injection in a stagnated flow leading edge region represents a condition that is not easily described by standard theory. Although attempts to extend standard boundary layer theory for predicting heat transfer phenomena within an actively cooled leading edge region (Ref 2 and 3) have met with some success, the related problem of predicting resultant recovery region phenomena for real airfoil geometries at simulated engine operating conditions has received little attention.

To realistically approach the problem, it was recognized that the availability of a relevant data base would be essential in guiding the development of a mathematical model for describing the highly complex, three-dimensional (3-D), coolant jet/mainstream flow interaction process in terms of a two-dimensional (2-D) boundary layer analysis framework. Consequently, an experimental effort

was conducted to generate a representative data base. Experiments were conducted in a 2-D linear cascade. The vane profile used was identical to one used in the nonfilm-cooled experiments reported in Ref 1. The data base generated in this study can therefore be viewed as an extension of the data base generated in the first study. Heat transfer measurements were taken downstream of a leading edge showerhead array consisting of five rows of cooling holes fed by a common plenum. Recovery region heat transfer measurements were taken at two transonic exit Mach number conditions with true chord Reynolds numbers of order 10^6. In addition, both blowing strength and coolant temperature were varied to quantify jet turbulence production and thermal dilution mechanisms. The experimental program is described in detail in section III.

Using the experimental data base, the primary objective of the analytical program was to develop a method for predicting recovery region external convective heat transfer phenomena associated with a leading edge film-cooling process. To build directly on the nonfilm-cooled airfoil heat transfer methods development effort conducted in Ref 1, a 2-D finite difference boundary layer analysis framework was used.

The purpose of this program was to develop a reliable procedure for predicting heat transfer that is consistent with accepted gas turbine airfoil heat transfer design philosophy. It is assumed that all domestic gas turbine design centers have ready access to and/or routinely use a 2-D finite difference boundary layer analysis code for the prediction of external convective heat transfer. Positive results from this program could be integrated with a design system without a major change in design method philosophy. The analytical program is discussed in section IV.

As computer technology evolves, boundary layer analysis design procedures are likely to be replaced by Reynolds and/or full Navier-Stokes (N-S) equation analyses. Even though the N-S framework is not currently an industry standard, its continued development improves future capability and reduces empiricism. In addition to the development of the boundary layer method reported in this volume, an N-S method development program was conducted by Scientific Research Associates (SRA) under subcontract to Allison. The N-S program is reported in Volume II.

III. EXPERIMENTAL PROGRAM

This section provides a detailed description of the facility and hardware used for the experimental program. A complete description of the cascade is given together with the precise locations of all facility and cascade instrumentation. The heat transfer measurement technique and data acquisition and reduction procedures are defined, and the uncertainties are assessed. Test conditions are cataloged in this section, but detailed tabulated results are reserved for the appendixes. This section provides all of the information necessary to permit use of the data to verify two-dimensional (2-D) heat transfer predictions.

3.1 HARDWARE AND INSTRUMENTATION

3.1.1 Facility Description

The experimental investigation portion of the contract was performed in the Allison Aerothermodynamic Cascade Facility (ACF). The purpose of this facility is to conduct experimental research in high-temperature turbine component models that embody advanced cooling techniques, aerodynamics, or materials. The experimental approach employs a 2-D model technique, with full dynamic similarity in free-stream Mach number (Ma) and boundary layer Reynolds number (Re) effects, and provides an experimental method to separate the effects on local heat transfer.

The facility consists of a burner, a convergent section, a free-stream section with instrumentation and optical access, a test section with instrumentation, a quench zone with back pressure regulation, and an exhaust system. The facility is shown schematically in Figure 1.

The Mach number and Reynolds number modeling considerations necessitate a burner with a large temperature, flow, and pressure range. This burner capability, coupled with the back pressure regulating valve, allows experimental separation of free-stream Mach number and boundary layer Reynolds number effects to accurately simulate a wide range of engine designs and operating conditions.

Torch ignitor Circumferential natural gas injection Flame holder Steam cooling annulus Pressure shell Transition section Quartz window Turbulence augmentation Exit control valve

Marquardt burner

Cooling water supply Cooling water dump Transition duct steam cooling supply Endwall cooling jackets Exit probe Exit probe traverse system Exhaust quench water

Filtered air supply regulated to set pressure or flow

Three vane cascade

TE80-513A

Figure 1. Schematic of the Aerothermodynamic Cascade Facility.

A constant cross section is provided downstream of the burner to establish uniform inlet velocity, temperature, and turbulence profiles. This section is provided with temperature-controlled cooled walls and isolates the test section from radiant heat transfer from the primary combustion zone. The walls of the test section are cooled with steam to keep them at, or close to, the vane surface temperature to prevent radiant exchange. The test section design is unique in that it incorporates both aerodynamic and heat transfer data acquisition in a single tunnel, thereby reducing costs and ensuring the correlation of heat transfer and aerodynamic data for the single set of airfoils.

3.1.2 Facility Instrumentation and Geometry

The various flow circuits of the ACF incorporate standard in-line instrumentation for measurement of flow rate, pressure, and temperature. American Society of Mechanical Engineers (ASME) standard sharp-edged orifices are used throughout to provide flow-rate measurements. The orifices used to meter the secondary flow systems for the current tests were calibrated to provide flow measurement accuracy to ±2%.

Facility and rig pressures are measured using a Scanivalve pressure scanner with six modules, each capable of handling 48 individual sense lines. Pressure transducers of appropriate ranges matched to the current experiment are inserted in these modules. These pressure transducers are calibrated before each test series with a precision Mensor quartz manometer, which, in turn, is periodically calibrated against a dead-weight system. There are 300 Chromel-Alumel (CA) thermocouple circuits available in the laboratory for temperature measurement. The circuits are coupled to the data acquisition system through temperature-stabilized reference junctions.

A two-axis computer-controlled traverse system permits surveys of inlet pressure and temperature fields to be made. Provisions also exist at the cascade inlet plane for optical access to the flow path to permit the measurements of free-stream velocity and turbulence with a laser Doppler anemometer (LDA). Specifications regarding facility instrumentation are detailed in Table I.

Table I.
Aerothermodynamic facility instrumentation.

Pressure scanner	Scanivalve system with 288 ports
Pressure transducers	Druck, with ranges from 0-68.9 kPa to 0-3447.4 kPa (0-10 psia to 0-500 psia)
Accuracy	+0.06% BSL
Thermocouple channels	300 CA and 40 Pt/Pt-10% Rh
Accuracy	+0.3°C with calibration
Traversing gear	United Sensor traversing probe mounts with computer interfaces
	Precision 2-axis digital traversing mount with discrete stepping capability to 0.00254 cm (0.001 in.)
Anemometers	LDA
Survey probes	Traversing CA thermocouple
	Traversing pressure probe

The flow path upstream of the cascade in the ACF takes the burner discharge from a 31.5 cm (12.4 in.) dia through a 50.8 cm (20 in.) long transition section to a 7.6 cm x 27.9 cm (3 in. x 11 in.) rectangular section. A photo of the transition duct is shown in Figure 2. Four removable 1.3 cm (0.5 in.) rods can be installed just downstream of the inlet to the transition section rectangular duct to augment the cascade inlet turbulence level. The rectangular
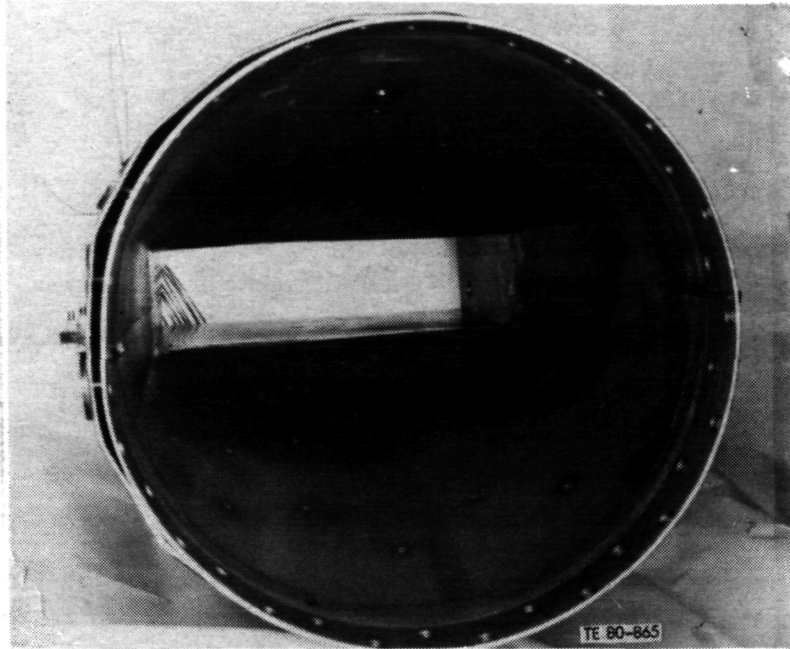
Figure 2. Burner-to-cascade inlet transition duct.

section upstream of the cascade is 36.83 cm (14.50 in.) long and contains inlet instrumentation and an optical access window. A schematic of the inlet and test section, showing the relative positions of the inlet and exit instrumentation, is shown in Figure 3. The inlet instrumentation consists of two inlet core total pressure rakes, two inlet core total temperature rakes, and nine endwall static pressure taps. The LDA inlet turbulence measurement cross-sectional position is also shown. Thirteen endwall static taps are located in the endwall of each cascade at the exit plane.

3.1.3 Cascade Description

The three-vane cascade employed in this test was the C3X cascade previously used in Ref 1. The center test vane was replaced with a leading edge film-cooled C3X vane. The vane was fabricated in two halves, allowing modifications to be made to the leading edge region, details of which are shown in Figure 4. A brazing process was then used to join the two halves. The test vane was instrumented for both heat transfer and aerodynamic measurements. Flow splitters adjacent to the outer vanes and a tailboard were used to ensure periodicity. The static pressure taps at the inlet and exit of the cascade provided the information necessary to establish periodicity.
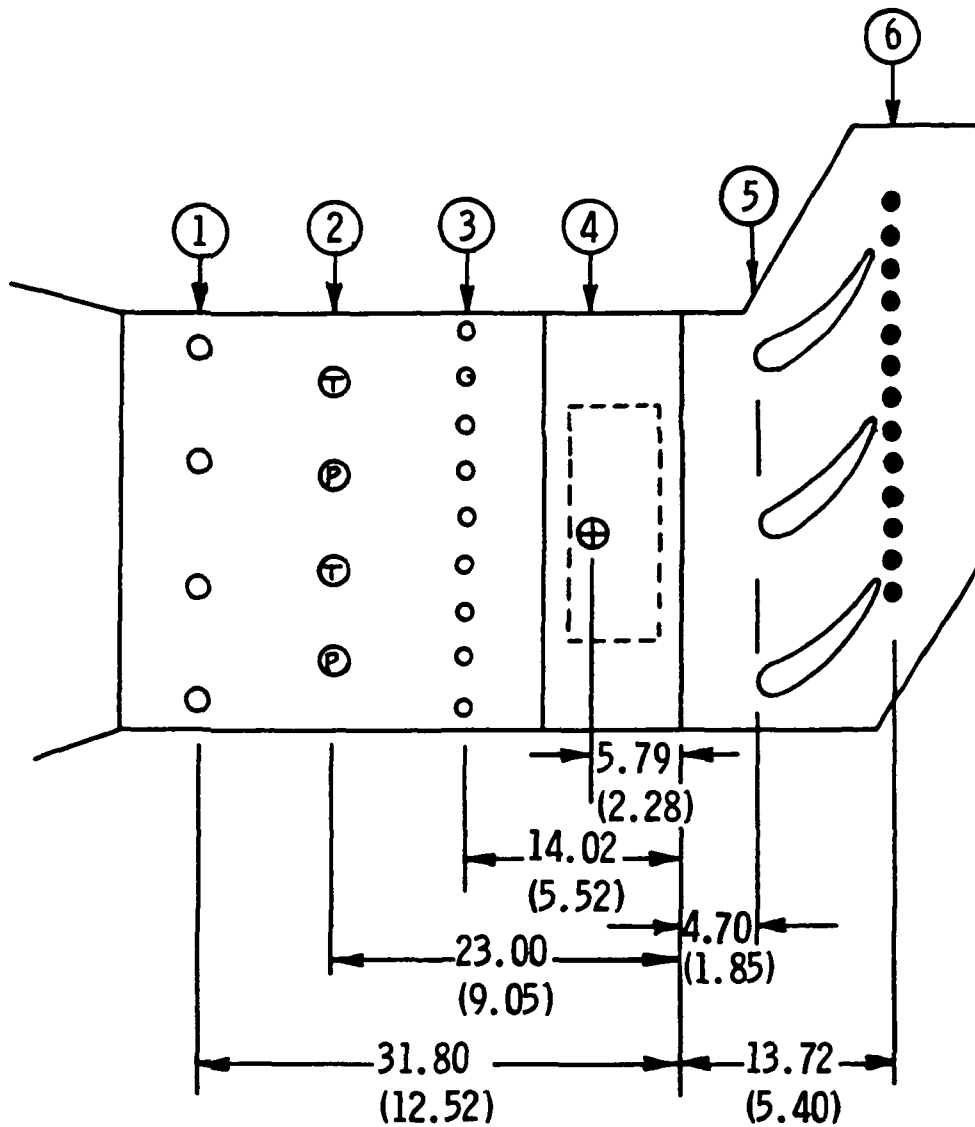
All dimensions in cm (in.)

① Turbulence augmentation rods
② Core rakes
③ Inlet static pressure taps
④ LDA measurement volume
⑤ Leading edge plane
⑥ Exit static pressure taps

TE82-6020B

Figure 3. Facility instrumentation schematic.
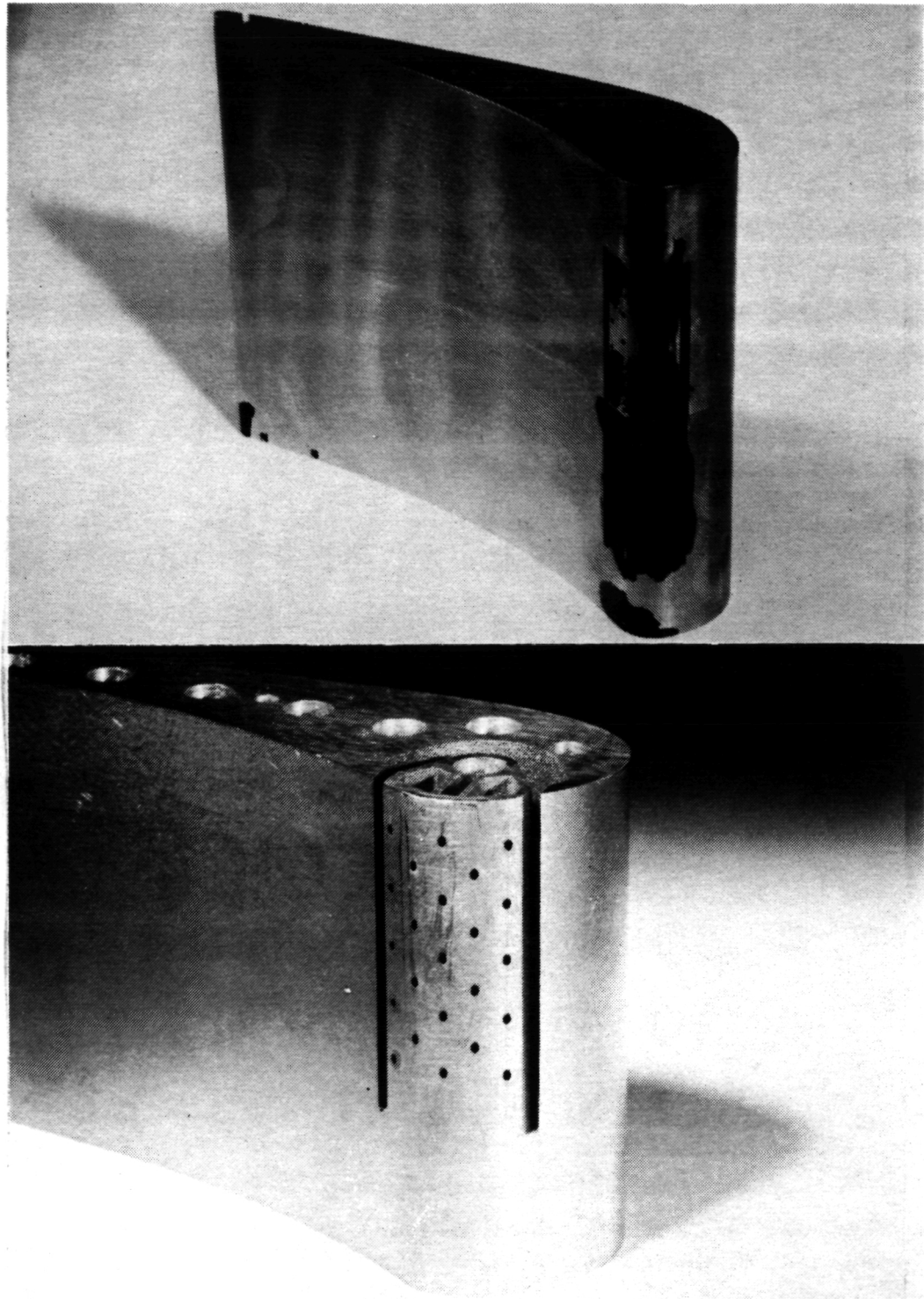
TE84-8611

Figure 4.   Leading edge film-cooled C3X test vane.

The vane coordinates for the C3X airfoil are given in Table II. Figure 5 shows the cascade coordinate system used to define the airfoil shape. Table III lists additional geometry information for the cascade.

The vane was internally cooled by an array of 10 radial cooling holes. The hole configuration is shown in Figure 6, which also depicts the finite element model (FEM) and film-cooling geometry. The radial cooling holes of each of the outer two slave vanes were supplied from a common plenum, whereas each hole in the test vane was supplied from a separate, metered line.

3.1.4 Leading Edge Film-Cooling Geometry Description

The leading edge film-cooling geometry design employed a showerhead array of five equally spaced rows of holes with the center row located at the predicted aerodynamic stagnation point. The hole array is staggered with the holes in the second row located midway (radially) between the holes in the first and third rows. The holes are angled at 45 deg to the surface in the radial (spanwise) direction. They are normal to the surface in the chordwise direction.

TE82-6022
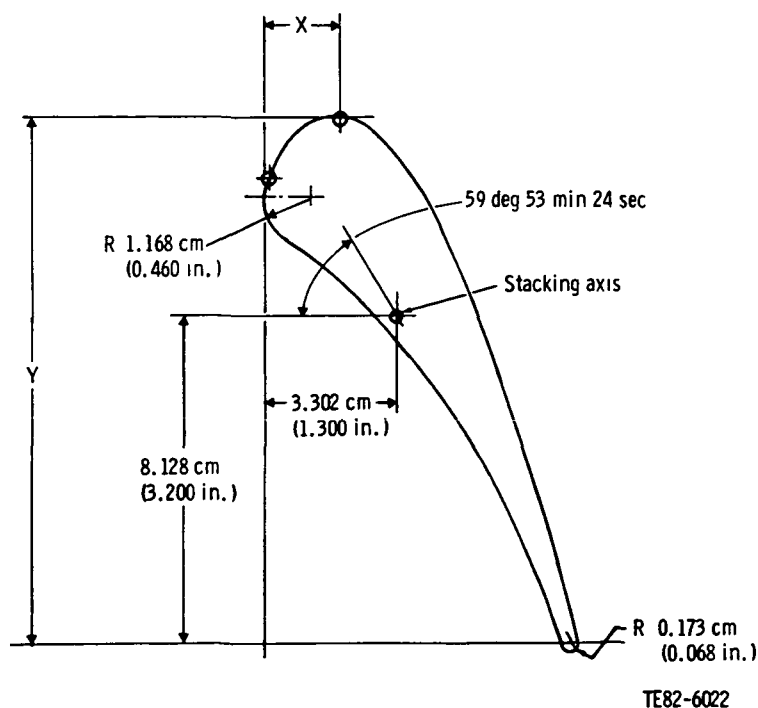
Figure 5. C3X vane coordinate system.

11

Table II.
C3X vane coordinates.

R_{LE} = 1.168 cm (0.460 in.) R_{TE} = 0.173 cm (0.068 in.)

Position number	x--cm (in.)		y--cm (in.)		Position number	x--cm (in.)		y--cm (in.)	
1	0.1097	(0.0432)	11.6548	(4.5885)	40	7.4849	(2.9468)	-0.0617	(-0.0243)
2	0.3894	(0.1533)	12.1890	(4.7988)	41	7.3188	(2.8814)	0.3559	(0.1401)
3	0.7658	(0.3015)	12.6764	(4.9907)	42	7.1483	(2.8143)	0.7737	(0.3046)
4	1.2723	(0.5009)	13.0233	(5.1273)	43	6.9736	(2.7455)	1.1895	(0.4683)
5	1.8743	(0.7379)	13.1376	(5.1723)	44	6.7950	(2.6752)	1.6035	(0.6313)
6	2.4707	(0.9727)	12.9939	(5.1157)	45	6.6116	(2.6030)	2.0155	(0.7935)
7	2.9835	(1.1746)	12.6538	(4.9818)	46	6.4237	(2.5290)	2.4254	(0.9549)
8	3.3985	(1.3380)	12.1976	(4.8022)	47	6.2309	(2.4531)	2.8329	(1.1153)
9	3.7376	(1.4715)	11.6817	(4.5991)	48	6.0328	(2.3751)	3.2380	(1.2748)
10	4.0272	(1.5855)	11.1364	(4.3844)	49	5.8296	(2.2951)	3.6406	(1.4333)
11	4.2885	(1.6884)	10.5766	(4.1640)	50	5.6203	(2.2127)	4.0401	(1.5906)
12	4.5326	(1.7845)	10.0094	(3.9407)	51	5.4051	(2.1280)	4.4364	(1.7466)
13	4.7648	(1.8759)	9.4369	(3.7153)	52	5.1834	(2.0407)	4.8290	(1.9012)
14	4.9870	(1.9634)	8.8605	(3.4884)	53	4.9548	(1.9507)	5.2177	(2.0542)
15	5.2019	(2.0480)	8.2814	(3.2604)	54	4.7191	(1.8579)	5.6020	(2.2055)
16	5.4110	(2.1303)	7.7003	(3.0316)	55	4.4760	(1.7622)	5.9817	(2.3550)
17	5.6157	(2.2109)	7.1176	(2.8022)	56	4.2248	(1.6633)	6.3564	(2.5025)
18	5.8171	(2.2902)	6.5336	(2.5723)	57	3.9654	(1.5612)	6.7249	(2.6476)
19	6.0160	(2.3685)	5.9487	(2.3420)	58	3.6975	(1.4557)	7.0874	(2.7903)
20	6.2126	(2.4459)	5.3632	(2.1115)	59	3.4204	(1.3466)	7.4430	(2.9303)
21	6.4074	(2.5226)	4.7767	(1.8806)	60	3.1339	(1.2338)	7.7909	(3.0673)
22	6.5997	(2.5983)	4.1897	(1.6495)	61	2.8374	(1.1171)	8.1308	(3.2011)
23	6.7894	(2.6730)	3.6015	(1.4179)	62	2.5314	(0.9966)	8.4615	(3.3313)
24	6.9756	(2.7463)	3.0122	(1.1859)	63	2.2149	(0.8720)	8.7826	(3.4577)
25	7.1575	(2.8179)	2.4221	(0.9536)	64	1.8885	(0.7435)	9.0935	(3.5801)
26	7.3335	(2.8872)	1.8301	(0.7205)	65	1.5519	(0.6110)	9.3932	(3.6981)
27	7.5024	(2.9537)	1.2357	(0.4865)	66	1.2052	(0.4745)	9.6815	(3.8116)
28	7.6624	(3.0167)	0.6391	(0.2516)	67	0.8494	(0.3344)	9.9578	(3.9204)
29	7.8115	(3.0754)	0.4115	(0.0162)	68	0.4999	(0.1968)	10.2116	(4.0203)
30	7.8161	(3.0772)	-0.0053	(-0.0021)	69	0.3848	(0.1515)	10.3035	(4.0565)
31	7.8082	(3.0741)	-0.0516	(-0.0203)	70	0.2822	(0.1111)	10.4094	(4.0982)
32	7.7879	(3.0661)	-0.0935	(-0.0368)	71	0.1938	(0.0763)	10.5273	(4.1446)
33	7.7572	(3.0540)	-0.1288	(-0.0507)	72	0.1212	(0.0477)	10.6556	(4.1951)
34	7.7180	(3.0386)	-0.1542	(-0.0607)	73	0.0650	(0.0256)	10.7920	(4.2488)
35	7.6736	(3.0211)	-0.1681	(-0.0662)	74	0.0264	(0.0104)	10.9342	(4.3048)
36	7.6269	(3.0027)	-0.1699	(-0.0669)	75	0.0064	(0.0025)	11.0802	(4.3623)
37	7.5816	(2.9849)	-0.1588	(-0.0625)	76	0.0046	(0.0018)	11.2278	(4.4204)
38	7.5408	(2.9688)	-0.1356	(-0.0534)	77	0.0216	(0.0085)	11.3741	(4.4780)
39	7.5077	(2.9558)	-0.1026	(-0.0404)	78	0.0569	(0.0224)	11.5171	(4.5343)

12

Table III.
Cascade geometry.

Setting angle—deg	59.89	
Air exit angle—deg	72.38	
Throat—cm (in.)	3.292	(1.296)
Vane height—cm (in.)	7.620	(3.000)
Vane spacing—cm (in.)	11.773	(4.635)
Suction surface arc-cm (in.)	17.782	(7.001)
Pressure surface arc-cm (in.)	13.723	(5.403)
True chord—cm (in.)	14.493	(5.706)
Axial chord—cm (in.)	7.816	(3.077)

This type of arrangement is typical of current leading edge showerhead film-cooling designs. Coordinates for the film-cooling hole rows are listed in Figure 6. Geometry information for the showerhead array is detailed in Table IV.

Three supply plenums, each with a separate, metered line, were designed to feed the five rows of holes. This system was designed to provide the capability of investigating various blowing configuations or to simulate a common plenum feed in a cost-effective manner. The film coolant supply was piped through an electric heating system that provided the capability to vary the coolant supply temperature.

The heat transfer measuring technique used for this test does not make heat transfer measurements in the actual film-cooling array area. Consequently, the showerhead area was thermally isolated from the downstream portion of the

Table IV.
Leading edge film-cooled geometry.

Geometric parameters	Value	
Rows of holes*	5	
Hole diameter—cm (in.)	0.099	(0.039)
Hole length—cm (in.)	0.335	(0.132)
Hole pitch-to-diameter ratio (P/D)	4.0	
Hole spacing-to-diameter ratio (S/D)	7.5	
Hole slant angle (α)—deg	45	
Hole skew angle (β)—deg	90	

*Centered around location of maximum surface static pressure

13
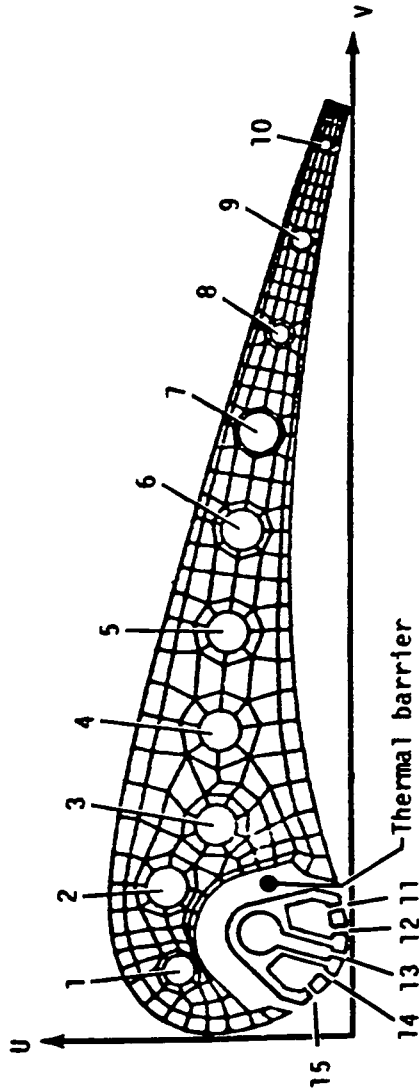
Radial cooling holes

Hole No.	U—cm (in.)	V—cm (in.)	Dia—cm (in.)	Cr
1	2.540 (0.999)	0.991 (0.390)	0.470 (0.185)	1.090
2	2.738 (1.078)	2.271 (0.894)	0.630 (0.248)	1.118
3	1.999 (0.787)	3.066 (1.207)	0.630 (0.248)	1.118
4	1.981 (0.780)	4.674 (1.840)	0.630 (0.248)	1.118
5	1.869 (0.736)	6.182 (2.434)	0.630 (0.248)	1.118
6	1.666 (0.656)	7.747 (3.050)	0.630 (0.248)	1.118
7	1.412 (0.556)	9.235 (3.636)	0.630 (0.248)	1.118
8	1.087 (0.428)	10.759 (4.236)	0.310 (0.122)	1.056
9	0.737 (0.290)	12.253 (4.824)	0.310 (0.122)	1.056
10	0.345 (0.136)	13.757 (5.416)	0.198 (0.078)	1.025

Film cooling holes

Hole No.	U—cm (in.)	V—cm (in.)
11	0.109 (0.043)	1.999 (0.787)
12	0.005 (0.002)	1.608 (0.633)
13	0.041 (0.016)	1.196 (0.471)
14	0.211 (0.083)	0.831 (0.327)
15	0.498 (0.196)	0.538 (0.212)

TE84-8612

Figure 6. Leading edge film-cooled C3X finite element grid structure showing internal geometry.

airfoil where the heat transfer measurements were made. A low conductivity cement, Ceramacast 511, provided a thermal barrier in the region illustrated in Figure 6.

3.1.5 Test Vane Instrumentation

The method used to obtain heat transfer measurements is based on the work of Turner (Ref 4), who employed a 2-D plane of the test vane as a fluxmeter. The technique is implemented by measuring the internal and external boundary conditions of the test piece at thermal equilibrium and solving the steady-state heat conduction equation for the internal temperature field of the test piece. The heat transfer coefficient distribution can be directly obtained from the normal temperature gradient at the surface.

For the current studies, the external boundary conditions were measured using thermocouples installed in grooves on the exterior surface of the test vane. Average heat transfer coefficients and coolant temperatures for each of 10 radial cooling holes provided the internal boundary conditions for the finite element solution. The heat transfer coefficient for each cooling hole was calculated from the hole diameter, measured flow rate, and coolant temperature with a correction (Cr in Figure 6) applied for thermal entry length.

Figure 7 shows the distribution of thermocouples for the C3X airfoil. The airfoil surface was instrumented with 81 0.5 mm (0.020 in.) dia sheathed CA thermocouples. The thermocouple junctions were located in the fully 2-D region of the airfoil in a plane near midspan. Thermocouple leads were brought off the vane in 0.58 mm (0.023 in.) deep radial grooves, covered with cement, and blended by hand to provide a smooth surface. The vane was fabricated of ASTM type 310 stainless steel, which has a relatively low thermal conductivity, thereby minimizing the error introduced by the grooves. The vane also contained grooved thermocouples and static pressure tap instrumentation on the surface within the showerhead array.

Each radial cooling tube of the test vane was instrumented with a static pressure tap and thermocouple at the vane inlet and exit. The static pressure tap was located upstream of the thermocouple in all cases. The flow to each cooling tube was measured using a calibrated orifice meter.

TE84-8613
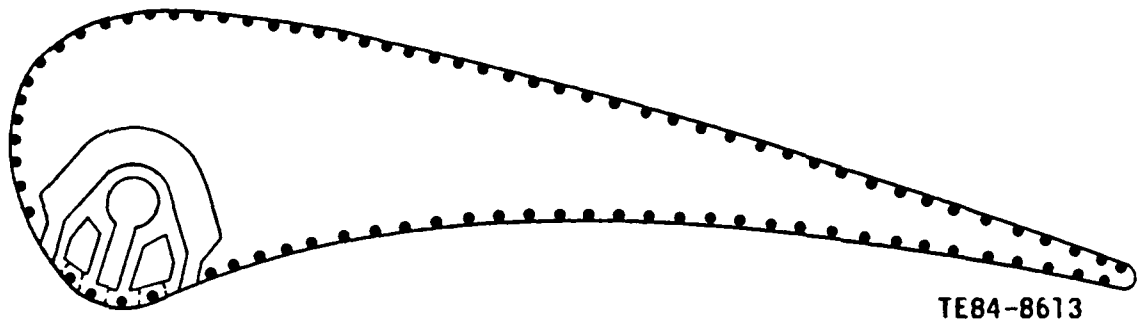
Figure 7. Surface thermocouple locations for leading edge film-cooled C3X airfoil.

Each film-cooling plenum was instrumented with thermocouples and pressure probes at various locations to provide the coolant supply temperature and pressure. The flow rate to each plenum was measured using a calibrated orifice meter.

The vane surface adjacent to the thermal barrier was instrumented with 11 1.0 mm (0.040 in.) dia closed tip CA thermocouples. These thermocouples were used to check the adiabatic boundary assumption and provided a backup boundary condition if the adiabatic assumption was proven invalid.

The test vane was instrumented with surface static pressure taps in addition to the heat transfer instrumentation. Twenty-seven taps were located around the airfoil outer surface in a plane near midspan. The spacing was varied to provide a higher density of instrumentation in high pressure gradient regions. Figure 8 illustrates the relative locations of surface pressure taps on the C3X airfoil. Figure 9 shows the technique used to install the static pressure taps. Stainless steel tubing, 0.51 mm (0.020 in.) dia, was laid in a radial surface groove, and the end of the tubing was bent 90 deg to achieve surface normal orientation. The tube was secured to the adjacent vane surface by laser welding. The excess tube length was then removed and dressed down to ensure a flush local condition. The remainder of the groove was filled with cement and hand blended smooth with the airfoil surface similar to the thermocouple installations.

3.2 DATA ACQUISITION AND REDUCTION

3.2.1 Data Acquisition System

The control room of the ACF contains a dedicated computer-controlled data acquisition system shown schematically in Figure 10. Data input signals are

16

TE84-8614
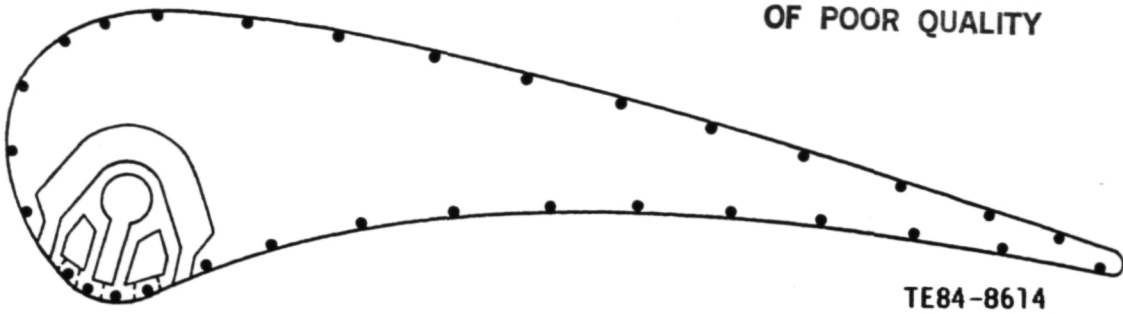
Figure 8. Surface static pressure tap locations for leading edge film-cooled C3X airfoil.
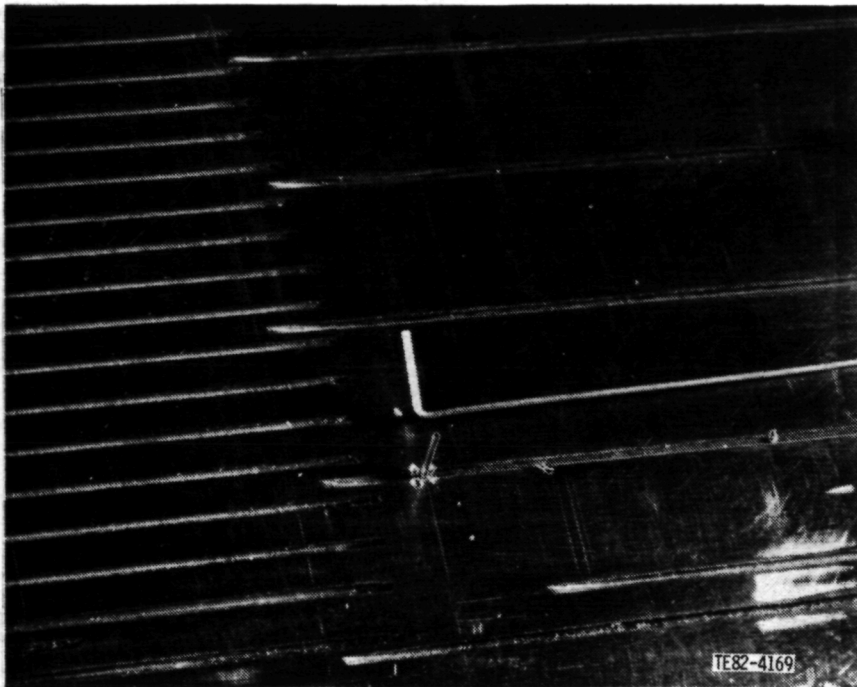
Figure 9. Installation of vane surface static pressure taps.

multiplexed by a Hewlett-Packard (HP) Model 2911A/B 200-channel random access signal scanner, with analog to digital (A/D) conversion performed by an HP 3456A integrating digital voltmeter. High-speed A/D conversion capabilities are provided by a 16-channel Model HP 2311A multiplexer-A/D converter system. The computer main frame is a Model HP 2112B with 192 K words of memory available under the RTE-IVB operating system.

Input/output devices complementing this central processing unit (CPU) consist of an HP 7900A magnetic disk drive (2.4 M words), line printer, cathode ray tube (CRT) terminal, dual cassette tape units, and digital pen plotter. A

17
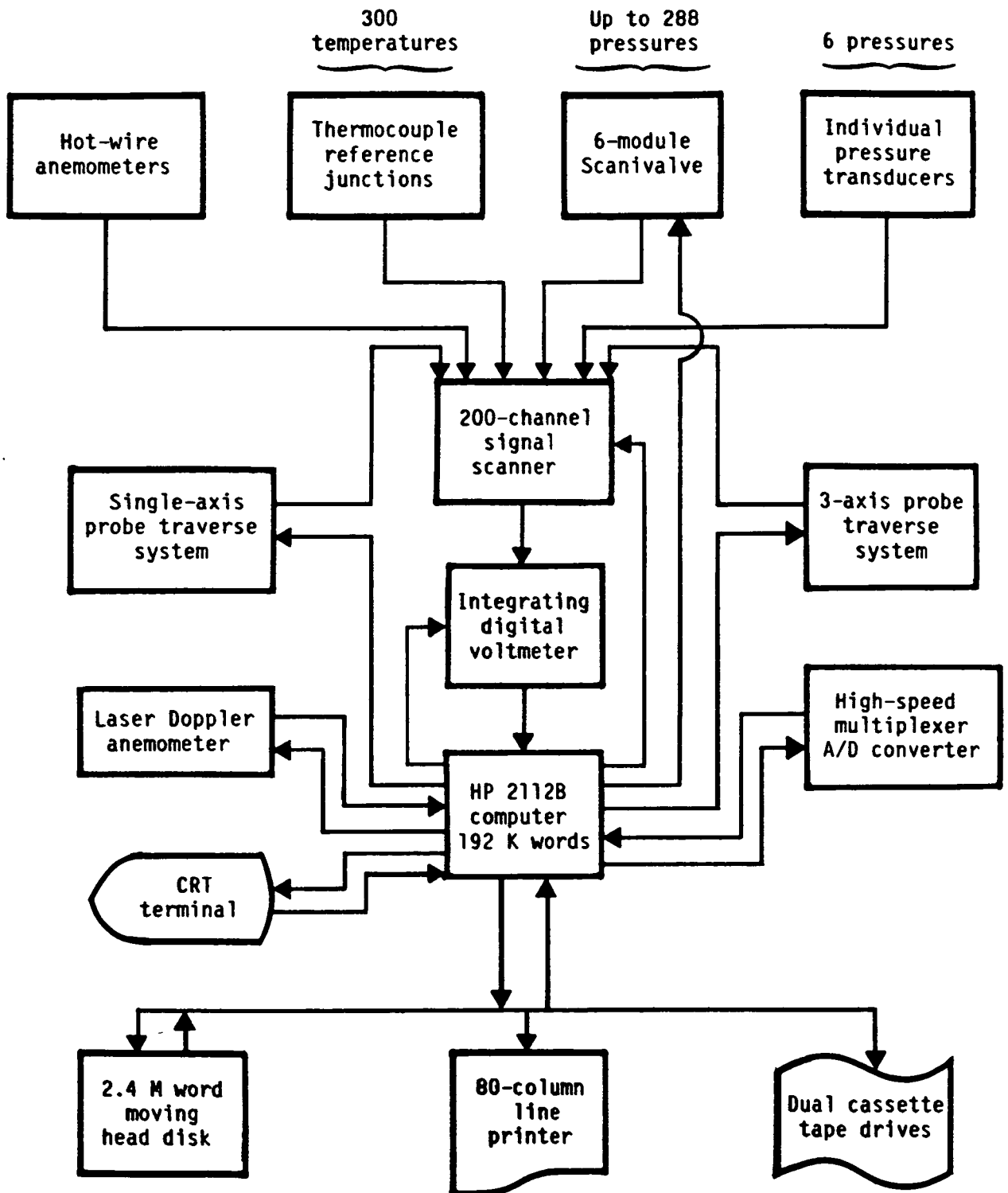
Figure 10. Schematic of computer-controlled data acquisition system.

multitask, facility-oriented software system that contains general subprograms to do all routine control and measurement tasks exists. The system is flexible and provides for real-time facility monitoring and diagnosis of instrumentation or control problems. Software routines developed to meet the specific data acquisition requirements of individual experiments are incorporated into the main system as interchangeable program segments.

3.2.2 Data Acquisition Software

The data acquisition software written for this experimental program operated in three phases. The first phase monitored and displayed the cascade operating condition as the desired run conditions were being established. The facility instrumentation used to determine the cascade operating point is described previously in this subsection in "Facility Instrumentation and Geometry." Cascade inlet total pressure and temperature were based on readings at the upstream core flow rakes. The cascade inlet static pressure was defined as the average of readings at nine endwall static pressure taps near the upstream core rakes. The average exit static pressure was taken as the average of readings of 13 endwall static pressure taps at the cascade exit plane. The average wall temperature was defined as the average of the midspan vane surface temperatures. Coolant total pressure and temperature were taken as the average of the coolant plenum pressures and temperatures, respectively. The operating conditions of the Mach number, the Reynolds number (based on true chord), coolant to free-stream pressure ratio, and coolant to free-stream temperature ratio were calculated from these averaged quantities and displayed periodically on a CRT during the setup procedure until a satisfactory steady-state condition was achieved. The change in temperature of the vane surface over a fixed period of time was then monitored until thermal equilibrium was established.

The second phase of the data acquisition software sampled, averaged, and stored the raw aerodynamic and heat transfer data after the desired steady-state operating conditions were achieved. All of the data were read in a single sweep that was repeated several times to provide time averaged, steady-state values. The averaged values for a given run were then stored in a permanent file on a magnetic disc in the laboratory.

All necessary calculations were performed in the third phase. The final run conditions, vane surface static pressure distributions, and temperature distributions were established. The change in vane surface temperature between readings was checked to verify thermal stability during data acquisition. Mass flow rates to the film-cooling plenums were established from the orifice meter data. The average coolant plenum to free-stream pressure ratio and temperature ratio were calculated along with a blowing ratio (mass flux ratio) based on inlet conditions. Mass flow rates for the radial cooling tubes were established from the orifice meter data.

The average coolant temperature for each tube at the vane surface temperature measurement plane was calculated, assuming a linear temperature rise through the vane cooling hole. The Reynolds number for each cooling tube was determined from the measured flow rate, cooling hole diameter, and viscosity based on the average coolant temperature. The Prandtl number (Pr) for the coolant flow was calculated from the average coolant temperature. The Nusselt number (Nu_D) was then calculated from the following relationship for turbulent flow in a smooth pipe:

$$Nu_D = Cr\ (0.022\ Pr^{0.5}\ Re_D^{0.8})$$

The correction factor (Cr) is a function of the Prandtl number, the cylinder diameter Reynolds number (Re_D), and the streamwise coordinate at the cooling hole diameter (x/D), which corrects the Nu expression for a fully developed thermal boundary layer to account for thermal entrance region effects. The constant correction factor found in Ref 5 ranged from approximately 1.03 to 1.12 for the Prandtl number, cylinder diameter Reynolds number, and streamwise coordinate at the cooling hole diameter values encountered in this experiment. The average heat transfer coefficient for each cooling hole was then calculated from the Nusselt number, hole diameter, and thermal conductivity.

After the third phase was completed, all of the aerodynamic and heat transfer data for one run were output to a cassette tape and transferred into the Panvalet mass storage system of the Allison Data Center. This data was then accessed by the finite element program.

20

3.2.3 Heat Transfer Measurement Technique

The heat transfer measurement technique used a finite element solution of the 2-D Laplacian heat conduction equation for the vane internal temperature field using measured surface temperatures and internal cooling hole heat transfer coefficients as boundary conditions. The technique is illustrated in Figure 11. Inputs to the program in addition to measured exterior surface temperatures and coolant hole heat transfer coefficients were the 2-D vane cross-sectional geometry, the thermal conductivity of the vane material, gas-stream total temperature, and the average coolant temperature for each radial hole.

An FEM of the midspan cross section of the airfoil was constructed by using Allison's computer-aided design/computer-aided manufacturing (CAD/CAM) facilities. The finite element grids used for the leading edge film-cooled airfoil were previously shown in Figure 6. Approximately 200 nodes were located around the airfoil outer surface. A special effort was made to arrange sufficient elements in the thin trailing edge region to ensure the quality of the solution in that region.

A linear fit of all measured midspan surface temperatures for a given run was used to provide the temperature for each surface nodal point of the FEM. Figure 12 shows a typical plot of vane surface to gas absolute temperature ratio (T_w/T_g) for one run. The finite element program solved for the vane internal temperature distribution, as previously indicated. Hot gas side local heat transfer coefficients were derived from the surface normal temperature gradient by equating the local normal conduction to the local convection.

3.2.4 Data Uncertainties

An uncertainty analysis was performed for the key experimental parameters, using the technique of Kline and McClintock (Ref 6). The accuracy of the external heat transfer coefficient measurement is primarily dependent on the accuracy of the external vane surface and free-stream gas temperature measurements, the geometry description for the finite element program, the radial cooling hole heat transfer coefficient calculation, and the knowledge of the thermal conductivity of the vane material.
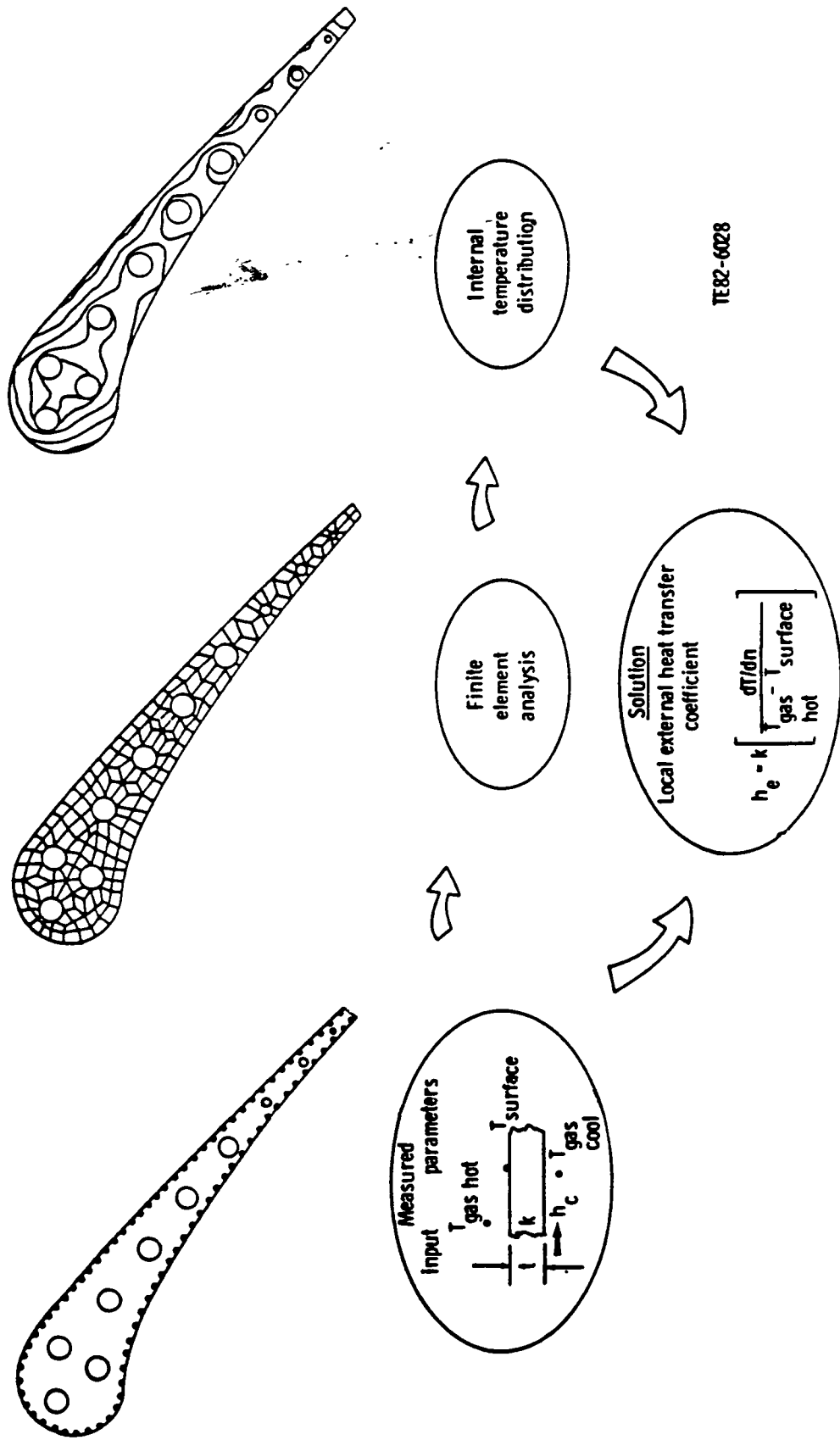
Figure 11. Heat transfer data reduction technique.
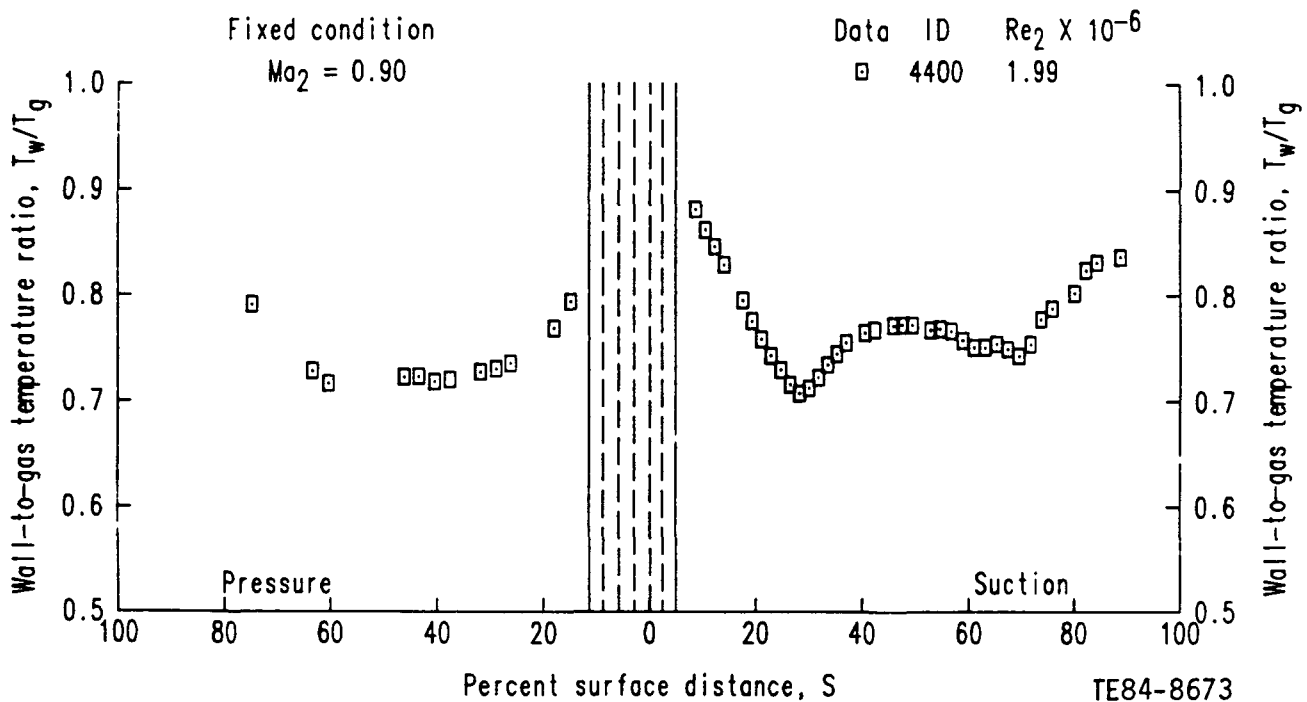
Figure 12. Vane surface to gas absolute temperature ratio
distribution of the leading edge film-cooled C3X vane.

Details on the uncertainties of the individual measurements are discussed in
Ref 1. Using the uncertainties of the individual measurements, a calculation
of the overall uncertainty in the external heat transfer coefficient was made
using the methods of Ref 6. Due to the variation in the airfoil thickness
along the chord, it was necessary to calculate the uncertainty at several
points. The maximum uncertainty, based on minimum wall thickness (distance
from cooling hole to exterior surface), was calculated at various regions on
the airfoil. The values ranged from ± 6.2% to ± 23.5%, as shown in Table V.
The uncertainties increase significantly beyond midchord due to a decrease in
airfoil thickness.

The uncertainty was also calculated for the test parameters, based on the
methods of Ref 6. The results are given in Table V.

The uncertainties presented in this subsection are intended to provide the
analyst with an indication of the uncertainty in absolute level in using the
data for verification purposes. In comparing data from runs for a given cas-
cade (i.e., looking for Reynolds number trends, etc), the uncertainty in the
comparisons is considerably less than the values just described. This

Table V.
Experimental uncertainties.

Uncertainty in heat transfer coefficient measurements

Pressure surface		Suction surface	
Percent surface arc	Percent uncertainty	Percent surface arc	Percent uncertainty
16-23	± 6.3	8-31	± 6.7
23-34	± 6.6	31-39	± 6.2
34-45	± 7.3	39-49	± 6.5
45-55	± 8.9	49-58	± 7.1
55-66	±13.3	58-67	± 8.6
66-78	±11.6	67-76	±11.9
78-89	±20.1	76-85	±10.9
89-100	±23.5	85-94	±15.8
		94-100	±23.5

Uncertainty in test parameters

Reynolds number, Re	±3.1%
Mach number, Ma	±0.9%
Wall to gas temperature ratio, T_w/T_g	±2.0%
Coolant to free-stream pressure ratio, P_c/P_t	±1.0%
Coolant to free-stream temperature ratio, T_c/T_g	±4.0%

difference is due to the fact that several of the variables contributing to the uncertainty do not change from run to run. For example, an error of 3% in the airfoil thermal conductivity would result in an error in the absolute value of the heat transfer coefficient, but would be of the same order for each run. Thus comparisons of runs from a given cascade would not be affected. Reproducibility for a given cascade is on the order of ±2%.

3.3 TEST CONDITIONS

Experimental results were obtained over the range of operating conditions shown in Figure 13. Each nominal test condition is represented by a four-digit code number. Each digit of the code number corresponds to one of the control variables of the experiment. The first digit corresponds to exit Mach number, the second to exit Reynolds number, the third to coolant to gas temperature ratio (T_c/T_g), and the fourth to coolant to free-stream pressure ratio (P_c/P_t). Exit Reynolds numbers referred to in the figure are based on airfoil true

Figure 13. Test matrix.
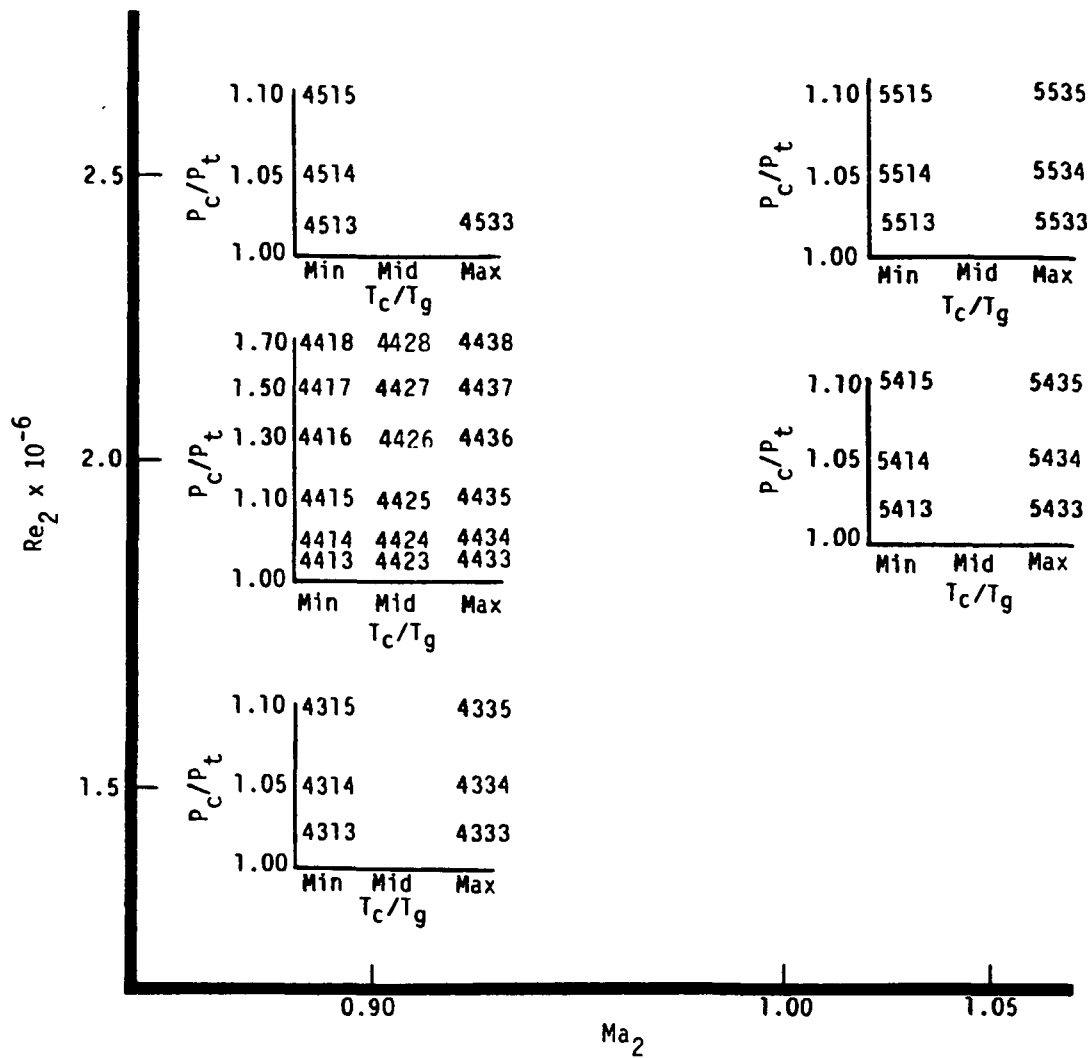
Code No.	Control variable by position			
	Position 1-- Ma$_2$	Position 2-- Re$_2$ x 10^{-6}	Position 3-- T$_c$/T$_g$	Position 4-- P$_c$/P$_t$
0			No coolant flow	1.00
1			Min	
2			Mid	
3		1.5	Max	1.02
4	0.90	2.0		1.05
5	1.05	2.5		1.10
6				1.30
7				1.50
8				1.70

TE84-8617

chord, and exit Mach numbers are based on measured inlet total pressure and average measured exit plane static pressure. All tests were conducted at a nominal gas stream total temperature of 689°K (1240°R), and a turbulence intensity level of 6.5%, based on LDA measurements taken previously as reported in Ref 1. The actual run conditions corresponding to each four-digit code number are given in Table VI.

In Table VI, P_t1 is the inlet total pressure, T_t1 is the gas stream inlet total temperature, Ma_1 and Ma_2 are inlet and exit Mach numbers, respectively, Re_1 and Re_2 are inlet and exit Reynolds numbers based on the true chord, T_w/T_g is the arc-distance weighted nodal average wall-to-gas absolute temperature ratio, T_c/T_g is the coolant to gas absolute temperature ratio, P_c/P_t is the average coolant to free-stream pressure ratio, and coolant (clnt) flow rate is the total film-coolant mass flow rate.

The cascade Reynolds number range was achieved by varying the cascade mass flow rate from approximately 2.27 kg/s (5 lbm/sec) to 4.54 kg/s (10 lbm/sec). At a given Reynolds number condition, exit Mach number levels were independently established by adjusting the cascade exit pressure with a controllable exhaust valve. The coolant to free-stream pressure ratio was varied by controlling the film-cooling mass flow rate. The coolant to gas absolute temperature ratio levels were controlled by an electric heating system. Some variation occurred in the coolant to gas absolute temperature ratio parameter due to the changes in the influence of the test hardware on the onboard coolant supply temperature as the other parameters were varied. The larger variations occur at the maximum and minimum coolant to gas absolute temperature ratio levels at the higher blowing rates (P_c/P_t = 1.3 to 1.7).

3.4 DISCUSSION OF EXPERIMENTAL RESULTS

Data from the experimental program are tabulated by run code in Appendix A. Included in the tabulation are the heat transfer coefficient distributions and the vane surface temperature distributions. The location of each measurement is expressed as a percent of surface length and a percent of axial chord. Appendix A also contains tabulated blowing ratio data. The baseline (i.e., no discrete injection) heat transfer coefficient distribution plots and all data

Table VI.
Test conditions summary.

RUN CODE	PT1 KPA	PT1 PSIA	TT1 DEG K	TT1 DEG R	MA1	RE1 X10E-6	MA2	RE2 X10E-6	TW/TG	PC/PT	TC/TG	CLNT FLOW RATE KG/SEC	CLNT FLOW RATE LBM/SEC
4300	208.65	30.26	692.	1246.	0.16	0.38	0.90	1.50	0.75	1.019	0.75	0.171E-02	0.378E-02
4313	207.36	30.07	692.	1246.	0.16	0.38	0.89	1.50	0.74	1.051	0.72	0.315E-02	0.695E-02
4314	207.71	30.13	691.	1244.	0.16	0.38	0.89	1.51	0.74	1.100	0.69	0.411E-02	0.906E-02
4315	207.35	30.07	691.	1244.	0.16	0.38	0.89	1.51	0.74	1.019	0.83	0.150E-02	0.330E-02
4333	209.55	30.39	695.	1251.	0.16	0.38	0.90	1.50	0.75	1.057	0.83	0.251E-02	0.553E-02
4334	206.19	29.91	688.	1238.	0.16	0.38	0.90	1.50	0.75	1.105	0.84	0.334E-02	0.736E-02
4335	206.66	29.97	687.	1241.	0.16	0.38	0.90	1.50	0.78		0.76		
4400	273.44	39.66	691.	1236.	0.16	0.51	0.90	1.99	0.77	1.018	0.74	0.264E-02	0.582E-02
4413	276.44	40.09	695.	1244.	0.16	0.50	0.89	1.99	0.77	1.058	0.71	0.408E-02	0.900E-02
4414	275.66	39.95	689.	1243.	0.16	0.51	0.90	1.99	0.77	1.100	0.69	0.604E-02	0.133E-01
4415	275.49	39.98	690.	1240.	0.16	0.50	0.89	1.99	0.76	1.310	0.65	0.994E-01	0.219E-01
4416	275.06	39.96	692.	1245.	0.16	0.51	0.89	2.00	0.77	1.501	0.82	0.138E-01	0.304E-01
4417	277.17	40.18	690.	1242.	0.16	0.51	0.89	2.00	0.77	1.679	0.83	0.166E-02	0.367E-01
4418	277.25	40.36	694.	1250.	0.16	0.51	0.90	2.00	0.78	1.019	0.82	0.246E-02	0.543E-02
4424	278.34	40.37	693.	1248.	0.16	0.50	0.89	2.00	0.78	1.050	0.82	0.342E-02	0.755E-02
4425	278.41	40.38	693.	1248.	0.16	0.50	0.89	2.01	0.77	1.101	0.81	0.466E-02	0.103E-01
4426	275.19	39.96	688.	1239.	0.16	0.51	0.90	2.00	0.77	1.300	0.84	0.753E-02	0.166E-01
4427	276.74	40.06	686.	1239.	0.16	0.50	0.90	1.99	0.79	1.518	0.84	0.166E-02	0.221E-01
4428	277.29	40.22	692.	1235.	0.16	0.50	0.89	2.00	0.79	1.715	0.86	0.100E-01	0.254E-02
4433	276.76	40.29	691.	1246.	0.16	0.50	0.90	2.00	0.79	1.050	0.89	0.115E-01	0.472E-02
4434	276.30	40.07	690.	1244.	0.16	0.50	0.90	2.00	0.81	1.099	0.90	0.214E-02	0.698E-02
4436	275.82	40.00	689.	1245.	0.16	0.63	0.89	2.49	0.80	1.298	0.90	0.316E-02	0.942E-02
4437	275.93	40.04	692.	1243.	0.16	0.62	0.90	2.48	0.79	1.505		0.427E-02	0.151E-01
4438	276.67	40.14	690.	1241.	0.16	0.62	0.90	2.48	0.81	1.721		0.683E-01	0.187E-01
4500	345.67	50.14	689.	1237.	0.16	0.63	0.89	2.50	0.76	1.020	0.78	0.847E-02	0.232E-01
4513	342.87	49.73	693.	1247.	0.16	0.49	1.05	2.00	0.77	1.051	0.74	0.105E-01	0.852E-02
4514	341.97	49.60	692.	1246.	0.16	0.49	1.04	2.00	0.77	1.101	0.72	0.387E-02	0.124E-01
4515	341.60	49.60	690.	1242.	0.16	0.49	1.04	2.00	0.76	1.022	0.85	0.564E-02	0.173E-01
4533	268.07	38.88	689.	1251.	0.16	0.49	1.05	2.00	0.76	1.051	0.77	0.786E-02	0.686E-02
5400	268.63	38.67	693.	1249.	0.16	0.49	1.05	2.00	0.77	1.102	0.75	0.311E-02	0.600E-02
5413	266.82	38.64	692.	1244.	0.16	0.49	1.05	2.00	0.76	1.019	0.72	0.272E-02	0.884E-02
5414	266.14	38.70	690.	1242.	0.16	0.49	1.05	2.00	0.76	1.050	0.86	0.401E-02	0.123E-01
5415	268.24	38.91	695.	1251.	0.16	0.61	1.05	2.49	0.79	1.103	0.84	0.557E-02	0.335E-02
5433	268.75	38.89	694.	1249.	0.16	0.62	1.05	2.49	0.78	1.021	0.74	0.152E-02	0.595E-02
5434	267.75	38.83	691.	1244.	0.16	0.61	1.05	2.50	0.78	1.057	0.71	0.270E-02	0.824E-02
5435	331.50	48.08	687.	1246.	0.16	0.61	1.05	2.49	0.79	1.107	0.68	0.374E-02	0.874E-02
5500	329.50	47.79	687.	1237.	0.16	0.62		2.49		1.016	0.86	0.397E-02	0.135E-01
5513	331.28	48.05	689.	1236.	0.16	0.61		2.50		1.048	0.86	0.612E-02	0.194E-01
5514	331.85	48.13	692.	1240.	0.16	0.62		2.49		1.097	0.88	0.878E-02	0.515E-02
5515	332.61	48.24	690.	1243.	0.16	0.61		2.49				0.234E-02	0.789E-02
5533	331.99	48.15	692.	1245.	0.16	0.61		2.49				0.358E-02	0.110E-01
5535	333.11	48.31	689.	1241.	0.16			2.51				0.498E-02	

27

comparison plots showing the effects of leading edge (showerhead) film cooling are contained in Appendix B, although some representative data comparison plots are presented and discussed in the following paragraphs.

The goal of presenting the experimental heat transfer results is to isolate the differences between nonfilm-cooled and leading edge film-cooled heat transfer phenomena downstream of the showerhead array. This goal can be accomplished by calculating the ratio of the experimentally determined local Stanton number for cases where coolant is being ejected from the leading edge to the local Stanton number determined for the case where no coolant is added.

Rather than simply form the film-cooled Stanton number to non-filmed-cooled Stanton number ratio (St_{FC}/St_{NFC}), which would take on values about a "no difference" value of unity, an alternate parameter referred to as Stanton number reduction (SNR) is used. SNR is defined as

$$SNR = 1 - (St_{FC}/St_{NFC}) \qquad (1)$$

When SNR is greater or less than zero, it implies reduced or increased heat transfer levels, respectively. When SNR is equal to zero, it implies no difference in the heat transfer level. Forming SNR values along the entire test surface gives the actual SNR distribution for the airfoil. In addition, if the film-cooled Stanton number to nonfilm-cooled Stanton number ratio were determined using data obtained at equivalent exit Mach number and exit Reynolds number conditions, SNR would be approximately equal to the actual heat transfer coefficient reduction,

$$SNR = 1 - h_{FC}/h_{NFC} \qquad (2)$$

because $(\rho\, c_p\, u)_{e,NFC}/(\rho\, c_p\, u)_{e,FC}$ would be near unity. SNR results shown here and in Appendix B were formed using Equation (2).

Figures 14 and 15 illustrate the formation and type of information given by vane surface SNR distributions. All data shown in these figures were obtained at fixed operating conditions; i.e., $Ma_2 = 0.90$, $Re_2 = 2.0 \times 10^6$, $T_c/T_g = 0.8$. Variable blowing strengths ($P_c/P_t = 1.0$, 1.02, 1.05, and 1.10) were set at these

28
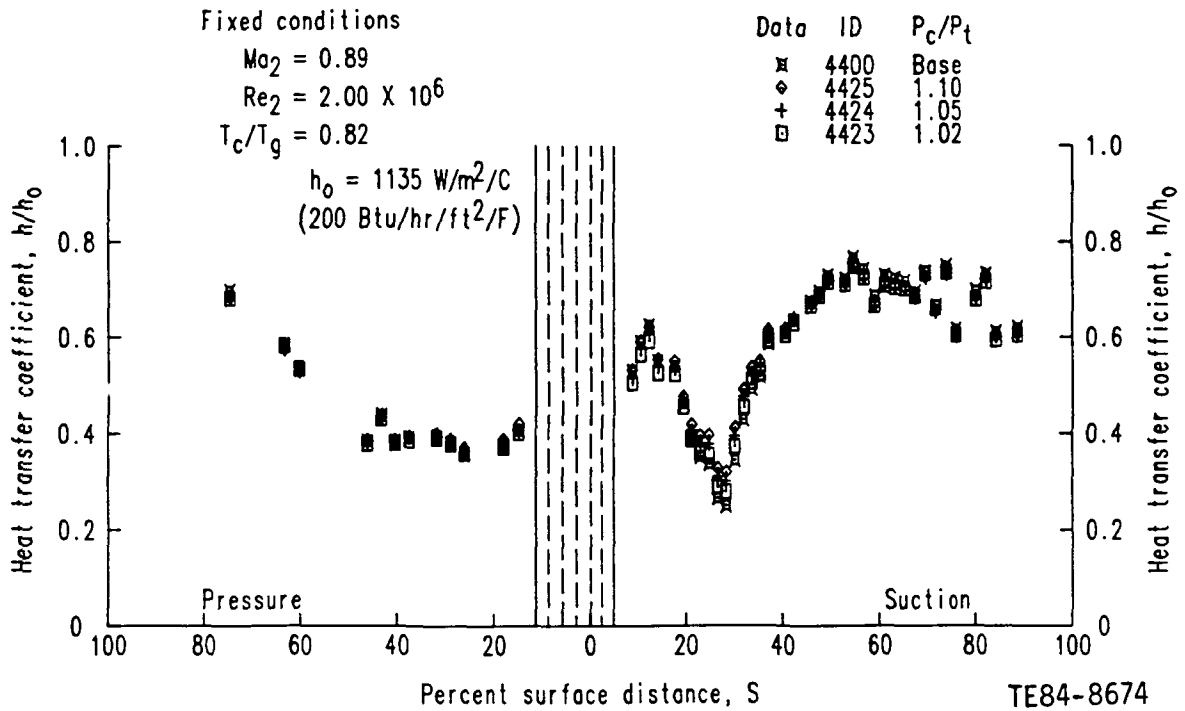
Figure 14. Variable blowing strength heat transfer coefficient data.
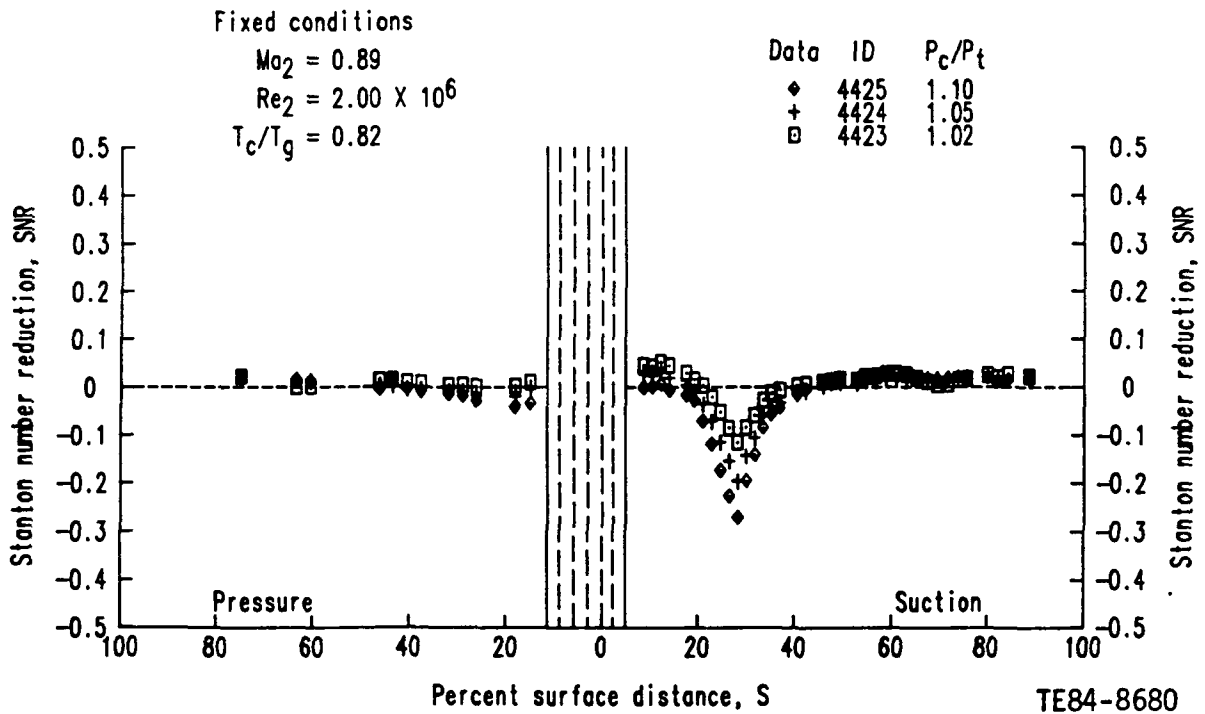
Figure 15. Variable blowing strength Stanton number reduction data.

conditions and heat transfer data were taken. The four different surface heat transfer coefficient distributions determined from the cascade data at the four coolant to free-stream pressure ratio conditions are shown in Figure 14. A value of $P_c/P_t = 1.0$ signifies that no coolant is being ejected and $P_c/P_t > 1.0$ signifies that coolant is being ejected. Using the results of Figure 14 and the SNR definition in Equation (2), surface SNR distributions can be constructed. These distributions are shown in Figure 15. Because each SNR distribution shows only the difference between a given film-cooled and baseline nonfilm-cooled condition, an SNR data presentation is useful for discussing phenomena unique to the film-cooled problem.

In addition, another parameter of significance in characterizing film cooling performance is the parameter theta, θ, defined as

$$\theta = (T_c - T_g)/(T_w - T_g) \tag{3}$$

Figure 16 shows the formation of local theta distributions for the data ($P_c/P_t > 1.0$) depicted in Figures 14 and 15. Because the coolant and gas temperatures are a constant, the local variation in theta is due to the vane surface temperature variation (see Figure 12).

Characteristic showerhead injection heat transfer trends were obtained for the C3X airfoil. Starting first with the exit Mach number effect, typical nonblown measured surface static pressure distributions corresponding to the two cascade expansion ratios tested are shown in Figure 17 and tabulated in Table VII. As observed previously in Reference 1, the primary effect of the exit Mach number variation is to alter the suction surface pressure distribution downstream of the throat (S > 40). The resultant effect on the measured baseline heat transfer coefficient distribution is shown in Figure 18. Figures 19 and 20, showing local SNR and theta distributions, respectively, illustrate the effect of the exit Mach number at blowing conditions. These figures show a comparison of two coolant injection runs at exit Mach numbers of 0.9 and 1.05 while holding all other parameters (such as Re_2, T_c/T_g, and P_c/P_t) constant. As indicated by this comparison, there is no apparent influence of exit Mach number on SNR distributions over the range tested. This conclusion is further supported by the Mach number effect results shown in Appendix B.

Table VII.
C3X vane surface static pressure data.

Surface distance--%	Axial chord--%	P_s/P_t	
		$Ma_2 = 0.90$	$Ma_2 = 1.05$
Suction surface			
15.65	21.81	0.7146	0.6941
19.54	30.49	0.6119	0.6063
27.40	44.01	0.5018	0.4945
34.35	51.96	0.5525	0.5424
41.32	58.35	0.5438	0.4792
55.16	69.63	0.6045	0.5127
68.60	79.58	0.5768	0.4736
76.06	84.90	0.5774	0.4738
89.98	94.22	0.5667	0.4310
94.81	97.17	0.5741	0.4107
Pressure surface			
20.21	23.00	0.9836	0.9831
28.87	33.84	0.9786	0.9781
37.42	43.61	0.9706	0.9695
45.43	52.69	0.9598	0.9564
54.55	60.91	0.9361	0.9341
71.67	75.62	0.8580	0.8525
80.60	82.51	0.7970	0.7860
88.80	88.35	0.7434	0.7224
97.30	94.14	0.6221	0.5818
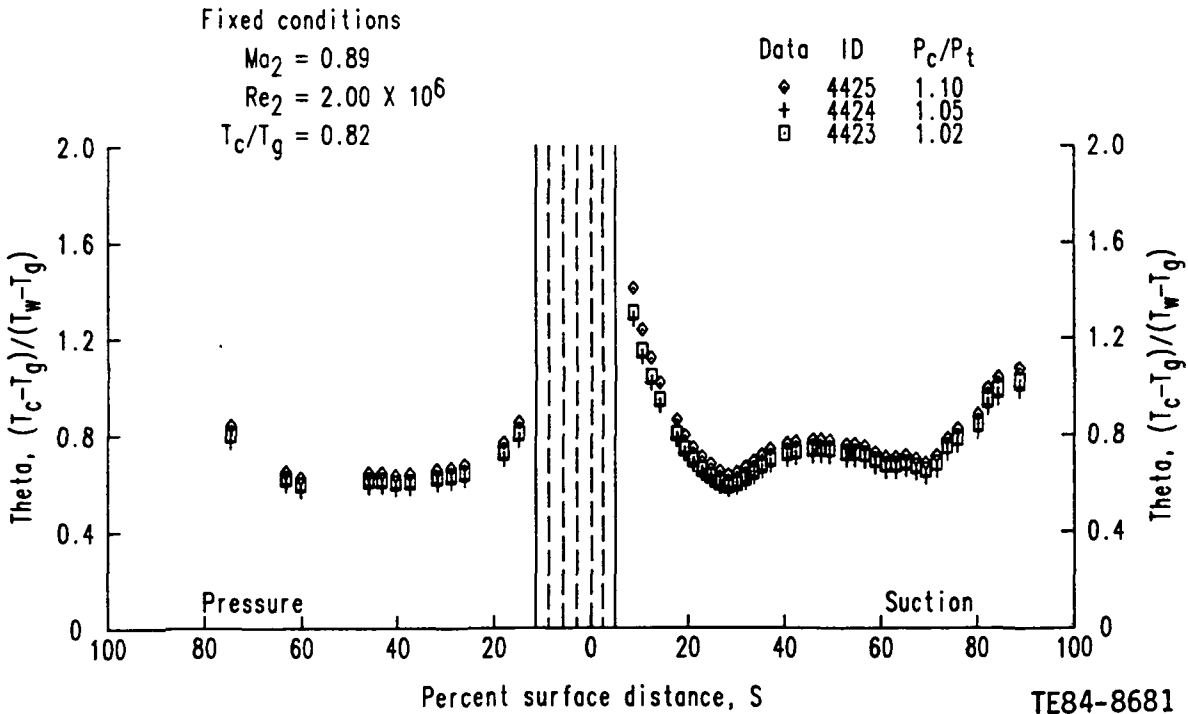
Figure 16. Variable blowing strength theta data.

TE84-8681

31
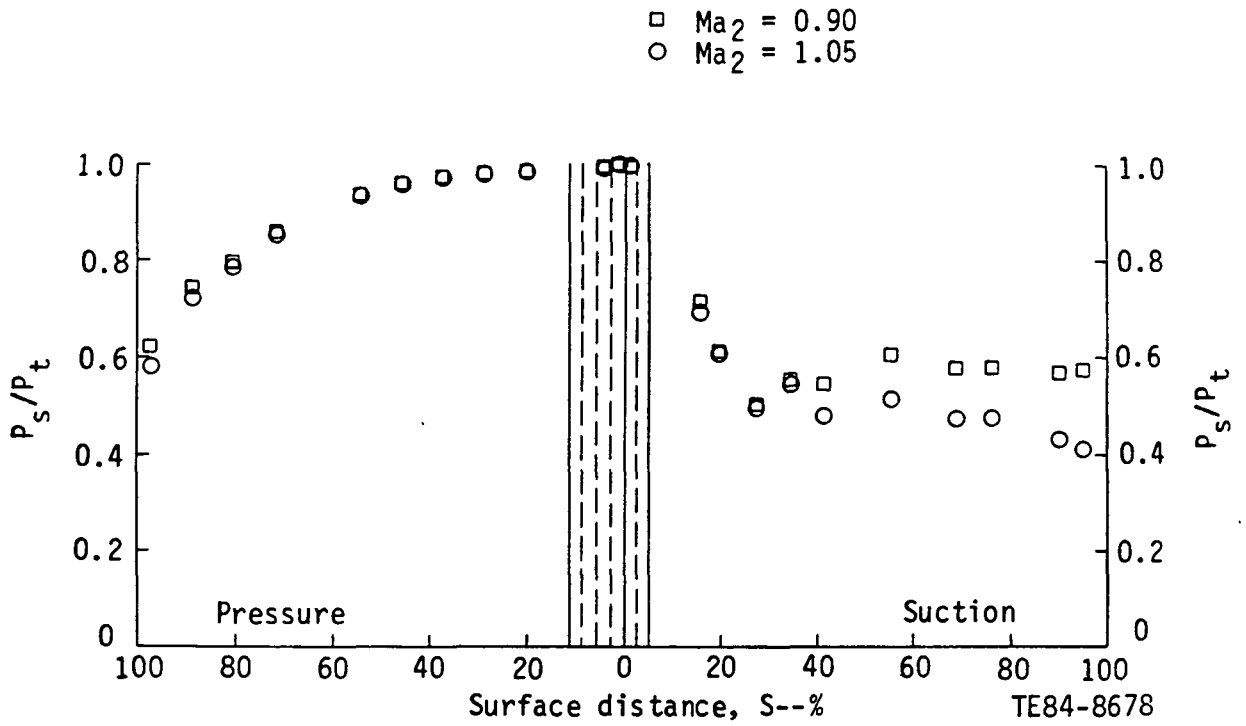
Figure 17.   The effect of the exit Mach number variation on the C3X vane
surface static pressure distribution.
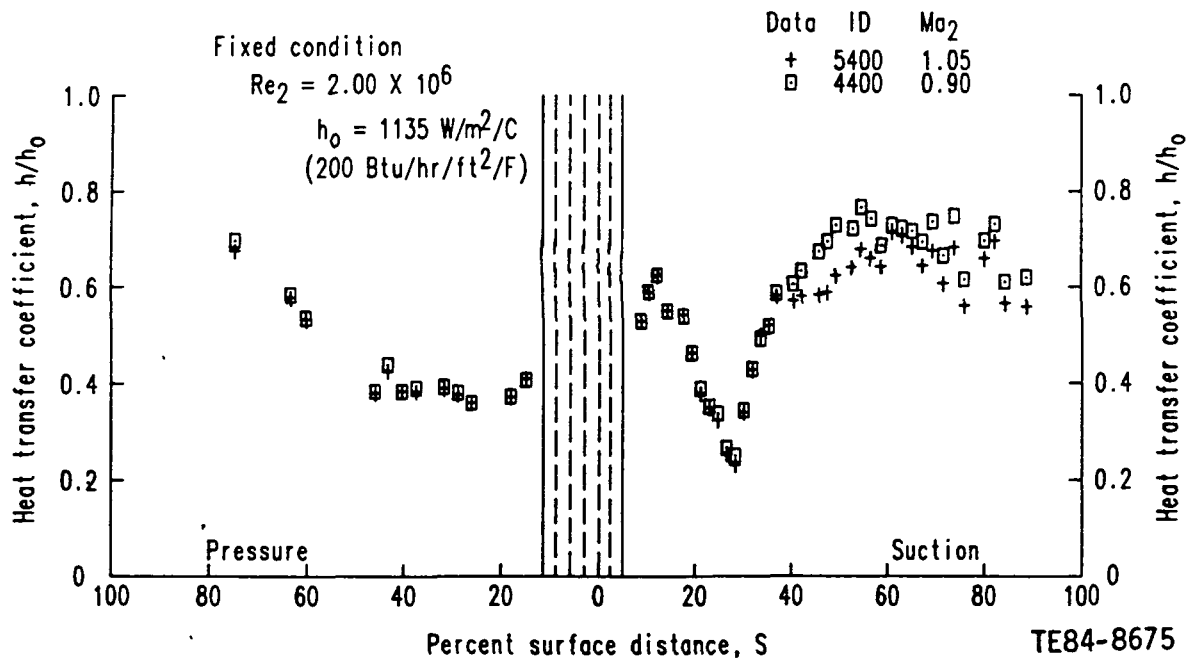
Figure 18.   The effect of the exit Mach number variation on the C3X vane heat
transfer coefficient distribution.
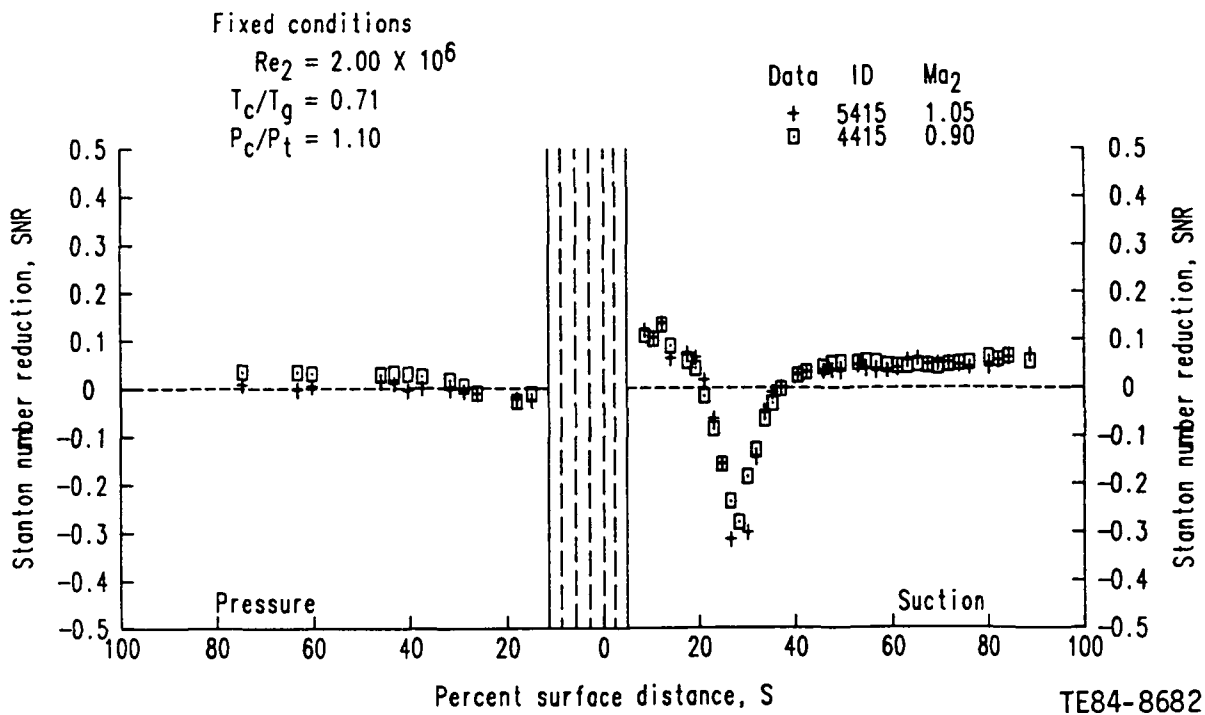
Figure 19.   The effect of the exit Mach number variation on Stanton
number reduction distribution.
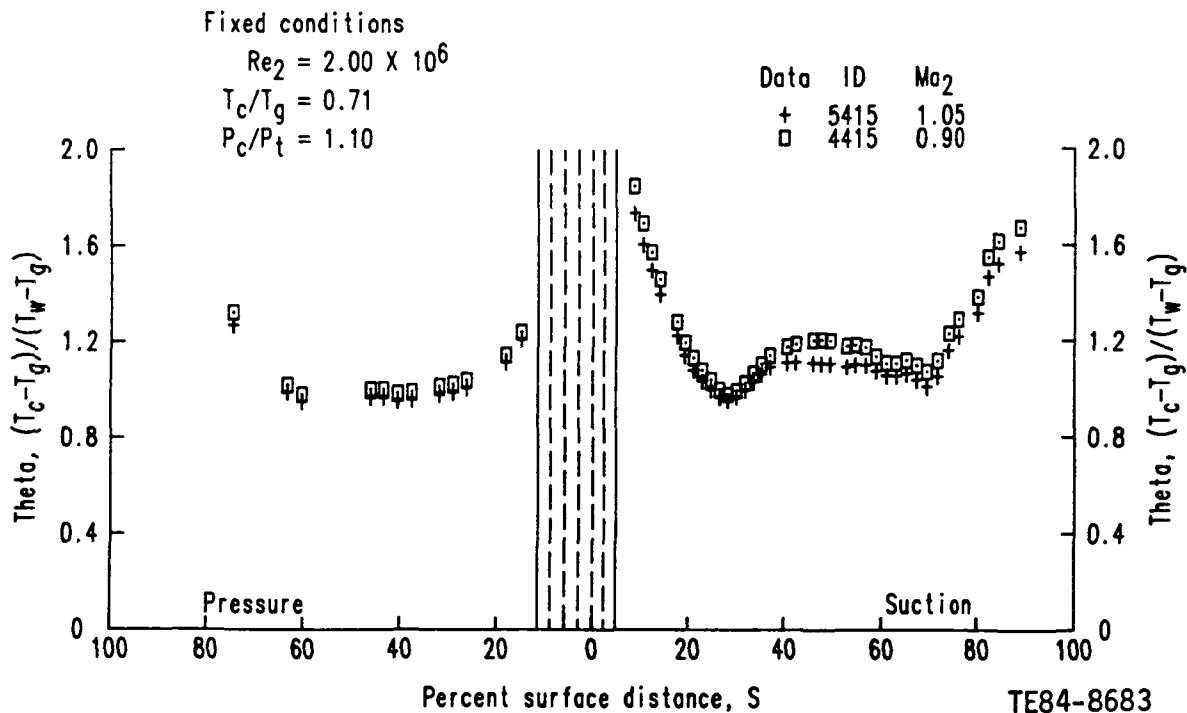
Figure 20.   Theta distribution for the exit Mach number variation.

The effect of exit Reynolds number variation on the baseline heat transfer co-efficient distribution is shown in Figure 21. As expected, the overall heat transfer levels systematically increase as the exit Reynolds number increases. In addition, the onset and extent of the indicated suction surface transitional zone also exhibits a marked response to the change in the exit Reynolds number levels. Representative SNR and theta data, indicative of differences associated with exit Reynolds number variation (Ma_2, T_c/T_g, and P_c/P_t fixed), are shown in Figures 22 and 23. The main qualitative difference in the results is the location of the zone of negative SNR (i.e., increased heat transfer) on the suction surface. Figures 21 and 22 together indicate that because the transition zone location changes as the exit Reynolds number is varied, the preturbulent region most affected by the injection process would be shifted. The progressively earlier location of the minimum suction surface SNR with increasing Reynolds number is consistent with the expected analytical transition origin versus Reynolds number models. The absence of a definitive trend difference on the pressure surface suggests a less well-defined transition process.
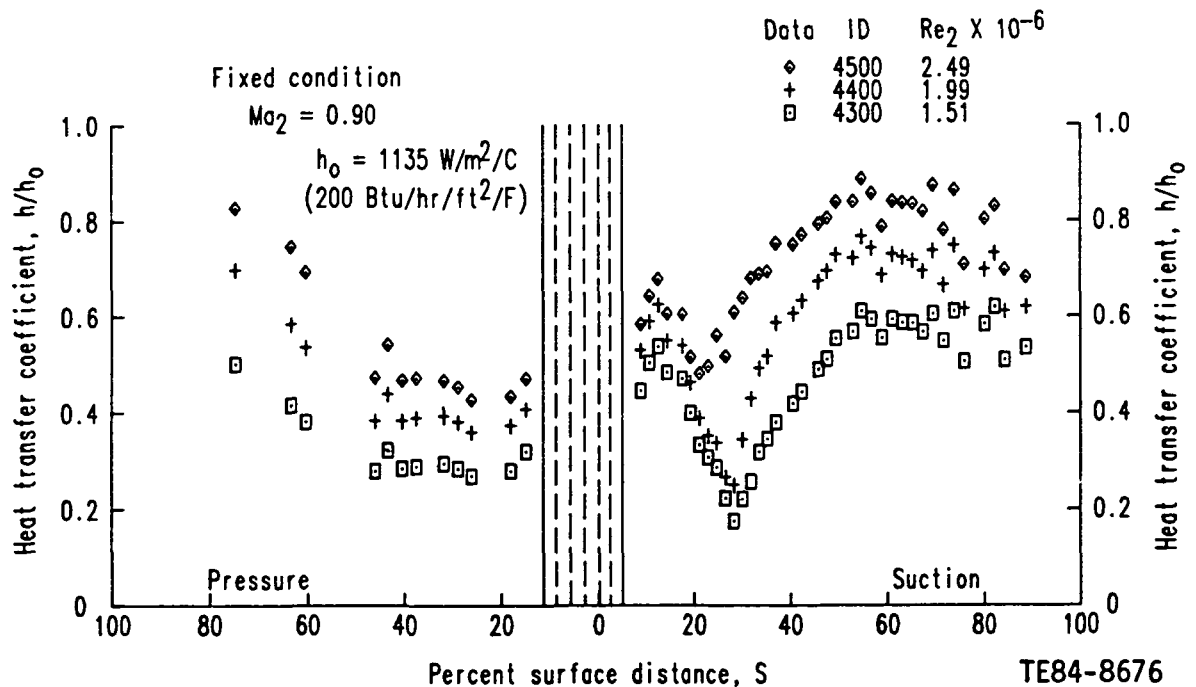
Figure 21. The effect of the exit Reynolds number variation on the C3X vane heat transfer coefficient distribution.

Fixed conditions

$Ma_2 = 0.90$

$T_c/T_g = 0.71$

$P_c/P_t = 1.10$

Data	ID	$Re_2 \times 10^{-6}$
◊	4515	2.48
+	4415	1.99
▣	4315	1.50

Pressure

Suction

Percent surface distance, S

TE84-8684
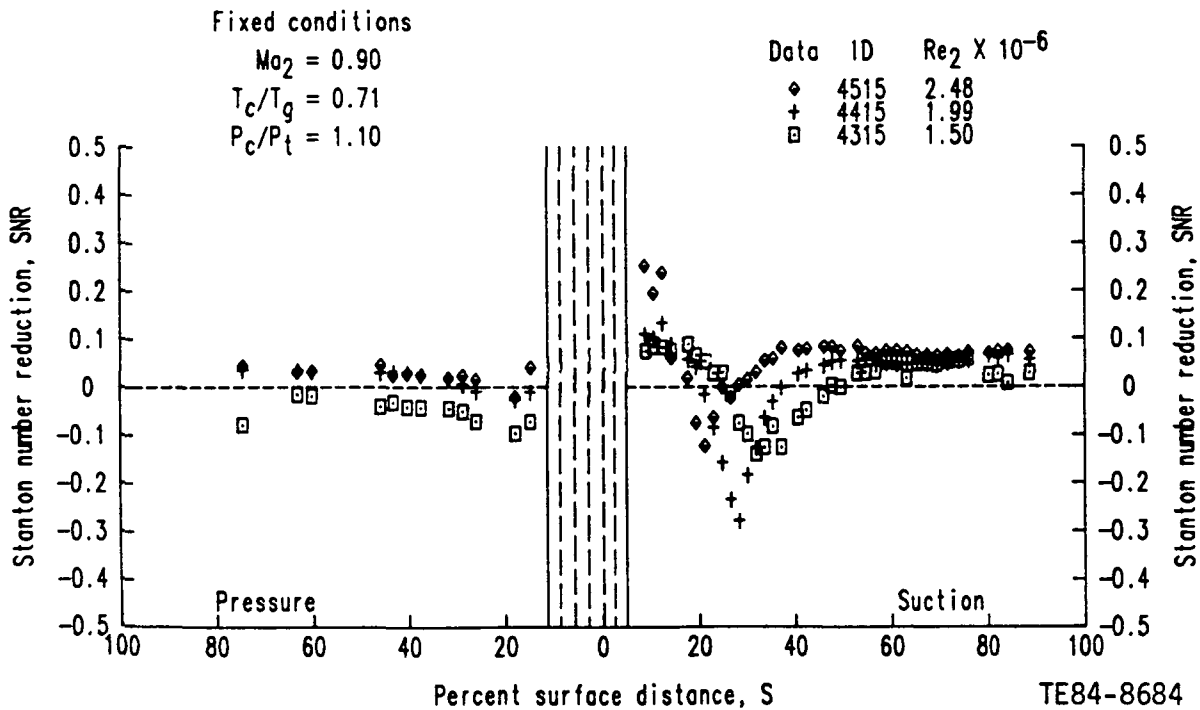
Figure 22.   The effect of the exit Reynolds number variation on Stanton number reduction distribution.

Fixed conditions

$Ma_2 = 0.90$

$T_c/T_g = 0.71$

$P_c/P_t = 1.10$

Data	ID	$Re_2 \times 10^{-6}$
◊	4515	2.48
+	4415	1.99
▣	4315	1.50

Pressure

Suction

Percent surface distance, S

TE84-8685
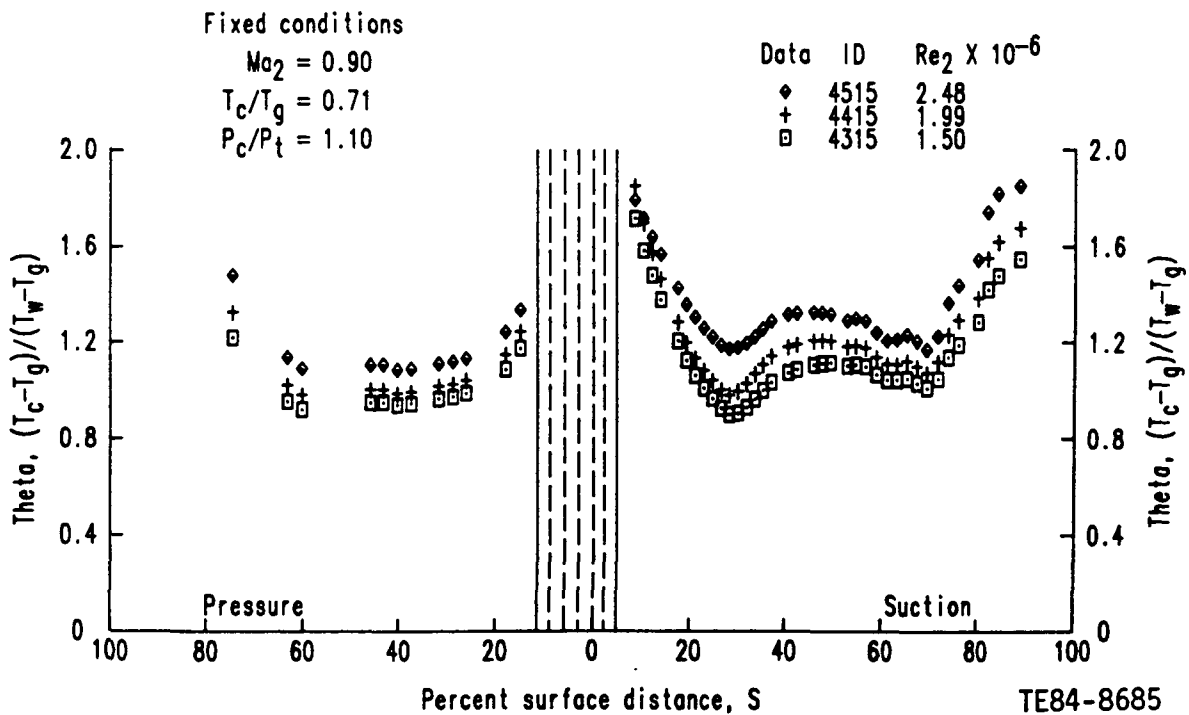
Figure 23.   Theta distribution for the exit Reynolds number variation.

The characteristic effect of blowing strength variation is illustrated by the SNR differences shown in Figure 15. These results indicate that the major differences in film-cooled heat transfer levels occur on the suction surface between 20% and 40% of the surface distance. This region corresponds to the suction surface transition zone. Over the range of blowing strengths represented in Figure 15 (P_c/P_t = 1.02 to 1.10), the primary effect of leading edge film cooling is to increase the preturbulent boundary layer heat transfer levels (i.e., SNR < 0 for S < 40).

This preturbulent increase is similar in character to the increase that would be expected to be caused by increasing the free-stream turbulence intensity from a baseline state. The discrete injection process apparently acts as a turbulence promoter. Although the pressure surface seems to be unaffected in view of the results shown in Figure 15, the same surface phenomenon that occurs on the suction surface is present but only to a lesser degree. This statement is supported by the results shown in Figures 24, 25, and 26. The data shown in these figures were obtained at the same fixed operating conditions (Ma_2, Re_2, and T_c/T_g) as those in Figures 14, 15, and 16 but at higher blowing strengths (P_c/P_t = 1.3 to 1.7).

Figure 25 clearly illustrates the preturbulent increase in heat transfer (SNR < 0) associated with the discrete injection process that occurs on both the
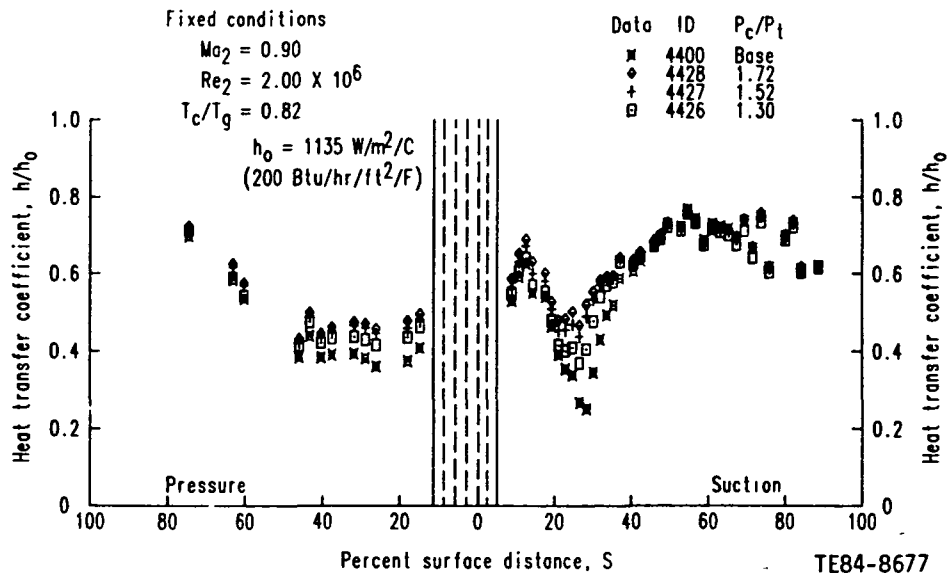
Figure 24. The effect of the coolant to free-stream pressure ratio variation on the heat transfer coefficient distribution.
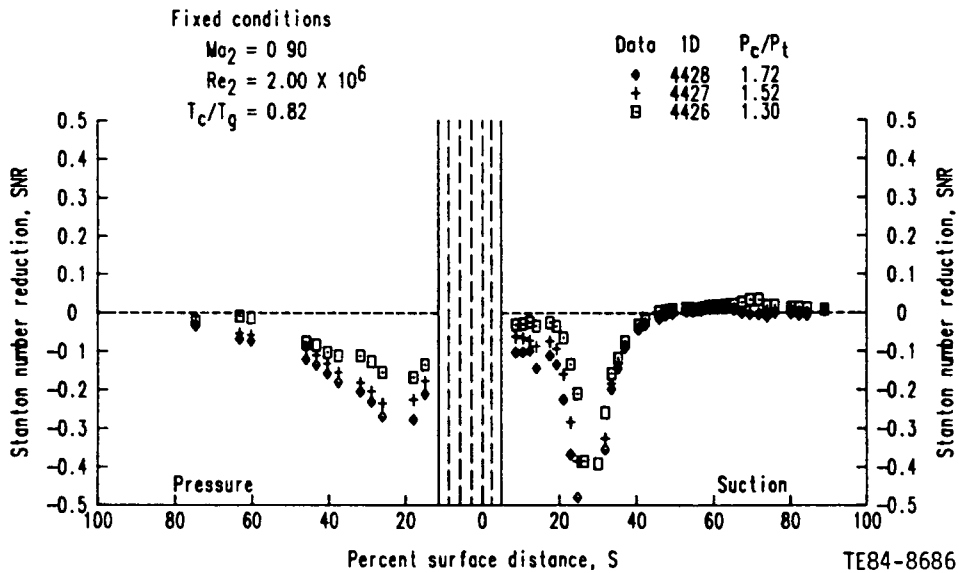
Figure 25.   The effect of the coolant to free-stream pressure ratio
variation on the Stanton number reduction distribution.
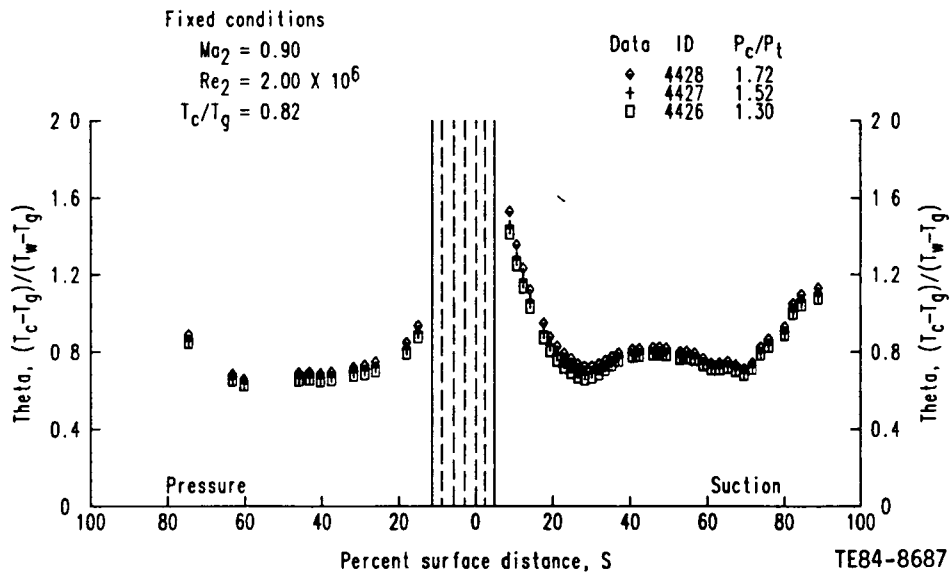
Figure 26.   Theta distribution for the coolant to free-stream pressure
ratio variation.

suction and pressure surfaces. Quantitative differences may be explained in
part by differences in surface static pressure levels and/or gradient between
the two surfaces, as illustrated in Figure 17.

One goal of this effort was to determine whether there were any benefits to be
extracted from leading edge injection in terms of recovery region surface pro-
tection.   Data shown in Figures 27 and 28 were obtained at variable plenum
coolant to mainstream total temperature ratios (T_c/T_g = 0.7, 0.8, and 0.9)

and at fixed Ma_2, Re_2, and P_c/P_t conditions. The overall increase in SNR (i.e., decreased heat transfer) as the coolant to gas absolute temperature ratio decreased indicates the positive effect that results from diluting the hot free-stream fluid with the relatively cooler leading edge ejectant. The positive shift in SNR is shown to correspond to the increasing shift in theta, due to decreasing coolant to gas absolute temperature ratio levels. However, as the pressure surface results indicate, the favorable thermal dilution phenomenon is offset by the adverse turbulence generation mechanism associated with the discrete injection process. The net result is that even for T_c/T_g = 0.7, SNR is still negative immediately downstream of the showerhead on the pressure surface.

Figure 27 also indicates that the thermal dilution and turbulence generation mechanisms interact on the suction surface. However, SNR results shown in Figure 25 indicate that in the fully turbulent region (S > 40) no significant effect is expected (i.e., SNR $\simeq$ 0 for S > 40) as a result of the leading edge injection process. Therefore, Figures 25 and 27 together support the notion that in preturbulent zones the SNR result obtained is governed by the competing thermal dilution/turbulence generation mechanisms, although in the fully turbulent zones the SNR result is determined by thermal dilution strength only. These results indicate that leading edge film-cooling by itself cannot be used to always offset high near recovery region heat loads even though far recovery region loads are reduced.

Finally, the data shown in Figure 14 and 15 suggest an interesting phenomenon regarding the convective heat transfer boundary layer transition process, i.e., Reynolds analogy deviation. Using the suction surface heat transfer coefficient data shown in Figure 14, it could be argued that transition in the thermodynamic boundary layer sense appears to complete near S = 60, or the location where the heat transfer coefficient appears to peak and then level off. In contrast, the SNR data of Figure 15 indicate that the upstream disturbance (leading edge discrete injection, in this case) causes little change beyond S = 40. From these data, it would appear that the S = 40 location delineates pretransition and posttransition zones resulting from the introduction of a particular disturbance mechanism. But the fact that between S = 40 and S = 60 the heat transfer coefficient is still increasing (Figure 14) is apparently

38
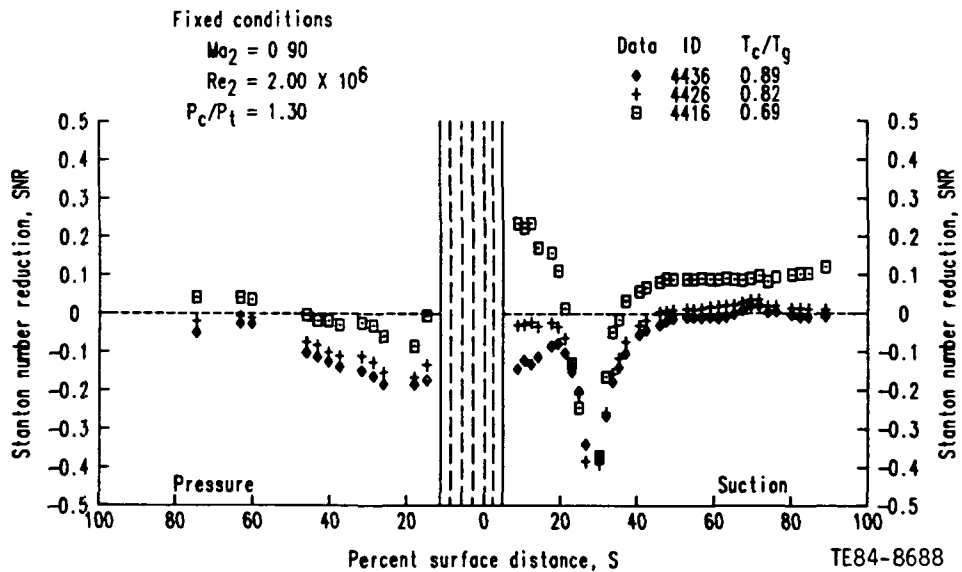
Figure 27. The effect of coolant to gas absolute temperature ratio variation on the Stanton number reduction distribution.
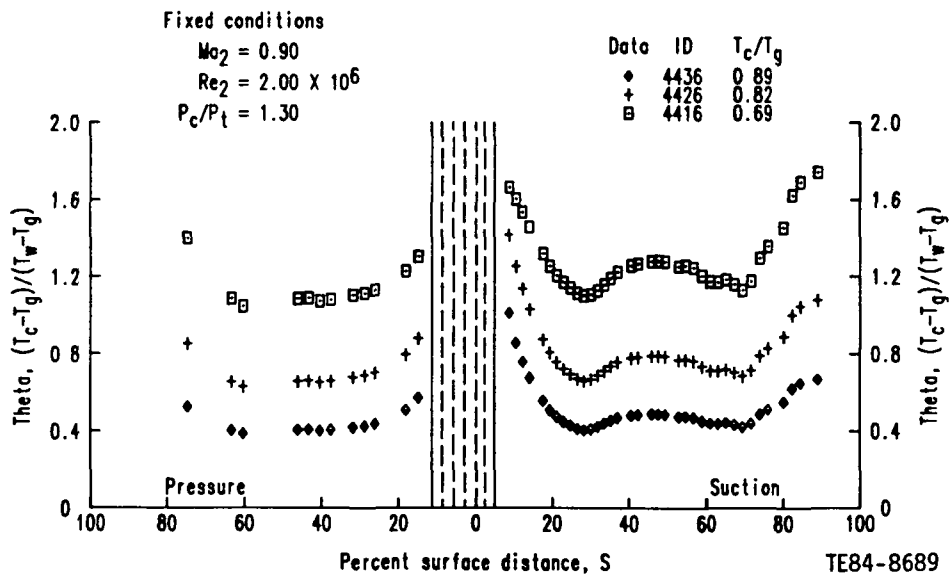
Figure 28. Theta distribution for the coolant to gas absolute temperature ratio variation.

inconsistent with this last statement. The same trend is also illustrated in the higher blowing strength data shown in Figures 24 and 25.

It is proposed that the transition endpoint differences suggested by the two different presentations shown in Figures 14 and 15 indicate actual transition rate differences between the hydrodynamic and thermodynamic boundary layers or equivalently a significant deviation of the Reynolds analogy concept through

transition. Because the SNR data of Figure 15 reflect the type behavior that results from introducing a type of boundary layer trip, then the lack of difference in the data beyond S = 40 might imply that the untripped hydrodynamic boundary layer had completed transition near S = 40. However, heat transfer coefficient data of Figure 14 indicate that both the disturbed and undisturbed thermodynamic boundary layers complete transition further downstream nearer S = 60. Because parallel measurements of the developing hydrodynamic boundary layer state were not made in this work (e.g., surface wall shear stress distributions), it is impossible to conclusively quantify the implied transition length differences between the hydrodynamic and thermodynamic boundary layers and the actual magnitude of the Reynolds analogy deviation.

However, the breakdown of Reynolds analogy through transition has been observed by Blair (Ref 23, 24) and Wang, et al (Ref 25), in their low speed wind tunnel experimental results where both heat transfer and fluid dynamic measurements were made in the transition zone. Therefore the concept is not without support and indicates that the deviation should be considered in developing a realistic modeling approach for transition prediction.

3.5 CONCLUSIONS OF THE EXPERIMENTAL PROGRAM

The results of the experimental program have provided a data base for characterizing the effects of leading edge (showerhead) film cooling on the external heat transfer of the C3X airfoil that can be used to guide the development and provide verification of current and future analytical modeling efforts. The following two dominant physical driving mechanisms were identified:

o turbulence promotion, due to the injection process
o thermal dilution, due to the injection of a relatively cold fluid into a hot gas stream

In the preturbulent boundary layer zones, these two mechanisms interact. The turbulence promotion causes an elevation of heat transfer levels, although the thermal dilution causes a decrease in heat transfer levels. This change is apparent on both the suction and pressure surfaces. Downstream of the suction surface boundary layer transition, however, only thermal dilution has an effect.

The influence of the exit Mach number, although having an effect on the baseline heat transfer coefficient levels, has no apparent effect on Stanton number reduction with film cooling for the range of the exit Mach number investigated. The effects of exit Reynolds number with leading edge film cooling indicates a movement forward of the boundary layer transition zone with increasing exit Reynolds number, as anticipated.

From suction surface results, variation of the coolant to free-stream pressure ratio over the practical design range investigated ($P_c/P_t < 1.10$) indicates that only the preturbulent boundary layer zones are affected by the turbulence promotion associated with the injection process. Increasing the blowing strength causes increasing turbulence, which in turn elevates the heat transfer levels. Off-design blowing strength data (P_c/P_t = 1.3 to 1.7) assisted in isolating this phenomena. The same phenomena appears to occur on the pressure surface, but lack of a well-defined transition zone deters a conclusion. Changes in the coolant to gas absolute temperature ratio indicate that by decreasing the coolant temperature, the hot mainstream gas becomes thermally diluted, thereby reducing the driving temperature and decreasing the heat transfer levels. This reduction in heat transfer occurs over the entire airfoil.

The discrete injection process exhibits an effect on boundary layer transitional zones as indicated by the suction surface results. Though not dramatic, even at the off-design blowing strength levels, the transition origin moves forward (i.e., the transition begins earlier) as the blowing strength increases. The data also suggest the possibility of transition rate differences between the hydrodynamic and the thermodynamic boundary layers. Although inconclusive, this is an apparent physical phenomena that warrants further investigation.

IV. ANALYTICAL PROGRAM

4.1 INTRODUCTION

The primary objective of the analytical program was to develop a method for predicting recovery region, external convective heat transfer phenomena associated with a leading edge film-cooling process. To build on the development of the nonfilm-cooled airfoil heat transfer methods of Hylton et al (Ref 1), a two-dimensional (2-D) finite difference boundary layer analysis framework was used.

The purpose of this program was to develop reliable methods of prediction that are consistent with accepted gas turbine airfoil heat transfer design philosophy. It was assumed that all domestic gas turbine design centers have ready access to and/or routinely use a 2-D finite difference boundary layer analysis code for the prediction of external convective heat transfer. Positive results from this program could be integrated with a design system without a major change in design method philosophy.

As computer technology evolves, boundary layer analysis design procedures are likely to be replaced by Reynolds and/or full Navier-Stokes (N-S) equation analyses. Even though the N-S framework is not currently an industry standard, its continued development improves future capability and reduces empircism. In addition to the development of the boundary layer method reported in this volume, a N-S method development program was conducted by Scientific Research Associates (SRA) under subcontract to Allison. The N-S program is reported in Volume II.

This report addresses boundary layer methods development. In particular, a procedure for directly extending a nonfilm-cooled model to simulate convective heat transfer phenomena downstream of an array of film-cooling holes located at the leading edge of a turbine vane is described. Included in the discussion are the modeling considerations used to define the overall approach to the leading edge film-cooled problem, a detailed description of the method, the presentation and discussion of computed results, and a final summary.

Although most of the program was devoted to the leading edge film-cooled problem, literature that reported turbulence model performance as related to non-film-cooled, airfoil convective heat transfer prediction was also evaluated. The results of this evaluation are reported in Appendix C.

4.2 MODELING CONSIDERATIONS FOR THE LEADING EDGE FILM-COOLED AIRFOIL HEAT TRANSFER PROBLEM

When using a 2-D boundary layer analysis framework to simulate the airfoil convective heat transfer phenomena resulting from a leading edge, discrete site injection process, it is important to develop a workable hypothetical description of the actual physical process that is consistent with boundary layer flow theory. Then an overall analytical/numerical method based on the assumed physical process model can be formulated. Finally, the method can be verified. The following discussion deals with developing a particular physical process model for the leading edge film-cooled problem. The discussion begins with a description of the idealized coolant jet/boundary layer interaction model assumed to represent the leading edge injection process. This hypothetical model is then analyzed in terms of the computational domain definition and the development of a two parameter boundary condition specification approach for modeling the recovery region.

4.2.1 Idealized Coolant Jet/Boundary Layer Interaction Model

It is difficult to think of the complex flow field surrounding a discrete site film-cooled leading edge as being characteristically 2-D and boundary layer in nature. If the problem were to develop a method for predicting convective heat transfer phenomena within the leading edge injection zone, the probability of developing a general boundary layer model would be small. In terms of the entire airfoil surface, however, the actively cooled leading edge represents a small percentage of the total area over which the flow field develops. Some distance downstream of the last injection site, a boundary layer flow field description has merit. It is to this recovery region zone on the airfoil surface that the boundary layer method development effort was directed.

For the special case of airfoil leading edge injection, the entire airfoil surface is influenced by the jet injection. To develop an overall recovery region formulation, it is important to use a model that accurately describes the way in which the complex, film-cooled leading edge flow field relaxes into a characteristic boundary layer flow field. The model used in this work is a simplification of the idealized coolant jet/boundary layer interaction model proposed by Crawford et al (Ref 7).

Figure 29 illustrates a hypothetical, 2-D, coolant jet/boundary layer interaction process. Without loss of generality, it may be assumed that the inviscid free-stream velocity (u_∞), total gas temperature ($T_{g,\infty}$), and free-stream turbulence intensity, (Tu_∞) are constant. The coolant, wall, and gas temperatures (T_c, T_w, and $T_{g,\infty}$) are related as follows: $T_c <$ $T_w < T_{g,\infty}$. Two modeling concepts contained in the Ref 7 representation shown in Figure 29 are important.

First, all of the coolant mass (m_c) introduced at the surface ($y = 0$) is added to the boundary layer. This assumption is shown by $\Delta m_c = 1$, where Δm_c represents the fraction of coolant mass entrained. In keeping with this complete coolant mass entrainment assumption, a jet penetration height, δ_p, depicted as $y = \delta_p$ was defined in Ref 7. By definition, $\delta_p \leq \delta_e$
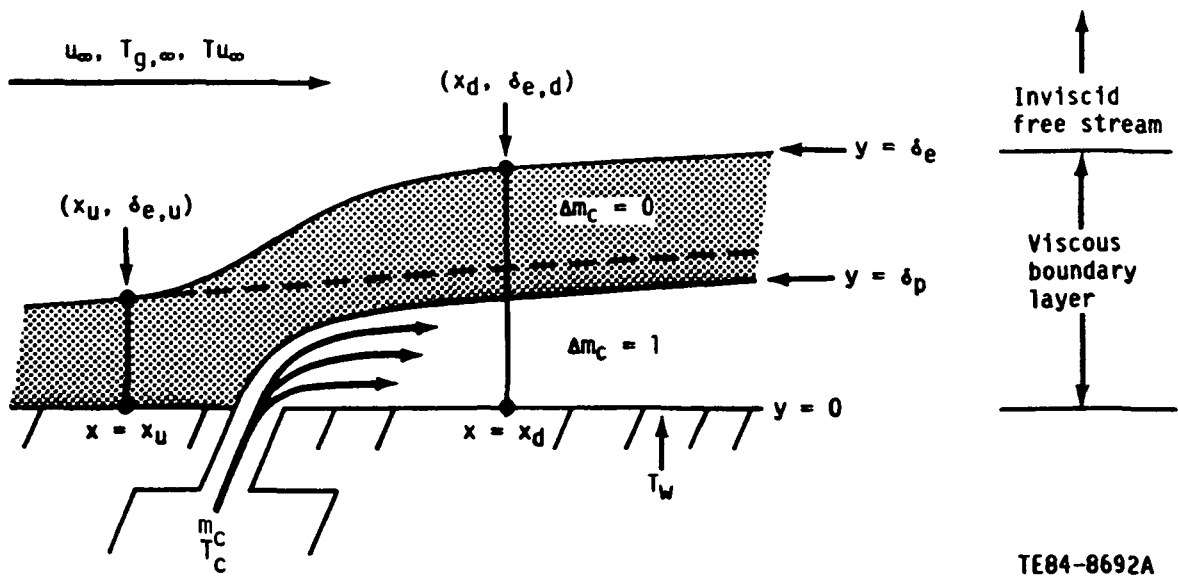
Figure 29. An idealized representation of the coolant/jet boundary layer interaction with complete coolant mass entrainment.

44

where δ_e is defined as the outer edge of the boundary layer. Based on this ideal representation, an analytical model altering the approach boundary layer velocity and thermal profiles at the injection site to account for the coolant mass addition was developed in Ref 7.

Second, the magnitude of the outer edge velocity, temperature, and free-stream turbulence intensity boundary conditions at arbitrarily chosen locations upstream (x_u, $\delta_{e,u}$) and downstream (x_d, $\delta_{e,d}$) of the injection site, as shown in Figure 29, would remain unchanged. However, this conclusion can be drawn only if $\delta_p \leq \delta_e$ or the coolant jets are assumed not to penetrate the boundary layer.

In the low velocity leading edge of a nonfilm-cooled airfoil, the boundary layers would be thin, low in momentum, and unable to completely entrain the potentially high momentum, jet injected coolant. If the leading edge injection process does not completely destroy the characteristic boundary layer structure as the coolant jets penetrate the boundary layer, a second idealized coolant jet/boundary layer interaction model is possible. This new model is illustrated in Figure 30.
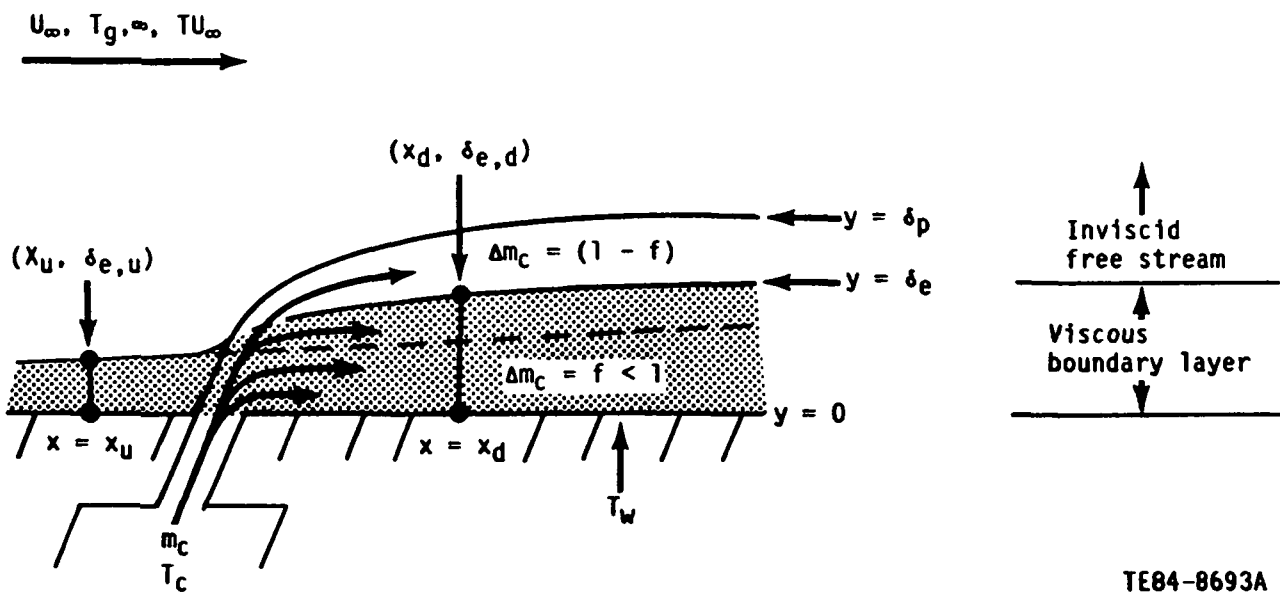
Figure 30. An idealized representation of the coolant jet/boundary layer interaction with partial coolant mass entrainment.

TE84-8693A

The major difference between this new model and that in Figure 29 is that it was assumed that only part of the coolant mass added at the surface was entrained by the boundary layer. This situation, depicted by $\Delta m_c = f < 1$, signified only partial mass addition within the boundary layer ($y < \delta_e$). The concept of partial mass entrainment is not new. Stepka and Gaugler (Ref 3) and Miller and Crawford (Ref 2) explored the validity of this type of model for predicting the heat transfer data of Luckey and L'Eucyer (Ref 8) for a film cooled cylinder in cross flow.

The assumption that at least some of the coolant mass was added to the boundary layer implied that the boundary layer profiles would be modified at the injection site to reflect the addition of coolant. This modeling aspect is in keeping with the representation shown in Figure 29. However, the same approach can not be used for outer edge boundary conditions.

As Figure 30 illustrates, the jet penetration height was greater than the boundary layer thickness. This difference was a direct result of the partial coolant mass entrainment representation and the definition of jet penetration height where it was implicitly assumed that $\Delta m_c = 1$ for $y < \delta_p$.

With $\delta_p < \delta_e$, the upstream and the downstream outer edge velocity, temperature, and turbulence intensity boundary conditions would no longer be equal.

The two dominant mechanisms of a discrete coolant injection process are jet turbulence production and thermal dilution. Therefore, the downstream turbulence intensity ($Tu_{e,d}$) and gas temperature ($T_{g,d}$) would be expected to be greater than and less than, respectively, the corresponding upstream quantities (i.e., $Tu_{e,d} > Tu_{e,u} = Tu_\infty$ and $T_{g,d} < T_{g,u} = T_{g,\infty}$). In addition, if the local surface static to free-stream total pressure ratio was not changed by the injection process, than the downstream outer edge velocity ($u_{e,d}$) would be less than the upstream value ($u_{e,u}$) based on the Bernoulli result that $(\rho u^2)_{e,d} = (\rho u^2)_{e,u}$ and the downstream outer edge density is greater than the upstream outer edge density because the downstream gas temperature is less than

the upstream gas temperature. Thus, in terms of modeling, the important difference between the complete and partial coolant mass entrainment representations illustrated in Figures 29 and 30, respectively, would be the treatment of the outer edge boundary conditions.

To describe the airfoil leading edge film-cooling process, a special case of the partial mass entrainment model was proposed as illustrated in Figure 31. In this idealized representation, the injection site is shown downstream but in close proximity of a stagnated flow zone. This representation implies that, like the situation in the leading edge of an airfoil, the approach boundary layers would be thin and low in momentum. The principle difference between this model and the model shown in Figure 30 is that it was assumed that no coolant mass was added directly into the boundary layer region ($y < \delta_e$). For the stagnated flow case, the position is taken that the approach boundary layer structure would be destroyed by the coolant jet injection. However downstream of the injection site a new boundary layer would develop. It follows that no coolant mass ($\Delta m_c = 0$ for $y < \delta_e$) would be added to an approach boundary layer. Unlike the situation for the complete and partial mass entrainment models discussed previously, explicitly modeling the downstream boundary layer structure modification due to coolant mass addition would not be required.

As indicated in Figure 31, the newly developing downstream boundary layer grew into a free-stream/coolant fluid mixing zone. This situation was similar to the model shown in Figure 30. In keeping with that model, the outer edge
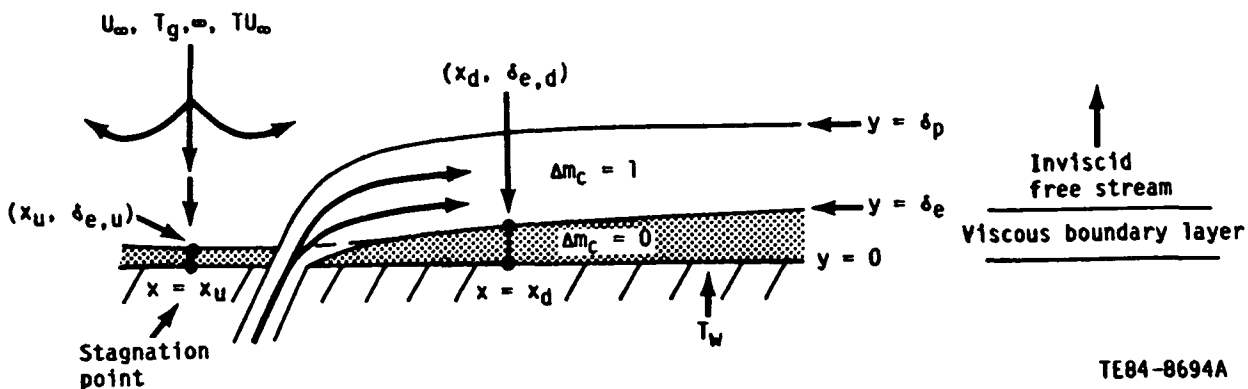
Figure 31. An idealized representation of the coolant jet/boundary layer with no coolant mass entrainment.

velocity, turbulence intensity, and gas temperature boundary conditions would be altered to reflect the fact that the jet penetration height was greater than the boundary layer thickness (i.e., $\delta_p > \delta_e$).

By adopting the idealized coolant jet/boundary layer interaction model illustrated in Figure 31, the specification of the boundary layer outer edge boundary conditions became the critical part of the overall method formulation. This specification was in contrast to the representation in Figure 29 where the emphasis was on internal boundary layer structure modification and boundary condition specification was handled no differently than for an equivalent non-film-cooled problem. However, the boundary condition aspects of the model problem were important only if the defined computational domain was restricted to the region where $y > \delta_e$ as indicated in Figure 31. If the domain of interest was defined as less than the greater of the jet penetration height, or the boundary layer thickness, then there would be no major implied modeling differences between the representations illustrated in Figures 29 and 31.

However, applying a standard boundary layer analysis to the implied two-layer problem defined by the region $y < \delta_p$ in Figure 31 was not a straightforward task.

4.2.2 Computational Domain Definition

It was assumed that the computational domain for the leading edge film-cooled recovery region problem was the same as that defined for an equivalent nonfilm-cooled problem. By restricting the computational domain so as not to explicitly include the zone between the outer edge of the boundary layer and the jet penetration height ($\delta_e < y < \delta_p$), the downstream effect of the coolant injection process would be modeled implicitly through the outer edge boundary conditions. Although using a nonfilm-cooled analysis framework as the foundation for a recovery region heat transfer prediction scheme is not a new idea, the concept of modeling the effects of the upstream injection process entirely through the outer edge boundary conditions is considered to be a unique element of the overall problem formulation.

Another modeling problem related to the computational domain definition deals
with the starting point location. Normally, when a numerical boundary layer
code is used to predict airfoil surface convective heat transfer, two separate
computations are made, one for the suction surface and one for the pressure
surface. These independent solutions are usually initiated in the leading edge
region, some small distance downstream of a predetermined stagnation point.
At the solution initiation points, boundary layer velocity and thermal profiles
must be specified. There are a number of standard procedures for generating
reasonable approximations in the stagnation region if the surface is impervi-
ous. However, with discrete site leading edge film cooling, initiating the
suction and pressure surface computations becomes a problem because the stag-
nation zone flow field is not easily described in terms of standard boundary
layer theory.

In this work, two initiation approaches were explored: the stagnation region
initiation scheme and the recovery region initiation scheme. The differences
between the two approaches are illustrated in Figure 32. This figure shows
the C3X vane profile with leading edge film-cooling sites.
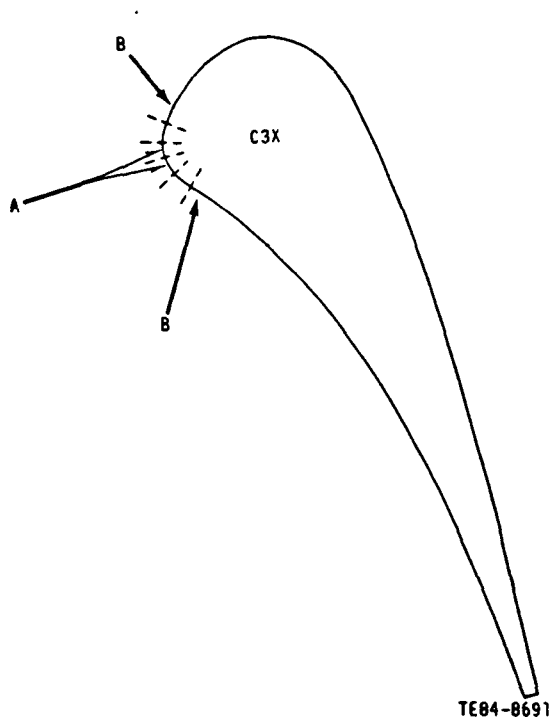
Figure 32. Computational domain definition in terms of stagnation region
initialization, A, or downstream (recovery) region initialization, B.

In the stagnation region initiation scheme, the standard nonfilm-cooled analysis approach of initiating suction/pressure surface computations a small distance away from a prescribed stagnation point was maintained. Starting locations for this approach are indicated by the arrows labeled A in Figure 32. The extent of the streamwise computational domain was defined as the entire airfoil surface.

The approach to the stagnation region solution initiation scheme implied that the computation marched across coolant injection sites, suggesting the need to explicitly model the coolant jet/boundary layer interaction process. The STANCOOL numerical boundary layer code was chosen for modeling the combined actively cooled leading edge and recovery regions. As documented in Ref 7, the STANCOOL 2-D boundary layer code is an extension of the STAN5 code with models for describing the coolant jet/boundary layer interaction process and recovery region relaxation. However, the STANCOOL injection model is based on the idealized representation shown in Figure 29. Because this type of model is inappropriate for the leading edge film-cooling problem, the stagnation region initiation/STANCOOL scheme was eventually abandoned in favor of the recovery region initiation approach. (The merits of the stagnation region initiation/STANCOOL scheme were tested. The qualitative and quantitative solution characteristics obtained are documented in Appendix D.)

As indicated by the arrows labeled B in Figure 32, in the recovery region initiation approach the streamwise computational domain consisted of only that portion of the airfoil suction and pressure surfaces downstream of the last row of cooling holes. By avoiding computation in the actively cooled leading edge region, the emphasis was placed on modeling the recovery region. For lack of a better definition, required initial location recovery region boundary layer profiles to go along with the redeveloping boundary layer flow model shown in Figure 31 were generated using solution results where local boundary conditions were used to define the Euler number, $Eu = (x_d/u_{e,d}) \, du_{e,d}/dx_d$. This procedure was the same as that used for defining profiles for the stagnation region initialization approach, but instead of using the theoretical stagnation flow result ($Eu = 1$), the local similarity condition definition was used.

Although this procedure solved the problem of defining required recovery region profiles, the implied local similarity assumption used to describe the re-developing boundary layer flow at the recovery region solution initiation point was questionable. However, in view of the simple coolant jet/boundary layer interaction model used in this program (refer to Figure 31), a more rigorous procedure was not justified.   .

By restricting the computational domain so as not to include the leading edge injection zone and the hypothetical zone between the boundary layer outer edge and the jet penetration height ($\delta_p < y < \delta_e$ in Figure 31), problems associated with explicitly modeling jet/free-stream interaction were completely avoided. Predicting recovery region heat transfer phenomena due to leading edge injection could thus be approached entirely as a special boundary condition specification problem for a nonfilm-cooled boundary layer analysis formulation. It was necessary then to define how the nonfilm-cooled boundary condition definitions were reformulated to allow simulation of the injection occurence.

4.2.3 Two Parameter Boundary Condition Reformulation Approach

It would be misleading to imply that the modeling approach to the leading edge film cooled heat transfer problem discussed in the previous sections was completely determined before any of the C3X experimental heat transfer data were available. On the contrary, the overall boundary condition approach was not finalized until careful study of the measured recovery region Stanton number reduction (SNR) trends were completed. With a particular effective viscosity formulation developed for predicting nonfilm-cooled airfoil heat transfer, these experimental trends could be simulated analytically by reformulating only two boundary conditions. Thus, even though the general modeling concepts adopted in this work were suggested before the experiments, the experimental results determined the minimum number (two) of boundary conditions that would have to be explicitly altered to simulate the observed recovery region phenomena. These two conditions were the outer edge free-stream turbulence intensity (Tu_e) and total gas temperature (T_g) [enthalpy (I_e)].

The free-stream turbulence intensity would not normally be considered a natural boundary condition of a boundary layer analysis framework. (The two conditions that are considered natural boundary conditions to 2-D, compressible governing equations are streamwise velocity and temperature.) The turbulence intensity boundary condition is usually introduced as an element of certain turbulence model formulations used to define the overall effective viscosity (e.g., a turbulent kinetic energy model). As a general rule, if the effective viscosity formulation is a function of free-stream turbulence intensity, then increasing the magnitude of that quantity will result in a predicted increase in the heat transfer level. As blowing strength (P_c/P_t) is increased experimentally, the observed effect is an increase in the measured recovery region heat transfer level for some distance downstream of the injection site. This effect is credited to a turbulence production mechanism associated with discrete jet injection. By defining a so-called effective free-stream turbulence intensity (Tu_e^*) as follows

$$Tu_e^* = FTU(Tu_e)$$

where Tu_e is defined as the free-stream turbulence intensity at a no-blowing (nonfilm-cooled) condition, the experimentally observed heat transfer increase due to discrete injection may be characterized analytically using the free-stream turbulence intensity factor (FTU) as a parameter.

The anticipated behavior of the FTU as a function of blowing strength and thermal dilution strength (T_c/T_g) is shown in Figure 33. In terms of the effective free-stream turbulence intensity, this figure indicates that at every blowing condition, both the blowing strength and the FTU are greater than one. Thus, the effective free-stream turbulence intensity would always be greater than the no-blowing value of the outer edge free-stream turbulence intensity. According to method definition, coolant jet turbulence production phenomena can be simulated by using the boundary condition Tu_e^* = FTU(Tu_e) with FTU > 1 as indicated by Figure 33.

Whether this strategy can be implemented depends on the particular form of the effective viscosity formulation being used to model nonfilm-cooled phenomena.
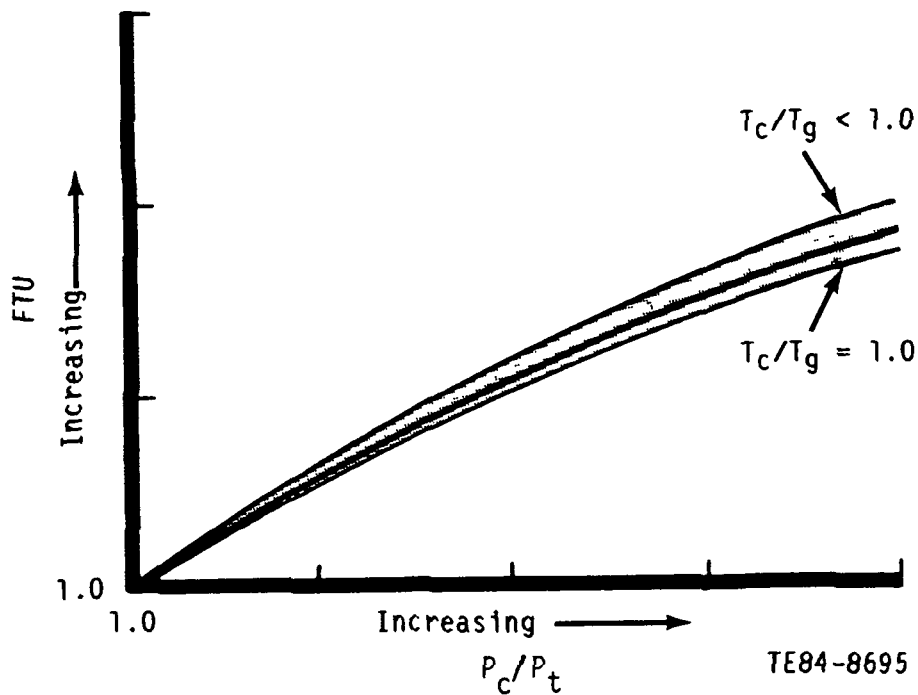
Figure 33. Variational character of the free-stream turbulence intensity factor implied by leading edge film-cooled C3X airfoil experimental results.

If the turbulent viscosity is not a function of the free-stream turbulence intensity, then modeling jet turbulence production phenomena through an effective boundary condition is impossible. However, as in this case, effective viscosity formulations developed for simulating the gas turbine environment usually took into account free-stream turbulence, regardless of whether or not film cooling was part of the problem.

An effective boundary condition formulation to simulate jet turbulence production phenomena was also used to define an effective gas total temperature, T_g^*, and to model thermal dilution phenomena. An important feature of the idealized coolant jet/boundary layer interaction model shown in Figure 31 is that the ejected coolant is assumed to be contained in a layer above the surface boundary layer (i.e., $\delta_e < y < \delta_p$). It is within reason to assume that the total temperature (i.e., enthalpy) in this coolant/free-stream fluid mixing layer would be less than the total temperature above the layer. If the total temperature in the mixing layer is defined as the effective gas temperature, and the total temperature above the layer is defined as T_g, the preceding statement implies that $T_g^* < T_g$. In keeping with the definition of

53

the effective gas total temperature, the inequality relation can be stated using the equality relation

$$T_g^* = FTG(T_g)$$

where the free-stream total gas temperature factor (FTG) is less than or equal to one. Like the FTU, the qualitative behavior of the FTG as a function of blowing strength and thermal dilution strength was suggested by the C3X airfoil experimental SNR data. This behavior is shown in Figure 34. This figure illustrates that at every blowing condition, the blowing strength is greater than one where the thermal dilution strength is less than one. Thus, the FTG would be less than one and $T_g^* < T_g$.

Implementing the effective total gas temperature boundary condition definition within a boundary layer analysis framework posed no problem because temperature is a natural boundary condition of the compressible boundary layer equation framework. Computationally the effect of reducing the outer edge total temperature (i.e., FTG < 1) would decrease the thermal driving potential [i.e.,
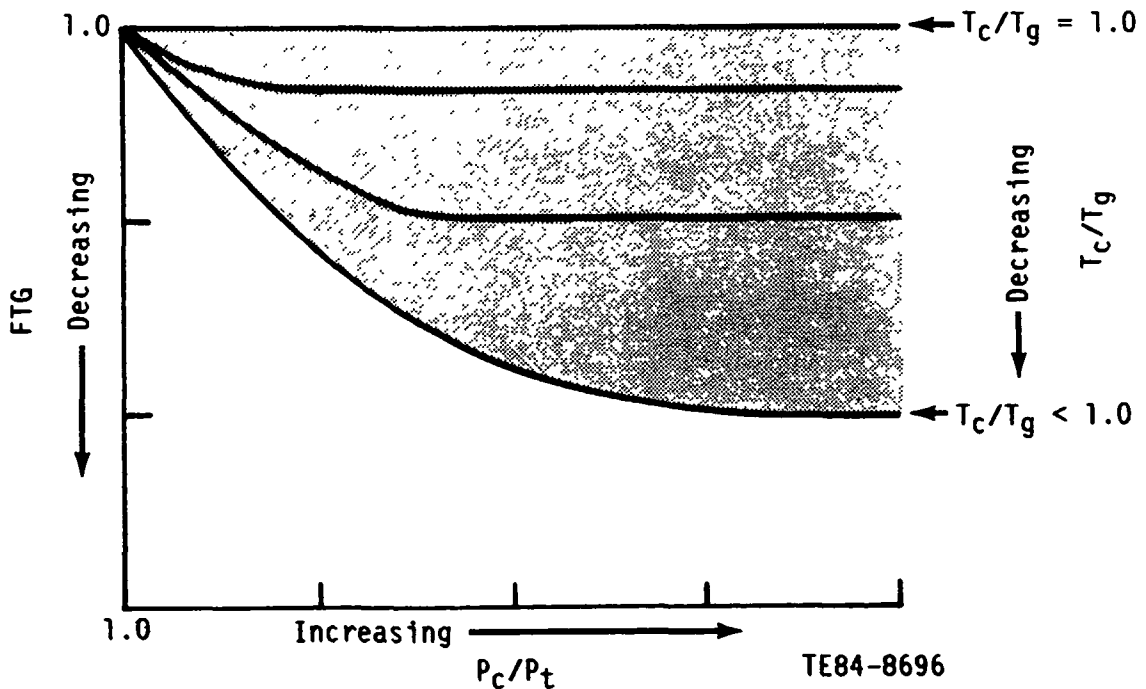
Figure 34. Variational character of the free-stream total gas temperature factor implied by leading edge film-cooled C3X airfoil experimental results.

$(T_w - T_g^*) < (T_w - T_g)]$ and thus the predicted heat transfer level. This effect is the same as that observed in the C3X vane SNR data.

The other natural outer edge boundary condition, velocity (u_e), was not explicitly redefined using a third effective value parameter. However, the so-called nonfilm-cooled value was reduced in the film-cooled simulation when FTG < 1. The amount of reduction is quantified in the following subsection that deals with the detailed method definition.

To implement the overall recovery region solution initiation/effective boundary condition approach proposed for modeling the leading edge film-cooled problem, a finite difference boundary layer code that is applicable for predicting non film-cooled airfoil convective heat transfer in a gas turbine environment was necessary. Starting from this nonfilm-cooled formulation, the only implied modifications that were needed to redefine the outer edge free-stream turbulence intensity and total gas temperature boundary conditions were $Tu_e^* =$ FTU (Tu_e) and $T_g^* =$ FTG (T_g), instead of Tu_e and T_g, respectively. To perform a recovery region heat transfer computation at a particular blowing condition, the two parameters, FTU and FTG, would have to be changed from their no-blowing values (FTU = FTG = 1.0) to values in keeping with the qualitative trends shown in Figures 33 and 34, respectively. Finally, the simple two parameter boundary condition approach proposed was assumed valid only for modeling recovery region heat transfer phenomena due to leading edge discrete site injection. If the coolant sites are located away from the low velocity stagnation region, then the idealized coolant jet/boundary layer interaction model adopted in this work (see Figure 31) would not apply, and one of the other two representations shown in Figures 29 and 30 would be used. Then the coolant mass being added to the boundary layer would have to be accounted for by modifying the recovery region boundary layer structure. This modification could not be accomplished using only two boundary condition parameters.

4.3 METHOD DEFINITION

In the following subsections, the modeling details of the overall leading edge nonfilm- and film-cooled method are presented. The emphasis is on defining the specific models and procedures required to quantify the two parameter

boundary condition approach proposed for simulating the recovery region heat transfer effects due to leading edge injection. However, because the method proposed is a direct extension of a particular nonfilm-cooled analysis approach, a general description of the 2-D boundary layer analysis framework used to model both film- and nonfilm-cooled airfoil convective heat transfer phenomena is appropriate. After defining the basic theoretical and computational framework, the necessary additional empirical relations and boundary condition information are defined to complete the method description.

4.3.1 General Description of the 2-D Boundary Layer Analysis Framework

The method used for predicting external convective heat transfer was based on the finite difference solution of the following compressible 2-D laminar/turbulent boundary layer equations:

o continuity

$$\frac{\partial(\rho u)}{\partial x} + \frac{\partial(\rho v)}{\partial y} = 0 \tag{4}$$

o streamwise momentum

$$\rho u \frac{\partial u}{\partial x} + \rho v \frac{\partial u}{\partial y} = \rho u_e \frac{du_e}{dx} + \frac{\partial}{\partial y} \left(\mu_{eff} \frac{\partial u}{\partial y} \right) \tag{5}$$

o energy (total enthalpy, I, form)

$$\rho u \frac{\partial I}{\partial x} + \rho v \frac{\partial I}{\partial y} = \frac{\partial}{\partial y} \left(\frac{\mu_{eff}}{Pr_{eff}} \frac{\partial I}{\partial y} \right) + \frac{\partial}{\partial y} \left[\left(\mu_{eff} - \frac{\mu_{eff}}{Pr_{eff}} \right) u \frac{\partial u}{\partial y} \right] \tag{6}$$

This system of equations is subject to the following boundary conditions:

o wall conditions, where y = 0

56

$$u = 0, \quad v = v_w(x), \quad \text{and} \quad \begin{cases} I = I_w(x) \quad \text{(level)} \\ \quad\quad\quad \text{or} \\ -\dfrac{k}{c_p} \dfrac{\partial I}{\partial y} = \dot{q}_w''(x) \quad \text{(flux)} \end{cases} \tag{7}$$

o outer edge conditions, where $y = \delta$

$$u = u_e(x) \text{ and } I = I_e \tag{8}$$

o initial location conditions, where $x = x_0$

$$u = u(x_0, y) \text{ and } I = I(x_0, y) \tag{9}$$

The general form of the effective viscosity, μ_{eff}, and effective Prandtl number, Pr_{eff}, is defined as follows

$$\mu_{eff} = \mu + \gamma_t \mu_t + \gamma_{Tu} \mu_{Tu} \tag{10}$$

$$Pr_{eff} = \frac{\mu_{eff}}{\dfrac{\mu}{Pr} + \gamma_t \dfrac{\mu_t}{Pr_t} + \gamma_{Tu} \dfrac{\mu_{Tu}}{Pr_{Tu}}} \tag{11}$$

A closed form numerical solution for the three unknowns (u, v, and I) in the governing equations [Equation (4) through (6)] was possible once appropriate boundary conditions [Equations (7) through (9)] were defined. Empirical models for the turbulent quantities (γ_t, μ_t, γ_{Tu}, μ_{Tu}, Pr_t, and Pr_{Tu}) in the effective viscosity/Prandtl number definitions [Equations (10) and (11)] were supplied. Relations for specifying the fluid properties, ρ, μ, and Pr, were given.

The numerical algorithm used for solving Equations (4) through (6) is based on the Patankar and Spalding (see Ref 9) discretization incorporated within the STAN5, 2-D numerical boundary layer analysis computer code by Crawford and Kays (see Ref 10). Although the particular numerical solution algorithm used to solve Equations (4) through (6) is important in terms of efficiency, algorithm

development was not an element of the leading edge film-cooled method development problem. Even though all proposed modeling modifications were implemented within the STAN5 code, it was assumed that similar results would be obtained using another discretization scheme.

The important elements of the leading edge film-cooled method development problem are considered to be the definition of boundary conditions [Equations (7) through (9)] and of effective viscosity/Prandtl number relations [Equations (10) and (11)] that are necessary for obtaining problem closure. These relations are described in detail in the following three subsections. The only other requirement for obtaining problem closure is the specification of fluid property relations. The values of the fluid properties were defined as a function of temperature using the Eckert and Drake (Ref 11) air tables as tabularized in the STAN5 computer code. Density, ρ, is related to pressure, p, and temperature, T, using the ideal gas law assumption, $p = \rho RT$ where R is the gas constant.

4.3.2 Effective Viscosity/Prandtl Number Formulation

Because the idealized coolant jet/boundary layer interaction model (see Figure 31) used to describe the leading edge injection process effectively reduces the modeling problem to one of specifying adjusted outer edge boundary conditions to an otherwise nonfilm-cooled formulation, defining the various terms of the general effective viscosity/Prandtl number formulations for the leading edge film-cooled method is conceptually no different than defining the same terms for a nonfilm-cooled problem. The only difference is that outer edge boundary condition terms for free-stream turbulence intensity and total temperature that appear explicitly in the empirical models must be replaced by their effective counterparts, Tu_e^* and T_g^*, respectively. It will be specifically mentioned whenever such a substitution is made. Otherwise the following discussion can be viewed as a presentation of a particular nonfilm-cooled analysis effective viscosity/Prandtl number formulation.

The turbulent Prandtl number, Pr_t, is defined as constant and equal to 0.86. The so-called laminar augmentation Prandtl number, Pr_{Tu}, appearing in the effective Prandtl number definition [Equation (1)] is also defined as constant and equal to 0.86.

58

The turbulent viscosity, μ_t, is defined using the Prandtl mixing length formulation suggested in Ref 10 and incorporated in the STAN5 computer code. This model is summarized as follows

$$\mu_t = \rho D^2 \ell^2 \left| \frac{\partial u}{\partial y} \right|$$

$$\ell = \begin{cases} \kappa y & 0 \le y \le \frac{\lambda \delta}{\kappa} \\ \lambda \delta & \frac{\lambda \delta}{\kappa} \le y \le \delta \end{cases}$$

$$\kappa = 0.41, \qquad \lambda = 0.086$$

$$D = 1.0 - \exp\left[-y^+/A^+\right]$$

$$y^+ = \frac{u_\tau y}{\nu}, \quad u_\tau = \sqrt{\frac{\tau_w}{\rho_w}}, \quad \tau_w = \mu_{eff} \left. \frac{\partial u}{\partial y} \right|_{y=0}$$

$$A^+ = \frac{A_0^+}{7.1 \, b \, P_{eff}^+ + 1.0} \qquad (12)$$

$$b = \begin{cases} 4.25 & P_{eff}^+ \le 0.0 \\ 2.90 & P_{eff}^+ > 0.0 \end{cases}$$

$$\frac{dP_{eff}^+}{dx^+} = - \frac{\left(P_{eff}^+ - P_{eq}^+\right)}{C}$$

$$A_0^+ = 25.0, \quad C = 4000, \quad P_{eq}^+ = \frac{\nu_w}{\rho_w u_\tau^3} \frac{dP}{dx}$$

The term γ_t serves to control the fractional amount ($0 \le \gamma_t \le 1$) of turbulent viscosity making up the total effective viscosity sum. The term is used to model transition from laminar to turbulent flow by defining it as follows

$$\gamma_t = \begin{cases} 0 & \text{Laminar flow} \\ 0 < \gamma_t < 1 & \text{Transitional flow} \\ 1 & \text{Turbulent flow} \end{cases} \qquad (13)$$

As a result of the preceding definition, γ_t is referred to as the transition model. As implied by Equation (13) the transition model consists of three specific submodels. The first controls the downstream location where γ_t begins to take on nonzero values and is referred to as the transition origin model. In this program, the transition origin model of Seyb (Ref 12 and 13) was used. The Seyb model defines transition origin in terms of momentum thickness Reynolds number, Re_θ, as follows

$$Re_{\theta,0} = \frac{1000}{1.2 + 70\ Tu_e^\star} + 10 \left[\frac{\lambda + 0.09}{0.0106 + 3.6\ Tu_e^\star} \right]^{2.62}$$

$$Re_\theta = \frac{u_e \theta}{\nu}, \quad \theta = \int_0^\delta \frac{\rho u}{\rho_e u_e} \left(1 - \frac{u}{u_e} \right)\ dy \tag{14}$$

$$\lambda = \frac{\theta^2}{\nu} \frac{du_e}{dx}$$

$$Tu_e^\star = FTU(Tu_e)$$

In addition, the model set the upper and lower limits for free-stream turbulence intensity as suggested by Brown and Burton in Ref 14

$$Tu_e^\star = \begin{cases} 0.015, & Tu_e^\star < 0.015 \\ Tu_e^\star, & 0.015 \le Tu_e^\star \le 0.04 \\ 0.04, & Tu_e^\star > 0.04 \end{cases} \tag{15}$$

As indicated by Equation (14), the transition origin momentum thickness Reynolds number is determined as a function of both local pressure (velocity) gradient and free-stream turbulence intensity using the Pohlhausen parameter, λ, and the local free-stream turbulence intensity boundary condition, respectively. ($Tu_e^\star$ is the so-called effective free-stream turbulence intensity defined previously.) As illustrated in Figure 33 and defined by Equation (14), the local effective quantity would always be greater than the local no-blowing value at every blowing condition, where blowing strength is greater than one because $FTU \ge 1$. The local no-blowing and/or nonfilm-cooled definition of

60

free-stream turbulence intensity is thought of as a boundary layer outer edge boundary condition, and its exact definition is deferred until the subject of boundary condition specification is discussed. However, the important point in terms of the overall leading edge film-cooled method is that because the effective free-stream turbulence intensity is greater than the outer edge free-stream turbulence intensity when blowing strength is greater than one, then the blowing condition when FTG > 1 and the transition origin Reynolds number, $Re_{\theta,o}$, will be less than the baseline, no-blowing counterpart when FTG = 1.0.

The second submodel of the overall transition model term is referred to as the transition endpoint model. In terms of Equation (13), this model defines the location where the transition model term obtains a value of one. In this program, the transition endpoint model of Dhawan and Narasimha (Ref 15) was used together with the 0-99% intermittency definition suggested in Ref 16 and discussed in Ref 1, that is

$$
\begin{aligned}
Re_{x,e} &= Re_{x,o} + Re_\Delta \\
Re_\Delta &= 16.8 \ Re_{x,o}{}^{0.8} \\
Re_x &= \frac{xu_e}{\nu}
\end{aligned}
$$

(16)

By definition, the transition endpoint ($Re_{x,e}$) is a function of the surface distance transition origin Reynolds number ($Re_{x,o}$), which is defined as the local surface distance Reynolds number (Re_x) where the local momentum thickness Reynolds number is equal to the transition origin value, [Equation (14)]. Implicitly, the transition endpoint is sensitive to leading edge blowing conditions, where the blowing strength is greater than one or FTU > 1, through the definition of the surface distance transition origin Reynolds number.

The third submodel of the overall transition origin model term is the path, or intermittency, model. In terms of Equation (13) this model defines the manner in which the transition origin model term varies from zero to one. Like the transition endpoint model, the path model of Dhawan and Narasimha (Ref 15) was used in this work. It is defined as

$$
\gamma_t = 1 - exp\left[-4.65 \left(\frac{Re_x - Re_{x,o}}{Re_\Delta} \right)^2 \right]
$$

(17)

61

where x_o and x_e correspond to the surface distance locations where Re_θ = $Re_{\theta,o}$ [transition origin, Equation (8)] and Re_x = $Re_{x,e}$ [transition endpoint, equation (16)], respectively.

The remaining two terms to be defined in the effective viscosity/Prandtl number formulations given by Equations (10) and (11) are γ_{Tu} and μ_{Tu}. As discussed in Ref 1, the combined term $\gamma_{Tu}\mu_{Tu}$ is introduced into the effective viscosity definition to explicitly model the effects of free-stream turbulence in nominally laminar flow regions or in equivalent regions where $\gamma_t\mu_t$ = 0 [Equation (13)]. A significant portion of the so-called nonfilm-cooled airfoil effective viscosity model development work reported in Ref 1 was devoted to the modeling of the $\gamma_{Tu}\mu_{Tu}$ term particularly for predicting airfoil pressure surface heat transfer augmentation in the nominally laminar zones where Re_θ < $Re_{\theta,o}$ ~ 200. [The importance of including the term $\gamma_{Tu}\mu_{Tu}$, referred to as the laminar augmentation model, is illustrated in the discussion on method characterization. In addition, the nonfilm-cooled turbulence model evaluation reported in Appendix C contains a discussion pertaining to the role of the laminar augmentation model.]

In this work, the stagnation region form of the laminar augmentation viscosity term, μ_{Tu}, suggested by Miyazaki and Sparrow (Ref 17) and adapted in Ref 1, was used. That is

$$\mu_{Tu} = T_1 \frac{y}{\delta} \rho\ell \, Tu_e^* \, u_\infty$$

$$T_1 = 0.5$$

$$\ell = \begin{cases} \kappa y & 0 \leq y \leq \frac{\lambda\delta}{\kappa} \\ \lambda\delta & \frac{\lambda\delta}{\kappa} \leq y \leq \delta \end{cases}$$

(18)

$$\kappa = 0.41, \quad \lambda = 0.086$$

$$Tu_e^* = FTU(Tu_e)$$

Like the turbulent viscosity, μ_t, the laminar augmentation viscosity is based on the Prandtl mixing length hypothesis but instead of defining $\ell \left| \partial u / \partial y \right|$ as the velocity scale, $Tu_e^* \, u_\infty$ is used. The velocity is defined as the up-

stream or blade row approach velocity, which is assumed to be constant. The free-stream turbulence intensity is the local boundary layer outer edge value. As defined by Equation (18), the free-stream turbulence intensity is the effective quantity used to simulate both leading edge blowing (FTU > 1, $P_c/P_t > 1$) or no-blowing (FTU = 1, $P_c/P_t = 1$) conditions. As indicated by Equation (18), an increase in laminar augmentation viscosity and likewise heat transfer is implied at all leading edge blowing conditions because the effective free-stream turbulence intensity would always be greater than the nonfilm-cooled (no-blowing) outer edge free-stream turbulent intensity.

Like the role of its turbulent viscosity counterpart, the transition model, the laminar augmentation intermittency model term (γ_{Tu}) is used to control the fractional portion ($0 \leq \gamma_{Tu} \leq 1$) of laminar augmentation viscosity making up the total effective viscosity sum [Equation (10)]. Because the laminar augmentation term is introduced to model phenomena in nominally laminar zones, one definition for the laminar augmentation intermittency model term might be $\gamma_{Tu} = 1 - \gamma_t$. However in this study the definition $\gamma_{Tu} = 1$ was used. The implication is that the full portion of laminar augmentation viscosity is added throughout the laminar-transitional and fully turbulent flow regions. However, the magnitude of the laminar augmentation viscosity is controlled by the decay of the free-stream turbulence intensity.

4.3.3 Outer Edge and Wall Boundary Condition Specification

This subsection discusses the procedure for specifying the nontrivial wall and outer edge boundary conditions. In addition, the required velocity and temperature (enthalpy) conditions [Equations (7) and (8)] and the local, outer edge free-stream turbulence intensity boundary condition are defined. The outer edge free-stream turbulence intensity boundary condition was introduced as an element of the overall effective viscosity formulation and was not considered a natural boundary condition of the base boundary layer equation framework given by Equations (4) through (6). However, its definition was required to obtain overall closure of the system given by Equations (4) through (11).

As when dealing with the effective viscosity/Prandtl number formulation, the procedure for defining required closure relationships for the proposed leading edge film-cooled method is essentially the same as the procedure that would be

followed in defining the same conditions for a complete nonfilm-cooled analysis. The only difference is that the effective free-stream turbulence intensity and free-stream total gas temperature values were used instead of the corresponding no-blowing condition values.

Beginning first with the outer edge boundary condition for velocity [Equation (8)], the local outer edge (free-stream) velocity boundary condition was calculated as for a design exercise, not with experimental results. The free-stream velocity was determined from the airfoil surface static pressure distribution that was numerically determined using a 2-D inviscid blade-to-blade analysis. Following the procedure adopted for the nonfilm-cooled method development work reported in Ref 1, the blade-to-blade Euler equation solver developed by Delaney (Ref 18) was used to generate airfoil surface static pressure distributions (P_s) at the two exit Mach number conditions ($Ma_2 = 0.90$ and 1.05) set experimentally. Figure 35 shows these two analytical distributions compared to the no-blowing experimental data shown previously in Figure 17. (Surface static pressure normalized using inlet total pressure.).

No attempt was made to model the leading edge injection in the inviscid blade-to-blade analysis. The two analytical static to inlet total pressure ratio (P_s/P_t) distributions shown in Figure 35 were used for both blowing and no-blowing condition computations even though the solutions were generated for the latter condition. To convert the local surface static to inlet total pressure to velocity, isentropic flow of an ideal gas was assumed. The isentropic flow relations of note are

$$\frac{P_s}{P_t} = \left(1 + \frac{k-1}{2} Ma^2\right)^{\frac{k}{1-k}}$$

$$\frac{T_s^*}{T_g^*} = \left(1 + \frac{k-1}{2} Ma^2\right)^{-1} = \frac{T_s}{T_g} \qquad (19)$$

$$u_e = Ma \sqrt{kRT_s}$$

$$u_e^* = Ma \sqrt{kRT_s^*}$$

$$T_g^* = FTG(T_g)$$

R = gas constant (air)

k = ratio of specific heats (c_p/c_v) (air)

P_t and T_g correspond to the total pressure and temperature conditions measured upstream of the blade row. In addition, k is assumed constant and is determined using measured inlet values of P_s, P_t, and T_g.

It follows directly from Equation (18) that the assumption of nonchanging local, static to inlet total pressure at blowing and no-blowing conditions is equivalent to assuming nonvarying local Mach numbers. The so-called effective static to total temperature ratio, T_s^*/T_g^*, which results by assuming a reduced total temperature (FTG < 1.0) at blowing conditions where blowing strength is less than one, is equivalent to the no-blowing ratio where the blowing strength equals one and FTG = 1.0. Solving for a so-called effective free-stream velocity, u_e^*, in terms of the no-blowing value and the total temperature factor it can be shown that $u_e = \sqrt{FTG}\ (u_e)$. The effect of introducing the effective total temperature condition is to reduce the nonfilm-cooled outer edge velocity boundary condition by the square root of FTG as implied by Equation (19) and Figure 34.

The outer edge total enthalpy boundary condition [Equation (8)] is also assumed to be constant. In keeping with the two parameter (FTU and FTG) boundary con-
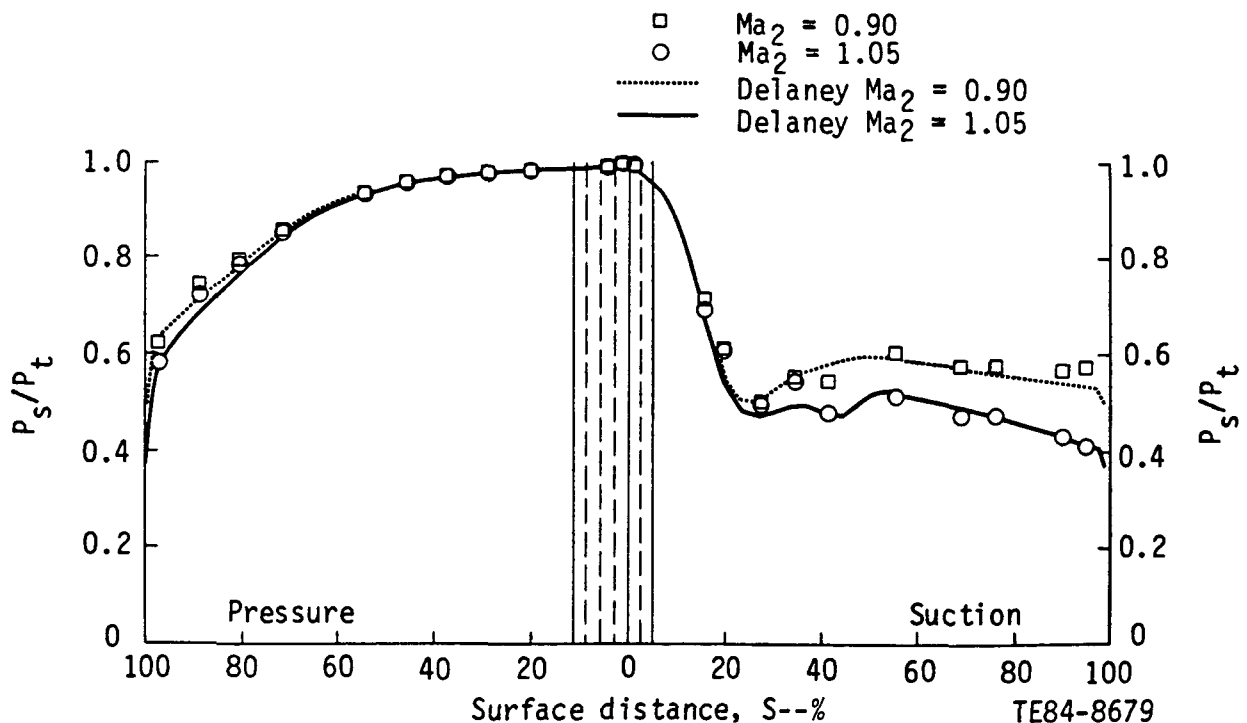
Figure 35. The surface static to inlet total pressure distributions.

dition models for the leading edge film-cooled method, it is specified using the effective total temperature definition, $T_g^* = FTG\ (T_g)$.

The remaining outer edge boundary condition is the local free-stream turbulence intensity. By definition, the outer edge free-stream turbulence intensity corresponds to the local level at no-blowing conditions. The nonfilm-cooled definition used in Ref 1 was also used in this formulation.

$$Tu_e = \begin{cases} Tu_\infty, & S > 1 \\ S(Tu_\infty), & 0 \le S \le 1 \end{cases}$$

where

$$S = \sqrt{\frac{1}{2c}\left(1 + \frac{F}{c^3}\right)}$$

$$c = \frac{(\rho u)_e}{(\rho u)_\infty}$$

$$F = \begin{cases} \dfrac{\tan^{-1}\sqrt{c^{-3}-1}}{\sqrt{c^{-3}-1}}, & c > 1 \\[4mm] \dfrac{\ln\left[c^{1.5}\left(1+\sqrt{1-c^{-3}}\right)\right]}{\sqrt{1-c^{-3}}}, & c > 1 \end{cases}$$

(20)

As indicated by Equation (20) the local free-stream turbulence intensity was constrained to be less than or equal to the inlet value. For all C3X vane computations performed in this program the experimentally determined (Ref 1) constant value $Tu_\infty = 0.066$ was used.

For defining the wall boundary conditions [Equation (7)], the normal to the wall velocity boundary condition was specified as $v_w = 0$ and the temperature (enthalpy) level condition was used instead of the flux-type condition. In keeping with the nonfilm-cooling method development effort reported in Ref 1, the original assumption was that the wall temperature was constant and equal to the surface averaged values reported in Table VI. However, the experimental hardware arrangement employed for the leading edge film-cooled experiments pro-

duced a significantly larger wall temperature gradient variation along the forward portions of the suction and pressure surfaces than that which was produced in the nonfilm-cooled experiments (Ref 1). Thus, a locally varying wall temperature boundary condition was ultimately specified for the boundary layer analysis using the measured distributions (such as the one shown in Figure 12) as a guide. The variable wall temperature boundary condition was defined only for the forward portion of the suction and pressure surfaces where the thermocouple density was the greatest and where the gradient difference between blowing and no-blowing conditions was the largest. Figure 36 illustrates specified analytical wall temperature boundary conditions (solid and dashed curves) compared with measured data distributions at a blowing (ID 4416) and a no-blowing condition (ID 4400).

As Figure 36 illustrates, the wall temperature was defined for the numerical simulation to reproduce the experimental data in the forward portions of the suction and pressure surfaces but relaxed to a constant value in the downstream regions where, as indicated, the gradient differences between the blowing and no-blowing conditions were negligible. In addition, the added realism of adopting a full nonconstant wall temperature boundary condition in the downstream region was considered unwarranted because the uncertainty of the measured heat transfer coefficient on the downstream suction and pressure surfaces approached ±20% due to decreasing airfoil thickness.

4.3.4 Starting Location Boundary Layer Profile Specification

This final subsection on method definition summarizes the procedure used to generate the computational starting point, boundary layer velocity, and temperature profile boundary conditions implied by Equation (9). In regards to the proposed modeling considerations for the leading edge film-cooled problem discussed previously, the boundary layer profiles immediately downstream of the last row of cooling holes are not altered in the sense that coolant mass has been added to the boundary layer. In addition, the computation domain does not include the actively cooled leading edge region and thus the suction and pressure surface starting locations would be chosen downstream of the last row of cooling holes on either surface.
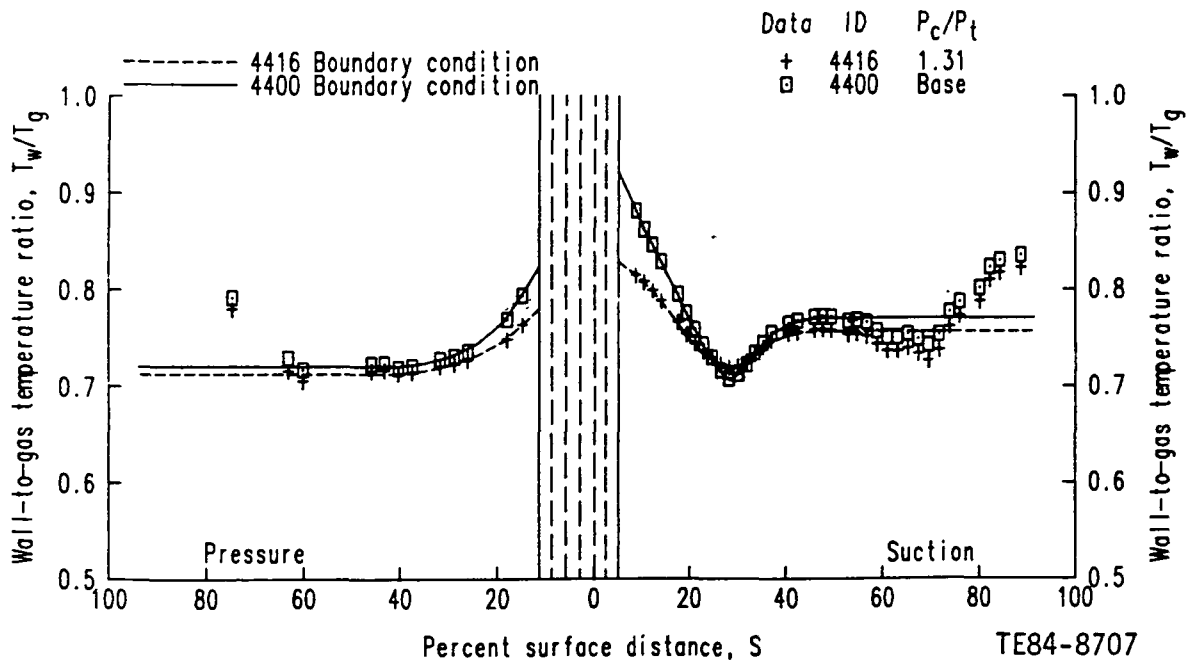
Figure 36. Variable wall temperature boundary conditions defined using measured distribution to account for significant gradient differences in the near downstream recovery region.

For the C3X vane computations, the suction and pressure surface computational starting locations were specified as the downstream boundaries of the leading edge/airfoil body, thermal barrier, and/or the beginning of the instrumented heat transfer surface. These suction and pressure surface starting locations are indicated as S_{so} and S_{po}, respectively, in Figure 37, which shows the leading edge film-cooled C3X profile and the thermal barrier region. No real significance was given to this particular choice of starting locations other than the fact that a realistic wall temperature value at the starting location was desired for generating the initial thermal profile. Also, a reasonable estimate of that value could be obtained only downstream of the thermal barrier boundary.

As mentioned previously, initial location boundary layer profiles were generated using a similarity solution technique. However, instead of using the stagnation region assumption that the Euler number, $Eu = (x/u_e) \, du_e/dx$, is equal to unity, suction and pressure surface starting point Euler numbers were determined using the local outer edge velocity boundary conditions at $x = S_{so}$ and $x = S_{po}$, respectively. The technique for generating starting location

68

profiles based on similarity solutions is only an approximation because the assumptions of constant Euler number and wall temperature required for ensuring similarity are not valid at the specified computational starting point locations. However, as a general rule, the boundary layer analysis quickly adjusts to the actual Euler number and wall temperature variation as reflected through the imposed outer edge and wall temperature boundary conditions.

The overall approach to the leading edge film-cooled heat transfer problem was to essentially reduce it to a two parameter (FTU and FTG) boundary condition problem, consequently the boundary layer analysis formulation became a direct extension of a nonfilm-cooled method. The manner in which the effective free-stream turbulence intensity and total gas temperature explicitly entered the formulation was discussed as related to the specification of closure relations [Equations (7) through (11)]. In addition, quantities, such as the local free-stream Reynolds number, that are functions of fluid properties, such as density, viscosity, etc, were also implicitly altered by the introduction of the effective gas temperature. However, as far as the numerical boundary layer computation was concerned, this posed no problem if the outer edge total temperature (enthalpy) boundary condition was correctly defined.
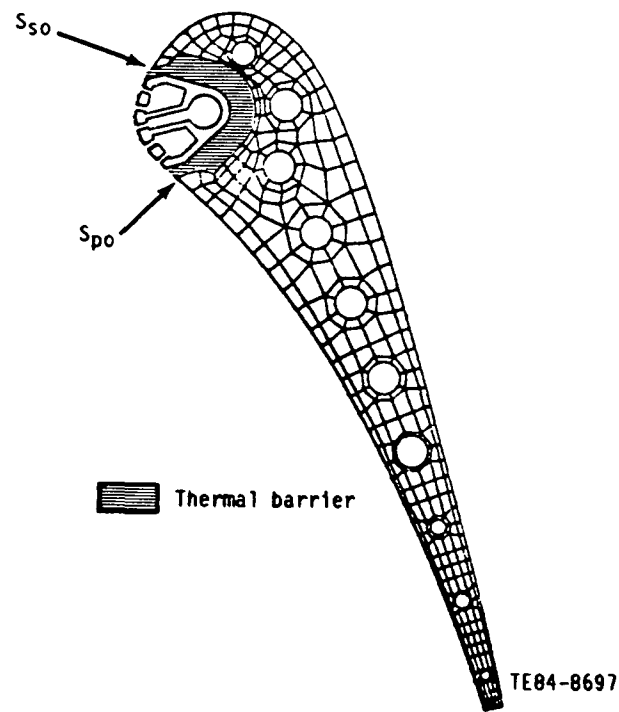
Figure 37. Airfoil suction and pressure surface locations at which numerical boundary layer computations were initiated.

4.4 METHOD CHARACTERIZATION

The leading edge film-cooled method defined previously may be used for comput-
ing airfoil surface convective heat transfer for cases with and without leading
edge film cooling. Performing a nonfilm-cooled or no-blowing condition analy-
sis corresponds to the condition where FTU = FTG = 1. A blowing condition
simulation where blowing strength is greater than one is performed by defining
FTU > 1 and/or FTG < 1. Because the overall boundary layer method is based on
a nonfilm-cooled formulation, most important characteristics of the method can
be demonstrated at no-blowing conditions. The method is discussed as a non
film-cooled airfoil convective heat transfer prediction scheme prior to demon-
strating the method performance as related to the prediction of the film-cool-
ing parameter, SNR.

4.4.1 Nonfilm-Cooled Heat Transfer Coefficient Prediction (FTU = FTG = 1)

This discussion highlights the differences in this program and that reported
previously in Ref 1. For example, because the work in Ref 1 addressed only
nonfilm-cooled airfoil convective heat transfer prediction, it was accepted
that all computations would be initiated in the leading edge stagnation region
where it was reasonable to assume that the Euler number is unity (Eu = 1). To
avoid computing through the actively cooled leading edge zone and consequently
modeling the jet boundary layer interaction, this program initiated solutions
in the recovery regions as indicated in Figure 37.

For either type of solution initiation (stagnation zone or recovery region),
the same scheme generated the initial location boundary layer profiles. This
scheme, based on the solution of approximate turbulent similarity equations,
is described in detail in Ref 1 and by Kwon et al (Ref 19). For solution ini-
tiation in the recovery region, rather than using the stagnation flow Euler
number assumption, Eu = 1, the Euler number was determined using the free-
stream conditions at the starting location. To evaluate anticipated prediction
differences associated with the two types of starts, test calculations were
performed. Results of these computations indicated that although solutions
were not identical downstream of the suction/pressure surface recovery region
starting locations, the differences were small in comparison with other aspects
of the overall method formulation, as shown in Figure 38.

70
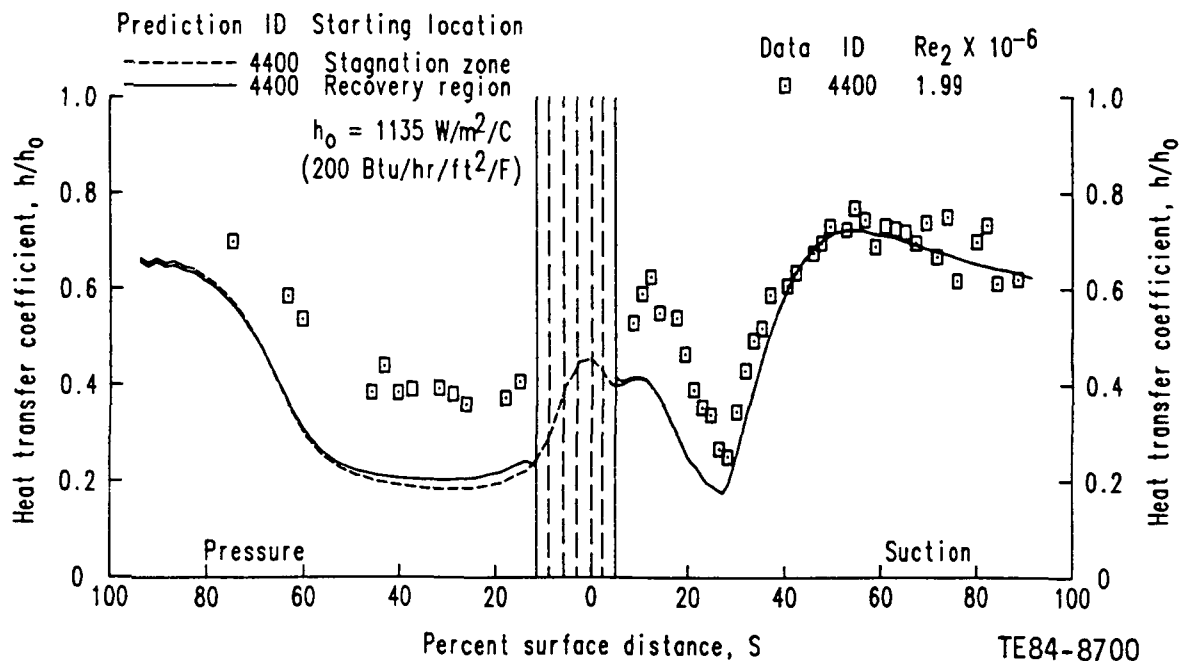
Figure 38. Computed no-blowing heat transfer coefficient distributions indicating differences due to starting location specifications $(T_w/T_g = 0.8, \; \Upsilon_{Tu} = 0)$.

This figure shows two predicted heat transfer coefficient distributions compared with the leading edge film-cooled C3X distribution obtained at a no-blowing condition. The vertical broken lines around S = 0 correspond to the locations of the five rows of cooling holes on the airfoil surface. The vertical solid lines around S = 0 correspond to the downstream thermal barrier boundaries on the suction and pressure surfaces, shown as S_{so} and S_{po}, respectively, in Figure 37. As in Ref 1, the suction and pressure surface predictions (broken curve) corresponding to the stagnation zone initiation approach were obtained by starting the computation at locations downstream of the stagnation point where the local Reynolds number (based on surface distance) was equal to five. [The stagnation point (center row of cooling holes) was predetermined from the inviscid blade-to-blade solution.] As indicated in Figure 38, the two predictions disagree for some distance downstream of the recovery region starting locations (two solid vertical lines around S = 0) to various degrees on the suction and pressure surfaces. But in comparison with the disagreement of either solution with the measured data, the difference is relatively insignificant. Accepting that the recovery region solution initiation approach is not likely to introduce significant errors in the

downstream solution, this is one possible way of avoiding computation in the leading edge film-cooled zone.

In the nonfilm-cooled method development work reported in Ref 1, the inclusion of the laminar augmentation term in Equation (10) was important to obtain reasonable predictions in the preturbulent zones on the airfoil (especially on the pressure surface). After developing a so-called preturbulent formulation [Equation (15)] that worked well for the pressure surface and the pretransition zone on the suction surface, the model was modified so that it would also apply to transition and fully turbulent flow zones. Conceptually the idea was to formulate the effective viscosity as $\mu_{eff} = \mu + \gamma_{Tu}\,\mu_{Tu}$ rather than the definition given by Equation (10). Although a fair degree of success was obtained with this approach, as reported in Ref 1 and in Appendix C, it was argued that suction surface transition/turbulent phenomena could better be addressed by using the full definition given by Equation (10). In this work the effective viscosity formulation based on the Equation (10) formulation including the preturbulent laminar augmentation model formulation developed in Ref 1 was used.

One other important aspect of the reduced formulation ($\mu_{eff} = \mu + \gamma_{Tu}\,\mu_{Tu}$) approach reported in Ref 1 was used in this program. The assumption was made that the pressure surface boundary layer does not go through a natural transition process, but is in some type of quasi laminar-turbulent state over most of the surface. To incorporate this assumption in the Equation (10) effective viscosity formulation, the transition model term, γ_t, was set to its fully turbulent value ($\gamma_t = 1$) for pressure surface computations.

Figures 38 through 40 illustrate the importance of including the various terms in the effective viscosity formulation [Equation (10)] as related to the prediction of a no-blowing condition, heat transfer coefficient distribution on the leading edge film-cooled C3X airfoil. Figure 38 was used previously to illustrate predicted differences associated with either a stagnation or recovery region solution initiation. However, no discussion was included to explain the significant differences between predicted and measured normalized heat transfer coefficient (h/h_o) levels over the entire pressure surface and forward part of the suction surface. In the complete effective viscosity

72
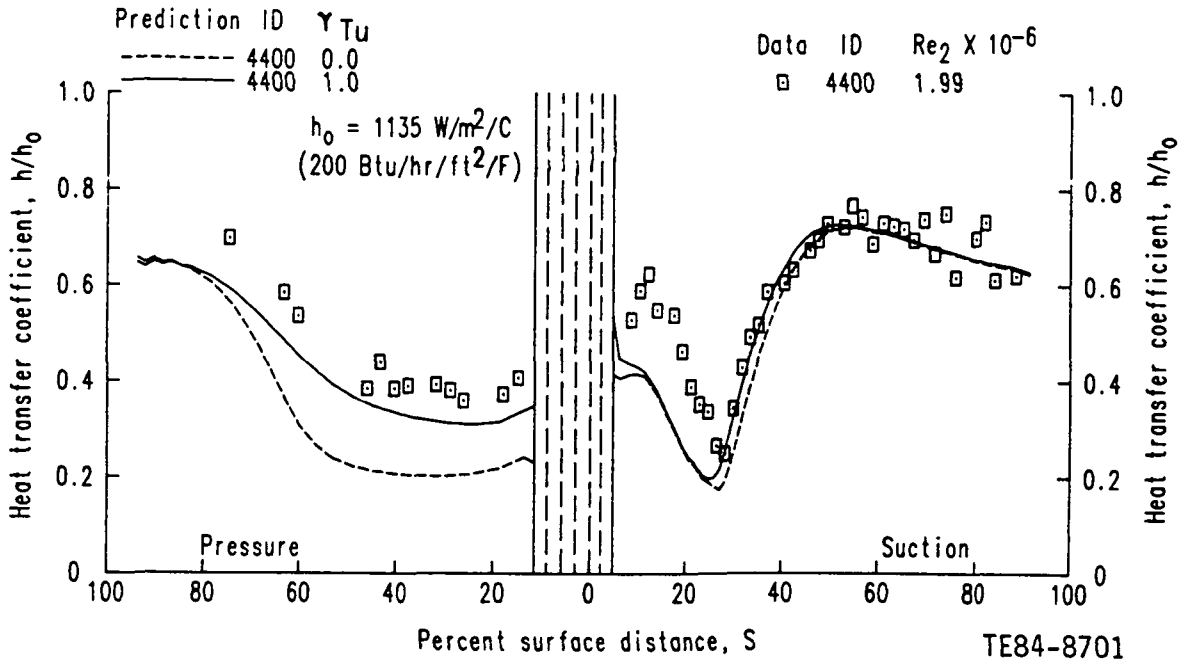
Figure 39. The effect of including (Υ_{Tu} = 1.0) or leaving out (Υ_{Tu} = 0.0) the laminar augmentation terms, $\Upsilon_{Tu}\mu_{Tu}$, in the effective viscosity formulation (T_w/T_g = 0.8).
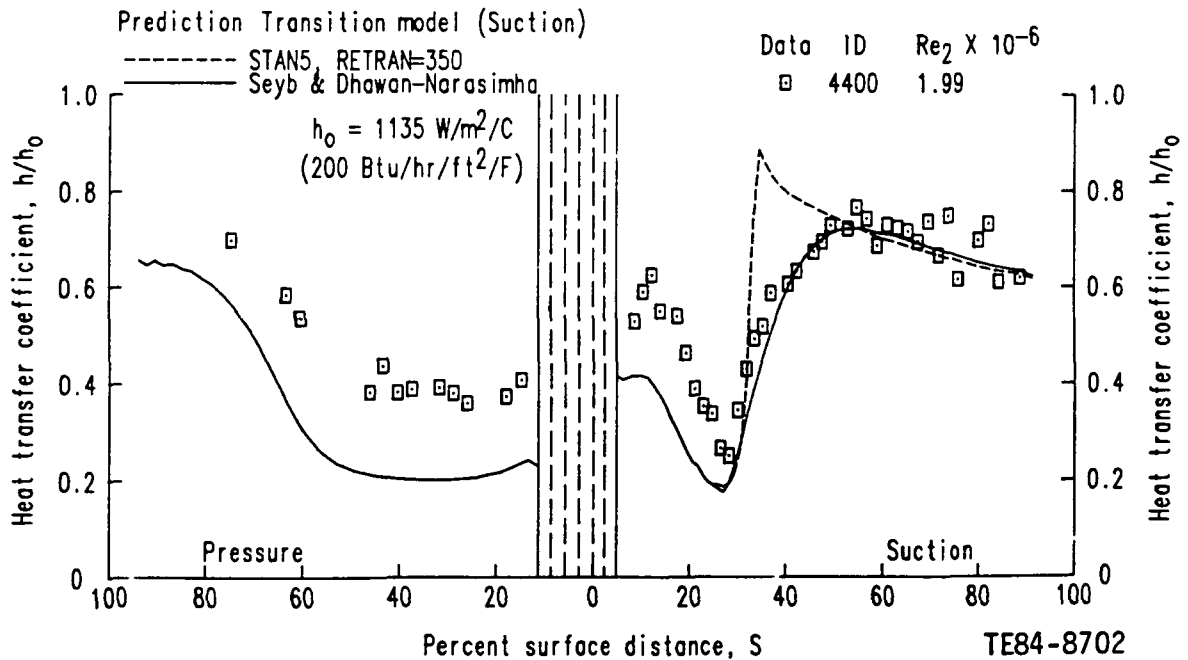
Figure 40. Differences in computed no-blowing suction surface heat transfer coefficient distributions due to turbulence model definition [Υ_{Tu} = 0, T_w/T_g = 0.8, Υ_t = 1 (pressure surface)].

73

formulation [Equation (10)], the predictions shown in Figure 38 were obtained with γ_{Tu} = 0. This reduced formulation would be in keeping with an effective viscosity formulation ($\mu_{eff} = \mu + \gamma_t\,\mu_t$) where laminar augmentation and/or free-stream turbulence intensity effects were not explicitly modeled. Formulated with γ_{Tu} = 0, the effective viscosity model used to generate the Figure 38 predictions is equivalent to the original STAN5 mixing length formulation in Ref 10, with the exception that the Seyb and Dhawan-Narasimha transition model was used for the suction surface prediction instead of that included in the original STAN5 code.

Figure 40 illustrates the differences associated with using the Seyb and Dhawan-Narasimha transition model over that contained in the Ref 10 version of STAN5. As given by Equation (14), the transition origin point ($Re_{\theta,o}$) is computed internally based on the local values of the pressure gradient parameter (λ) and the free-stream turbulence intensity. As originally set up in Ref 10, the transition origin point is supplied to the code through the input variable RETRAN. For the comparison shown in Figure 40, RETRAN was defined as the value of the transition origin point determined from the computation using the Seyb definition (RETRAN $\simeq$ 350). In the original STAN5 code, the transition endpoint is defined as twice the origin value [i.e., $Re_{\theta,e}$ = 2 ($Re_{\theta,o}$) = 700 in this example]. The Dhawan-Narasimha endpoint definition is given by Equation (16) in terms of Re_x. In terms of the momentum thickness Reynolds number, the Dhawan-Narasimha model prediction for this case indicates $Re_{\theta,e} \simeq 5$ ($Re_{\theta,o}$). Because of this longer transition zone length indication, the Seyb and Dhawan-Narasimha prediction gives a better representation of the measured heat transfer coefficient data trends than the original STAN5 model. Although this long transition zone length appears to be in keeping with the thermodynamic boundary layer transition as implied by the measured heat transfer coefficient distribution, it may not be consistent with the hydrodynamic (velocity) boundary layer transition zone length.

Because the nontransitionary (fully turbulent) effective viscosity formulation assumption (γ_t = 1) is used for dealing with pressure surface phenomena, there is no difference between the Seyb, Dhawan-Narasimha, and the STAN5 pressure surface predictions as shown in Figure 40. It should be clear from the pressure surface predictions shown in Figures 37 and 38, with γ_t = 1, that

no other definition of the transition model combined with the turbulent viscosity definition given by Equation (12) will improve the pressure surface prediction. Using the effective viscosity formulation, $\mu_{eff} = \mu + \gamma_t \mu_t$ where $\gamma_t = 1$ over the entire pressure surface, means that the full amount of turbulent viscosity is being added to the overall effective sum, which in turn translates into the maximum possible predicted heat transfer coefficient (heat flux) level. Therefore any definition where $\gamma_t < 1$ would have the effect of reducing the predicted pressure surface levels shown in Figure 40. Thus the predictions shown in Figures 38 and 40 indicate that although the reduced effective viscosity formulation is acceptable for reproducing trends, it is unacceptable for reproducing measured levels, especially on the pressure surface.

This conclusions leads to the characterization of the full effective viscosity formulation shown in Figure 39. In this figure the Seyb and Dhawan-Narasimha transition model prediction shown in Figure 40 ($\gamma_{Tu} = 0$) is compared with a full formulation prediction (i.e., $\gamma_{Tu} = 1$). As shown in Figure 39, the result of including the laminar augmentation term is a significant improvement in the predicted pressure surface heat transfer levels. As indicated by the laminar augmentation viscosity model defined by Equation (18), the idea behind the addition of the laminar augmentation terms is to model heat transfer augmentation due to free-stream turbulence by explicitly defining a velocity scale (Tu_e^* (u_∞)) based on the local free-stream turbulence intensity in a Prandtl mixing length formulation. The merge of the $\gamma_{Tu} = 0$ and $\gamma_{Tu} = 1$ predictions shown in Figure 39 downstream along the suction and pressure surfaces is a result of the decay definition used for the local effective free-stream turbulence intensity [Equation (20)]. By definition, as the Reynolds number increases, the magnitude of the laminar augmentation viscosity decreases. Because the magnitude of the turbulent viscosity increases as the Reynolds number increases, the net result is that as the Reynolds number increases the effective viscosity magnitude, $\mu_{eff} = \mu + \gamma_t \mu_t + \gamma_{Tu} \mu_{Tu}$, approaches the reduced quantity, $\mu_{eff} = \mu + \gamma_t \mu_t$, which is illustrated in Figure 39.

The last topic of this discussion, relating to the differences in the nonfilm-cooled predictions of airfoil heat transfer coefficient distributions between this approach and that of Ref 1, deals with the specification of the wall

temperature boundary condition. The heat transfer coefficient distribution predictions shown in Figures 38, 39, and 40 for the no-blowing data (ID 4400) were all obtained using a constant wall temperature boundary condition (T_w/T_g = 0.8). The constant wall temperature definition is in keeping with that used throughout Ref 1 and thus was used initially in this method development effort. However, the measured temperature gradients in the near downstream, recovery region were significantly larger for the leading edge film-cooled C3X airfoil than for the nonfilm-cooled C3X vane used in Ref 1. This difference was a result of using a thermal barrier to isolate the film-cooled leading edge from the remainder (recovery region) of the airfoil surface (see Figure 6).

In addition, there could be an appreciable near downstream recovery region wall temperature gradient difference between certain blowing and no-blowing conditions (see Figure 36). It seemed appropriate, therefore, to replace the constant wall temperature boundary condition with a more realistic variable condition. Also, preliminary no-blowing condition prediction/data comparisons, obtained using the complete method but with a constant wall temperature boundary condition, indicated that significant predicted discrepancies occurred along the near downstream recovery region (especially along the suction surface). This observation is demonstrated in Figure 39. The γ_{Tu} = 1 curve corresponds to a complete method prediction [complete meaning that the Equation (10) effective viscosity formulation was used]. This analytical observation was used as further evidence to justify the use of a variable wall temperature boundary condition.

It is stressed, however, that the important aspect of the wall temperature boundary condition definition is the simulation of gradient effects not overall level effects. To illustrate this as related to the prediction of near downstream recovery region heat transfer phenomena at a no-blowing condition, predicted heat transfer coefficient results using the three wall temperature boundary condition assumptions (T_w/T_g) shown in Figure 41 are presented in Figure 42. As indicated in Figure 41, the constant wall boundary conditions, T_w/T_g = 0.9 and 0.7, were chosen to bracket the measured distribution (C3X ID 4400 no-blowing data). The variable boundary condition was defined to simulate the measured distribution in the near downstream recovery region. As the
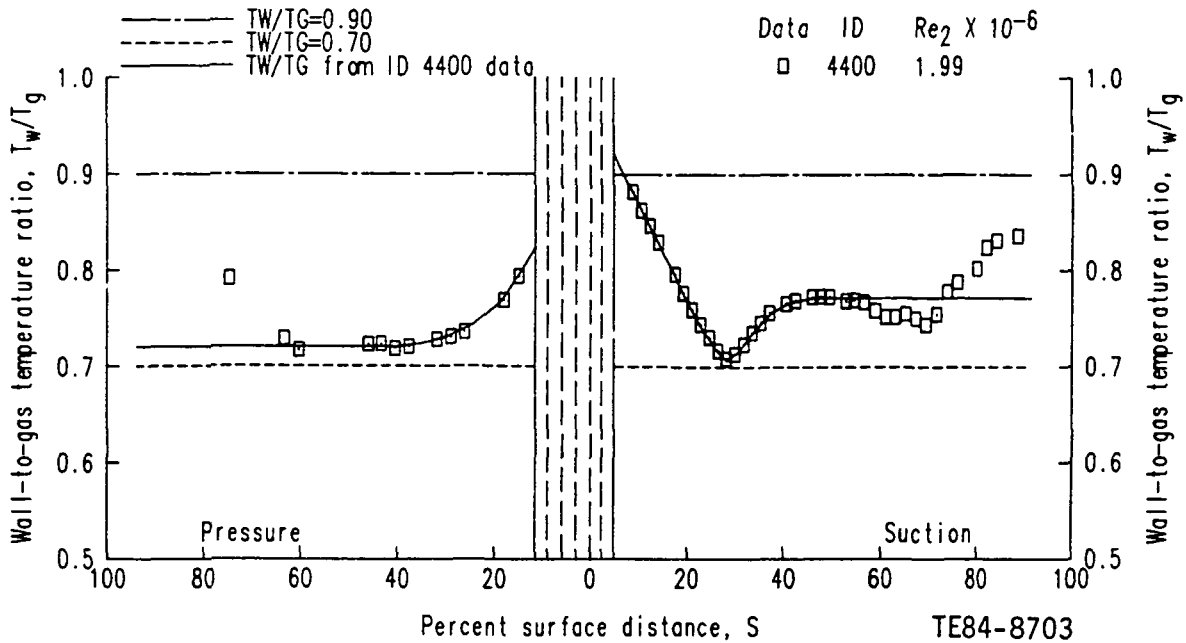
Figure 41. Comparison of three normalized wall temperature boundary condition distributions to measured distribution for run 4400 with no blowing.

corresponding heat transfer coefficient predictions shown in Figure 42 illustrate, bracketing the overall measured wall boundary conditions with a constant wall temperature condition does not result in a bracket on the predicted heat transfer coefficient. The prediction in the near downstream suction/pressure recovery regions where $d(T_w/T_g)/dS < 0$ gives a much better representation of the measured heat transfer coefficient levels. Thus the sample prediction/data comparisons shown in Figure 42 suggest that wall temperature gradient modeling rather than constant level difference modeling could be a more important aspect of an overall design formulation. Although this is not a new concept, it is appropriate to mention it because real engine hardware does not usually operate at a constant wall temperature even though that assumption is commonly used in preliminary design analyses.

In summary, only two aspects of the recovery region solution initiation and variable wall temperature boundary condition definition differ markedly from the formulation proposed in Ref 1. The effective viscosity formulation used in this program is comprised of models tested and/or developed in Ref 1 and is considered to be a better overall suction/pressure surface model. Figures 43 and 44 graphically summarize the final wall temperature boundary condition and
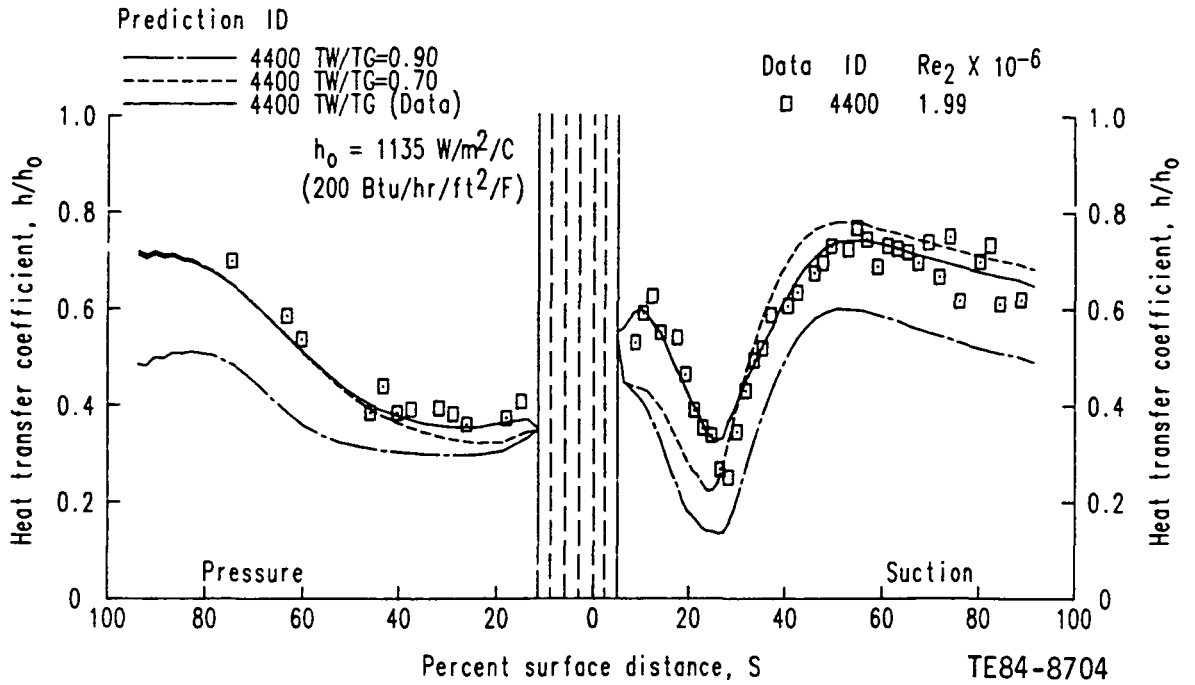
Figure 42. Computed no-blowing heat transfer coefficient distributions indicating the influence of wall temperature boundary condition specifications.
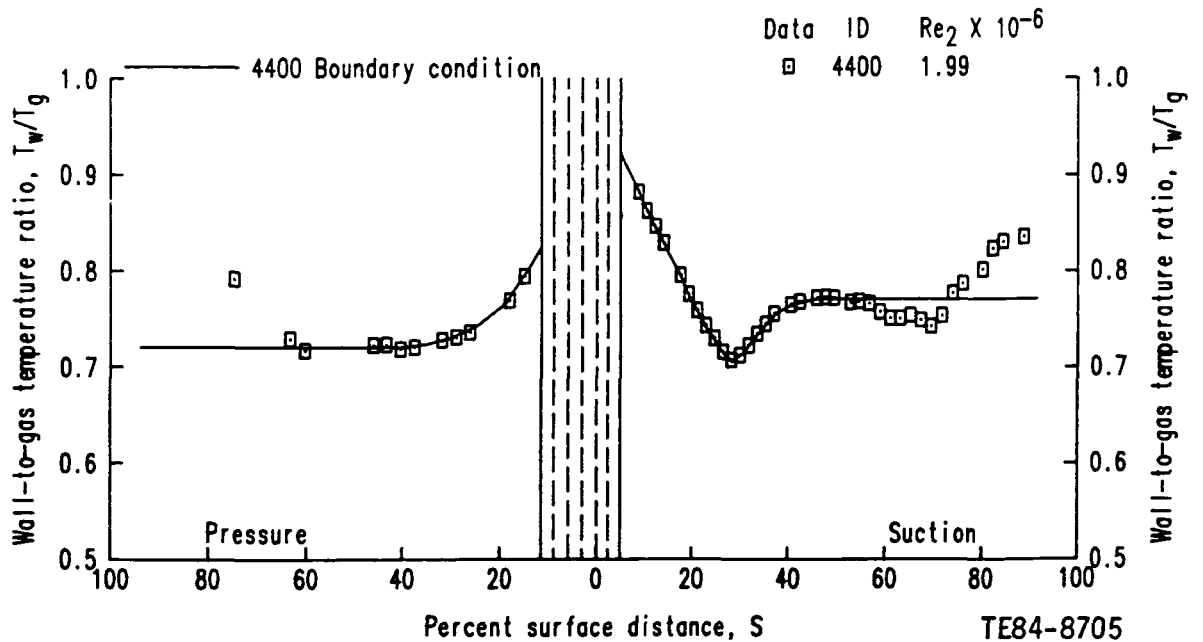
Figure 43. Variable wall temperature boundary condition defined using measured distribution for run 4400 with no blowing.
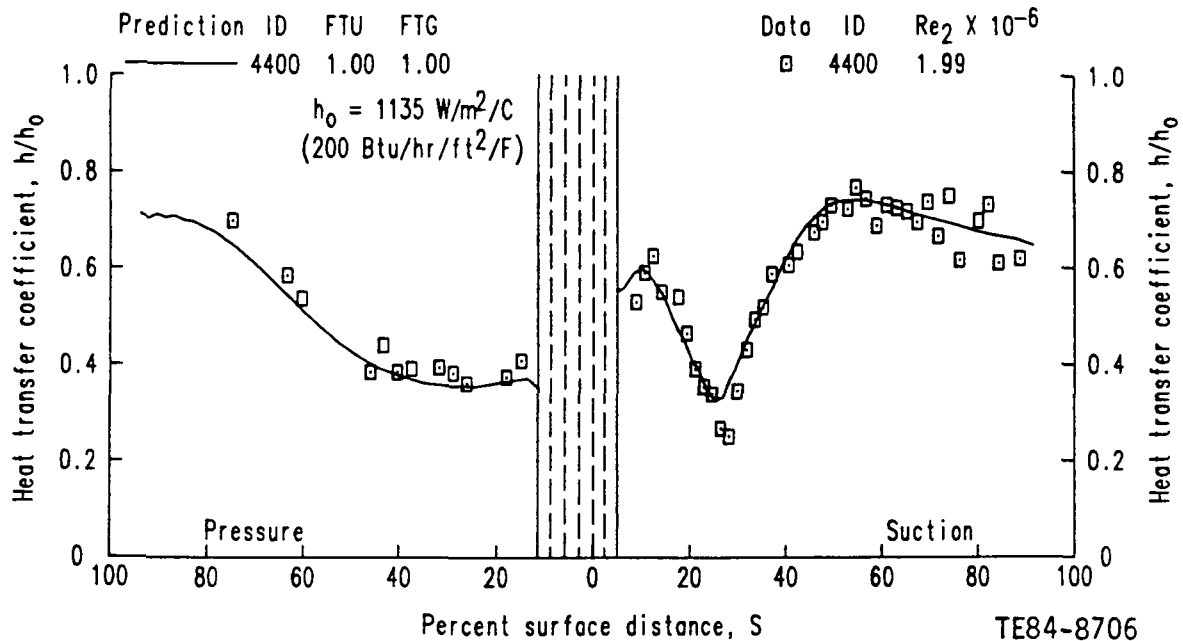
Figure 44. Predicted no-blowing heat transfer coefficient distributions using the leading edge film-cooled method for run 4400.

the resulting predicted heat transfer coefficient distribution obtained for the leading edge film-cooled C3X airfoil simulation at the no-blowing condition (ID 4400). To assist any independent attempts to reproduce this formulation, STAN5-formatted suction/pressure input decks for this particular no-blowing case (ID 4400) are given in Appendix C.

4.4.2 SNR Prediction (FTU and/or FTG ≠ 1)

In keeping with the presentation of the leading edge film-cooled C3X airfoil experimental results, a predicted SNR presentation was used to evaluate the method's potential for predicting the effects of leading edge film cooling on recovery region heat transfer. Prediction and data comparisons illustrating the effects of analytically and experimentally varying the four parameters (exit Mach number, Ma_2, exit Reynolds number, Re_2, blowing strength, and cooling strength) at blowing conditions are discussed. However, it is appropriate to review the procedure used to analytically define the SNR distribution corresponding to each blowing condition simulated in terms of the two parameters FTU and FTG. SNR is defined as follows

$$SNR = 1 - (St_{FC}/St_{NFC}) \tag{1}$$

79

where St_{FC} and St_{NFC} correspond to the Stanton numbers at blowing and no-blowing conditions, respectively. The Stanton numbers are defined using the following general definition

$$St = \frac{\dot{q}_w''}{(\rho c_p u)_e (T_w - T_g)}$$ (21)

Using the method developed in this work, the Stanton number at no-blowing condition distribution is computed with the two parameters FTU and FTG set equal to one. In the effective free-stream turbulence intensity and total gas temperature boundary condition definitions, the effective boundary conditions are then equivalent to $T_g^* = T_g = T_{g,\infty}$ or an explicit function $[Tu_e^* = Tu_e = f(Tu_\infty)]$ of quantities experimentally measured upstream of the vane row. For computing the Stanton number at blowing condition, the two parameters FTU and FTG would take on nonunity values in keeping with the qualitative representations shown previously in Figures 33 and 34 and all quantities in Equation (18), with the exception of the vane surface temperature, would be defined in keeping with the effective quantity definition (e.g., T_g becomes T_g^*).

The procedure for computing SNR by first performing a computation corresponding to a particular no-blowing operating condition followed by a computation corresponding to a particular blowing condition would be relatively straight-forward if appropriate analytical definitions of FTU and FTG could be directly coded in the numerical boundary layer scheme. However, no such definitions were given in this program. This lack of definition is in keeping with the scope of this investigation. The method proposed in this work is characterized by its potential for predicting the leading edge film-cooled heat transfer data obtained for the C3X vane. Although analytical definitions for FTU and FTG could be formulated based on the qualitative descriptions shown in Figures 33 and 34, these definitions would be considered premature based on the single data base prediction/data comparison study conducted in this program. Establishing these functions at this time could lead to the erroneous conclusion that appropriate analytical definitions for FTU and FTG that are valid for any leading edge film-cooled airfoil configuration had been discovered. To predict an experimental blowing condition case, FTU and FTG were externally set in

keeping with the Figure 33 and 34 representations that were developed using the C3X experimental results. In developing an empirical model to simulate experimentally observed phenomena, this approach is viewed as an important step in demonstrating both method potential and the suggestion that only two empirical model parameters (FTU and FTG) are necessary to reproduce leading edge film-cooled recovery region heat transfer phenomena.

Because in most blowing condition simulations both FTU and FTG would be set to nonunity values to simulate both turbulence production and thermal dilution phenomena, it is worthwhile to present the results of sample calculations where FTU and FTG were varied independently over a range of values. In this way, the role of each parameter can be demonstrated along with providing an indication of how particular values might be selected for simulating arbitrarily blowing condition cases. Figure 45 shows four predicted SNR distributions compared to the experimental data for the 4416 operating condition summarized in Table VI. For the numerator term (St_{FC}) in the 4416 SNR predictions, FTG was equal to 1.00 and FTU was varied from 1.00 to 2.50. The no-blowing denominator term (St_{NFC}) is the same in all cases and corresponds to case 4400 summarized in Table VI and generated with FTU = FTG = 1.00. The results shown illustrate several important features of the overall method that have been previously discussed.

First, predictions are shown for only the recovery regions (downstream of the solid vertical lines around S = 0), in keeping with the recovery region solution initiation approach. For all four cases, the level of SNR predicted at the initial location was approximately equal to zero. This level indicates that the boundary layer profiles specified at the first computational station did not reflect the increase in free-stream turbulence intensity corresponding to FTU > 1. However, even though these blowing condition initial location profiles were poor approximations, the profiles were quickly readjusted as the computation proceeded downstream and did not appreciably influence the predicted results over much of the airfoil surface. This lack of influence is indicated by the predicted pressure surface SNR results in Figure 45.
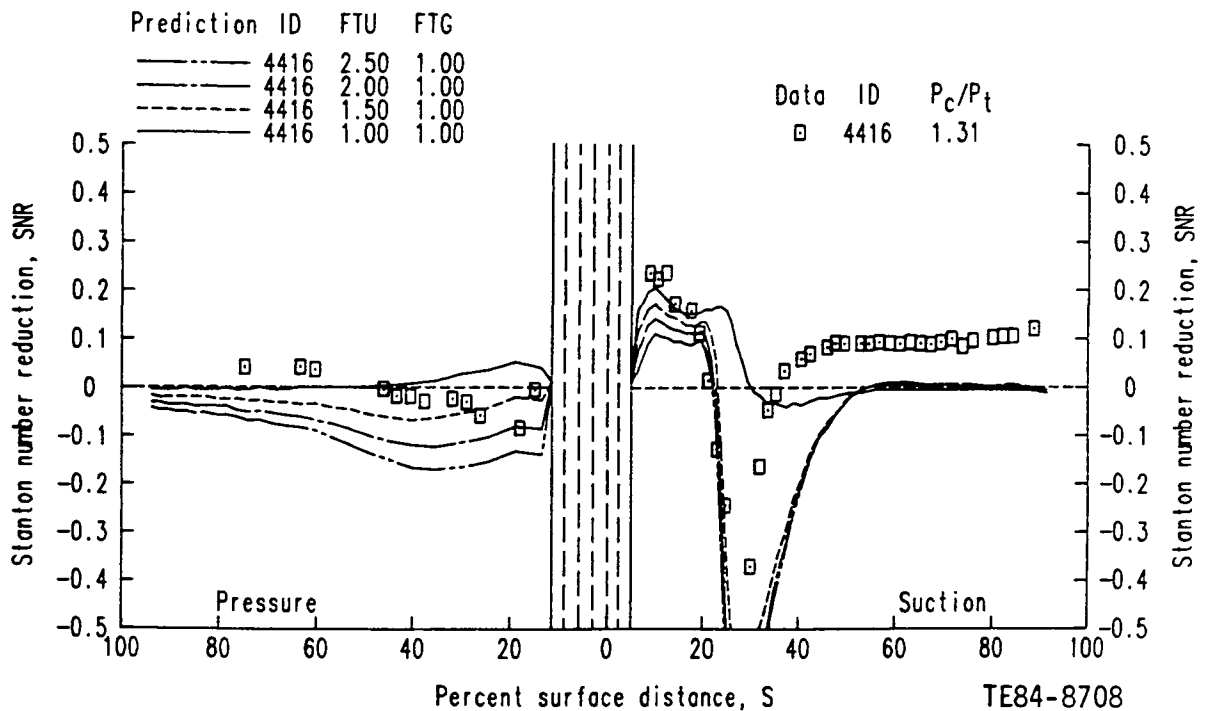
Figure 45. Characteristic influence of the free-stream turbulence intensity factor variation on the predicted Stanton number reduction using run 4416 blowing condition data.

The predicted SNR distribution corresponding to the case of FTU = FTG = 1.00 is significant because this particular value corresponds to the specification for a no-blowing condition prediction. Therefore, it might be anticipated that the predicted SNR = 0 along the entire surface. However, since the wall temperature boundary condition for the blowing condition case (ID 4416) is different from the nonblown baseline (ID 4400), as shown in Figure 36, the two Stanton number quantities (St_{FC} and St_{NFC}) forming the SNR definition would not be expected to be equal, even though in both cases FTU = FTG = 1. Thus by correctly simulating the experimentally measured wall temperature gradient differences that occur at blowing and no-blowing condition in the near downstream recovery region, the effects of the upstream injection are partially accounted for in a direct manner. Together, the blowing (4416) and no-blowing (4400) wall temperature distributions shown in Figure 36 and the corresponding FTU = FTG = 1.00 SNR prediction shown in Figure 45 indicate that the effect of decreasing the near downstream recovery region wall temperature gradient is to reduce the blowing condition heat transfer levels giving the SNR > 0 result.

Increasing FTU and/or equivalently the specified free-stream turbulence intensity boundary condition results in an increasing predicted heat transfer level or reduced SNR. However, as the SNR results shown in Figure 45 illustrate, the shift in SNR levels is not uniform over the entire surface. This result is explained by first noting that the only place where the parameter FTU explicitly enters the formulation is in the laminar augmentation viscosity and transition model terms in the effective viscosity formulation. As stated previously, pressure surface computations are performed with $\gamma_t = 1$ and thus the SNR level shift along the pressure surface is due to the magnitude of the laminar augmentation viscosity term. Because a decay definition is used for local free-stream turbulence intensity [Equation (20)] the ratio of the laminar augmentation viscosity to the turbulent viscosity (μ_{Tu}/μ_t) decreases as the computation proceeds downstream. This decrease, combined with the fact that local heat transfer coefficient levels are higher along the aft portions of the pressure surface than along the forward portions, results in the nonuniform SNR shift illustrated in Figure 45.

On the suction surface, the effect of increasing the laminar augmentation viscosity magnitude while increasing the FTU is small in comparison with the effect caused by changing the transition origin location that is defined as part of the transition model term. That is, the result of increasing the FTU is to move the predicted transition origin location forward along the suction surface, which explains the predicted negative SNR trough along the suction surface $(20 < S < 50)$ caused by the fact that the turbulent viscosity begins sooner [(Equation (10)].

Finally, the results shown in Figure 45 indicate that the FTU parameter is only significant in determining the predicted SNR in the forward portion of the recovery region. Because the effective free-stream turbulence intensity quantity $Tu_e^* = FTU(Tu_e)$ was introduced to simulate the turbulence production mechanism associated with the leading edge injection process, this result is in keeping with the idea that the disturbance introduced in the nominally laminar (low Reynolds number) zone would have a greater effect there than in the turbulent (high Reynolds number) zones along the aft suction and pressure surfaces.

It was suggested in the discussion on experimental results that the positive SNR result observed along the downstream suction and pressure surfaces was due to thermal dilution resulting from the introduction of a relatively cool fluid into the hot free-stream gas. To model this so-called far downstream effect, the concept of effective total gas temperature was introduced and incorporated in the overall formulation using the parameter FTG. Figure 46 illustrates the effect of varying the FTG independently of the FTU. Four predictions are shown for the same 4416 test condition data shown in Figure 45. For all four predictions, the FTU was equal to 2.00 and only the FTG was varied. The prediction labeled FTU = 2.00, FTG = 1.00 corresponds to the one in Figure 45 and may be used to contrast the roles of the FTU and FTG. In keeping with the suggested data trends and the fact that $T_c/T_g < 1$, the effective total gas temperature is reduced by setting FTG < 1 [i.e., $T_g^* = FTG(T_g)$]. Results shown in Figure 46 along the suction surface beyond S > 50, clearly indicate that the effective total gas temperature boundary condition approach is one way of reproducing both the data trend and level. As would be anticipated, reducing the FTG and/ or the effective gas temperature results in a decreased heat transfer prediction or increasing SNR result. However as indicated by the results shown in Figure 46, the FTG variation does not influence predicted results in the near downstream recovery region.
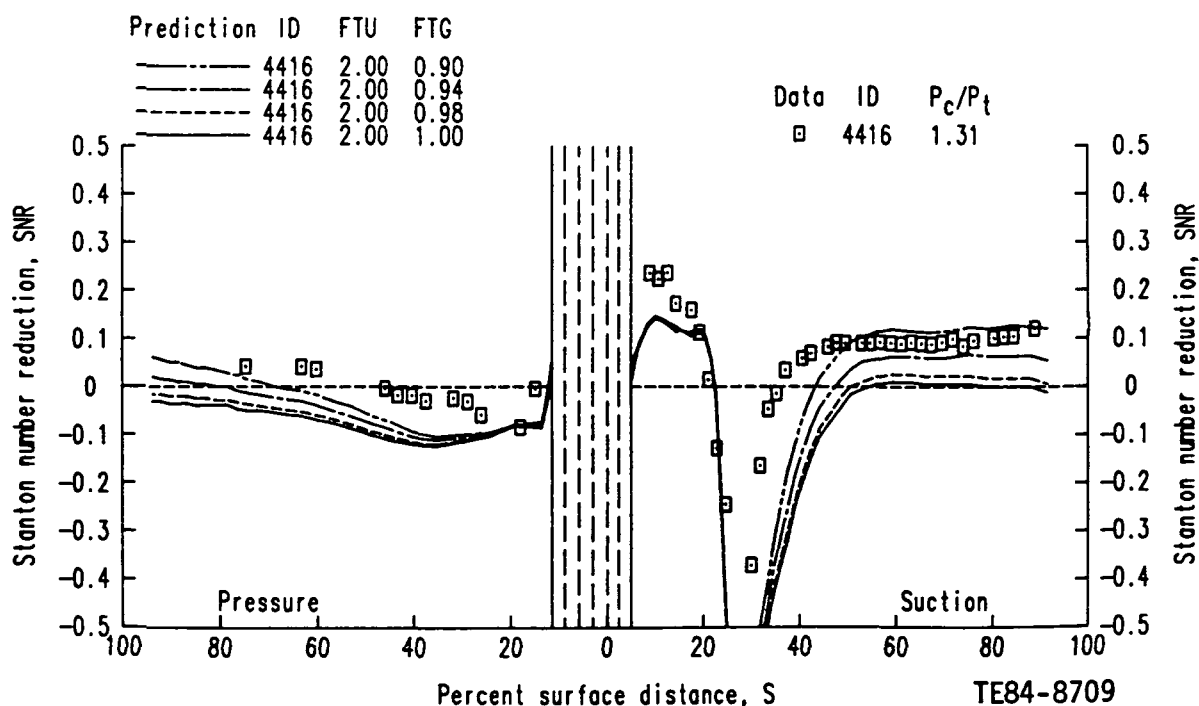
Figure 46. Characteristic influence of the free-stream total gas temperature factor variation on the predicted Stanton number reduction using run 4416 blowing condition data.

Together the sample calculations shown in Figures 45 and 46 indicate the respective roles of the FTU and FTG for simulating near recovery region turbulent production and far recovery region thermal dilution phenomena. In the following prediction/data comparison section, the values of the FTU and FTG are consistent with the functional trends shown in Figures 33 and 34 and reflect the solution behavior indicated in the sample predictions shown in Figures 45 and 46.

4.5 DATA BASE PREDICTION/DATA COMPARISON

In subsection 3.4, a select group of experimental results from the film-cooled C3X vane data base was presented. These data sets were selected to illustrate the characteristic influences of the exit Mach number, exit Reynolds number, cooling strength, and blowing strength variations as related to recovery region heat transfer phenomena. As a final demonstration of the film-cooled method developed in this program, computations were performed to numerically simulate the experimental observations corresponding to variation of the exit Mach number, exit Reynolds number, cooling strength, and blowing strength.

4.5.1 Exit Mach Number Variation

A conclusion of the experimental program was that SNR is essentially independent of exit Mach number, at least over the range tested $(0.90 < Ma_2 < 1.05)$, as illustrated in Figure 19. To test whether this conclusion could be arrived at from the results of a numerical simulation, SNR predictions were made for the two test conditions (4415 and 5415) shown in Figure 19. In defining the local SNR distribution, the no-blowing condition cases (4400 and 5400) were computed to determine the denominator (St_{NFC}) of the SNR definition given by Equation 1. Predicted recovery region heat transfer coefficient (h) distributions for these two no-blowing condition cases (4400 and 5400) are shown in Figure 47 along with the corresponding experimental data. In general, agreement between the predictions and data is good along the pressure surface and the forward part of the suction surface. However, beyond S > 40 on the suction surface, the prediction corresponding to $Ma_2 = 1.05$ (5400) deviates from the measured data.
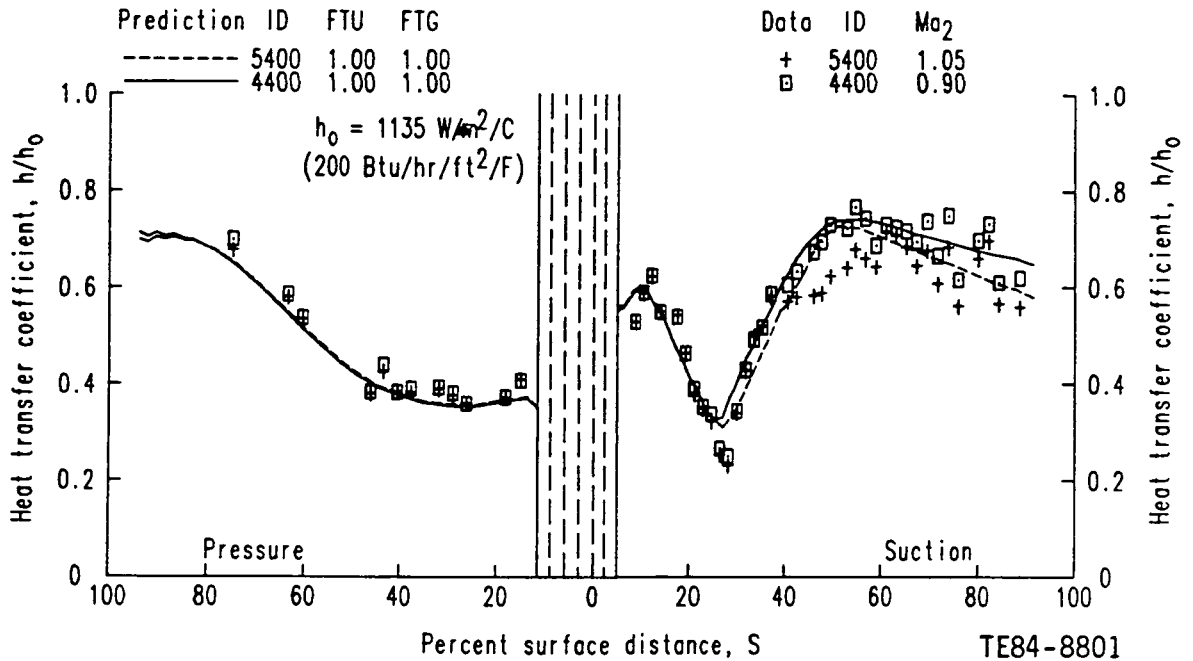
Figure 47. Predicted and measured no-blowing heat transfer coefficient distributions for two exit Mach number conditions.

To complete the definition of SNR, boundary layer computations were made for the blowing condition cases 4415 and 5415 to generate the numerator (St_{FC}). The resulting predicted SNR distributions are compared to the experimental data in Figure 48. The results shown in this figure illustrate that although the data trends are adequately reproduced, the predicted differences in the local SNR at the two exit Mach number conditions are larger than those indicated by the data. Based on the predicted results, SNR is at least a weak function of exit Mach number.

4.5.2 Exit Reynolds Number Variation

The effect of exit Reynolds number variation as related to measured SNR is illustrated in Figure 22. The interesting result of the effect is the shifted location of the suction surface trough, which can be explained in terms of transition location differences due to the exit Reynolds number variation. For the numerical simulation, SNR predictions corresponding to the variable exit Reynolds number blowing conditions (4315, 4415, and 4515) were generated by first computing the respective no-blowing baseline conditions (4300, 4400,
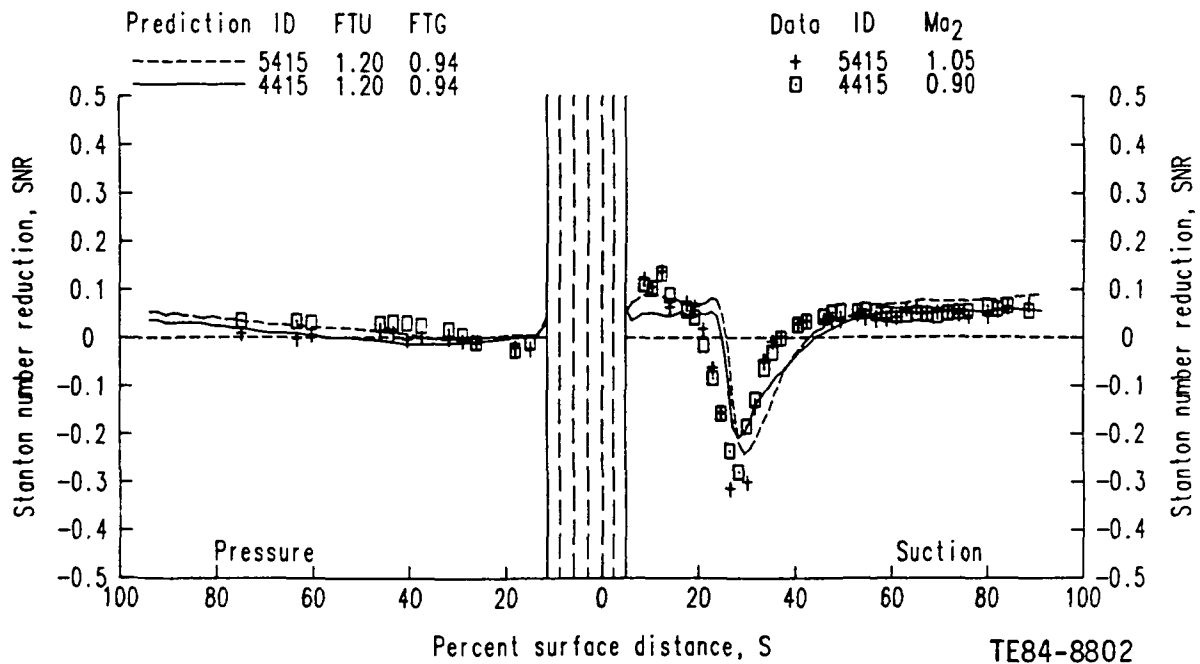
Figure 48. Predicted Stanton number reduction distributions for two exit Mach number conditions compared with runs 4415 and 5415 blowing condition data.

and 4500). The predicted recovery region heat transfer coefficient distributions for these three no-blowing cases are shown in Figure 49 together with the experimental data. In general the two lowest Reynolds number predictions (4300 and 4400) show good agreement with the data over the entire airfoil surface. The highest exit Reynolds number predictions (4500) indicates good agreement on the pressure surface. But on the suction surface, the prediction in the indicated transition zone (20 < S < 50) deviates significantly from the experimental data. This deviation suggests a weakness in the transition model. In terms of overall method performance, the suction surface transition model caused the most trouble. The most significant prediction/data discrepancies were always found to occur along the suction surface between 20 < S < 50, which roughly corresponds to what appears to be the zone where transition occurs on the C3X vane.

One set of the predicted SNR distributions for the blowing condition cases (4315, 4415, and 4515) are shown in Figure 50 along with the corresponding experimental data. From the pressure surface results, it can be concluded that this method predicts an almost negligible effect on the SNR due to the exit
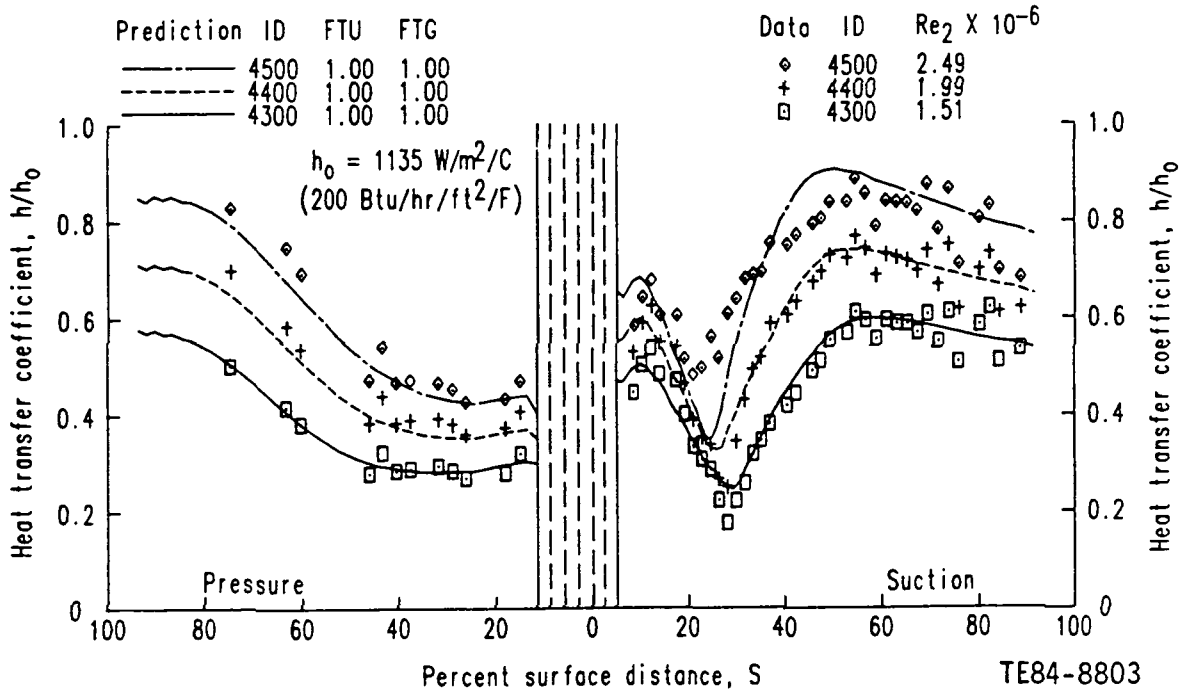
Figure 49. Predicted and measured no-blowing heat transfer coefficient distributions for three exit Reynolds number conditions.
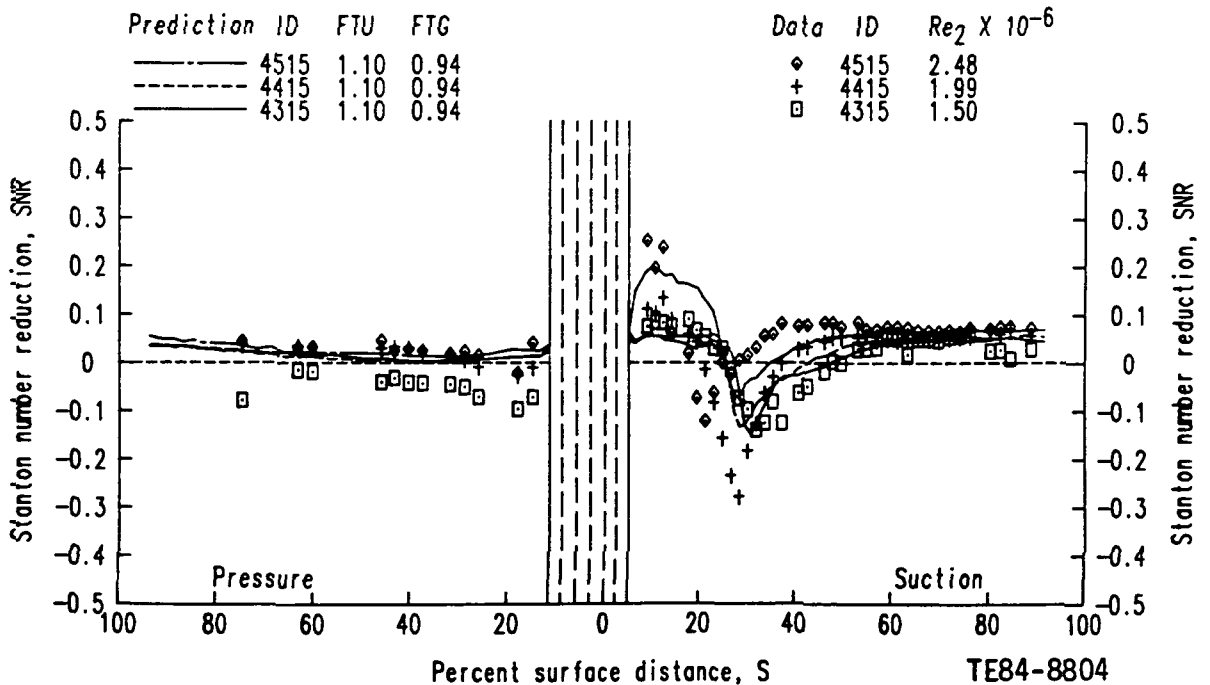
Figure 50. Predicted Stanton number reduction distributions for three exit Reynolds number conditions compared with blowing condition data from runs 4315, 4415, and 4515 where FTU = 1.10.

Reynolds number variation. Although this same conclusion can be drawn from the experimental data using only the 4415 and 4515 results, it becomes questionable if the 4315 data are also considered. On the suction surface, data trends are reproduced along with the SNR levels in the far downstream recovery region (S > 60). However the magnitude, location, and extent of the suction surface transition zone troughs are not simulated well. This inadequacy is related to the transition model performance and suggests that to improve the formulation, additional consideration must be given to transition model development.

To define the Stanton number with blowing condition for the SNR predictions shown in Figure 50, the blowing condition (4315, 4415, and 4515) boundary layer computations were performed at FTU = 1.10 and FTG = 0.94. Because the magnitude of the FTU influences the predicted transition origin location, predictions made at FTU = 1.20 are shown in Figure 51 to illustrate that adjusting this parameter does little in the way of improving the overall result within the zone 20 < S < 50 along the suction surface. The SNR predictions shown in
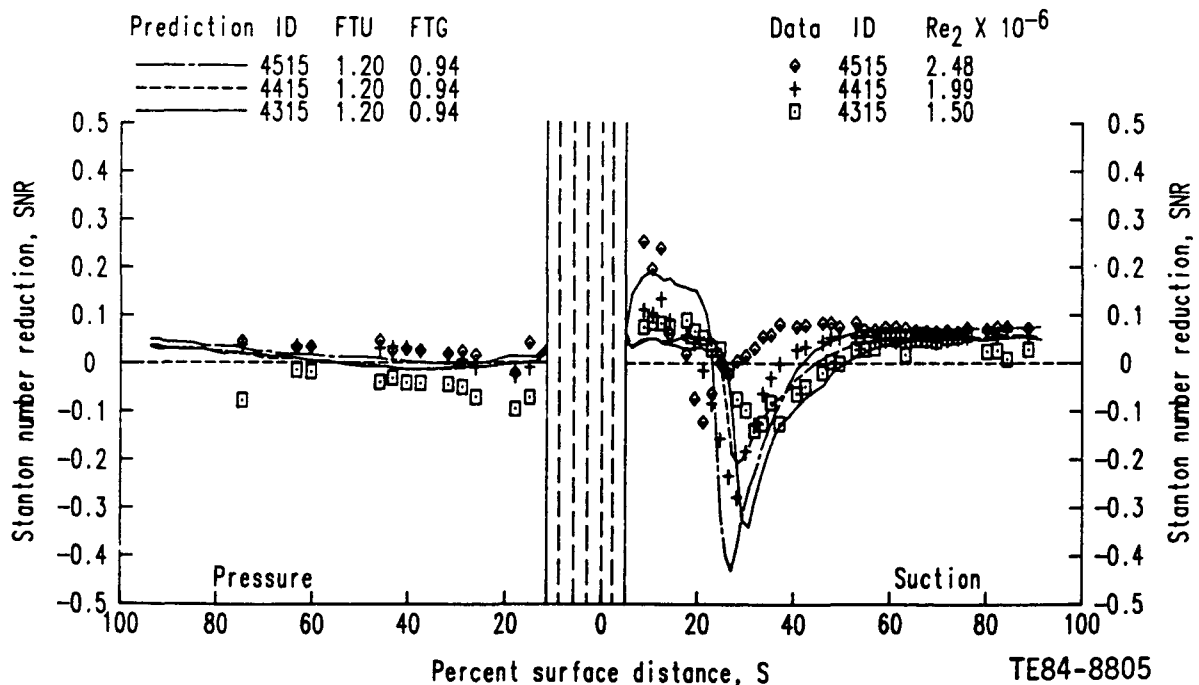
Figure 51. Predicted Stanton number reduction distributions for three exit Reynolds number conditions compared with blowing condition data from runs 4315, 4415, and 4515 where FTU = 1.20.

Figure 50 with FTU = 1.10 indicate that although the downstream portion of the SNR trough is simulated reasonably well, the upstream portion and overall magnitude is poorly predicted. Figure 51 predictions indicate that at FTU = 1.20, the upstream portion and magnitude of the trough are better simulated but the downstream portion is poorly simulated. The final conclusion from this numerical simulation of the effects of the exit Reynolds number variation is that although this method is capable of predicting the global transition zone shift phenomena observed in the data, its overall potential could be significantly improved with a better transition model definition.

4.5.3 Coolant Strength Variation

SNR predictions for the blowing conditions (4416, 4426, and 4436) are shown in Figure 52. These predictions are compared with data presented in Figure 27, which illustrated the characteristic effect of coolant temperature variation. As illustrated in Figure 52, the two parameter (FTU and FTG) method does a reasonable job in predicting all of the trends indicated in the data. For these predictions, the turbulence intensity parameter was held constant (FTU = 2.00) to be consistent with the concept that FTU is introduced to simulate only turbulence production phenomena related to blowing strength. Because all three data sets were obtained at a constant blowing condition (P_c/P_t = 1.3), a constant value of FTU is implied. However even though the blowing strength is constant, the mass flux ratio [$M = (\rho_w v_u)/(\rho_e u_e)$] is not because the coolant temperature is changing. Because it could be argued that M might be a better parameter to characterize blowing strength and/or discrete jet turbulence production phenomena than P_c/P_t, the implication that FTU is a function of P_c/P_t rather than M or some other parameter, such as momentum ratio, needs to be explored further.

The values of the FTG shown in Figure 52 were selected to match measured SNR levels along the downstream suction surface (S > 50). FTG was introduced into the formulation to simulate thermal dilution phenomena in a reduced gas temperature [$T_g^* = FTG(T_g)$]. And, in keeping with the operating conditions, FTG is reduced as the thermal dilution strength is reduced; the net effect is reduced heat transfer or increased SNR.

90
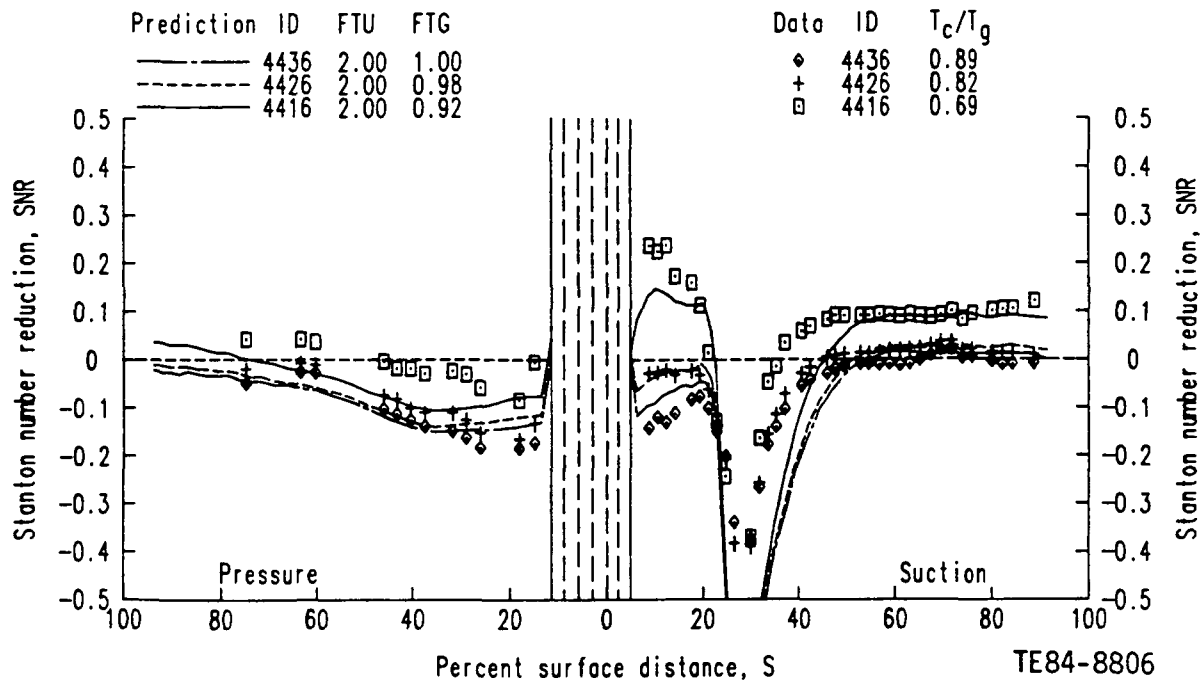
Figure 52. Predicted Stanton number reduction distributions for three coolant to gas temperature ratio conditions compared with blowing ratio data for runs 4416, 4426, and 4436.

4.5.4 Blowing Strength Variation

For simulating the recovery region heat transfer phenomena due to coolant temperature variation, the parameter FTG was varied and FTU was held constant. For simulating variable blowing strength conditions and turbulence production phenomena related to variable jet strength, the turbulence intensity parameter FTU becomes the variable quantity and FTG is held constant. SNR distributions were computed for the six blowing condition data sets shown in Figures 15 and 25. Figure 53 shows the SNR prediction/data comparisons for the three lowest blowing strength conditions (4423, 4424, and 4425) and Figure 54 shows the predicted and measured blowing condition heat transfer coefficient distribution along with the no-blowing baseline (4400). SNR and heat transfer coefficient prediction/data comparisons for the three highest blowing strength conditions (4426, 4427, and 4428) are shown in Figures 55 and 56, respectively.

The comparisons shown in Figures 53 and 54 indicate that with the exception of the suction surface transition zone (trough), there is little measured and/or predicted effect due to the leading edge injection. This small effect result is significant, because the blowing levels shown ($P_c/P_t \leq 1.10$) are more repre-
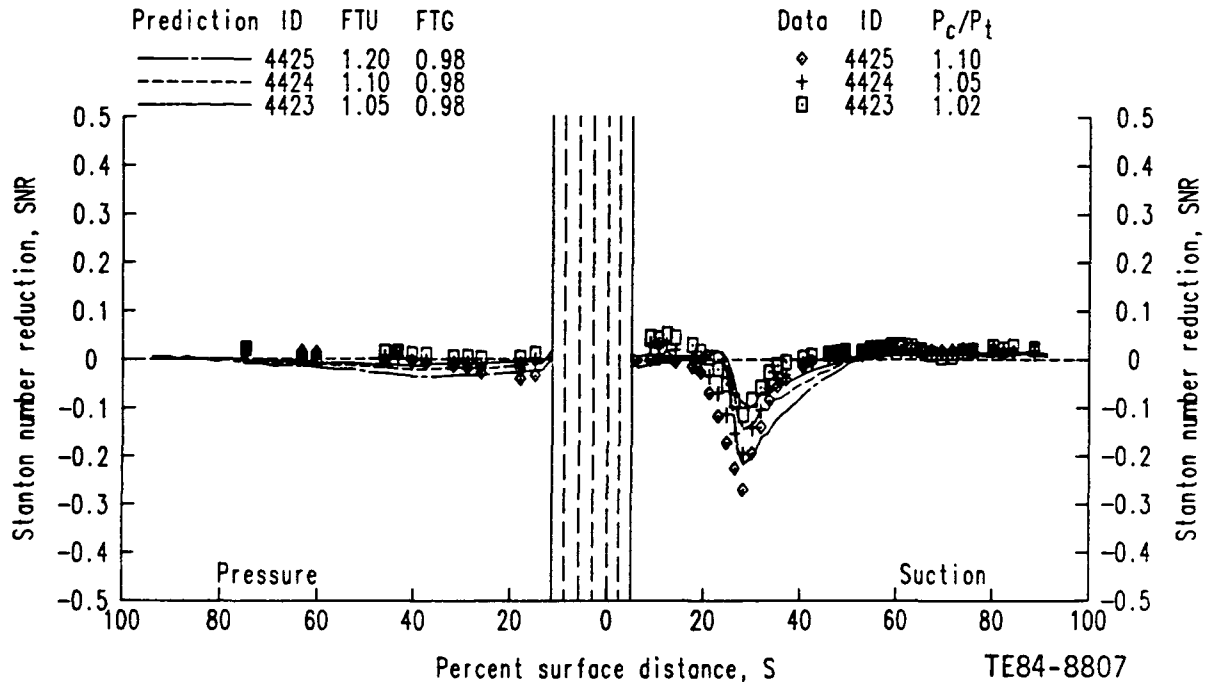
Figure 53. Predicted Stanton number reduction distributions for three coolant to free-stream pressure ratio conditions compared with blowing condition data for runs 4423, 4424, and 4425.

sentative of actual design conditions than the higher blowing cases (P_c/P_t > 1.10) shown in Figures 55 and 56. For the strong blowing condition SNR predictions shown in Figure 55, the proposed two parameter method predicts trends reasonably well but quantitative discrepancies exist.

The heat transfer coefficient distribution prediction/data comparisons shown in Figure 56 again indicate that the major source of error can be related to the transition model performance. The results shown in Figure 56 show that between 20 < S < 50 on the suction surface, the blowing condition predictions (4426, 4427, and 4428) are a poor representation of the measured data trends and levels.

When predicting transition zone heat transfer coefficient distribution trends, the no-blowing prediction (4400) follows the data trends but the blowing condition predictions do not. Because the blowing and no-blowing condition heat transfer coefficient distributions merged along the suction surface near S = 40, the hydrodynamic boundary layer may have completed transition near that location while the thermodynamic boundary layer completes transition downstream nearer S = 55 where the heat transfer coefficient distributions begin to level off. If this is the case, it would imply that distinct transition modeling
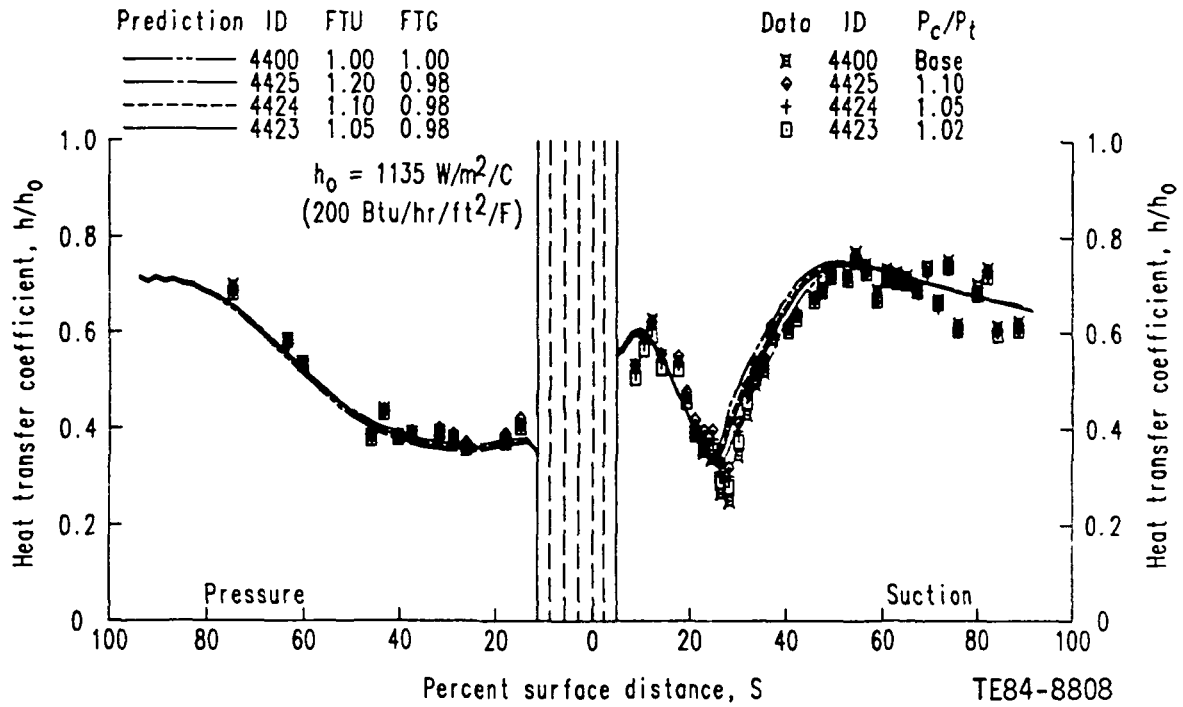
Figure 54. Predicted and measured heat transfer coefficient distributions for three coolant to free-stream pressure ratio blowing conditions (runs 4423, 4424, and 4425) and the no-blowing, baseline condition (run 4400).
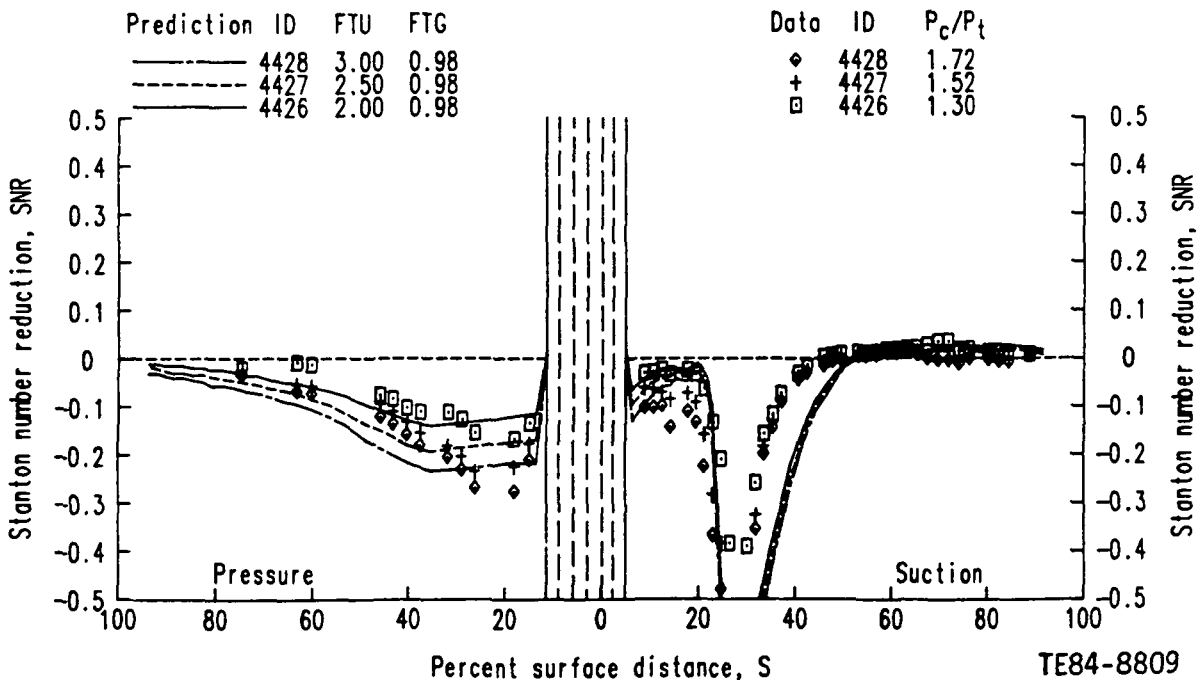
Figure 55. Predicted Stanton number reduction distributions for three coolant to free-stream pressure ratio conditions compared with blowing condition data from runs 4426, 4427, and 4428.

93

Prediction ID   FTU   FTG   Data   ID P_c/P_t
————⋅—— 4400   1.00   1.00   ⌗   4400   Base
————⋅— 4428   3.00   0.98   ◇   4428   1.72
———————— 4427   2.50   0.98   +   4427   1.52
————— 4426   2.00   0.98   □   4426   1.30

$h_0 = 1135 \ W/m^2/C$

$(200 \ Btu/hr/ft^2/F)$

Heat transfer coefficient, h/h_0

1.0
0.8
0.6
0.4
0.2
0

Pressure   Suction

100 80 60 40 20 0 20 40 60 80 100

Percent surface distance, S   TE84-8810
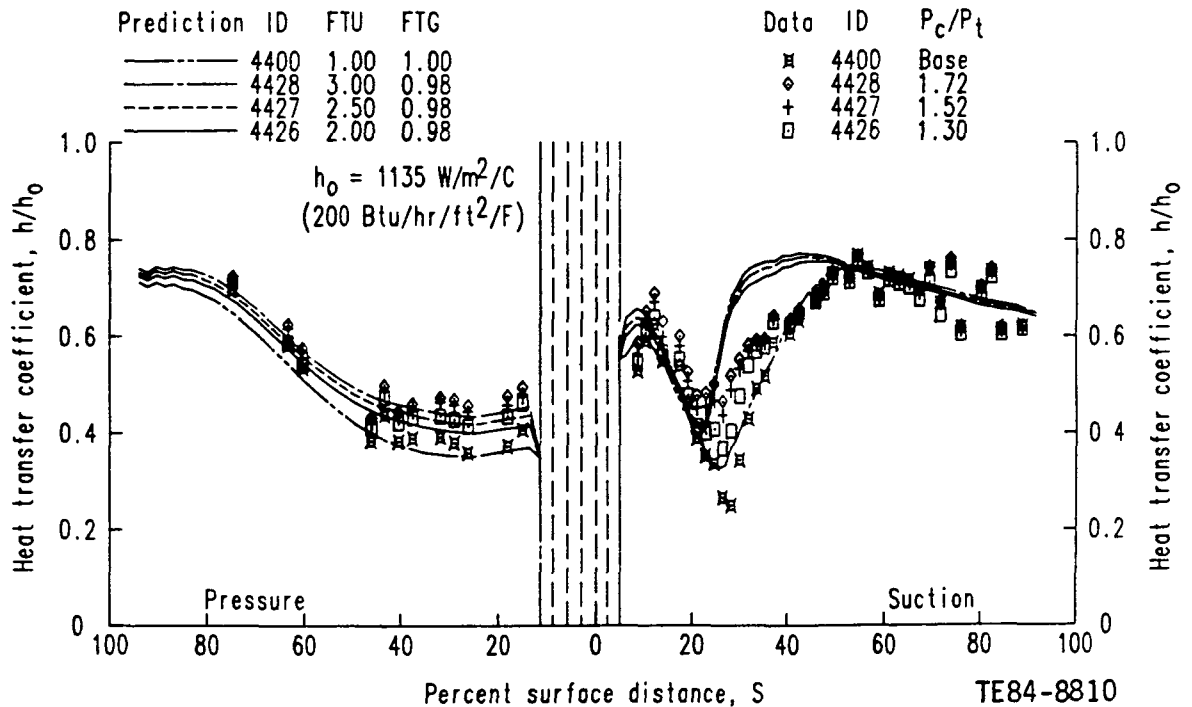
Figure 56. Predicted and measured heat transfer coefficient distributions for three coolant to free-stream pressure ratio blowing conditions (runs 4426, 4427, and 4428) and the no-blowing, baseline condition (run 4400).

terms would have to be included in both the effective viscosity and effective Prandtl number formulations. This interesting modeling concept needs to be explored further to test its validity and its potential for resolving problems related to the prediction of airfoil transition phenomena in a gas turbine environment.

4.6 CONCLUSIONS AND RECOMMENDATIONS

This study describes one method for simulating recovery region convective heat transfer phenomena caused by leading edge discrete site injection. The method is a simple, direct extension of a nonfilm-cooled 2-D boundary layer analysis formulation. Two parameters, FTU and FTG, are defined to model turbulence production and thermal dilution phenomena. Computationally, these two parameters are used to alter the boundary layer outer edge free-stream turbulence intensity and total gas temperature (enthalpy) boundary conditions. From the results of the prediction/data comparisons presented for both blowing and noblowing conditions, the following conclusions regarding overall method performance can be made:

o The method as formulated is able to qualitatively reproduce the measured C3X airfoil SNR distributions for all blowing conditions tested. In the

practical design domain ($P_c/P_t < 1.10$) good quantitative agreement was obtained, but at high blowing levels ($P_c/P_t > 1.3$) the agreement is marginal.

o The recovery region solution initiation approach was an acceptable procedure for avoiding computation in the actively cooled leading edge region. Overall, the errors introduced by specifying initial location boundary layer profiles based on the local similarity assumption are negligible.

o Accounting for near downstream recovery region wall temperature gradient differences by using a variable wall temperature boundary condition was important for obtaining good quantitative agreement in that zone.

o The suction surface transition zone proved the most difficult area to simulate, which indicates that the transition model formulation is inadequate.

o Although results suggest that the FTU and the FTG parameters could be analytically defined as functions of characteristic film cooling parameters, data from this program should be compared with data from studies of other airfoils to verify the validity of the methods before making a serious attempt to develop these empirical relations.

o As formulated, this method can be easily implemented and tested in any turbine airfoil design system that contains a finite difference boundary layer code even without generalized definitions for FTU and FTG.

After analyzing the progress made in this program toward developing a practical design tool and some of the problems encountered that were not fully resolved, the following recommendations regarding future work and method application were developed:

o This method should be tested further against additional leading edge film-cooled airfoil data to verify the method's overall validity for reproducing trends and levels in the recovery region. Two open literature data sets that could be used for this purpose are those of Louis (Ref 20) and Camci and Arts (Ref 21).

o To improve the present method, emphasis should be placed on developing a
  better transition model for simulating both film- and nonfilm-cooled
  conditions, on modeling the coolant jet turbulence decay independently of
  the free-stream turbulence intensity, and on developing analytical func-
  tions for defining the FTU and FTG boundary condition parameters.

o Differences in hydrodynamic and thermodynamic transition rate phenomena
  suggested by the data need to be further quantified and explicitly modeled.

o Finally, because it is based on a specific, idealized, stagnated flow cool-
  ant jet/boundary layer interaction model, this method is valid only for
  simulating recovery region convective heat transfer phenomena related to a
  leading edge discrete site injection process. For cases involving down-
  stream injection, the idealized model suggested in Ref 7 and implemented
  in the STANCOOL formulation would be more appropriate. For addressing the
  multiple zone airfoil film-cooling problem, the leading edge approach
  should be coupled to a specified downstream injection approach to arrive
  at an overall zonal formulation.

APPENDIX A
TABULATED EXPERIMENTAL DATA

Tabulated data for each run code of the leading edge film-cooled C3X cascade are presented in Table VIII. The data sets are listed in run code number order, and the actual operating conditions associated with each run code were given previously in Table VI. Vane surface to gas absolute temperature ratio (T_w/T_g) data and normalized heat transfer coefficients (h/ho) are tabulated versus percent of surface arc length and percent of axial chord. The heat transfer coefficients are normalized with respect to 1135 $W/m^2/°C$ (200 BTU/hr/$ft^2/°F$). The surface arc and axial chord lengths were given in Table III.

Tabulated blowing ratio data for each run code are presented in Table IX. The blowing ratio is defined as the coolant to free-stream mass flux ratio $(M = \rho_c u_c/\rho_\infty u_\infty)$. M, as defined under the column heading Global, is based on the upstream free-stream conditions and the total coolant mass flow rate. The blowing ratios defined under the Row 1, Row 2, etc headings are calculated local blowing ratios, based on coolant exit conditions and local free-stream conditions. The rows are defined so that Row 1 refers to the row of holes farthest downstream on the pressure surface and Row 5 refers to the row farthest downstream on the suction surface.

Table VIII.
Run code data.

RUN CODE 4300

% Surface Distance	% Axial Chord	Tw/Tg	h/ho
Suction Surface			
8.74	8.24	.8603	.4466
10.54	11.17	.8406	.5045
12.34	14.55	.8243	.5384
14.09	18.19	.8067	.4850
17.60	26.10	.7718	.4722
19.38	30.02	.7511	.4007
21.11	33.60	.7334	.3333
22.95	37.04	.7168	.3076
24.73	40.02	.7015	.2867
26.49	42.62	.6851	.2224
28.26	45.01	.6717	.1756
30.06	47.23	.6711	.2209
31.80	49.21	.6764	.2577
33.53	50.99	.6871	.3184
35.29	52.76	.6965	.3459
37.06	54.42	.7058	.3804
40.55	57.57	.7175	.4198
42.33	59.17	.7217	.4442
45.83	62.01	.7285	.4907
47.55	63.49	.7306	.5114
49.34	64.94	.7320	.5543
52.83	67.63	.7308	.5683
54.59	69.04	.7328	.6113
56.69	70.61	.7315	.5943
58.88	72.27	.7241	.5554
60.96	73.78	.7185	.5944
63.05	75.41	.7181	.5874
65.23	76.90	.7210	.5864
67.31	78.44	.7162	.5677
69.44	80.02	.7107	.6055
71.64	81.60	.7214	.5493
73.75	83.12	.7432	.6107
75.94	84.58	.7533	.5069
80.10	87.58	.7697	.5841
82.25	89.03	.7916	.6196
84.34	90.43	.7994	.5097
88.71	93.01	.8093	.5357
Pressure Surface			
14.93	15.92	.7608	.3191
18.03	20.09	.7341	.2790
26.10	30.47	.6988	.2683
28.94	33.92	.6930	.2840
31.85	37.33	.6898	.2947
37.56	43.82	.6823	.2886
40.45	46.96	.6804	.2842
43.34	50.00	.6847	.3221
46.07	52.78	.6842	.2791
60.24	66.08	.6774	.3815
63.25	68.73	.6892	.4164
74.71	78.11	.7543	.5016

Table VIII. (cont)

RUN CODE 4313

% Surface Distance	% Axial Chord	Tw/Tg	h/ho
Suction Surface			
8.74	8.24	.8340	.4221
10.54	11.17	.8168	.4698
12.34	14.55	.8019	.5075
14.09	18.19	.7854	.4548
17.60	26.10	.7519	.4426
19.38	30.02	.7328	.3836
21.11	33.60	.7156	.3220
22.95	37.04	.6998	.3021
24.73	40.02	.6852	.2814
26.49	42.62	.6697	.2226
28.26	45.01	.6583	.1758
30.06	47.23	.6583	.2229
31.80	49.21	.6657	.2647
33.53	50.99	.6772	.3293
35.29	52.76	.6884	.3522
37.06	54.42	.6982	.3956
40.55	57.57	.7104	.4272
42.33	59.17	.7146	.4496
45.83	62.01	.7212	.4919
47.55	63.49	.7233	.5072
49.34	64.94	.7247	.5544
52.83	67.63	.7231	.5656
54.59	69.04	.7247	.6037
56.69	70.61	.7231	.5857
58.88	72.27	.7151	.5393
60.96	73.78	.7092	.5756
63.05	75.41	.7094	.5883
65.23	76.90	.7113	.5689
67.31	78.44	.7059	.5509
69.44	80.02	.7001	.5887
71.64	81.60	.7108	.5315
73.75	83.12	.7335	.5924
75.94	84.58	.7447	.4954
80.10	87.58	.7628	.5846
82.25	89.03	.7855	.6196
84.34	90.43	.7936	.5141
88.71	93.01	.8032	.5349
Pressure Surface			
14.93	15.92	.7450	.3296
18.03	20.09	.7214	.2946
26.10	30.47	.6893	.2753
28.94	33.92	.6838	.2876
31.85	37.33	.6810	.2977
37.56	43.82	.6742	.2932
40.45	46.96	.6727	.2896
43.34	50.00	.6768	.3254
46.07	52.78	.6765	.2846
60.24	66.08	.6679	.3809
63.25	68.73	.6797	.4162
74.71	78.11	.7478	.5193

Table VIII. (cont)

RUN CODE 4314

% Surface Distance	% Axial Chord	Tw/Tg	h/ho
Suction Surface			
8.74	8.24	.8286	.4234
10.54	11.17	.8125	.4693
12.34	14.55	.7983	.5093
14.09	18.19	.7822	.4536
17.60	26.10	.7494	.4381
19.38	30.02	.7307	.3809
21.11	33.60	.7138	.3197
22.95	37.04	.6984	.3013
24.73	40.02	.6841	.2796
26.49	42.62	.6692	.2224
28.26	45.01	.6586	.1783
30.06	47.23	.6596	.2287
31.80	49.21	.6678	.2757
33.53	50.99	.6796	.3417
35.29	52.76	.6911	.3629
37.06	54.42	.7012	.4145
40.55	57.57	.7131	.4416
42.33	59.17	.7170	.4633
45.83	62.01	.7228	.5017
47.55	63.49	.7246	.5131
49.34	64.94	.7256	.5598
52.83	67.63	.7233	.5661
54.59	69.04	.7245	.6014
56.69	70.61	.7226	.5828
58.88	72.27	.7143	.5333
60.96	73.78	.7081	.5697
63.05	75.41	.7083	.5828
65.23	76.90	.7101	.5629
67.31	78.44	.7048	.5495
69.44	80.02	.6989	.5846
71.64	81.60	.7096	.5262
73.75	83.12	.7326	.5865
75.94	84.58	.7441	.4870
80.10	87.58	.7628	.5780
82.25	89.03	.7856	.6126
84.34	90.43	.7939	.5100
88.71	93.01	.8035	.5344
Pressure Surface			
14.93	15.92	.7434	.3411
18.03	20.09	.7207	.3022
26.10	30.47	.6903	.2832
28.94	33.92	.6850	.2955
31.85	37.33	.6823	.3058
37.56	43.82	.6753	.2988
40.45	46.96	.6736	.2932
43.34	50.00	.6776	.3303
46.07	52.78	.6771	.2869
60.24	66.08	.6680	.3857
63.25	68.73	.6798	.4205
74.71	78.11	.7494	.5400

Table VIII. (cont)

RUN CODE 4315

% Surface Distance	% Axial Chord	Tw/Tg	h/ho
Suction Surface			
8.74	8.24	.8214	.4138
10.54	11.17	.8063	.4623
12.34	14.55	.7928	.4941
14.09	18.19	.7774	.4482
17.60	26.10	.7457	.4303
19.38	30.02	.7275	.3743
21.11	33.60	.7111	.3157
22.95	37.04	.6962	.2988
24.73	40.02	.6826	.2783
26.49	42.62	.6687	.2254
28.26	45.01	.6592	.1889
30.06	47.23	.6611	.2428
31.80	49.21	.6699	.2941
33.53	50.99	.6819	.3587
35.29	52.76	.6932	.3746
37.06	54.42	.7031	.4286
40.55	57.57	.7142	.4467
42.33	59.17	.7177	.4661
45.83	62.01	.7228	.5004
47.55	63.49	.7242	.5102
49.34	64.94	.7249	.5549
52.83	67.63	.7218	.5525
54.59	69.04	.7230	.5937
56.69	70.61	.7210	.5760
58.88	72.27	.7125	.5269
60.96	73.78	.7061	.5646
63.05	75.41	.7062	.5774
65.23	76.90	.7081	.5577
67.31	78.44	.7026	.5401
69.44	80.02	.6966	.5780
71.64	81.60	.7075	.5208
73.75	83.12	.7306	.5771
75.94	84.58	.7421	.4775
80.10	87.58	.7611	.5704
82.25	89.03	.7840	.6037
84.34	90.43	.7924	.5056
88.71	93.01	.8017	.5218
Pressure Surface			
14.93	15.92	.7391	.3421
18.03	20.09	.7179	.3059
26.10	30.47	.6899	.2873
28.94	33.92	.6851	.2982
31.85	37.33	.6825	.3079
37.56	43.82	.6756	.3009
40.45	46.96	.6738	.2959
43.34	50.00	.6775	.3323
46.07	52.78	.6768	.2903
60.24	66.08	.6670	.3883
63.25	68.73	.6787	.4225
74.71	78.11	.7482	.5404

Table VIII. (cont)

RUN CODE 4333

% Surface Distance	% Axial Chord	Tw/Tg	h/ho
Suction Surface			
8.74	8.24	.8563	.4543
10.54	11.17	.8373	.5104
12.34	14.55	.8211	.5386
14.09	18.19	.8037	.4879
17.60	26.10	.7687	.4714
19.38	30.02	.7487	.4009
21.11	33.60	.7307	.3334
22.95	37.04	.7142	.3087
24.73	40.02	.6989	.2872
26.49	42.62	.6827	.2236
28.26	45.01	.6705	.1777
30.06	47.23	.6695	.2243
31.80	49.21	.6758	.2642
33.53	50.99	.6864	.3270
35.29	52.76	.6969	.3518
37.06	54.42	.7062	.3939
40.55	57.57	.7180	.4283
42.33	59.17	.7222	.4521
45.83	62.01	.7291	.5024
47.55	63.49	.7314	.5212
49.34	64.94	.7326	.5640
52.83	67.63	.7309	.5749
54.59	69.04	.7325	.6141
56.69	70.61	.7311	.5967
58.88	72.27	.7235	.5542
60.96	73.78	.7174	.5909
63.05	75.41	.7170	.5829
65.23	76.90	.7196	.5786
67.31	78.44	.7151	.5650
69.44	80.02	.7097	.5989
71.64	81.60	.7203	.5429
73.75	83.12	.7423	.6044
75.94	84.58	.7529	.5037
80.10	87.58	.7700	.5848
82.25	89.03	.7923	.6220
84.34	90.43	.8005	.5155
88.71	93.01	.8106	.5466
Pressure Surface			
14.93	15.92	.7619	.3448
18.03	20.09	.7362	.2978
26.10	30.47	.7010	.2842
28.94	33.92	.6949	.2987
31.85	37.33	.6915	.3088
37.56	43.82	.6838	.3009
40.45	46.96	.6819	.2955
43.34	50.00	.6857	.3316
46.07	52.78	.6851	.2857
60.24	66.08	.6780	.3877
63.25	68.73	.6897	.4236
74.71	78.11	.7558	.5249

Table VIII. (cont)

RUN CODE 4334

% Surface Distance	% Axial Chord	Tw/Tg	h/ho
Suction Surface			
8.74	8.24	.8610	.4715
10.54	11.17	.8416	.5278
12.34	14.55	.8251	.5564
14.09	18.19	.8073	.4974
17.60	26.10	.7718	.4791
19.38	30.02	.7516	.4040
21.11	33.60	.7335	.3366
22.95	37.04	.7170	.3112
24.73	40.02	.7018	.2906
26.49	42.62	.6857	.2263
28.26	45.01	.6739	.1837
30.06	47.23	.6736	.2330
31.80	49.21	.6805	.2761
33.53	50.99	.6915	.3401
35.29	52.76	.7024	.3651
37.06	54.42	.7120	.4128
40.55	57.57	.7239	.4456
42.33	59.17	.7279	.4707
45.83	62.01	.7340	.5160
47.55	63.49	.7357	.5318
49.34	64.94	.7363	.5724
52.83	67.63	.7337	.5828
54.59	69.04	.7349	.6184
56.69	70.61	.7330	.5997
58.88	72.27	.7251	.5574
60.96	73.78	.7187	.5941
63.05	75.41	.7181	.5847
65.23	76.90	.7207	.5806
67.31	78.44	.7161	.5657
69.44	80.02	.7105	.5976
71.64	81.60	.7211	.5421
73.75	83.12	.7432	.6046
75.94	84.58	.7538	.5014
80.10	87.58	.7713	.5843
82.25	89.03	.7940	.6297
84.34	90.43	.8023	.5219
88.71	93.01	.8124	.5485
Pressure Surface			
14.93	15.92	.7666	.3565
18.03	20.09	.7406	.3048
26.10	30.47	.7052	.2891
28.94	33.92	.6989	.3030
31.85	37.33	.6952	.3128
37.56	43.82	.6869	.3040
40.45	46.96	.6846	.2979
43.34	50.00	.6883	.3380
46.07	52.78	.6873	.2902
60.24	66.08	.6787	.3849
63.25	68.73	.6903	.4198
74.71	78.11	.7573	.5286

Table VIII. (cont)

RUN CODE 4335

% Surface Distance	% Axial Chord	Tw/Tg	h/ho
Suction Surface			
8.74	8.24	.8642	.4850
10.54	11.17	.8443	.5401
12.34	14.55	.8274	.5704
14.09	18.19	.8092	.5049
17.60	26.10	.7730	.4850
19.38	30.02	.7525	.4075
21.11	33.60	.7342	.3383
22.95	37.04	.7176	.3118
24.73	40.02	.7024	.2900
26.49	42.62	.6864	.2244
28.26	45.01	.6750	.1839
30.06	47.23	.6752	.2376
31.80	49.21	.6827	.2869
33.53	50.99	.6940	.3527
35.29	52.76	.7050	.3768
37.06	54.42	.7147	.4261
40.55	57.57	.7265	.4589
42.33	59.17	.7304	.4836
45.83	62.01	.7360	.5261
47.55	63.49	.7374	.5411
49.34	64.94	.7377	.5787
52.83	67.63	.7344	.5835
54.59	69.04	.7352	.6168
56.69	70.61	.7331	.5980
58.88	72.27	.7249	.5555
60.96	73.78	.7184	.5926
63.05	75.41	.7177	.5840
65.23	76.90	.7203	.5819
67.31	78.44	.7155	.5669
69.44	80.02	.7099	.6031
71.64	81.60	.7207	.5475
73.75	83.12	.7430	.6072
75.94	84.58	.7538	.5002
80.10	87.58	.7716	.5844
82.25	89.03	.7946	.6309
84.34	90.43	.8030	.5252
88.71	93.01	.8127	.5527
Pressure Surface			
14.93	15.92	.7694	.3636
18.03	20.09	.7433	.3133
26.10	30.47	.7080	.3004
28.94	33.92	.7016	.3142
31.85	37.33	.6979	.3230
37.56	43.82	.6893	.3133
40.45	46.96	.6868	.3075
43.34	50.00	.6900	.3433
46.07	52.78	.6891	.2994
60.24	66.08	.6796	.3979
63.25	68.73	.6913	.4358
74.71	78.11	.7588	.5505

Table VIII. (cont)

RUN CODE 4400

% Surface Distance	% Axial Chord	Tw/Tg	h/ho
Suction Surface			
8.74	8.24	.8813	.5294
10.54	11.17	.8621	.5901
12.34	14.55	.8462	.6252
14.09	18.19	.8288	.5502
17.60	26.10	.7953	.5394
19.38	30.02	.7757	.4633
21.11	33.60	.7590	.3891
22.95	37.04	.7433	.3521
24.73	40.02	.7298	.3370
26.49	42.62	.7159	.2658
28.26	45.01	.7074	.2495
30.06	47.23	.7124	.3438
31.80	49.21	.7224	.4293
33.53	50.99	.7346	.4924
35.29	52.76	.7449	.5177
37.06	54.42	.7555	.5870
40.55	57.57	.7648	.6056
42.33	59.17	.7680	.6329
45.83	62.01	.7717	.6731
47.55	63.49	.7725	.6941
49.34	64.94	.7719	.7284
52.83	67.63	.7673	.7213
54.59	69.04	.7683	.7657
56.69	70.61	.7662	.7421
58.88	72.27	.7575	.6861
60.96	73.78	.7509	.7289
63.05	75.41	.7507	.7227
65.23	76.90	.7541	.7161
67.31	78.44	.7491	.6938
69.44	80.02	.7425	.7363
71.64	81.60	.7537	.6648
73.75	83.12	.7771	.7475
75.94	84.58	.7871	.6154
80.10	87.58	.8014	.6966
82.25	89.03	.8233	.7312
84.34	90.43	.8307	.6102
88.71	93.01	.8359	.6194
Pressure Surface			
14.93	15.92	.7940	.4070
18.03	20.09	.7689	.3724
26.10	30.47	.7359	.3589
28.94	33.92	.7306	.3802
31.85	37.33	.7277	.3922
37.56	43.82	.7203	.3891
40.45	46.96	.7184	.3827
43.34	50.00	.7231	.4382
46.07	52.78	.7226	.3830
60.24	66.08	.7167	.5354
63.25	68.73	.7286	.5836
74.71	78.11	.7912	.6975

Table VIII. (cont)

RUN CODE 4413

% Surface Distance	% Axial Chord	Tw/Tg	h/ho
Suction Surface			
8.74	8.24	.8574	.5140
10.54	11.17	.8403	.5660
12.34	14.55	.8253	.5940
14.09	18.19	.8088	.5161
17.60	26.10	.7773	.5245
19.38	30.02	.7593	.4526
21.11	33.60	.7431	.3877
22.95	37.04	.7287	.3586
24.73	40.02	.7165	.3578
26.49	42.62	.7039	.2926
28.26	45.01	.6971	.2807
30.06	47.23	.7019	.3733
31.80	49.21	.7123	.4531
33.53	50.99	.7239	.5082
35.29	52.76	.7347	.5282
37.06	54.42	.7439	.5850
40.55	57.57	.7536	.6015
42.33	59.17	.7566	.6290
45.83	62.01	.7604	.6651
47.55	63.49	.7611	.6807
49.34	64.94	.7604	.7102
52.83	67.63	.7561	.7106
54.59	69.04	.7569	.7441
56.69	70.61	.7550	.7225
58.88	72.27	.7467	.6741
60.96	73.78	.7399	.7154
63.05	75.41	.7398	.7091
65.23	76.90	.7429	.7021
67.31	78.44	.7374	.6797
69.44	80.02	.7309	.7272
71.64	81.60	.7423	.6592
73.75	83.12	.7665	.7421
75.94	84.58	.7769	.5989
80.10	87.58	.7919	.6726
82.25	89.03	.8147	.7128
84.34	90.43	.8225	.5886
88.71	93.01	.8285	.6069
Pressure Surface			
14.93	15.92	.7725	.4120
18.03	20.09	.7502	.3760
26.10	30.47	.7205	.3559
28.94	33.92	.7158	.3769
31.85	37.33	.7133	.3853
37.56	43.82	.7067	.3812
40.45	46.96	.7053	.3745
43.34	50.00	.7103	.4247
46.07	52.78	.7106	.3788
60.24	66.08	.7047	.5329
63.25	68.73	.7165	.5799
74.71	78.11	.7819	.6903

Table VIII. (cont)

RUN CODE 4414

% Surface Distance	% Axial Chord	Tw/Tg	h/ho
Suction Surface			
8.74	8.24	.8497	.4902
10.54	11.17	.8339	.5450
12.34	14.55	.8196	.5509
14.09	18.19	.8046	.5120
17.60	26.10	.7750	.5140
19.38	30.02	.7579	.4456
21.11	33.60	.7431	.3897
22.95	37.04	.7299	.3687
24.73	40.02	.7188	.3748
26.49	42.62	.7069	.3112
28.26	45.01	.7006	.3014
30.06	47.23	.7051	.3912
31.80	49.21	.7149	.4672
33.53	50.99	.7257	.5148
35.29	52.76	.7358	.5304
37.06	54.42	.7447	.5868
40.55	57.57	.7536	.5987
42.33	59.17	.7561	.6208
45.83	62.01	.7593	.6528
47.55	63.49	.7599	.6688
49.34	64.94	.7591	.7016
52.83	67.63	.7542	.6901
54.59	69.04	.7554	.7379
56.69	70.61	.7534	.7134
58.88	72.27	.7449	.6610
60.96	73.78	.7382	.7025
63.05	75.41	.7381	.6970
65.23	76.90	.7411	.6890
67.31	78.44	.7358	.6700
69.44	80.02	.7292	.7120
71.64	81.60	.7405	.6424
73.75	83.12	.7645	.7221
75.94	84.58	.7751	.5882
80.10	87.58	.7903	.6588
82.25	89.03	.8130	.6983
84.34	90.43	.8208	.5788
88.71	93.01	.8268	.5903
Pressure Surface			
14.93	15.92	.7694	.4107
18.03	20.09	.7481	.3764
26.10	30.47	.7198	.3550
28.94	33.92	.7152	.3733
31.85	37.33	.7127	.3817
37.56	43.82	.7059	.3780
40.45	46.96	.7044	.3719
43.34	50.00	.7092	.4242
46.07	52.78	.7090	.3687
60.24	66.08	.7031	.5211
63.25	68.73	.7150	.5668
74.71	78.11	.7803	.6757

Table VIII. (cont)

RUN CODE 4415

% Surface Distance	% Axial Chord	Tw/Tg	h/ho
Suction Surface			
8.74	8.24	.8426	.4721
10.54	11.17	.8283	.5301
12.34	14.55	.8151	.5429
14.09	18.19	.8009	.5019
17.60	26.10	.7730	.5094
19.38	30.02	.7568	.4442
21.11	33.60	.7429	.3957
22.95	37.04	.7306	.3822
24.73	40.02	.7202	.3907
26.49	42.62	.7088	.3286
28.26	45.01	.7026	.3195
30.06	47.23	.7070	.4068
31.80	49.21	.7165	.4843
33.53	50.99	.7268	.5245
35.29	52.76	.7363	.5343
37.06	54.42	.7447	.5886
40.55	57.57	.7528	.5900
42.33	59.17	.7552	.6125
45.83	62.01	.7583	.6442
47.55	63.49	.7588	.6591
49.34	64.94	.7580	.6901
52.83	67.63	.7533	.6838
54.59	69.04	.7542	.7239
56.69	70.61	.7523	.7031
58.88	72.27	.7438	.6541
60.96	73.78	.7371	.6964
63.05	75.41	.7370	.6906
65.23	76.90	.7401	.6820
67.31	78.44	.7349	.6619
69.44	80.02	.7284	.7046
71.64	81.60	.7395	.6334
73.75	83.12	.7635	.7101
75.94	84.58	.7744	.5836
80.10	87.58	.7895	.6525
82.25	89.03	.8121	.6887
84.34	90.43	.8199	.5707
88.71	93.01	.8260	.5854
Pressure Surface			
14.93	15.92	.7657	.4115
18.03	20.09	.7461	.3825
26.10	30.47	.7201	.3624
28.94	33.92	.7157	.3783
31.85	37.33	.7133	.3856
37.56	43.82	.7065	.3795
40.45	46.96	.7048	.3713
43.34	50.00	.7096	.4243
46.07	52.78	.7094	.3721
60.24	66.08	.7029	.5186
63.25	68.73	.7146	.5639
74.71	78.11	.7798	.6733

Table VIII. (cont)

RUN CODE 4416

% Surface Distance	% Axial Chord	Tw/Tg	h/ho
Suction Surface			
8.74	8.24	.8143	.4063
10.54	11.17	.8073	.4583
12.34	14.55	.7986	.4773
14.09	18.19	.7880	.4554
17.60	26.10	.7657	.4539
19.38	30.02	.7533	.4111
21.11	33.60	.7435	.3839
22.95	37.04	.7356	.3973
24.73	40.02	.7291	.4197
26.49	42.62	.7221	.3993
28.26	45.01	.7187	.4422
30.06	47.23	.7201	.4686
31.80	49.21	.7252	.4989
33.53	50.99	.7323	.5155
35.29	52.76	.7400	.5252
37.06	54.42	.7469	.5673
40.55	57.57	.7536	.5704
42.33	59.17	.7555	.5896
45.83	62.01	.7580	.6177
47.55	63.49	.7583	.6313
49.34	64.94	.7575	.6633
52.83	67.63	.7527	.6566
54.59	69.04	.7536	.6973
56.69	70.61	.7515	.6736
58.88	72.27	.7429	.6243
60.96	73.78	.7360	.6646
63.05	75.41	.7355	.6567
65.23	76.90	.7385	.6526
67.31	78.44	.7329	.6333
69.44	80.02	.7258	.6695
71.64	81.60	.7368	.5998
73.75	83.12	.7611	.6855
75.94	84.58	.7720	.5574
80.10	87.58	.7873	.6272
82.25	89.03	.8093	.6555
84.34	90.43	.8170	.5465
88.71	93.01	.8224	.5466
Pressure Surface			
14.93	15.92	.7629	.4090
18.03	20.09	.7480	.4037
26.10	30.47	.7261	.3796
28.94	33.92	.7220	.3917
31.85	37.33	.7199	.4014
37.56	43.82	.7134	.4004
40.45	46.96	.7115	.3897
43.34	50.00	.7157	.4461
46.07	52.78	.7146	.3844
60.24	66.08	.7042	.5157
63.25	68.73	.7151	.5591
74.71	78.11	.7790	.6684

Table VIII. (cont)

RUN CODE 4417

% Surface Distance	% Axial Chord	Tw/Tg	h/ho
Suction Surface			
8.74	8.24	.8080	.4025
10.54	11.17	.8030	.4640
12.34	14.55	.7953	.4706
14.09	18.19	.7860	.4673
17.60	26.10	.7655	.4646
19.38	30.02	.7542	.4274
21.11	33.60	.7453	.4079
22.95	37.04	.7380	.4255
24.73	40.02	.7314	.4432
26.49	42.62	.7244	.4238
28.26	45.01	.7207	.4664
30.06	47.23	.7212	.4858
31.80	49.21	.7255	.5084
33.53	50.99	.7317	.5192
35.29	52.76	.7386	.5271
37.06	54.42	.7449	.5578
40.55	57.57	.7515	.5647
42.33	59.17	.7534	.5845
45.83	62.01	.7560	.6155
47.55	63.49	.7563	.6265
49.34	64.94	.7554	.6582
52.83	67.63	.7508	.6549
54.59	69.04	.7516	.6910
56.69	70.61	.7496	.6704
58.88	72.27	.7413	.6233
60.96	73.78	.7346	.6634
63.05	75.41	.7341	.6540
65.23	76.90	.7371	.6495
67.31	78.44	.7317	.6336
69.44	80.02	.7245	.6574
71.64	81.60	.7355	.5942
73.75	83.12	.7597	.6842
75.94	84.58	.7705	.5575
80.10	87.58	.7855	.6249
82.25	89.03	.8075	.6522
84.34	90.43	.8151	.5430
88.71	93.01	.8207	.5394
Pressure Surface			
14.93	15.92	.7516	.3789
18.03	20.09	.7392	.3860
26.10	30.47	.7211	.3720
28.94	33.92	.7176	.3811
31.85	37.33	.7158	.3915
37.56	43.82	.7098	.3902
40.45	46.96	.7079	.3775
43.34	50.00	.7126	.4431
46.07	52.78	.7112	.3698
60.24	66.08	.7014	.4985
63.25	68.73	.7123	.5376
74.71	78.11	.7766	.6551

Table VIII. (cont)

RUN CODE 4418

% Surface Distance	% Axial Chord	Tw/Tg	h/ho
Suction Surface			
8.74	8.24	.8034	.3878
10.54	11.17	.8002	.4566
12.34	14.55	.7940	.4748
14.09	18.19	.7858	.4710
17.60	26.10	.7673	.4739
19.38	30.02	.7570	.4410
21.11	33.60	.7492	.4286
22.95	37.04	.7427	.4506
24.73	40.02	.7367	.4707
26.49	42.62	.7301	.4551
28.26	45.01	.7263	.4980
30.06	47.23	.7261	.5111
31.80	49.21	.7292	.5216
33.53	50.99	.7344	.5271
35.29	52.76	.7404	.5297
37.06	54.42	.7459	.5493
40.55	57.57	.7520	.5575
42.33	59.17	.7538	.5751
45.83	62.01	.7564	.6039
47.55	63.49	.7569	.6204
49.34	64.94	.7562	.6534
52.83	67.63	.7517	.6519
54.59	69.04	.7525	.6879
56.69	70.61	.7506	.6663
58.88	72.27	.7425	.6243
60.96	73.78	.7359	.6671
63.05	75.41	.7355	.6586
65.23	76.90	.7384	.6571
67.31	78.44	.7327	.6329
69.44	80.02	.7257	.6679
71.64	81.60	.7366	.6054
73.75	83.12	.7604	.6942
75.94	84.58	.7710	.5689
80.10	87.58	.7852	.6284
82.25	89.03	.8069	.6601
84.34	90.43	.8143	.5495
88.71	93.01	.8196	.5403
Pressure Surface			
14.93	15.92	.7526	.3865
18.03	20.09	.7433	.4211
26.10	30.47	.7267	.3969
28.94	33.92	.7230	.4018
31.85	37.33	.7208	.4084
37.56	43.82	.7138	.4035
40.45	46.96	.7115	.3912
43.34	50.00	.7152	.4429
46.07	52.78	.7138	.3814
60.24	66.08	.7013	.4948
63.25	68.73	.7116	.5299
74.71	78.11	.7744	.6262

Table VIII. (cont)

RUN CODE 4423

% Surface Distance	% Axial Chord	Tw/Tg	h/ho
Suction Surface			
8.74	8.24	.8648	.5056
10.54	11.17	.8463	.5647
12.34	14.55	.8303	.5930
14.09	18.19	.8131	.5257
17.60	26.10	.7799	.5235
19.38	30.02	.7615	.4558
21.11	33.60	.7451	.3876
22.95	37.04	.7305	.3594
24.73	40.02	.7179	.3546
26.49	42.62	.7050	.2884
28.26	45.01	.6980	.2784
30.06	47.23	.7028	.3725
31.80	49.21	.7132	.4544
33.53	50.99	.7247	.5056
35.29	52.76	.7355	.5242
37.06	54.42	.7450	.5907
40.55	57.57	.7543	.6040
42.33	59.17	.7569	.6287
45.83	62.01	.7604	.6657
47.55	63.49	.7611	.6853
49.34	64.94	.7604	.7161
52.83	67.63	.7557	.7107
54.59	69.04	.7565	.7488
56.69	70.61	.7544	.7250
58.88	72.27	.7456	.6668
60.96	73.78	.7388	.7083
63.05	75.41	.7387	.7036
65.23	76.90	.7418	.7018
67.31	78.44	.7364	.6861
69.44	80.02	.7296	.7332
71.64	81.60	.7407	.6611
73.75	83.12	.7649	.7357
75.94	84.58	.7758	.6042
80.10	87.58	.7911	.6786
82.25	89.03	.8138	.7160
84.34	90.43	.8216	.5942
88.71	93.01	.8275	.6050
Pressure Surface			
14.93	15.92	.7802	.4028
18.03	20.09	.7557	.3713
26.10	30.47	.7227	.3583
28.94	33.92	.7173	.3784
31.85	37.33	.7144	.3908
37.56	43.82	.7071	.3857
40.45	46.96	.7054	.3791
43.34	50.00	.7103	.4317
46.07	52.78	.7101	.3776
60.24	66.08	.7031	.5347
63.25	68.73	.7149	.5830
74.71	78.11	.7803	.6820

Table VIII. (cont)

RUN CODE 4424

% Surface Distance	% Axial Chord	Tw/Tg	h/ho
Suction Surface			
8.74	8.24	.8681	.5157
10.54	11.17	.8496	.5769
12.34	14.55	.8336	.6064
14.09	18.19	.8165	.5402
17.60	26.10	.7835	.5378
19.38	30.02	.7653	.4672
21.11	33.60	.7494	.4032
22.95	37.04	.7353	.3774
24.73	40.02	.7231	.3762
26.49	42.62	.7104	.3071
28.26	45.01	.7034	.2987
30.06	47.23	.7078	.3930
31.80	49.21	.7178	.4752
33.53	50.99	.7288	.5229
35.29	52.76	.7391	.5396
37.06	54.42	.7482	.6063
40.55	57.57	.7568	.6153
42.33	59.17	.7592	.6389
45.83	62.01	.7622	.6723
47.55	63.49	.7626	.6884
49.34	64.94	.7617	.7224
52.83	67.63	.7568	.7162
54.59	69.04	.7576	.7564
56.69	70.61	.7554	.7336
58.88	72.27	.7465	.6744
60.96	73.78	.7396	.7179
63.05	75.41	.7395	.7129
65.23	76.90	.7426	.7049
67.31	78.44	.7372	.6865
69.44	80.02	.7302	.7239
71.64	81.60	.7413	.6529
73.75	83.12	.7655	.7330
75.94	84.58	.7764	.6025
80.10	87.58	.7918	.6799
82.25	89.03	.8146	.7183
84.34	90.43	.8225	.6013
88.71	93.01	.8283	.6110
Pressure Surface			
14.93	15.92	.7825	.4070
18.03	20.09	.7581	.3800
26.10	30.47	.7249	.3657
28.94	33.92	.7193	.3843
31.85	37.33	.7162	.3953
37.56	43.82	.7087	.3922
40.45	46.96	.7067	.3843
43.34	50.00	.7114	.4376
46.07	52.78	.7111	.3815
60.24	66.08	.7040	.5300
63.25	68.73	.7156	.5757
74.71	78.11	.7812	.6859

Table VIII. (cont)

RUN CODE 4425

% Surface Distance	% Axial Chord	Tw/Tg	h/ho
Suction Surface			
8.74	8.24	.8700	.5305
10.54	11.17	.8517	.5905
12.34	14.55	.8360	.6212
14.09	18.19	.8192	.5542
17.60	26.10	.7867	.5489
19.38	30.02	.7688	.4761
21.11	33.60	.7535	.4172
22.95	37.04	.7400	.3944
24.73	40.02	.7283	.3959
26.49	42.62	.7158	.3263
28.26	45.01	.7089	.3175
30.06	47.23	.7130	.4107
31.80	49.21	.7223	.4900
33.53	50.99	.7327	.5344
35.29	52.76	.7424	.5476
37.06	54.42	.7511	.6129
40.55	57.57	.7589	.6153
42.33	59.17	.7610	.6365
45.83	62.01	.7636	.6684
47.55	63.49	.7639	.6840
49.34	64.94	.7629	.7162
52.83	67.63	.7579	.7124
54.59	69.04	.7585	.7491
56.69	70.61	.7563	.7266
58.88	72.27	.7474	.6681
60.96	73.78	.7404	.7096
63.05	75.41	.7402	.7055
65.23	76.90	.7433	.7016
67.31	78.44	.7379	.6814
69.44	80.02	.7310	.7244
71.64	81.60	.7422	.6537
73.75	83.12	.7662	.7332
75.94	84.58	.7772	.6035
80.10	87.58	.7926	.6829
82.25	89.03	.8154	.7216
84.34	90.43	.8233	.6014
88.71	93.01	.8294	.6055
Pressure Surface			
14.93	15.92	.7845	.4210
18.03	20.09	.7603	.3879
26.10	30.47	.7275	.3692
28.94	33.92	.7219	.3873
31.85	37.33	.7188	.3982
37.56	43.82	.7109	.3928
40.45	46.96	.7088	.3842
43.34	50.00	.7131	.4326
46.07	52.78	.7130	.3848
60.24	66.08	.7048	.5285
63.25	68.73	.7164	.5750
74.71	78.11	.7817	.6834

Table VIII. (cont)

RUN CODE 4426

% Surface Distance	% Axial Chord	Tw/Tg	h/ho
Suction Surface			
8.74	8.24	.8727	.5455
10.54	11.17	.8560	.6066
12.34	14.55	.8413	.6394
14.09	18.19	.8251	.5686
17.60	26.10	.7935	.5526
19.38	30.02	.7762	.4789
21.11	33.60	.7615	.4143
22.95	37.04	.7492	.3993
24.73	40.02	.7392	.4081
26.49	42.62	.7295	.3677
28.26	45.01	.7251	.4040
30.06	47.23	.7285	.4766
31.80	49.21	.7362	.5400
33.53	50.99	.7449	.5701
35.29	52.76	.7533	.5785
37.06	54.42	.7607	.6306
40.55	57.57	.7672	.6243
42.33	59.17	.7688	.6443
45.83	62.01	.7707	.6712
47.55	63.49	.7709	.6898
49.34	64.94	.7697	.7219
52.83	67.63	.7642	.7132
54.59	69.04	.7649	.7583
56.69	70.61	.7625	.7332
58.88	72.27	.7534	.6747
60.96	73.78	.7460	.7164
63.05	75.41	.7455	.7085
65.23	76.90	.7483	.7010
67.31	78.44	.7425	.6751
69.44	80.02	.7353	.7113
71.64	81.60	.7464	.6420
73.75	83.12	.7709	.7343
75.94	84.58	.7819	.6039
80.10	87.58	.7971	.6878
82.25	89.03	.8196	.7221
84.34	90.43	.8272	.6035
88.71	93.01	.8326	.6151
Pressure Surface			
14.93	15.92	.7945	.4618
18.03	20.09	.7728	.4347
26.10	30.47	.7424	.4143
28.94	33.92	.7367	.4284
31.85	37.33	.7333	.4360
37.56	43.82	.7248	.4324
40.45	46.96	.7220	.4219
43.34	50.00	.7256	.4748
46.07	52.78	.7242	.4120
60.24	66.08	.7126	.5418
63.25	68.73	.7236	.5881
74.71	78.11	.7878	.7125

Table VIII. (cont)

RUN CODE 4427

% Surface Distance	% Axial Chord	Tw/Tg	h/ho
Suction Surface			
8.74	8.24	.8751	.5631
10.54	11.17	.8592	.6285
12.34	14.55	.8451	.6701
14.09	18.19	.8295	.5981
17.60	26.10	.7989	.5792
19.38	30.02	.7825	.5066
21.11	33.60	.7691	.4518
22.95	37.04	.7583	.4525
24.73	40.02	.7493	.4672
26.49	42.62	.7402	.4354
28.26	45.01	.7357	.4878
30.06	47.23	.7368	.5321
31.80	49.21	.7419	.5686
33.53	50.99	.7487	.5835
35.29	52.76	.7560	.5870
37.06	54.42	.7626	.6378
40.55	57.57	.7680	.6302
42.33	59.17	.7694	.6505
45.83	62.01	.7712	.6792
47.55	63.49	.7713	.6950
49.34	64.94	.7702	.7253
52.83	67.63	.7649	.7179
54.59	69.04	.7655	.7557
56.69	70.61	.7631	.7318
58.88	72.27	.7539	.6741
60.96	73.78	.7465	.7169
63.05	75.41	.7459	.7110
65.23	76.90	.7488	.7086
67.31	78.44	.7430	.6926
69.44	80.02	.7355	.7382
71.64	81.60	.7466	.6672
73.75	83.12	.7712	.7498
75.94	84.58	.7823	.6112
80.10	87.58	.7976	.6923
82.25	89.03	.8202	.7293
84.34	90.43	.8279	.6097
88.71	93.01	.8332	.6162
Pressure Surface			
14.93	15.92	.7978	.4796
18.03	20.09	.7765	.4565
26.10	30.47	.7466	.4436
28.94	33.92	.7408	.4582
31.85	37.33	.7371	.4641
37.56	43.82	.7280	.4497
40.45	46.96	.7248	.4337
43.34	50.00	.7281	.4870
46.07	52.78	.7263	.4196
60.24	66.08	.7132	.5665
63.25	68.73	.7240	.6148
74.71	78.11	.7882	.7159

Table VIII. (cont)

RUN CODE 4428

% Surface Distance	% Axial Chord	Tw/Tg	h/ho
Suction Surface			
8.74	8.24	.8779	.5848
10.54	11.17	.8623	.6509
12.34	14.55	.8485	.6876
14.09	18.19	.8334	.6303
17.60	26.10	.8032	.6000
19.38	30.02	.7872	.5257
21.11	33.60	.7745	.4776
22.95	37.04	.7642	.4819
24.73	40.02	.7555	.4994
26.49	42.62	.7464	.4647
28.26	45.01	.7416	.5183
30.06	47.23	.7417	.5514
31.80	49.21	.7458	.5809
33.53	50.99	.7518	.5907
35.29	52.76	.7584	.5931
37.06	54.42	.7646	.6413
40.55	57.57	.7696	.6329
42.33	59.17	.7709	.6539
45.83	62.01	.7726	.6846
47.55	63.49	.7728	.7000
49.34	64.94	.7716	.7312
52.83	67.63	.7662	.7200
54.59	69.04	.7670	.7642
56.69	70.61	.7646	.7389
58.88	72.27	.7555	.6800
60.96	73.78	.7480	.7224
63.05	75.41	.7474	.7154
65.23	76.90	.7503	.7121
67.31	78.44	.7444	.6953
69.44	80.02	.7368	.7401
71.64	81.60	.7480	.6685
73.75	83.12	.7728	.7574
75.94	84.58	.7839	.6171
80.10	87.58	.7991	.6996
82.25	89.03	.8217	.7375
84.34	90.43	.8294	.6159
88.71	93.01	.8346	.6188
Pressure Surface			
14.93	15.92	.8003	.4933
18.03	20.09	.7796	.4760
26.10	30.47	.7495	.4559
28.94	33.92	.7435	.4686
31.85	37.33	.7396	.4732
37.56	43.82	.7304	.4599
40.45	46.96	.7273	.4438
43.34	50.00	.7305	.4982
46.07	52.78	.7288	.4299
60.24	66.08	.7153	.5747
63.25	68.73	.7260	.6236
74.71	78.11	.7897	.7219

Table VIII. (cont)

RUN CODE 4433

% Surface Distance	% Axial Chord	Tw/Tg	h/ho
Suction Surface			
8.74	8.24	.8732	.5328
10.54	11.17	.8537	.5980
12.34	14.55	.8368	.6055
14.09	18.19	.8193	.5508
17.60	26.10	.7848	.5336
19.38	30.02	.7660	.4730
21.11	33.60	.7490	.4056
22.95	37.04	.7329	.3499
24.73	40.02	.7198	.3490
26.49	42.62	.7064	.2789
28.26	45.01	.6992	.2688
30.06	47.23	.7041	.3683
31.80	49.21	.7148	.4601
33.53	50.99	.7262	.5021
35.29	52.76	.7371	.5264
37.06	54.42	.7467	.5940
40.55	57.57	.7563	.6100
42.33	59.17	.7590	.6359
45.83	62.01	.7628	.6729
47.55	63.49	.7638	.7093
49.34	64.94	.7625	.7218
52.83	67.63	.7576	.7183
54.59	69.04	.7583	.7549
56.69	70.61	.7562	.7335
58.88	72.27	.7472	.6713
60.96	73.78	.7404	.7162
63.05	75.41	.7403	.7143
65.23	76.90	.7434	.7044
67.31	78.44	.7379	.6860
69.44	80.02	.7310	.7326
71.64	81.60	.7422	.6579
73.75	83.12	.7664	.7329
75.94	84.58	.7774	.6026
80.10	87.58	.7928	.6791
82.25	89.03	.8157	.7147
84.34	90.43	.8236	.5954
88.71	93.01	.8295	.6045
Pressure Surface			
14.93	15.92	.7864	.4161
18.03	20.09	.7608	.3829
26.10	30.47	.7254	.3594
28.94	33.92	.7195	.3800
31.85	37.33	.7164	.3937
37.56	43.82	.7088	.3849
40.45	46.96	.7071	.3750
43.34	50.00	.7129	.4476
46.07	52.78	.7127	.3872
60.24	66.08	.7055	.5396
63.25	68.73	.7172	.5878
74.71	78.11	.7831	.6997

Table VIII.   (cont)

RUN CODE   4434

% Surface Distance	% Axial Chord	Tw/Tg	h/ho
Suction Surface			
8.74	8.24	.8758	.5469
10.54	11.17	.8563	.6181
12.34	14.55	.8393	.6138
14.09	18.19	.8220	.5670
17.60	26.10	.7876	.5444
19.38	30.02	.7690	.4829
21.11	33.60	.7525	.4213
22.95	37.04	.7369	.3675
24.73	40.02	.7242	.3704
26.49	42.62	.7109	.2986
28.26	45.01	.7038	.2905
30.06	47.23	.7084	.3894
31.80	49.21	.7186	.4794
33.53	50.99	.7293	.5168
35.29	52.76	.7397	.5352
37.06	54.42	.7490	.6041
40.55	57.57	.7579	.6173
42.33	59.17	.7603	.6406
45.83	62.01	.7636	.6763
47.55	63.49	.7644	.7132
49.34	64.94	.7630	.7281
52.83	67.63	.7575	.7191
54.59	69.04	.7582	.7581
56.69	70.61	.7559	.7332
58.88	72.27	.7469	.6721
60.96	73.78	.7399	.7150
63.05	75.41	.7399	.7132
65.23	76.90	.7429	.7063
67.31	78.44	.7375	.6924
69.44	80.02	.7306	.7432
71.64	81.60	.7418	.6707
73.75	83.12	.7660	.7381
75.94	84.58	.7769	.6047
80.10	87.58	.7922	.6756
82.25	89.03	.8151	.7108
84.34	90.43	.8231	.5929
88.71	93.01	.8291	.6069
Pressure Surface			
14.93	15.92	.7874	.4203
18.03	20.09	.7622	.3901
26.10	30.47	.7268	.3655
28.94	33.92	.7207	.3837
31.85	37.33	.7174	.3976
37.56	43.82	.7094	.3902
40.45	46.96	.7075	.3806
43.34	50.00	.7130	.4520
46.07	52.78	.7126	.3883
60.24	66.08	.7049	.5477
63.25	68.73	.7166	.5961
74.71	78.11	.7827	.7016

Table VIII. (cont)

RUN CODE 4435

% Surface Distance	% Axial Chord	Tw/Tg	h/ho
Suction Surface			
8.74	8.24	.8804	.5598
10.54	11.17	.8605	.6348
12.34	14.55	.8433	.6263
14.09	18.19	.8260	.5851
17.60	26.10	.7915	.5591
19.38	30.02	.7730	.4954
21.11	33.60	.7569	.4378
22.95	37.04	.7417	.3865
24.73	40.02	.7292	.3916
26.49	42.62	.7160	.3192
28.26	45.01	.7086	.3110
30.06	47.23	.7128	.4093
31.80	49.21	.7225	.4991
33.53	50.99	.7327	.5311
35.29	52.76	.7426	.5468
37.06	54.42	.7515	.6157
40.55	57.57	.7596	.6211
42.33	59.17	.7617	.6441
45.83	62.01	.7645	.6773
47.55	63.49	.7653	.7146
49.34	64.94	.7637	.7262
52.83	67.63	.7580	.7171
54.59	69.04	.7587	.7551
56.69	70.61	.7564	.7314
58.88	72.27	.7475	.6767
60.96	73.78	.7407	.7240
63.05	75.41	.7406	.7204
65.23	76.90	.7436	.7074
67.31	78.44	.7381	.6865
69.44	80.02	.7313	.7343
71.64	81.60	.7424	.6601
73.75	83.12	.7665	.7322
75.94	84.58	.7774	.6035
80.10	87.58	.7926	.6751
82.25	89.03	.8156	.7111
84.34	90.43	.8237	.5919
88.71	93.01	.8297	.6078
Pressure Surface			
14.93	15.92	.7907	.4248
18.03	20.09	.7654	.3979
26.10	30.47	.7300	.3782
28.94	33.92	.7237	.3958
31.85	37.33	.7202	.4075
37.56	43.82	.7119	.3994
40.45	46.96	.7097	.3867
43.34	50.00	.7150	.4591
46.07	52.78	.7145	.3981
60.24	66.08	.7059	.5415
63.25	68.73	.7175	.5887
74.71	78.11	.7835	.7089

Table VIII. (cont)

RUN CODE 4436

% Surface Distance	% Axial Chord	Tw/Tg	h/ho
Suction Surface			
8.74	8.24	.8929	.6061
10.54	11.17	.8734	.6625
12.34	14.55	.8570	.7084
14.09	18.19	.8392	.6129
17.60	26.10	.8046	.5853
19.38	30.02	.7859	.5000
21.11	33.60	.7701	.4293
22.95	37.04	.7565	.4059
24.73	40.02	.7452	.4060
26.49	42.62	.7342	.3562
28.26	45.01	.7289	.3876
30.06	47.23	.7324	.4713
31.80	49.21	.7407	.5439
33.53	50.99	.7499	.5805
35.29	52.76	.7587	.5911
37.06	54.42	.7663	.6489
40.55	57.57	.7726	.6395
42.33	59.17	.7743	.6608
45.83	62.01	.7763	.6942
47.55	63.49	.7764	.7088
49.34	64.94	.7751	.7393
52.83	67.63	.7696	.7290
54.59	69.04	.7703	.7744
56.69	70.61	.7678	.7517
58.88	72.27	.7587	.6941
60.96	73.78	.7512	.7390
63.05	75.41	.7506	.7307
65.23	76.90	.7534	.7188
67.31	78.44	.7476	.6897
69.44	80.02	.7403	.7235
71.64	81.60	.7514	.6523
73.75	83.12	.7756	.7471
75.94	84.58	.7865	.6135
80.10	87.58	.8017	.7006
82.25	89.03	.8241	.7392
84.34	90.43	.8318	.6169
88.71	93.01	.8372	.6264
Pressure Surface			
14.93	15.92	.8096	.4782
18.03	20.09	.7848	.4419
26.10	30.47	.7502	.4254
28.94	33.92	.7438	.4426
31.85	37.33	.7399	.4512
37.56	43.82	.7310	.4437
40.45	46.96	.7281	.4312
43.34	50.00	.7315	.4884
46.07	52.78	.7299	.4225
60.24	66.08	.7178	.5502
63.25	68.73	.7289	.5994
74.71	78.11	.7928	.7332

Table VIII. (cont)

RUN CODE 4437

% Surface Distance	% Axial Chord	Tw/Tg	h/ho
Suction Surface			
8.74	8.24	.8981	.6315
10.54	11.17	.8786	.6870
12.34	14.55	.8623	.7349
14.09	18.19	.8449	.6452
17.60	26.10	.8107	.6095
19.38	30.02	.7927	.5231
21.11	33.60	.7780	.4576
22.95	37.04	.7658	.4495
24.73	40.02	.7556	.4558
26.49	42.62	.7454	.4147
28.26	45.01	.7402	.4630
30.06	47.23	.7416	.5197
31.80	49.21	.7473	.5687
33.53	50.99	.7546	.5903
35.29	52.76	.7621	.5979
37.06	54.42	.7689	.6536
40.55	57.57	.7744	.6441
42.33	59.17	.7757	.6646
45.83	62.01	.7773	.6958
47.55	63.49	.7774	.7144
49.34	64.94	.7761	.7474
52.83	67.63	.7707	.7420
54.59	69.04	.7712	.7835
56.69	70.61	.7688	.7564
58.88	72.27	.7596	.6952
60.96	73.78	.7522	.7383
63.05	75.41	.7516	.7295
65.23	76.90	.7544	.7207
67.31	78.44	.7486	.6923
69.44	80.02	.7412	.7246
71.64	81.60	.7522	.6548
73.75	83.12	.7765	.7525
75.94	84.58	.7874	.6179
80.10	87.58	.8024	.7058
82.25	89.03	.8249	.7442
84.34	90.43	.8326	.6231
88.71	93.01	.8381	.6315
Pressure Surface			
14.93	15.92	.8148	.4966
18.03	20.09	.7895	.4615
26.10	30.47	.7536	.4401
28.94	33.92	.7467	.4553
31.85	37.33	.7423	.4599
37.56	43.82	.7329	.4552
40.45	46.96	.7299	.4431
43.34	50.00	.7333	.4995
46.07	52.78	.7316	.4311
60.24	66.08	.7191	.5547
63.25	68.73	.7299	.6035
74.71	78.11	.7934	.7350

Table VIII. (cont)

RUN CODE 4438

% Surface Distance	% Axial Chord	Tw/Tg	h/ho
Suction Surface			
8.74	8.24	.9045	.6912
10.54	11.17	.8850	.7413
12.34	14.55	.8690	.7850
14.09	18.19	.8520	.7089
17.60	26.10	.8181	.6518
19.38	30.02	.8003	.5571
21.11	33.60	.7863	.4979
22.95	37.04	.7750	.5001
24.73	40.02	.7652	.5163
26.49	42.62	.7550	.4683
28.26	45.01	.7493	.5233
30.06	47.23	.7494	.5636
31.80	49.21	.7536	.6000
33.53	50.99	.7597	.6104
35.29	52.76	.7664	.6106
37.06	54.42	.7727	.6653
40.55	57.57	.7774	.6501
42.33	59.17	.7784	.6694
45.83	62.01	.7798	.6991
47.55	63.49	.7798	.7182
49.34	64.94	.7785	.7528
52.83	67.63	.7730	.7469
54.59	69.04	.7737	.7918
56.69	70.61	.7712	.7650
58.88	72.27	.7620	.7054
60.96	73.78	.7545	.7500
63.05	75.41	.7540	.7420
65.23	76.90	.7568	.7304
67.31	78.44	.7510	.7023
69.44	80.02	.7436	.7347
71.64	81.60	.7546	.6640
73.75	83.12	.7788	.7603
75.94	84.58	.7896	.6271
80.10	87.58	.8045	.7156
82.25	89.03	.8270	.7557
84.34	90.43	.8348	.6331
88.71	93.01	.8401	.6484
Pressure Surface			
14.93	15.92	.8198	.5279
18.03	20.09	.7947	.4904
26.10	30.47	.7582	.4537
28.94	33.92	.7511	.4674
31.85	37.33	.7467	.4736
37.56	43.82	.7373	.4704
40.45	46.96	.7341	.4561
43.34	50.00	.7375	.5191
46.07	52.78	.7356	.4458
60.24	66.08	.7219	.5658
63.25	68.73	.7326	.6136
74.71	78.11	.7957	.7490

Table VIII. (cont)

RUN CODE 4500

% Surface Distance	% Axial Chord	Tw/Tg	h/ho
Suction Surface			
8.74	8.24	.8955	.5839
10.54	11.17	.8776	.6433
12.34	14.55	.8628	.6784
14.09	18.19	.8472	.6061
17.60	26.10	.8182	.6046
19.38	30.02	.8020	.5161
21.11	33.60	.7912	.4816
22.95	37.04	.7825	.4971
24.73	40.02	.7765	.5604
26.49	42.62	.7683	.5165
28.26	45.01	.7662	.6085
30.06	47.23	.7664	.6387
31.80	49.21	.7712	.6802
33.53	50.99	.7775	.6890
35.29	52.76	.7838	.6937
37.06	54.42	.7909	.7527
40.55	57.57	.7954	.7505
42.33	59.17	.7966	.7706
45.83	62.01	.7971	.7932
47.55	63.49	.7965	.8040
49.34	64.94	.7950	.8371
52.83	67.63	.7901	.8382
54.59	69.04	.7911	.8850
56.69	70.61	.7890	.8548
58.88	72.27	.7803	.7871
60.96	73.78	.7739	.8396
63.05	75.41	.7743	.8359
65.23	76.90	.7785	.8345
67.31	78.44	.7736	.8178
69.44	80.02	.7663	.8718
71.64	81.60	.7771	.7796
73.75	83.12	.8007	.8620
75.94	84.58	.8106	.7083
80.10	87.58	.8234	.8019
82.25	89.03	.8445	.8293
84.34	90.43	.8512	.6966
88.71	93.01	.8533	.6812
Pressure Surface			
14.93	15.92	.8158	.4707
18.03	20.09	.7916	.4340
26.10	30.47	.7604	.4263
28.94	33.92	.7556	.4539
31.85	37.33	.7529	.4671
37.56	43.82	.7462	.4720
40.45	46.96	.7446	.4671
43.34	50.00	.7501	.5407
46.07	52.78	.7498	.4724
60.24	66.08	.7459	.6925
63.25	68.73	.7570	.7459
74.71	78.11	.8146	.8259

Table VIII. (cont)

RUN CODE 4513

% Surface Distance	% Axial Chord	Tw/Tg	h/ho
Suction Surface			
8.74	8.24	.8608	.4850
10.54	11.17	.8487	.5539
12.34	14.55	.8373	.5621
14.09	18.19	.8257	.5561
17.60	26.10	.8036	.5900
19.38	30.02	.7917	.5391
21.11	33.60	.7828	.5313
22.95	37.04	.7749	.5310
24.73	40.02	.7683	.5684
26.49	42.62	.7606	.5252
28.26	45.01	.7572	.6016
30.06	47.23	.7578	.6258
31.80	49.21	.7621	.6617
33.53	50.99	.7680	.6638
35.29	52.76	.7745	.6689
37.06	54.42	.7806	.7183
40.55	57.57	.7858	.7190
42.33	59.17	.7868	.7378
45.83	62.01	.7875	.7584
47.55	63.49	.7873	.7695
49.34	64.94	.7862	.8066
52.83	67.63	.7817	.8052
54.59	69.04	.7829	.8573
56.69	70.61	.7809	.8270
58.88	72.27	.7722	.7605
60.96	73.78	.7655	.8080
63.05	75.41	.7660	.8048
65.23	76.90	.7700	.8030
67.31	78.44	.7650	.7878
69.44	80.02	.7577	.8335
71.64	81.60	.7685	.7437
73.75	83.12	.7925	.8269
75.94	84.58	.8032	.6804
80.10	87.58	.8170	.7742
82.25	89.03	.8383	.7986
84.34	90.43	.8453	.6672
88.71	93.01	.8477	.6547
Pressure Surface			
14.93	15.92	.7943	.4498
18.03	20.09	.7750	.4310
26.10	30.47	.7491	.4178
28.94	33.92	.7451	.4438
31.85	37.33	.7433	.4582
37.56	43.82	.7379	.4650
40.45	46.96	.7370	.4608
43.34	50.00	.7426	.5383
46.07	52.78	.7422	.4604
60.24	66.08	.7383	.6751
63.25	68.73	.7493	.7261
74.71	78.11	.8085	.8121

Table VIII. (cont)

RUN CODE 4514

% Surface Distance	% Axial Chord	Tw/Tg	h/ho
Suction Surface			
8.74	8.24	.8528	.4760
10.54	11.17	.8430	.5511
12.34	14.55	.8330	.5470
14.09	18.19	.8233	.5774
17.60	26.10	.8029	.6034
19.38	30.02	.7915	.5548
21.11	33.60	.7827	.5430
22.95	37.04	.7745	.5350
24.73	40.02	.7678	.5690
26.49	42.62	.7603	.5314
28.26	45.01	.7570	.6079
30.06	47.23	.7576	.6301
31.80	49.21	.7617	.6635
33.53	50.99	.7673	.6636
35.29	52.76	.7737	.6655
37.06	54.42	.7796	.7105
40.55	57.57	.7846	.7106
42.33	59.17	.7856	.7280
45.83	62.01	.7863	.7474
47.55	63.49	.7860	.7576
49.34	64.94	.7850	.7962
52.83	67.63	.7806	.7983
54.59	69.04	.7818	.8476
56.69	70.61	.7799	.8186
58.88	72.27	.7712	.7529
60.96	73.78	.7646	.8025
63.05	75.41	.7651	.7996
65.23	76.90	.7692	.7952
67.31	78.44	.7642	.7833
69.44	80.02	.7570	.8311
71.64	81.60	.7678	.7429
73.75	83.12	.7918	.8210
75.94	84.58	.8024	.6711
80.10	87.58	.8161	.7644
82.25	89.03	.8373	.7862
84.34	90.43	.8442	.6565
88.71	93.01	.8467	.6395
Pressure Surface			
14.93	15.92	.7907	.4600
18.03	20.09	.7727	.4390
26.10	30.47	.7481	.4162
28.94	33.92	.7444	.4411
31.85	37.33	.7428	.4571
37.56	43.82	.7376	.4646
40.45	46.96	.7367	.4618
43.34	50.00	.7422	.5361
46.07	52.78	.7418	.4587
60.24	66.08	.7383	.6794
63.25	68.73	.7492	.7307
74.71	78.11	.8078	.8022

Table VIII. (cont)

RUN CODE 4515

% Surface Distance	% Axial Chord	Tw/Tg	h/ho
Suction Surface			
8.74	8.24	.8411	.4394
10.54	11.17	.8341	.5183
12.34	14.55	.8261	.5172
14.09	18.19	.8182	.5705
17.60	26.10	.8003	.5942
19.38	30.02	.7899	.5551
21.11	33.60	.7815	.5414
22.95	37.04	.7734	.5294
24.73	40.02	.7669	.5613
26.49	42.62	.7599	.5289
28.26	45.01	.7569	.6065
30.06	47.23	.7576	.6301
31.80	49.21	.7614	.6607
33.53	50.99	.7666	.6525
35.29	52.76	.7726	.6540
37.06	54.42	.7783	.6935
40.55	57.57	.7831	.6952
42.33	59.17	.7840	.7111
45.83	62.01	.7847	.7282
47.55	63.49	.7845	.7380
49.34	64.94	.7836	.7760
52.83	67.63	.7792	.7688
54.59	69.04	.7806	.8251
56.69	70.61	.7788	.7976
58.88	72.27	.7702	.7297
60.96	73.78	.7637	.7786
63.05	75.41	.7644	.7769
65.23	76.90	.7685	.7808
67.31	78.44	.7635	.7656
69.44	80.02	.7565	.8173
71.64	81.60	.7673	.7292
73.75	83.12	.7911	.8088
75.94	84.58	.8017	.6592
80.10	87.58	.8154	.7475
82.25	89.03	.8364	.7687
84.34	90.43	.8433	.6453
88.71	93.01	.8459	.6336
Pressure Surface			
14.93	15.92	.7864	.4520
18.03	20.09	.7706	.4437
26.10	30.47	.7483	.4198
28.94	33.92	.7449	.4434
31.85	37.33	.7434	.4587
37.56	43.82	.7382	.4605
40.45	46.96	.7372	.4544
43.34	50.00	.7425	.5277
46.07	52.78	.7420	.4512
60.24	66.08	.7383	.6704
63.25	68.73	.7492	.7233
74.71	78.11	.8073	.7903

Table VIII. (cont)

RUN CODE 4533

% Surface Distance	% Axial Chord	Tw/Tg	h/ho
Suction Surface			
8.74	8.24	.8896	.5806
10.54	11.17	.8738	.6441
12.34	14.55	.8601	.6812
14.09	18.19	.8454	.5989
17.60	26.10	.8182	.6076
19.38	30.02	.8041	.5254
21.11	33.60	.7939	.5023
22.95	37.04	.7865	.5297
24.73	40.02	.7807	.5915
26.49	42.62	.7736	.5549
28.26	45.01	.7705	.6433
30.06	47.23	.7710	.6682
31.80	49.21	.7752	.7061
33.53	50.99	.7809	.7051
35.29	52.76	.7871	.7036
37.06	54.42	.7931	.7623
40.55	57.57	.7975	.7527
42.33	59.17	.7982	.7717
45.83	62.01	.7985	.7934
47.55	63.49	.7978	.7988
49.34	64.94	.7962	.8308
52.83	67.63	.7913	.8318
54.59	69.04	.7920	.8749
56.69	70.61	.7899	.8433
58.88	72.27	.7814	.7760
60.96	73.78	.7749	.8238
63.05	75.41	.7754	.8217
65.23	76.90	.7795	.8220
67.31	78.44	.7747	.8095
69.44	80.02	.7678	.8604
71.64	81.60	.7784	.7730
73.75	83.12	.8016	.8580
75.94	84.58	.8116	.6966
80.10	87.58	.8249	.7990
82.25	89.03	.8457	.8189
84.34	90.43	.8526	.6905
88.71	93.01	.8550	.6741
Pressure Surface			
14.93	15.92	.8139	.4905
18.03	20.09	.7923	.4545
26.10	30.47	.7627	.4360
28.94	33.92	.7577	.4606
31.85	37.33	.7550	.4718
37.56	43.82	.7483	.4734
40.45	46.96	.7467	.4639
43.34	50.00	.7519	.5400
46.07	52.78	.7517	.4682
60.24	66.08	.7475	.6817
63.25	68.73	.7584	.7386
74.71	78.11	.8161	.8236

Table VIII. (cont)

RUN CODE 5400

% Surface Distance	% Axial Chord	Tw/Tg	h/ho
Suction Surface			
8.74	8.24	.8751	.5282
10.54	11.17	.8541	.5875
12.34	14.55	.8365	.6219
14.09	18.19	.8177	.5502
17.60	26.10	.7811	.5415
19.38	30.02	.7605	.4632
21.11	33.60	.7419	.3784
22.95	37.04	.7252	.3485
24.73	40.02	.7102	.3217
26.49	42.62	.6954	.2529
28.26	45.01	.6871	.2297
30.06	47.23	.6926	.3379
31.80	49.21	.7044	.4268
33.53	50.99	.7176	.4988
35.29	52.76	.7290	.5191
37.06	54.42	.7380	.5795
40.55	57.57	.7447	.5695
42.33	59.17	.7456	.5793
45.83	62.01	.7458	.5819
47.55	63.49	.7456	.5866
49.34	64.94	.7451	.6216
52.83	67.63	.7423	.6389
54.59	69.04	.7441	.6770
56.69	70.61	.7434	.6581
58.88	72.27	.7374	.6413
60.96	73.78	.7329	.7123
63.05	75.41	.7333	.7053
65.23	76.90	.7355	.6823
67.31	78.44	.7285	.6433
69.44	80.02	.7205	.6743
71.64	81.60	.7317	.6059
73.75	83.12	.7566	.6808
75.94	84.58	.7684	.5596
80.10	87.58	.7857	.6580
82.25	89.03	.8089	.6946
84.34	90.43	.8167	.5644
88.71	93.01	.8228	.5583
Pressure Surface			
14.93	15.92	.7866	.4089
18.03	20.09	.7589	.3700
26.10	30.47	.7205	.3580
28.94	33.92	.7137	.3751
31.85	37.33	.7099	.3876
37.56	43.82	.7020	.3811
40.45	46.96	.7005	.3816
43.34	50.00	.7051	.4243
46.07	52.78	.7052	.3781
60.24	66.08	.6991	.5314
63.25	68.73	.7106	.5770
74.71	78.11	.7762	.6750

Table VIII. (cont)

RUN CODE 5413

% Surface Distance	% Axial Chord	Tw/Tg	h/ho
Suction Surface			
8.74	8.24	.8569	.5149
10.54	11.17	.8401	.5714
12.34	14.55	.8250	.5897
14.09	18.19	.8086	.5344
17.60	26.10	.7759	.5208
19.38	30.02	.7572	.4474
21.11	33.60	.7402	.3700
22.95	37.04	.7251	.3438
24.73	40.02	.7119	.3234
26.49	42.62	.6994	.2628
28.26	45.01	.6933	.2552
30.06	47.23	.6994	.3608
31.80	49.21	.7106	.4435
33.53	50.99	.7226	.5038
35.29	52.76	.7332	.5184
37.06	54.42	.7417	.5776
40.55	57.57	.7479	.5641
42.33	59.17	.7487	.5732
45.83	62.01	.7489	.5754
47.55	63.49	.7487	.5782
49.34	64.94	.7482	.6149
52.83	67.63	.7457	.6346
54.59	69.04	.7473	.6682
56.69	70.61	.7467	.6490
58.88	72.27	.7410	.6284
60.96	73.78	.7366	.6975
63.05	75.41	.7368	.6856
65.23	76.90	.7390	.6636
67.31	78.44	.7325	.6325
69.44	80.02	.7248	.6622
71.64	81.60	.7359	.5954
73.75	83.12	.7602	.6684
75.94	84.58	.7717	.5486
80.10	87.58	.7884	.6464
82.25	89.03	.8105	.6719
84.34	90.43	.8179	.5448
88.71	93.01	.8237	.5394
Pressure Surface			
14.93	15.92	.7770	.4280
18.03	20.09	.7540	.3799
26.10	30.47	.7223	.3586
28.94	33.92	.7166	.3742
31.85	37.33	.7136	.3868
37.56	43.82	.7067	.3816
40.45	46.96	.7055	.3845
43.34	50.00	.7099	.4212
46.07	52.78	.7101	.3752
60.24	66.08	.7054	.5336
63.25	68.73	.7167	.5805
74.71	78.11	.7797	.6730

Table VIII. (cont)

RUN CODE 5414

% Surface Distance	% Axial Chord	Tw/Tg	h/ho
Suction Surface			
8.74	8.24	.8517	.5072
10.54	11.17	.8362	.5582
12.34	14.55	.8222	.5855
14.09	18.19	.8067	.5299
17.60	26.10	.7756	.5170
19.38	30.02	.7577	.4438
21.11	33.60	.7419	.3706
22.95	37.04	.7284	.3547
24.73	40.02	.7170	.3437
26.49	42.62	.7063	.2933
28.26	45.01	.7018	.3082
30.06	47.23	.7074	.4053
31.80	49.21	.7172	.4733
33.53	50.99	.7278	.5221
35.29	52.76	.7371	.5268
37.06	54.42	.7449	.5875
40.55	57.57	.7499	.5647
42.33	59.17	.7503	.5708
45.83	62.01	.7501	.5715
47.55	63.49	.7499	.5779
49.34	64.94	.7494	.6142
52.83	67.63	.7468	.6328
54.59	69.04	.7486	.6686
56.69	70.61	.7482	.6532
58.88	72.27	.7424	.6382
60.96	73.78	.7377	.7043
63.05	75.41	.7374	.6844
65.23	76.90	.7392	.6569
67.31	78.44	.7327	.6212
69.44	80.02	.7253	.6532
71.64	81.60	.7366	.5878
73.75	83.12	.7610	.6607
75.94	84.58	.7729	.5510
80.10	87.58	.7895	.6449
82.25	89.03	.8117	.6740
84.34	90.43	.8190	.5468
88.71	93.01	.8245	.5411
Pressure Surface			
14.93	15.92	.7747	.4294
18.03	20.09	.7528	.3804
26.10	30.47	.7232	.3606
28.94	33.92	.7179	.3755
31.85	37.33	.7151	.3876
37.56	43.82	.7084	.3839
40.45	46.96	.7072	.3864
43.34	50.00	.7115	.4234
46.07	52.78	.7118	.3799
60.24	66.08	.7069	.5330
63.25	68.73	.7183	.5801
74.71	78.11	.7810	.6746

Table VIII. (cont)

RUN CODE 5415

% Surface Distance	% Axial Chord	Tw/Tg	h/ho
Suction Surface			
8.74	8.24	.8386	.4658
10.54	11.17	.8255	.5265
12.34	14.55	.8130	.5375
14.09	18.19	.7993	.5167
17.60	26.10	.7708	.5024
19.38	30.02	.7544	.4339
21.11	33.60	.7404	.3723
22.95	37.04	.7290	.3711
24.73	40.02	.7193	.3730
26.49	42.62	.7100	.3324
28.26	45.01	.7063	.3641
30.06	47.23	.7105	.4378
31.80	49.21	.7184	.4882
33.53	50.99	.7275	.5232
35.29	52.76	.7358	.5243
37.06	54.42	.7429	.5797
40.55	57.57	.7472	.5543
42.33	59.17	.7475	.5610
45.83	62.01	.7471	.5618
47.55	63.49	.7468	.5653
49.34	64.94	.7462	.6012
52.83	67.63	.7433	.6098
54.59	69.04	.7452	.6514
56.69	70.61	.7448	.6361
58.88	72.27	.7390	.6187
60.96	73.78	.7342	.6847
63.05	75.41	.7340	.6662
65.23	76.90	.7361	.6418
67.31	78.44	.7297	.6123
69.44	80.02	.7222	.6410
71.64	81.60	.7335	.5753
73.75	83.12	.7581	.6506
75.94	84.58	.7699	.5367
80.10	87.58	.7867	.6309
82.25	89.03	.8087	.6566
84.34	90.43	.8159	.5301
88.71	93.01	.8215	.5227
Pressure Surface			
14.93	15.92	.7683	.4192
18.03	20.09	.7481	.3784
26.10	30.47	.7209	.3623
28.94	33.92	.7159	.3778
31.85	37.33	.7133	.3890
37.56	43.82	.7066	.3814
40.45	46.96	.7054	.3837
43.34	50.00	.7096	.4202
46.07	52.78	.7096	.3733
60.24	66.08	.7046	.5290
63.25	68.73	.7161	.5788
74.71	78.11	.7788	.6700

Table VIII. (cont)

RUN CODE 5433

% Surface Distance	% Axial Chord	Tw/Tg	h/ho
Suction Surface			
8.74	8.24	.8703	.5195
10.54	11.17	.8500	.5774
12.34	14.55	.8329	.6134
14.09	18.19	.8144	.5397
17.60	26.10	.7788	.5365
19.38	30.02	.7587	.4601
21.11	33.60	.7406	.3786
22.95	37.04	.7246	.3518
24.73	40.02	.7103	.3304
26.49	42.62	.6961	.2646
28.26	45.01	.6885	.2467
30.06	47.23	.6941	.3557
31.80	49.21	.7056	.4432
33.53	50.99	.7181	.5084
35.29	52.76	.7289	.5248
37.06	54.42	.7375	.5816
40.55	57.57	.7435	.5679
42.33	59.17	.7443	.5773
45.83	62.01	.7443	.5783
47.55	63.49	.7440	.5821
49.34	64.94	.7433	.6149
52.83	67.63	.7405	.6338
54.59	69.04	.7421	.6679
56.69	70.61	.7413	.6498
58.88	72.27	.7353	.6350
60.96	73.78	.7307	.7073
63.05	75.41	.7311	.7008
65.23	76.90	.7334	.6759
67.31	78.44	.7264	.6321
69.44	80.02	.7184	.6603
71.64	81.60	.7296	.5926
73.75	83.12	.7543	.6668
75.94	84.58	.7662	.5515
80.10	87.58	.7836	.6487
82.25	89.03	.8068	.6866
84.34	90.43	.8146	.5584
88.71	93.01	.8207	.5585
Pressure Surface			
14.93	15.92	.7833	.4114
18.03	20.09	.7566	.3768
26.10	30.47	.7193	.3623
28.94	33.92	.7125	.3775
31.85	37.33	.7087	.3881
37.56	43.82	.7007	.3791
40.45	46.96	.6991	.3784
43.34	50.00	.7036	.4233
46.07	52.78	.7036	.3771
60.24	66.08	.6970	.5195
63.25	68.73	.7084	.5623
74.71	78.11	.7741	.6659

Table VIII. (cont)

RUN CODE 5434

% Surface Distance	% Axial Chord	Tw/Tg	h/ho
Suction Surface			
8.74	8.24	.8707	.5342
10.54	11.17	.8507	.5891
12.34	14.55	.8337	.6236
14.09	18.19	.8155	.5484
17.60	26.10	.7803	.5432
19.38	30.02	.7605	.4654
21.11	33.60	.7429	.3870
22.95	37.04	.7274	.3638
24.73	40.02	.7136	.3465
26.49	42.62	.6999	.2810
28.26	45.01	.6925	.2665
30.06	47.23	.6980	.3750
31.80	49.21	.7091	.4614
33.53	50.99	.7210	.5231
35.29	52.76	.7312	.5338
37.06	54.42	.7393	.5894
40.55	57.57	.7449	.5723
42.33	59.17	.7454	.5805
45.83	62.01	.7451	.5799
47.55	63.49	.7447	.5839
49.34	64.94	.7440	.6176
52.83	67.63	.7409	.6342
54.59	69.04	.7424	.6689
56.69	70.61	.7416	.6500
58.88	72.27	.7355	.6333
60.96	73.78	.7308	.7031
63.05	75.41	.7310	.6943
65.23	76.90	.7333	.6734
67.31	78.44	.7265	.6382
69.44	80.02	.7183	.6657
71.64	81.60	.7294	.5985
73.75	83.12	.7541	.6766
75.94	84.58	.7653	.5354
80.10	87.58	.7834	.6467
82.25	89.03	.8066	.6815
84.34	90.43	.8144	.5551
88.71	93.01	.8206	.5560
Pressure Surface			
14.93	15.92	.7829	.4214
18.03	20.09	.7568	.3859
26.10	30.47	.7201	.3662
28.94	33.92	.7133	.3796
31.85	37.33	.7094	.3900
37.56	43.82	.7012	.3804
40.45	46.96	.6996	.3808
43.34	50.00	.7040	.4247
46.07	52.78	.7038	.3749
60.24	66.08	.6969	.5245
63.25	68.73	.7084	.5697
74.71	78.11	.7741	.6651

Table VIII. (cont)

RUN CODE 5435

% Surface Distance	% Axial Chord	Tw/Tg	h/ho
Suction Surface			
8.74	8.24	.8740	.5448
10.54	11.17	.8539	.5996
12.34	14.55	.8371	.6449
14.09	18.19	.8188	.5590
17.60	26.10	.7837	.5539
19.38	30.02	.7642	.4748
21.11	33.60	.7470	.3981
22.95	37.04	.7321	.3803
24.73	40.02	.7188	.3668
26.49	42.62	.7053	.3009
28.26	45.01	.6980	.2880
30.06	47.23	.7030	.3952
31.80	49.21	.7135	.4776
33.53	50.99	.7248	.5367
35.29	52.76	.7346	.5448
37.06	54.42	.7424	.6015
40.55	57.57	.7471	.5774
42.33	59.17	.7474	.5850
45.83	62.01	.7467	.5828
47.55	63.49	.7462	.5866
49.34	64.94	.7454	.6204
52.83	67.63	.7423	.6382
54.59	69.04	.7437	.6697
56.69	70.61	.7428	.6496
58.88	72.27	.7367	.6329
60.96	73.78	.7318	.6993
63.05	75.41	.7318	.6880
65.23	76.90	.7339	.6682
67.31	78.44	.7269	.6303
69.44	80.02	.7188	.6571
71.64	81.60	.7300	.5920
73.75	83.12	.7547	.6649
75.94	84.58	.7666	.5493
80.10	87.58	.7840	.6443
82.25	89.03	.8072	.6826
84.34	90.43	.8149	.5515
88.71	93.01	.8211	.5458
Pressure Surface			
14.93	15.92	.7851	.4242
18.03	20.09	.7591	.3901
26.10	30.47	.7228	.3749
28.94	33.92	.7159	.3883
31.85	37.33	.7120	.3981
37.56	43.82	.7037	.3880
40.45	46.96	.7019	.3873
43.34	50.00	.7061	.4293
46.07	52.78	.7057	.3777
60.24	66.08	.6979	.5204
63.25	68.73	.7092	.5642
74.71	78.11	.7748	.6681

Table VIII. (cont)

RUN CODE 5500

% Surface Distance	% Axial Chord	Tw/Tg	h/ho
Suction Surface			
8.74	8.24	.8922	.6285
10.54	11.17	.8722	.6929
12.34	14.55	.8552	.6957
14.09	18.19	.8375	.6198
17.60	26.10	.8052	.6001
19.38	30.02	.7882	.5215
21.11	33.60	.7777	.5048
22.95	37.04	.7689	.5199
24.73	40.02	.7624	.5675
26.49	42.62	.7539	.5285
28.26	45.01	.7512	.6025
30.06	47.23	.7523	.6459
31.80	49.21	.7583	.7037
33.53	50.99	.7650	.7151
35.29	52.76	.7713	.7197
37.06	54.42	.7774	.7612
40.55	57.57	.7790	.7374
42.33	59.17	.7781	.7376
45.83	62.01	.7742	.7157
47.55	63.49	.7721	.7099
49.34	64.94	.7697	.7314
52.83	67.63	.7649	.7572
54.59	69.04	.7655	.7784
56.69	70.61	.7635	.7442
58.88	72.27	.7565	.7191
60.96	73.78	.7512	.7836
63.05	75.41	.7524	.7894
65.23	76.90	.7565	.7807
67.31	78.44	.7504	.7493
69.44	80.02	.7421	.7889
71.64	81.60	.7533	.7092
73.75	83.12	.7778	.7839
75.94	84.58	.7880	.6359
80.10	87.58	.8023	.7309
82.25	89.03	.8251	.7741
84.34	90.43	.8318	.6193
88.71	93.01	.8344	.5944
Pressure Surface			
14.93	15.92	.8095	.5002
18.03	20.09	.7819	.4514
26.10	30.47	.7444	.4266
28.94	33.92	.7382	.4529
31.85	37.33	.7341	.4606
37.56	43.82	.7259	.4586
40.45	46.96	.7238	.4517
43.34	50.00	.7293	.5276
46.07	52.78	.7281	.4504
60.24	66.08	.7218	.6368
63.25	68.73	.7330	.6814
74.71	78.11	.7942	.7786

Table VIII. (cont)

RUN CODE 5513

% Surface Distance	% Axial Chord	Tw/Tg	h/ho
Suction Surface			
8.74	8.24	.8556	.5346
10.54	11.17	.8433	.5877
12.34	14.55	.8313	.5938
14.09	18.19	.8186	.5650
17.60	26.10	.7950	.5660
19.38	30.02	.7842	.5320
21.11	33.60	.7776	.5637
22.95	37.04	.7717	.5907
24.73	40.02	.7661	.6301
26.49	42.62	.7588	.5954
28.26	45.01	.7547	.6572
30.06	47.23	.7545	.6689
31.80	49.21	.7583	.7040
33.53	50.99	.7635	.6970
35.29	52.76	.7692	.6959
37.06	54.42	.7742	.7321
40.55	57.57	.7762	.7073
42.33	59.17	.7752	.7070
45.83	62.01	.7717	.6858
47.55	63.49	.7699	.6782
49.34	64.94	.7678	.7070
52.83	67.63	.7634	.7310
54.59	69.04	.7641	.7568
56.69	70.61	.7623	.7246
58.88	72.27	.7553	.6951
60.96	73.78	.7502	.7597
63.05	75.41	.7515	.7635
65.23	76.90	.7553	.7549
67.31	78.44	.7493	.7197
69.44	80.02	.7419	.7643
71.64	81.60	.7527	.6812
73.75	83.12	.7768	.7562
75.94	84.58	.7875	.6154
80.10	87.58	.8025	.7186
82.25	89.03	.8247	.7483
84.34	90.43	.8314	.6012
88.71	93.01	.8345	.5749
Pressure Surface			
14.93	15.92	.7865	.4784
18.03	20.09	.7667	.4434
26.10	30.47	.7392	.4157
28.94	33.92	.7343	.4370
31.85	37.33	.7315	.4448
37.56	43.82	.7248	.4472
40.45	46.96	.7232	.4403
43.34	50.00	.7285	.5132
46.07	52.78	.7277	.4387
60.24	66.08	.7226	.6222
63.25	68.73	.7334	.6648
74.71	78.11	.7943	.7606

Table VIII. (cont)

RUN CODE 5514

% Surface Distance	% Axial Chord	Tw/Tg	h/ho
Suction Surface			
8.74	8.24	.8414	.4895
10.54	11.17	.8326	.5475
12.34	14.55	.8231	.5590
14.09	18.19	.8129	.5594
17.60	26.10	.7932	.5744
19.38	30.02	.7842	.5584
21.11	33.60	.7784	.5986
22.95	37.04	.7721	.6062
24.73	40.02	.7658	.6281
26.49	42.62	.7582	.5932
28.26	45.01	.7540	.6513
30.06	47.23	.7534	.6613
31.80	49.21	.7568	.6905
33.53	50.99	.7617	.6848
35.29	52.76	.7671	.6790
37.06	54.42	.7718	.7136
40.55	57.57	.7737	.6890
42.33	59.17	.7726	.6880
45.83	62.01	.7692	.6665
47.55	63.49	.7674	.6591
49.34	64.94	.7655	.6886
52.83	67.63	.7613	.7139
54.59	69.04	.7621	.7405
56.69	70.61	.7603	.7078
58.88	72.27	.7532	.6739
60.96	73.78	.7481	.7370
63.05	75.41	.7495	.7444
65.23	76.90	.7534	.7389
67.31	78.44	.7477	.7171
69.44	80.02	.7402	.7654
71.64	81.60	.7509	.6787
73.75	83.12	.7750	.7451
75.94	84.58	.7860	.6058
80.10	87.58	.8014	.7069
82.25	89.03	.8233	.7328
84.34	90.43	.8301	.5896
88.71	93.01	.8332	.5643
Pressure Surface			
14.93	15.92	.7821	.4816
18.03	20.09	.7639	.4483
26.10	30.47	.7380	.4160
28.94	33.92	.7333	.4336
31.85	37.33	.7306	.4411
37.56	43.82	.7239	.4429
40.45	46.96	.7223	.4337
43.34	50.00	.7275	.5065
46.07	52.78	.7268	.4323
60.24	66.08	.7218	.6298
63.25	68.73	.7326	.6732
74.71	78.11	.7934	.7505

Table VIII. (cont)

RUN CODE 5515

% Surface Distance	% Axial Chord	Tw/Tg	h/ho
Suction Surface			
8.74	8.24	.8292	.4426
10.54	11.17	.8226	.5102
12.34	14.55	.8148	.5187
14.09	18.19	.8067	.5545
17.60	26.10	.7895	.5720
19.38	30.02	.7813	.5646
21.11	33.60	.7758	.6003
22.95	37.04	.7692	.5952
24.73	40.02	.7628	.6100
26.49	42.62	.7555	.5817
28.26	45.01	.7513	.6393
30.06	47.23	.7505	.6461
31.80	49.21	.7534	.6707
33.53	50.99	.7578	.6614
35.29	52.76	.7629	.6534
37.06	54.42	.7674	.6861
40.55	57.57	.7695	.6675
42.33	59.17	.7685	.6671
45.83	62.01	.7653	.6481
47.55	63.49	.7636	.6406
49.34	64.94	.7619	.6737
52.83	67.63	.7574	.6889
54.59	69.04	.7583	.7196
56.69	70.61	.7566	.6881
58.88	72.27	.7495	.6514
60.96	73.78	.7445	.7141
63.05	75.41	.7460	.7214
65.23	76.90	.7500	.7161
67.31	78.44	.7443	.6874
69.44	80.02	.7370	.7336
71.64	81.60	.7477	.6473
73.75	83.12	.7720	.7207
75.94	84.58	.7830	.5861
80.10	87.58	.7986	.6909
82.25	89.03	.8206	.7127
84.34	90.43	.8274	.5747
88.71	93.01	.8306	.5512
Pressure Surface			
14.93	15.92	.7765	.4719
18.03	20.09	.7604	.4532
26.10	30.47	.7369	.4246
28.94	33.92	.7325	.4399
31.85	37.33	.7299	.4473
37.56	43.82	.7232	.4486
40.45	46.96	.7214	.4370
43.34	50.00	.7264	.5095
46.07	52.78	.7253	.4307
60.24	66.08	.7199	.6123
63.25	68.73	.7306	.6532
74.71	78.11	.7913	.7462

Table VIII. (cont)

RUN CODE 5533

% Surface Distance	% Axial Chord	Tw/Tg	h/ho
Suction Surface			
8.74	8.24	.8881	.6219
10.54	11.17	.8693	.6826
12.34	14.55	.8530	.6953
14.09	18.19	.8358	.6099
17.60	26.10	.8043	.5995
19.38	30.02	.7887	.5194
21.11	33.60	.7776	.5036
22.95	37.04	.7693	.5217
24.73	40.02	.7625	.5696
26.49	42.62	.7546	.5314
28.26	45.01	.7510	.6052
30.06	47.23	.7526	.6461
31.80	49.21	.7582	.6987
33.53	50.99	.7649	.7123
35.29	52.76	.7714	.7119
37.06	54.42	.7766	.7516
40.55	57.57	.7784	.7279
42.33	59.17	.7771	.7271
45.83	62.01	.7728	.7035
47.55	63.49	.7704	.6918
49.34	64.94	.7679	.7140
52.83	67.63	.7629	.7400
54.59	69.04	.7634	.7620
56.69	70.61	.7615	.7308
58.88	72.27	.7546	.7051
60.96	73.78	.7495	.7707
63.05	75.41	.7512	.7804
65.23	76.90	.7554	.7759
67.31	78.44	.7497	.7430
69.44	80.02	.7424	.7907
71.64	81.60	.7535	.7118
73.75	83.12	.7774	.7735
75.94	84.58	.7880	.6259
80.10	87.58	.8033	.7190
82.25	89.03	.8263	.7666
84.34	90.43	.8338	.6164
88.71	93.01	.8381	.5936
Pressure Surface			
14.93	15.92	.8057	.4958
18.03	20.09	.7802	.4501
26.10	30.47	.7437	.4225
28.94	33.92	.7369	.4466
31.85	37.33	.7327	.4523
37.56	43.82	.7239	.4470
40.45	46.96	.7217	.4380
43.34	50.00	.7268	.5101
46.07	52.78	.7262	.4428
60.24	66.08	.7215	.6321
63.25	68.73	.7327	.6775
74.71	78.11	.7947	.7567

Table VIII. (cont)

RUN CODE 5534

% Surface Distance	% Axial Chord	Tw/Tg	h/ho
Suction Surface			
8.74	8.24	.8914	.6357
10.54	11.17	.8727	.6917
12.34	14.55	.8569	.7237
14.09	18.19	.8400	.6373
17.60	26.10	.8088	.6238
19.38	30.02	.7932	.5425
21.11	33.60	.7821	.5248
22.95	37.04	.7735	.5418
24.73	40.02	.7663	.5790
26.49	42.62	.7580	.5412
28.26	45.01	.7542	.6139
30.06	47.23	.7554	.6551
31.80	49.21	.7605	.7050
33.53	50.99	.7669	.7154
35.29	52.76	.7731	.7173
37.06	54.42	.7781	.7542
40.55	57.57	.7797	.7290
42.33	59.17	.7783	.7275
45.83	62.01	.7740	.7043
47.55	63.49	.7717	.6954
49.34	64.94	.7693	.7212
52.83	67.63	.7646	.7582
54.59	69.04	.7648	.7710
56.69	70.61	.7630	.7390
58.88	72.27	.7561	.7140
60.96	73.78	.7508	.7778
63.05	75.41	.7522	.7818
65.23	76.90	.7562	.7742
67.31	78.44	.7506	.7461
69.44	80.02	.7431	.7894
71.64	81.60	.7542	.7132
73.75	83.12	.7784	.7860
75.94	84.58	.7884	.6123
80.10	87.58	.8044	.7251
82.25	89.03	.8275	.7691
84.34	90.43	.8350	.6178
88.71	93.01	.8390	.5840
Pressure Surface			
14.93	15.92	.8083	.5063
18.03	20.09	.7828	.4607
26.10	30.47	.7461	.4288
28.94	33.92	.7392	.4515
31.85	37.33	.7349	.4580
37.56	43.82	.7260	.4577
40.45	46.96	.7237	.4484
43.34	50.00	.7286	.5197
46.07	52.78	.7279	.4494
60.24	66.08	.7226	.6355
63.25	68.73	.7338	.6809
74.71	78.11	.7960	.7639

Table VIII. (cont)

RUN CODE 5535

% Surface Distance	% Axial Chord	Tw/Tg	h/ho
Suction Surface			
8.74	8.24	.8977	.6615
10.54	11.17	.8788	.7261
12.34	14.55	.8627	.7395
14.09	18.19	.8461	.6739
17.60	26.10	.8148	.6500
19.38	30.02	.7993	.5689
21.11	33.60	.7884	.5546
22.95	37.04	.7797	.5701
24.73	40.02	.7722	.6072
26.49	42.62	.7637	.5669
28.26	45.01	.7596	.6431
30.06	47.23	.7603	.6819
31.80	49.21	.7650	.7268
33.53	50.99	.7709	.7312
35.29	52.76	.7768	.7273
37.06	54.42	.7816	.7668
40.55	57.57	.7828	.7389
42.33	59.17	.7813	.7373
45.83	62.01	.7766	.7132
47.55	63.49	.7741	.6991
49.34	64.94	.7714	.7215
52.83	67.63	.7662	.7468
54.59	69.04	.7666	.7688
56.69	70.61	.7647	.7364
58.88	72.27	.7574	.7037
60.96	73.78	.7523	.7686
63.05	75.41	.7542	.7818
65.23	76.90	.7587	.7851
67.31	78.44	.7530	.7575
69.44	80.02	.7453	.8025
71.64	81.60	.7563	.7221
73.75	83.12	.7804	.7850
75.94	84.58	.7910	.6303
80.10	87.58	.8064	.7247
82.25	89.03	.8296	.7714
84.34	90.43	.8372	.6232
88.71	93.01	.8413	.5924
Pressure Surface			
14.93	15.92	.8137	.5132
18.03	20.09	.7878	.4683
26.10	30.47	.7505	.4415
28.94	33.92	.7434	.4643
31.85	37.33	.7388	.4688
37.56	43.82	.7293	.4619
40.45	46.96	.7267	.4506
43.34	50.00	.7314	.5232
46.07	52.78	.7304	.4473
60.24	66.08	.7251	.6474
63.25	68.73	.7363	.6940
74.71	78.11	.7988	.7813

Table IX.
Blowing ratio data.

Run Code	Row 1	Row 2	Row 3	Row 4	Row 5	Global
4300	0.0	0.0	0.0	0.0	0.0	0.0
4313	0.69	0.80	1.22	0.80	0.59	0.53
4314	1.33	1.60	2.37	1.43	0.97	0.98
4315	1.75	2.14	3.18	1.86	1.22	1.28
4333	0.69	0.80	1.16	0.75	0.56	0.52
4334	1.19	1.44	2.13	1.26	0.85	0.88
4335	1.56	1.91	2.90	1.70	1.10	1.17
4400	0.0	0.0	0.0	0.0	0.0	0.0
4413	0.81	0.94	1.43	0.91	0.68	0.61
4414	1.30	1.57	2.29	1.40	0.95	0.97
4415	1.91	2.34	3.49	2.08	1.35	1.42
4416	3.48	4.31	6.52	3.84	2.41	2.62
4417	4.81	5.97	9.08	5.31	3.30	3.60
4418	5.84	7.25	10.97	6.34	3.93	4.33
4423	0.75	0.88	1.29	0.86	0.64	0.58
4424	1.10	1.33	1.87	1.15	0.79	0.81
4425	1.46	1.79	2.68	1.59	1.03	1.08
4426	2.64	3.27	4.99	2.88	1.81	1.98
4427	3.50	4.34	6.58	3.84	2.39	2.64
4428	4.06	5.03	7.57	4.39	2.72	3.00
4433	0.69	0.81	1.12	0.70	0.53	0.50
4434	0.99	1.20	1.78	1.08	0.73	0.75
4435	1.34	1.65	2.46	1.48	0.96	1.02
4436	2.40	2.97	4.54	2.61	1.64	1.78
4437	2.98	3.70	5.63	3.23	2.01	2.22
4438	3.68	4.58	6.92	4.07	2.52	2.77
4500	0.0	0.0	0.0	0.0	0.0	0.0
4513	0.97	1.14	1.63	1.08	0.79	0.74
4514	1.45	1.75	2.58	1.53	1.05	1.07
4515	2.02	2.47	3.69	2.15	1.40	1.50
4533	0.87	1.02	1.54	0.93	0.69	0.66
5400	0.0	0.0	0.0	0.0	0.0	0.0
5413	0.87	1.02	1.49	0.94	0.70	0.66
5414	1.28	1.56	2.32	1.39	0.95	0.97
5415	1.79	2.20	3.30	1.94	1.26	1.34
5433	0.48	0.57	0.77	0.54	0.40	0.37
5434	0.87	1.05	1.55	0.93	0.64	0.65
5435	1.19	1.47	2.21	1.31	0.85	0.90
5500	0.0	0.0	0.0	0.0	0.0	0.0
5513	1.03	1.21	1.76	1.10	0.82	0.77
5514	1.58	1.91	2.84	1.71	1.16	1.18
55'5	2.26	2.79	4.20	2.46	1.60	1.69
5533	0.59	0.68	1.03	0.65	0.50	0.46
5534	0.92	1.12	1.67	1.00	0.68	0.70
5535	1.28	1.57	2.35	1.40	0.91	0.96

APPENDIX B
DATA COMPARISON PLOTS

Figures 57-110 contain data comparison plots for the leading edge film-cooled C3X cascade. Figures 57 and 58 show normalized heat transfer coefficients and the corresponding vane surface to gas absolute temperature ratio (T_w/T_g) distribution plots for the baseline (i.e., no discrete injection) runs. The remaining figures contain Stanton number reduction (SNR) and the corresponding theta distribution plots for all combinations of the parametric variation. The figure titles describe which parameter is varied and display the run codes for the data series. For a complete explanation of the run code, refer to Test Conditions in Section III. The values of the remaining parameters, which are held constant, are displayed in the plot descriptor. The values in the descriptor reflect nominal values for the run series. The actual run conditions for each individual run were listed previously in Table VI.

144
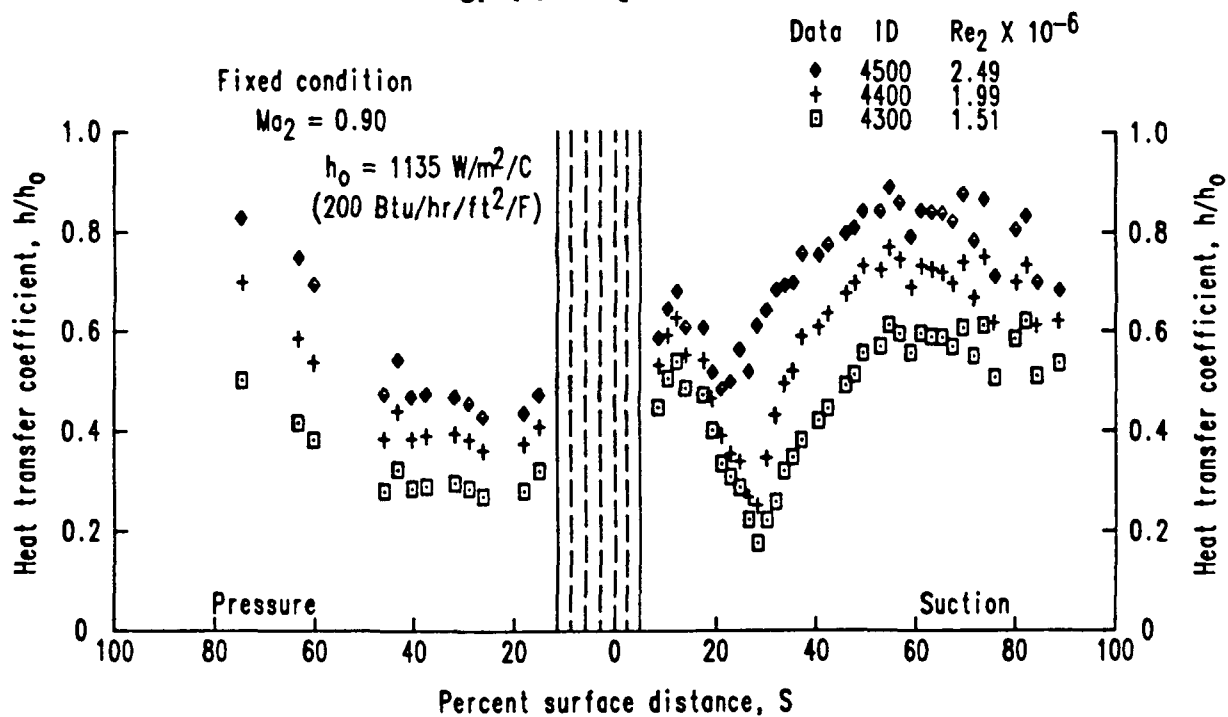
a. Heat transfer coefficient distributions
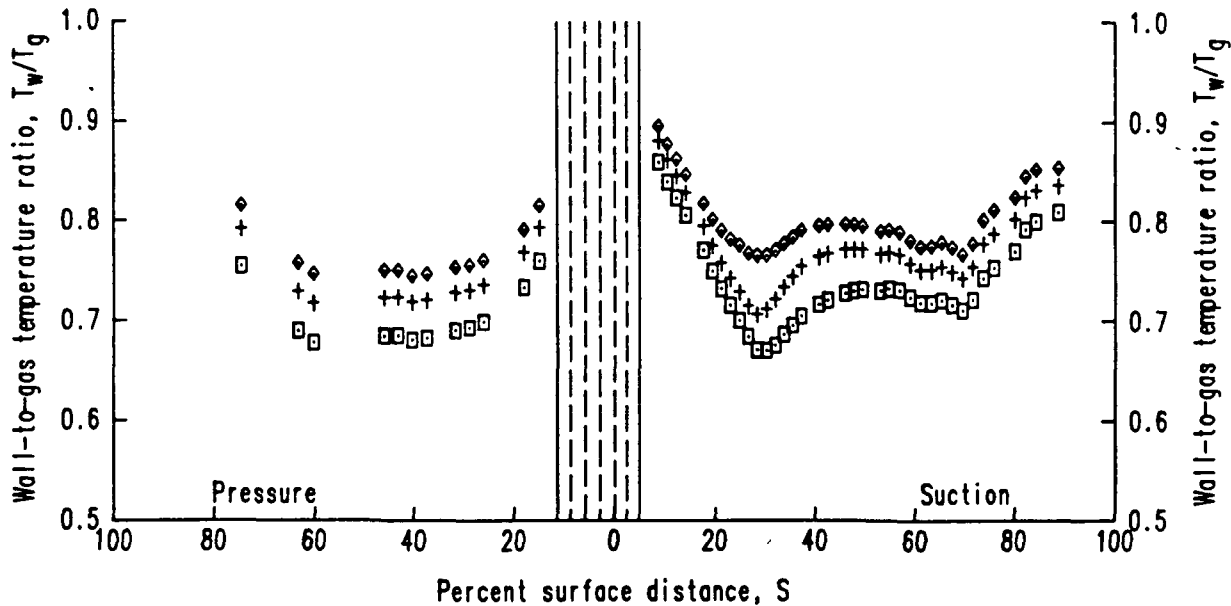
b. T_w/T_g distributions

TE84-8618

Figure 57. Baseline runs (no discrete injection) 4300, 4400, and 4500.

145
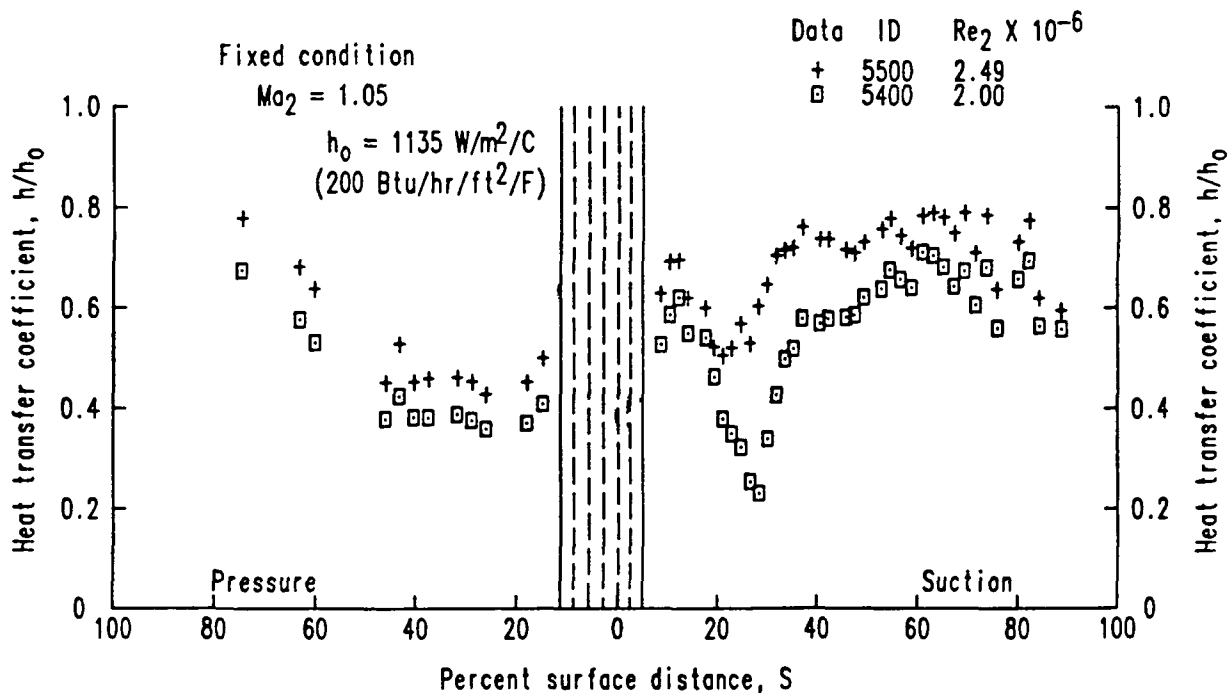
a. Heat transfer coefficient distributions
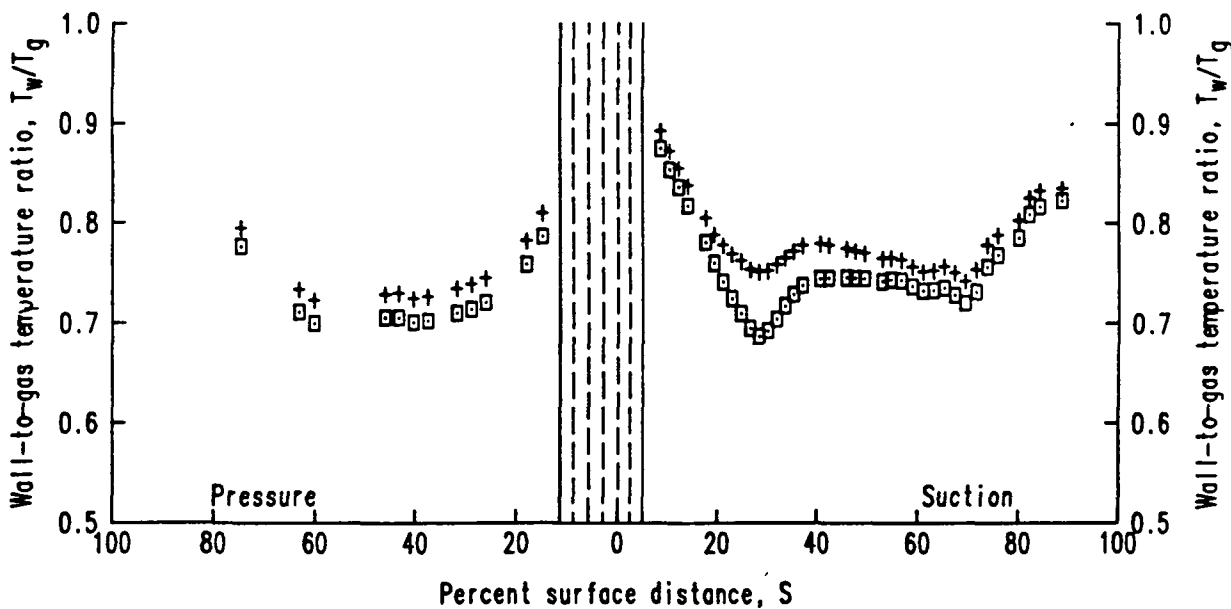
b. T_w/T_g distributions

TE84-8619

Figure 58. Baseline runs (no discrete injection) 5400 and 5500.

Fixed conditions

$Ma_2 = 0.89$

$Re_2 = 1.50 \times 10^6$

$T_c/T_g = 0.72$

Data	ID	P_c/P_t
◆	4315	1.10
+	4314	1.05
▣	4313	1.02

Stanton number reduction, SNR

Pressure   Suction

Percent surface distance, S

a. SNR distributions

Theta, $(T_c-T_g)/(T_w-T_g)$

Pressure   Suction

Percent surface distance, S

b. Theta distributions
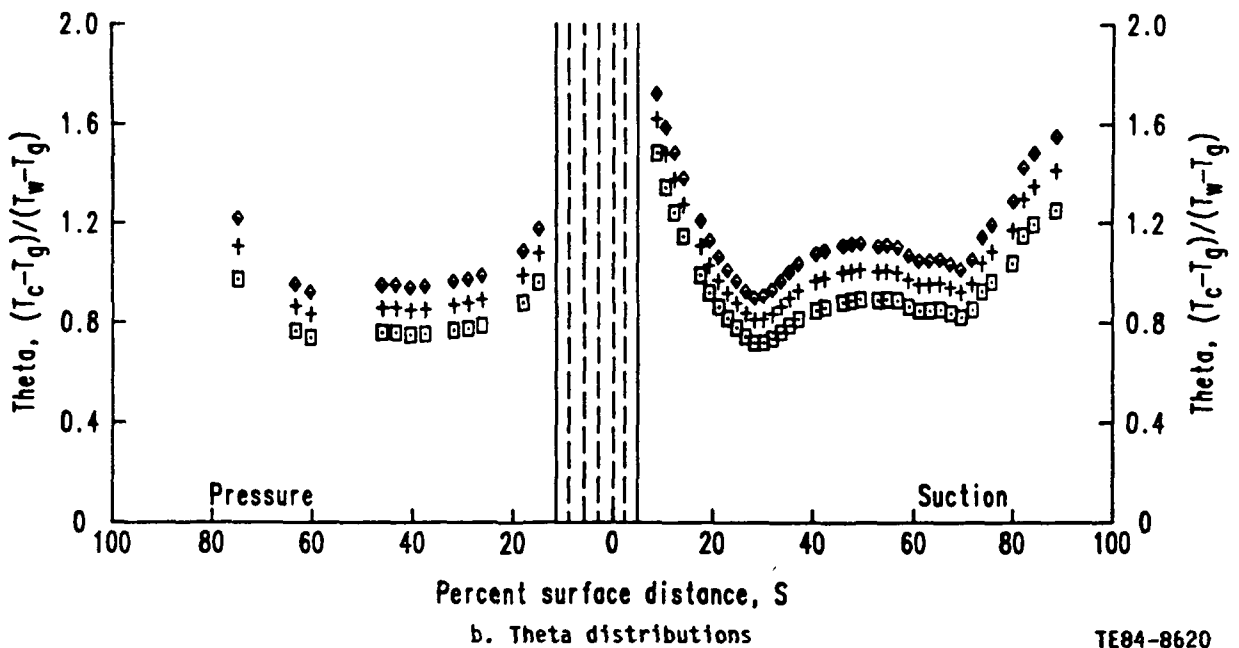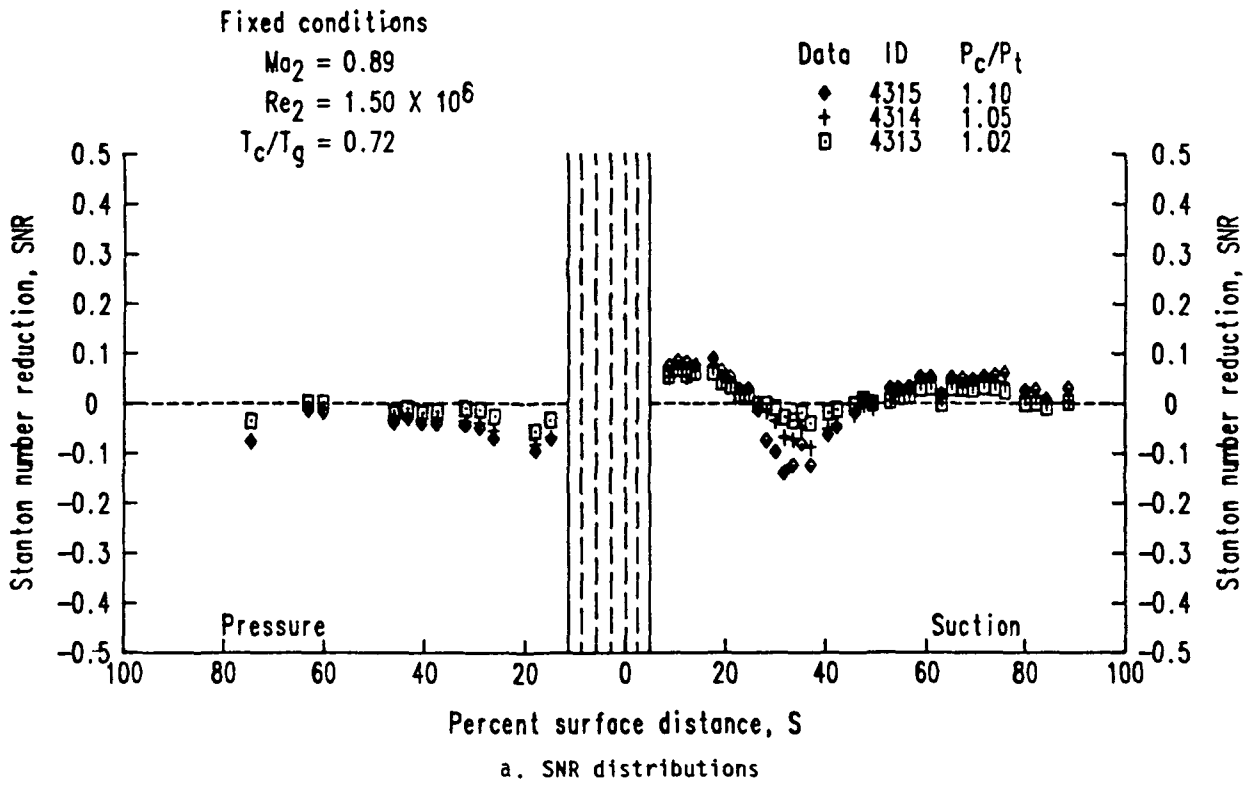
TE84-8620

Figure 59. Effects of coolant to free-stream pressure ratio variation--
series 431X.
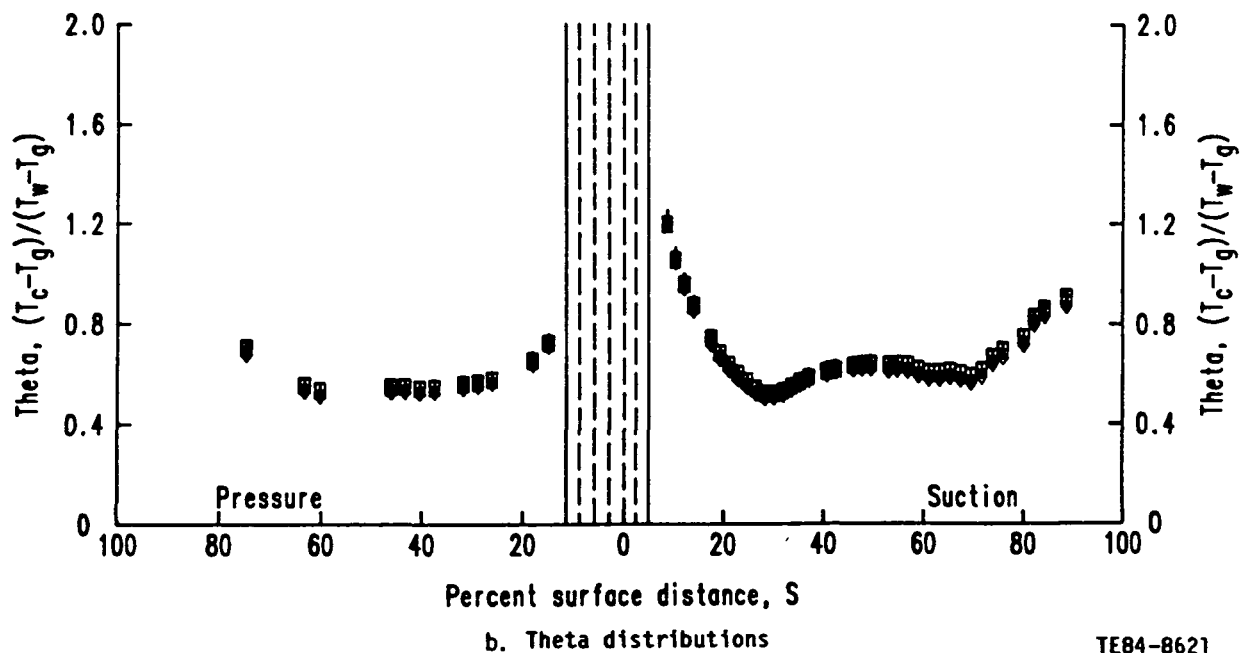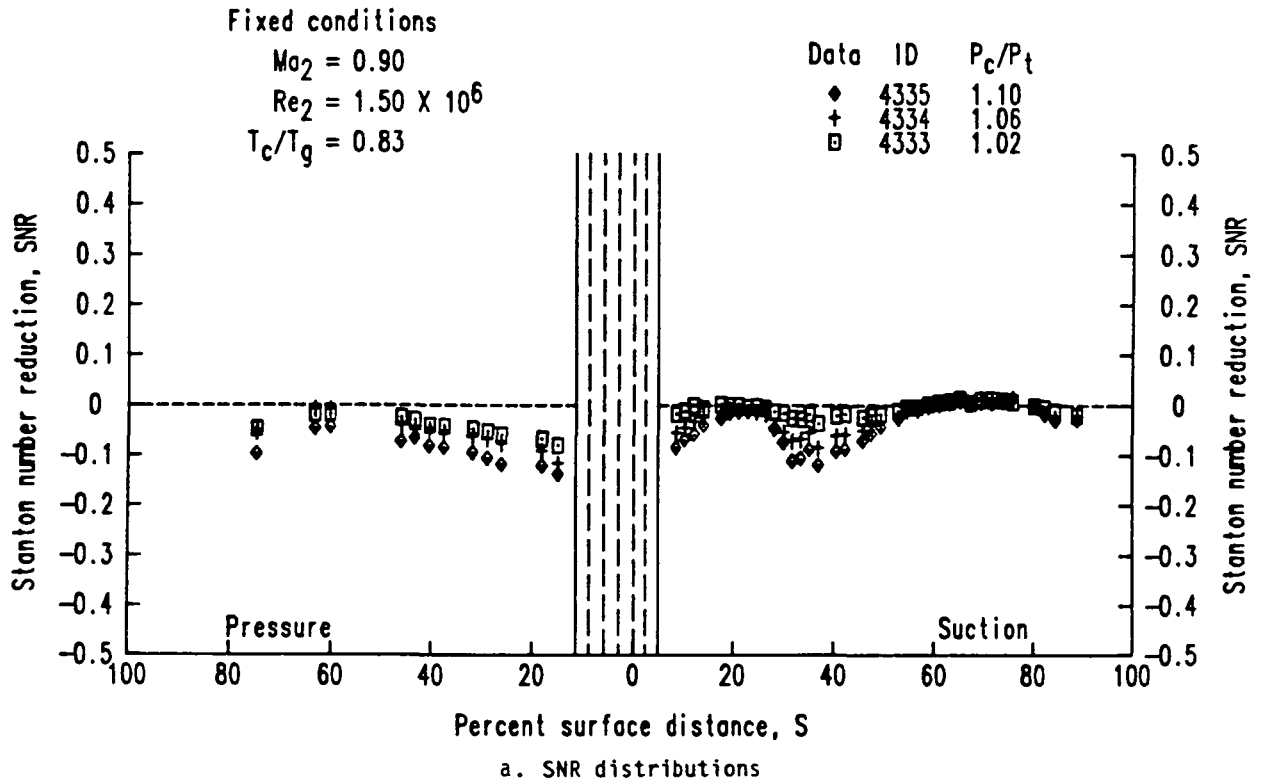
Figure 60.   Effects of coolant to free-stream pressure ratio variation--
series 433X.
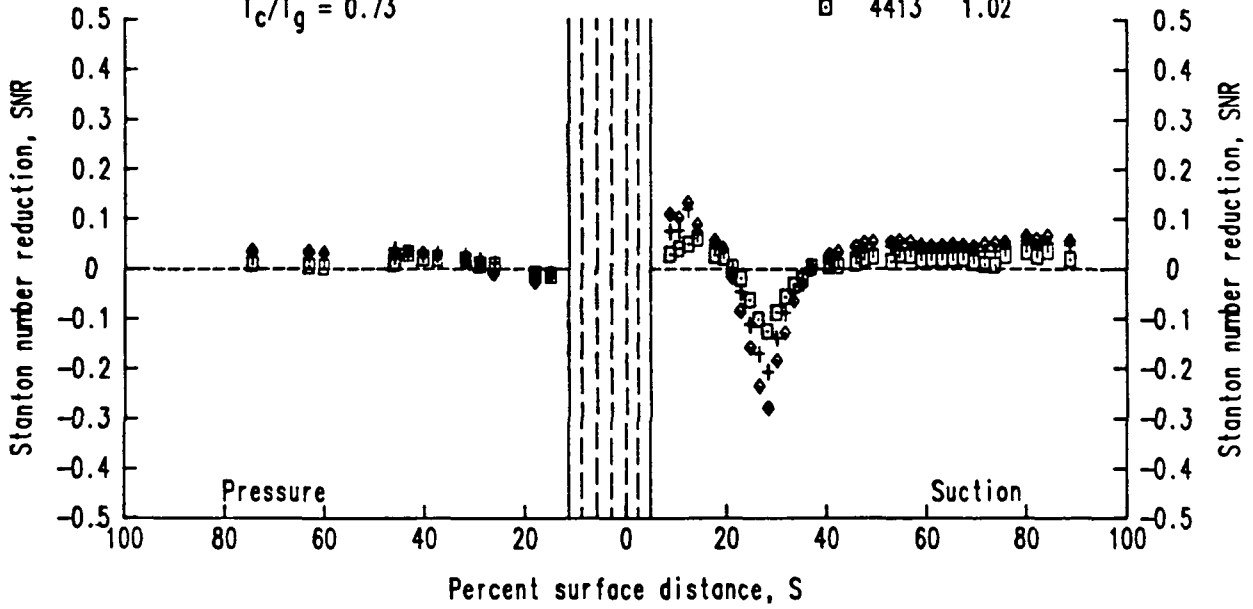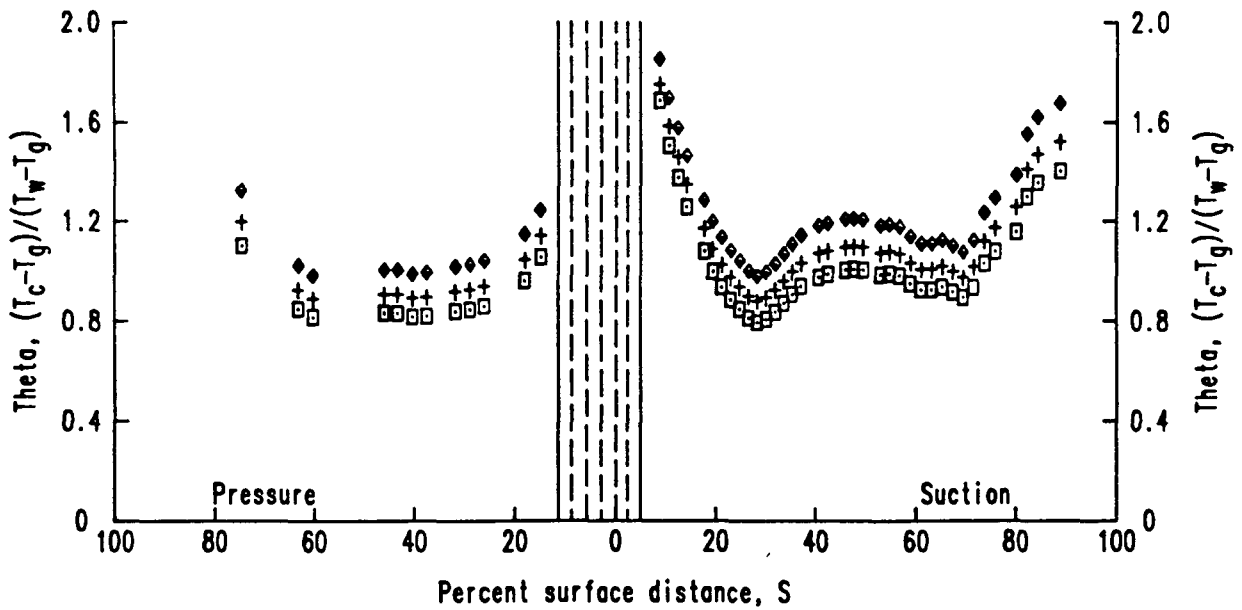
Figure 61. Effects of coolant to free-stream pressure ratio variation-- series 441X.
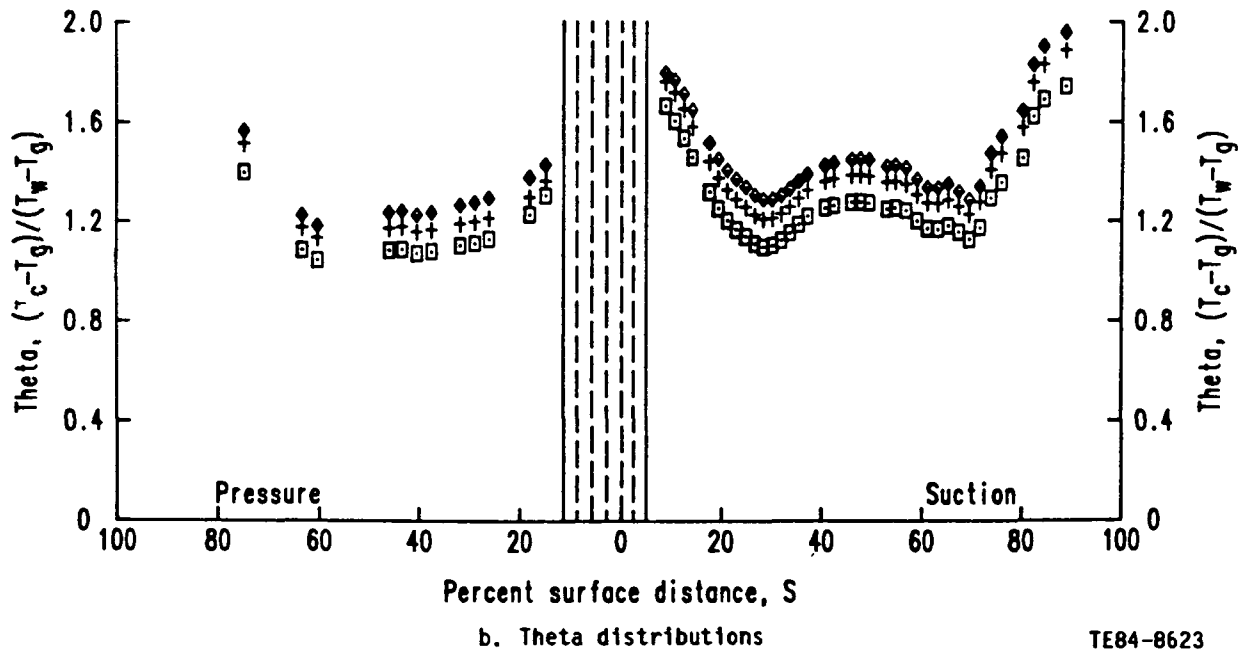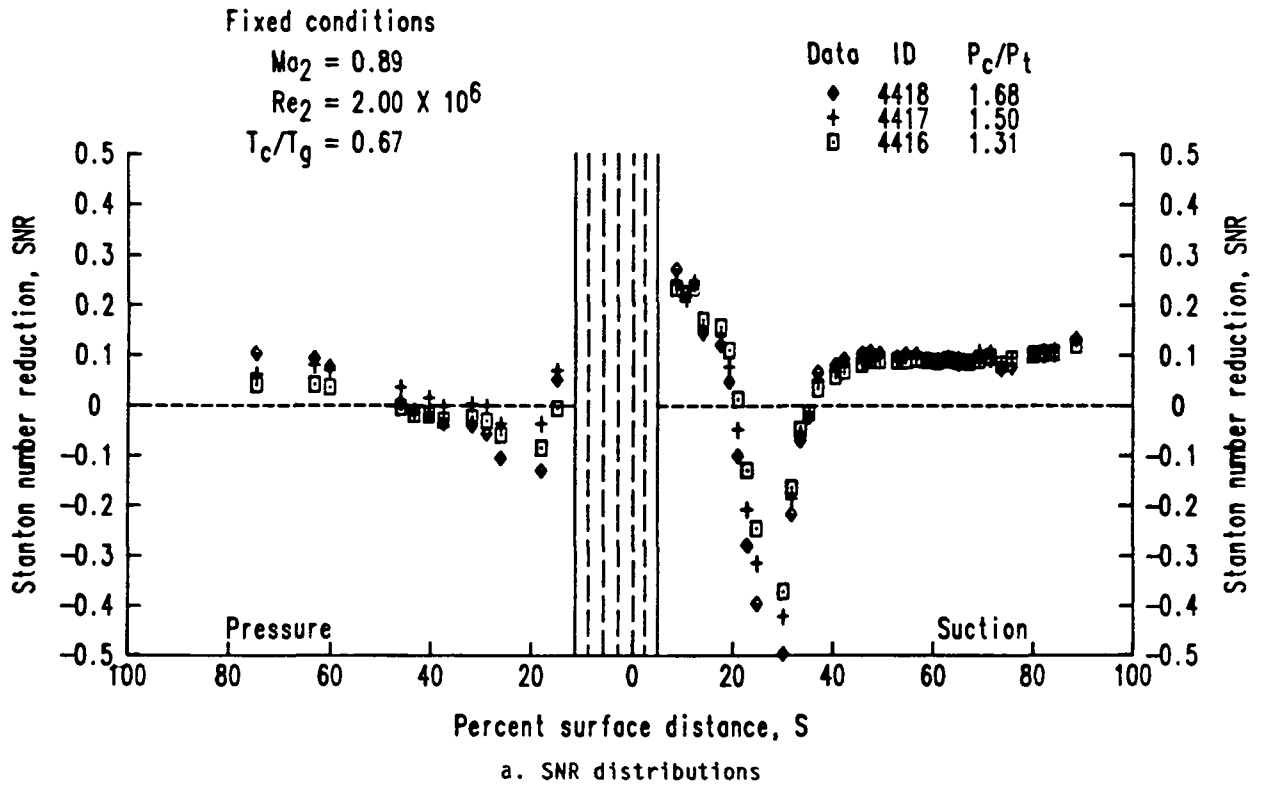
Figure 62. Effects of coolant to free-stream pressure ratio variation—
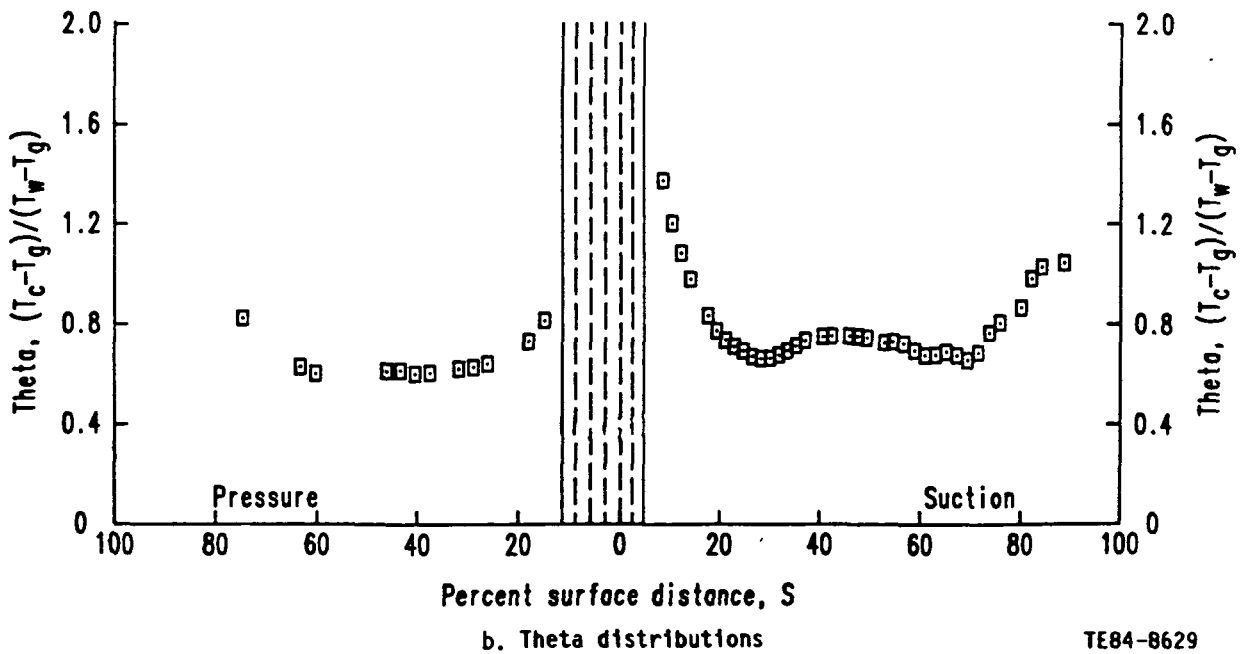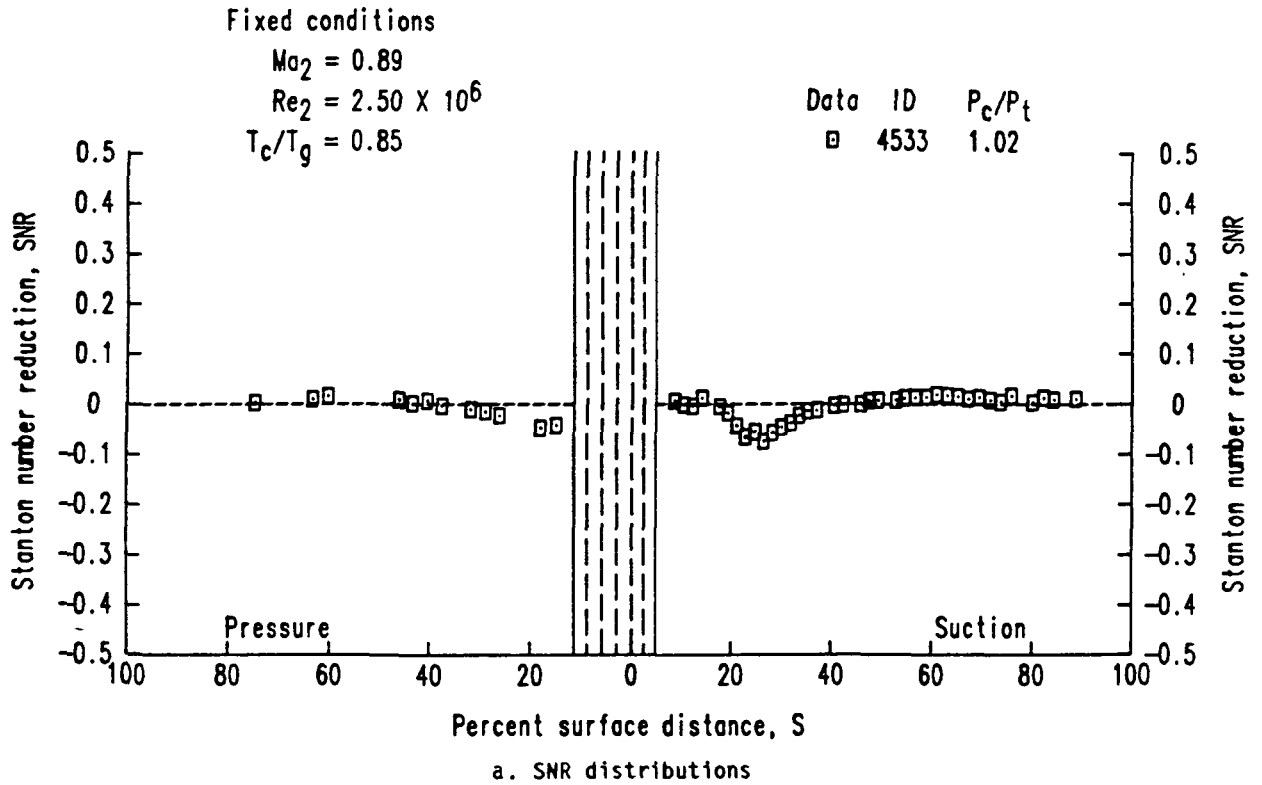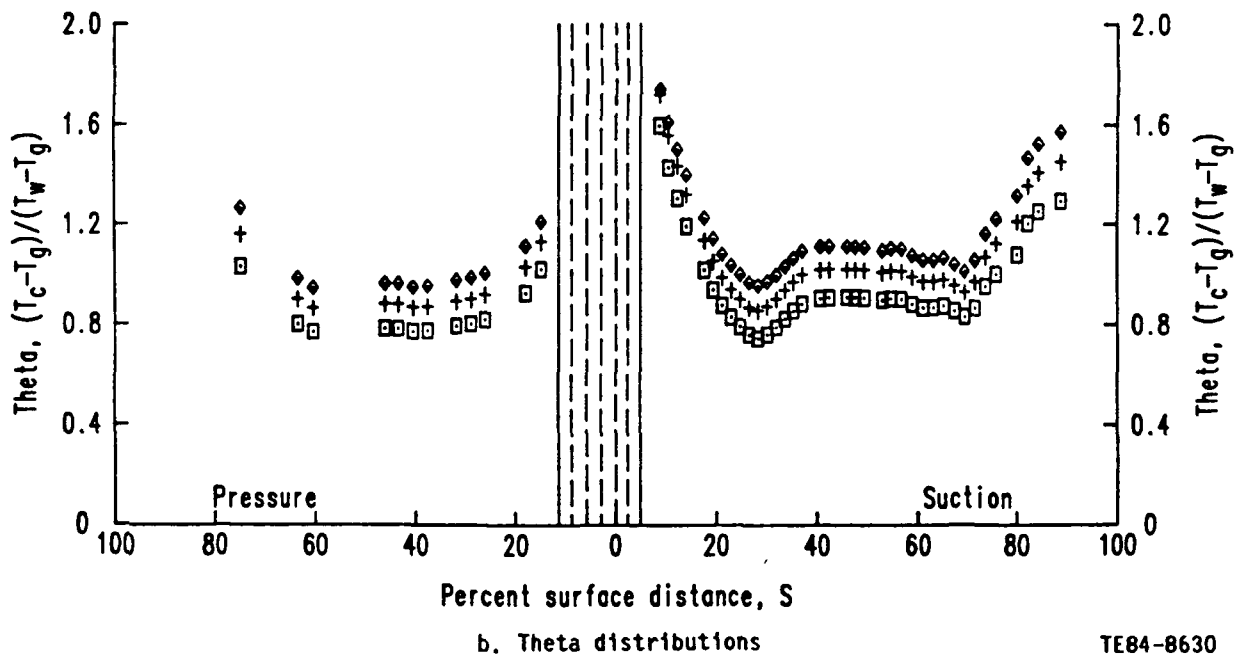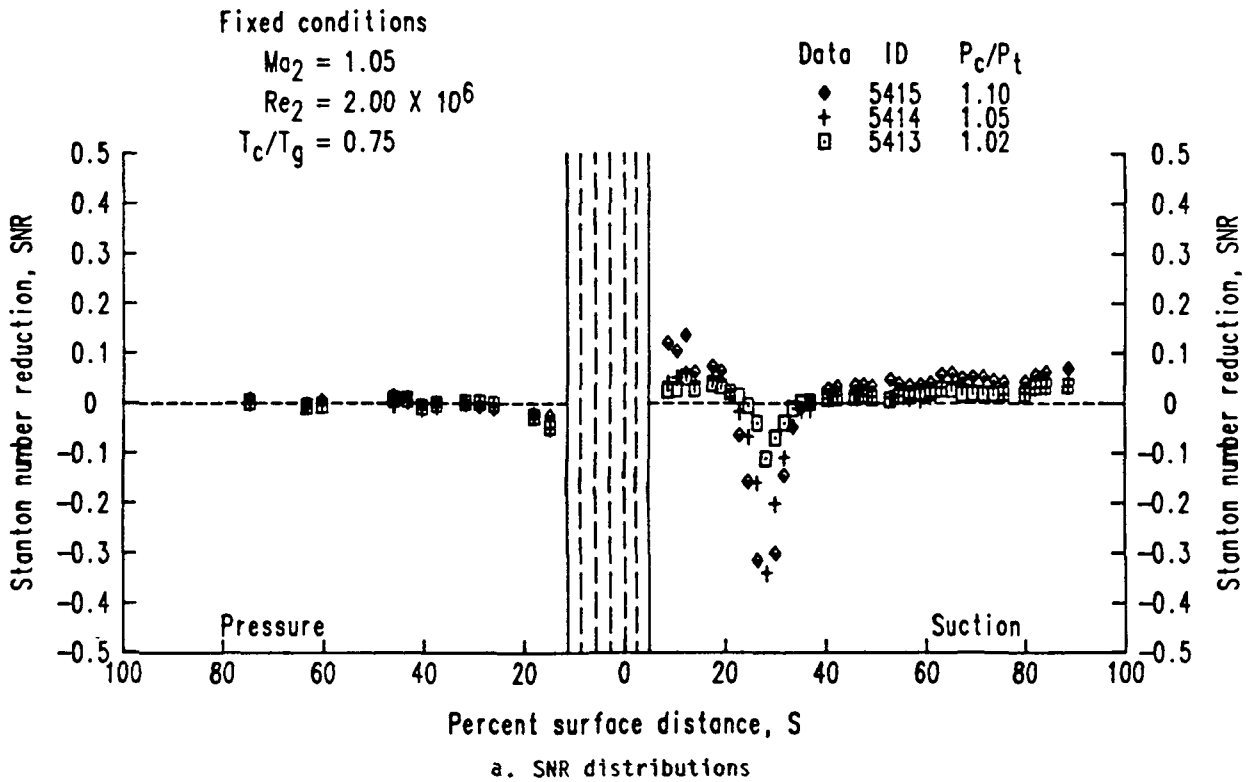series 441X (higher blowing strengths).
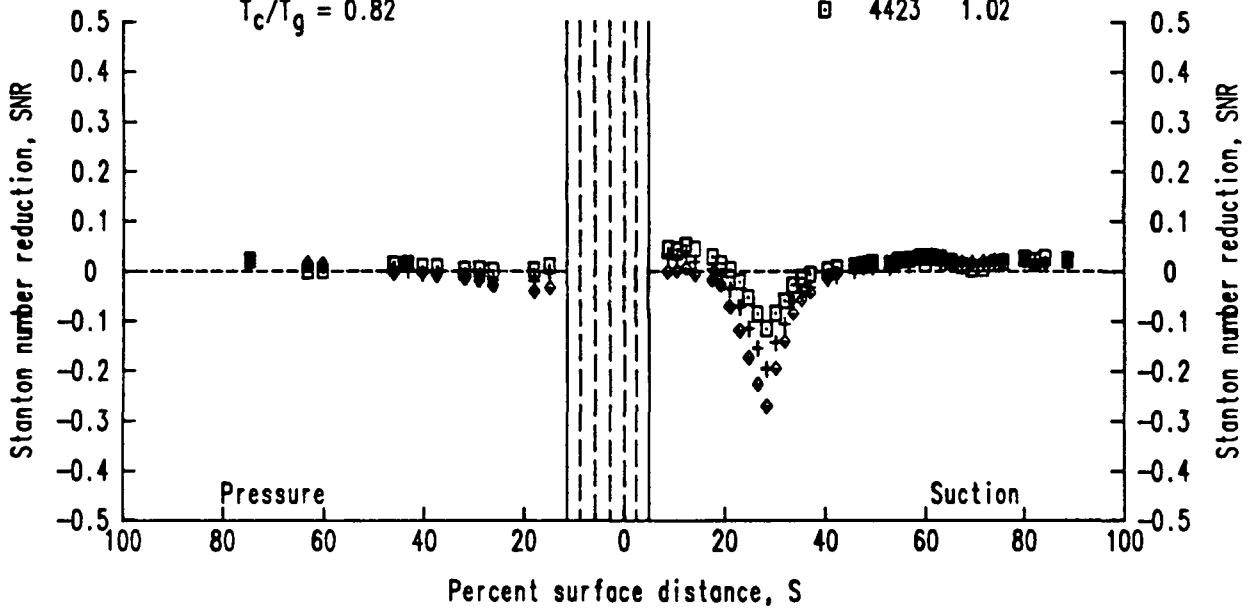
a. SNR distributions
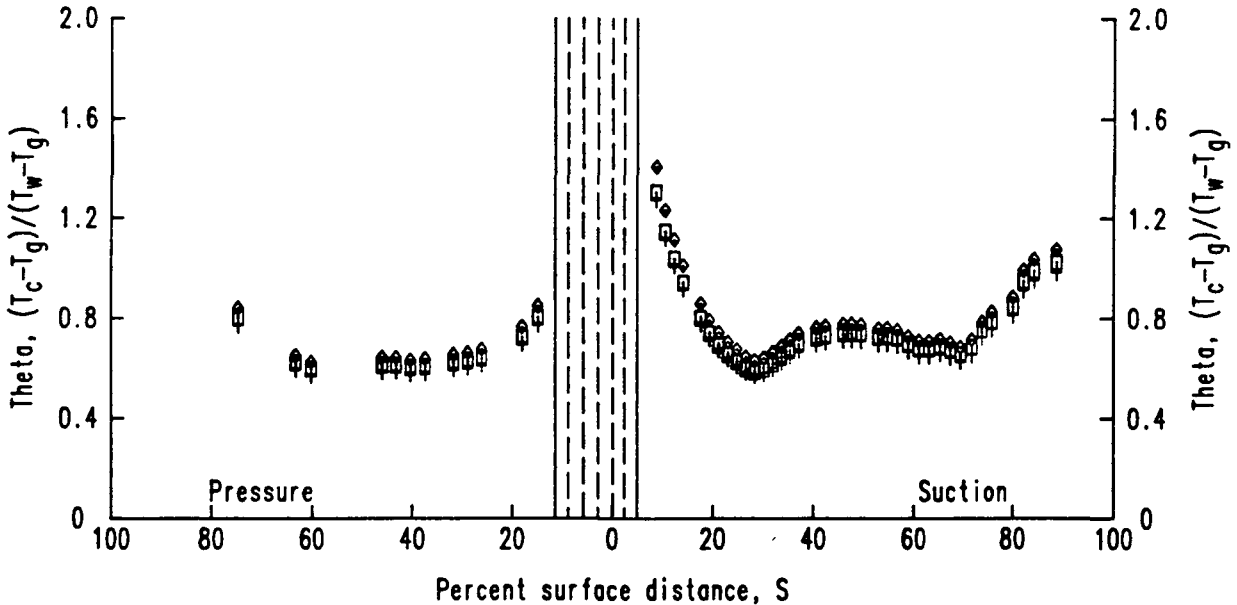
b. Theta distributions

TE84-8624

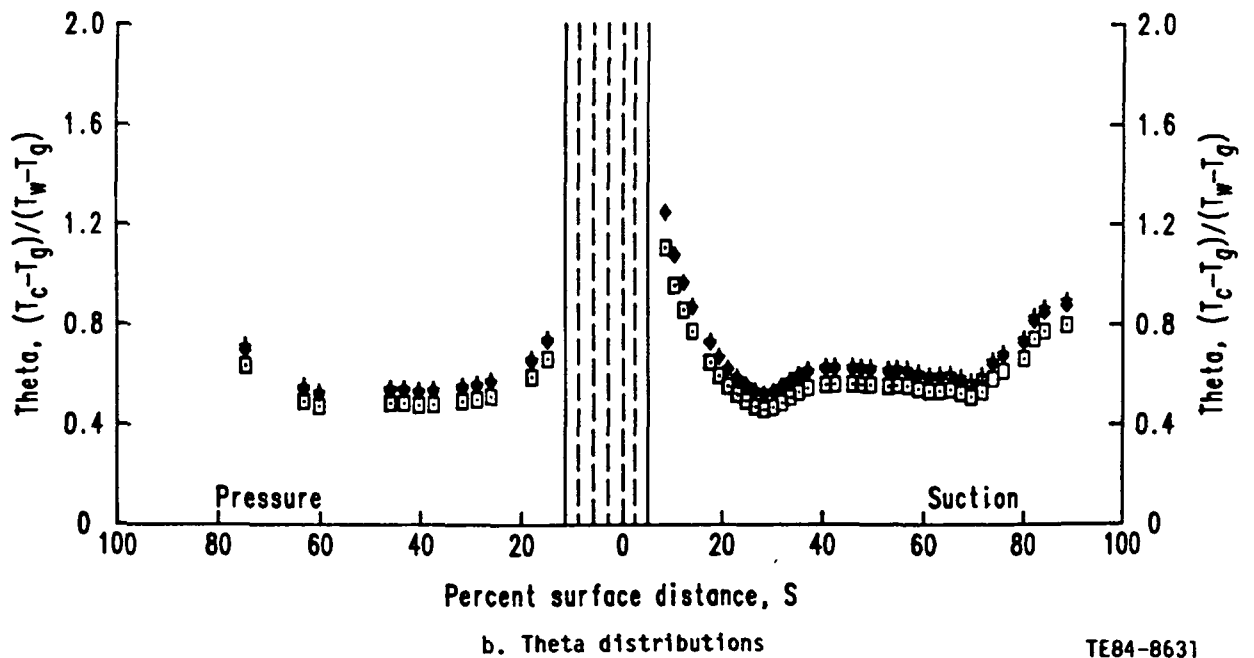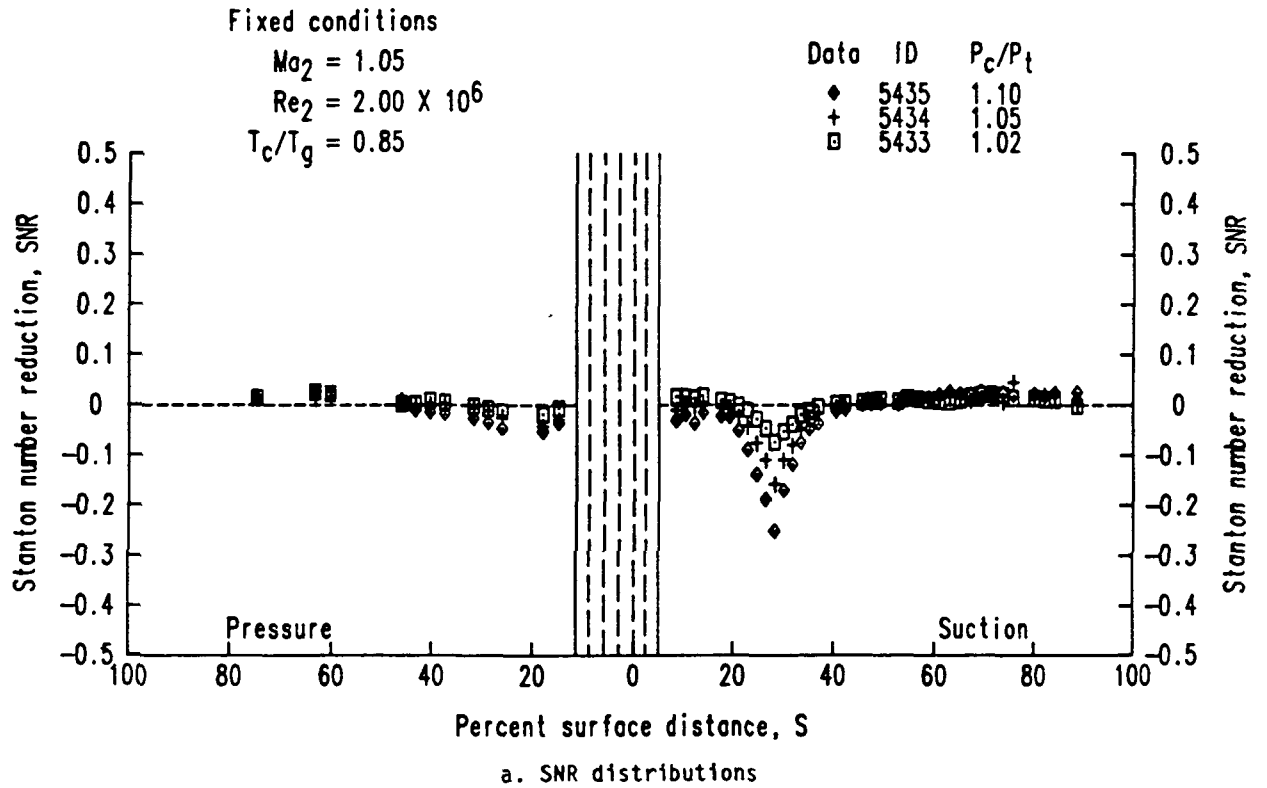Figure 63.   Effects of coolant to free-stream pressure ratio variation--
series 442X.
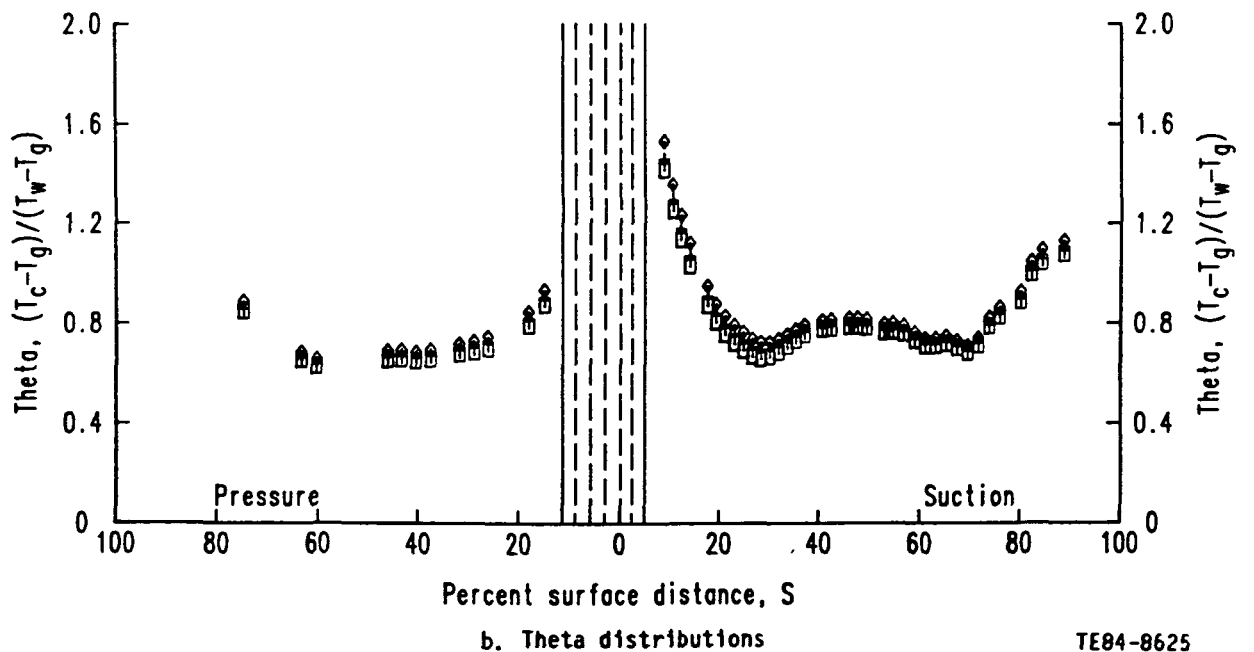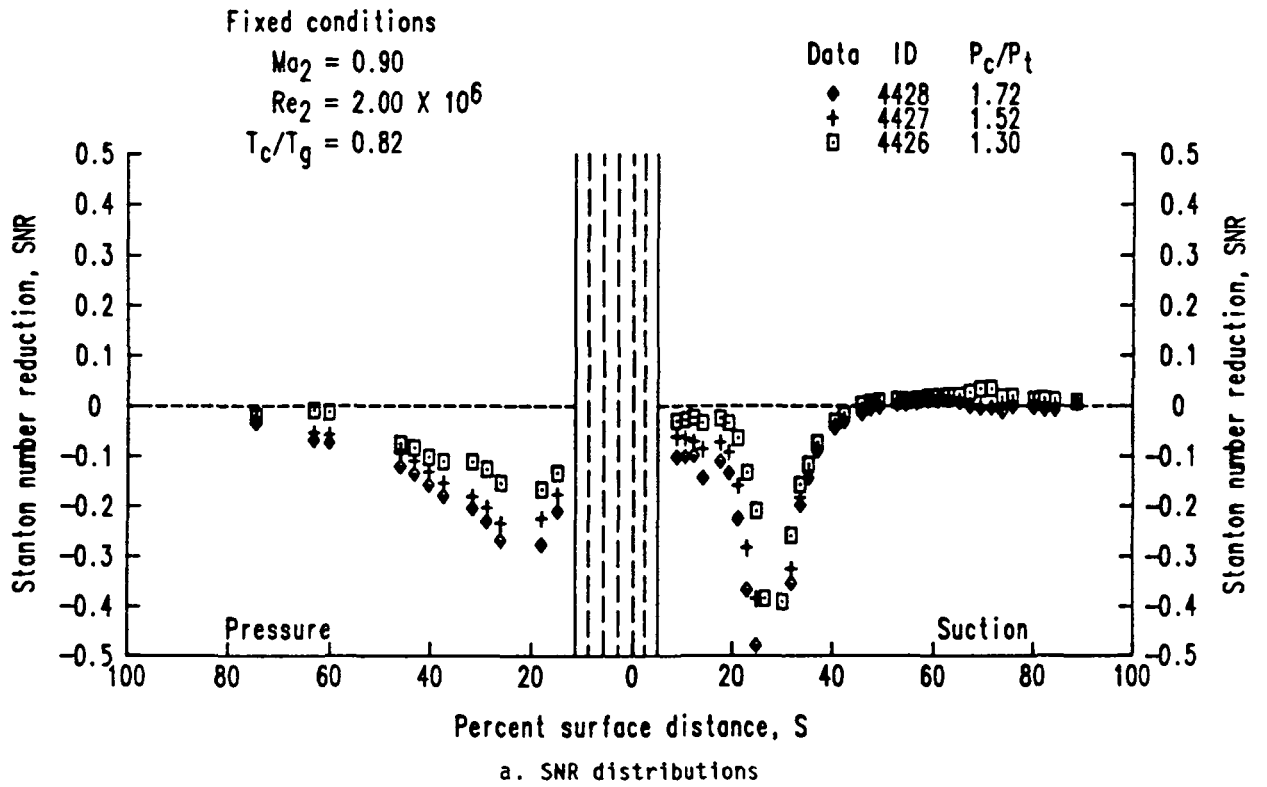
Figure 64. Effects of coolant to free-stream pressure ratio variation--
series 442X (higher blowing strengths).
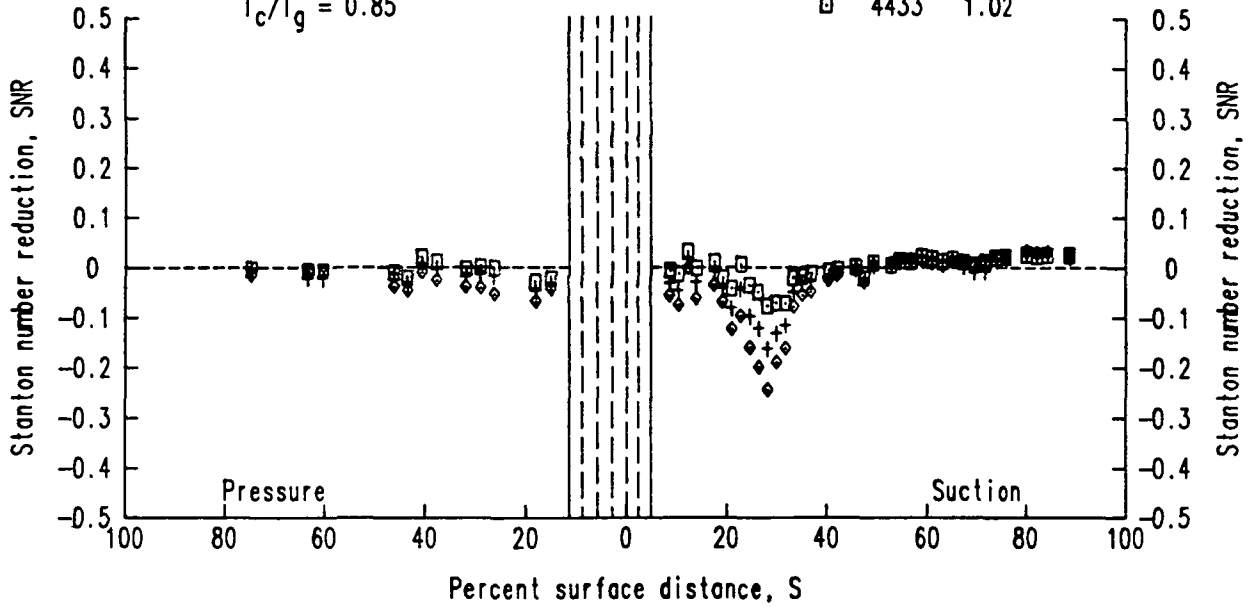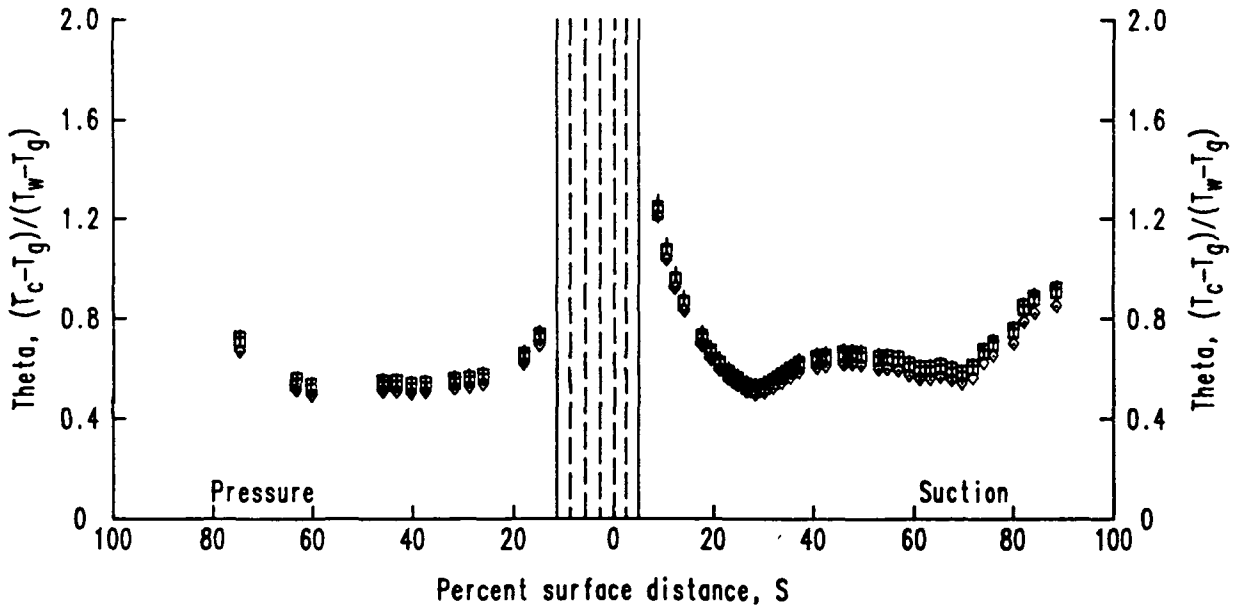
Figure 65. Effects of coolant to free-stream pressure ratio variation—series 443X.
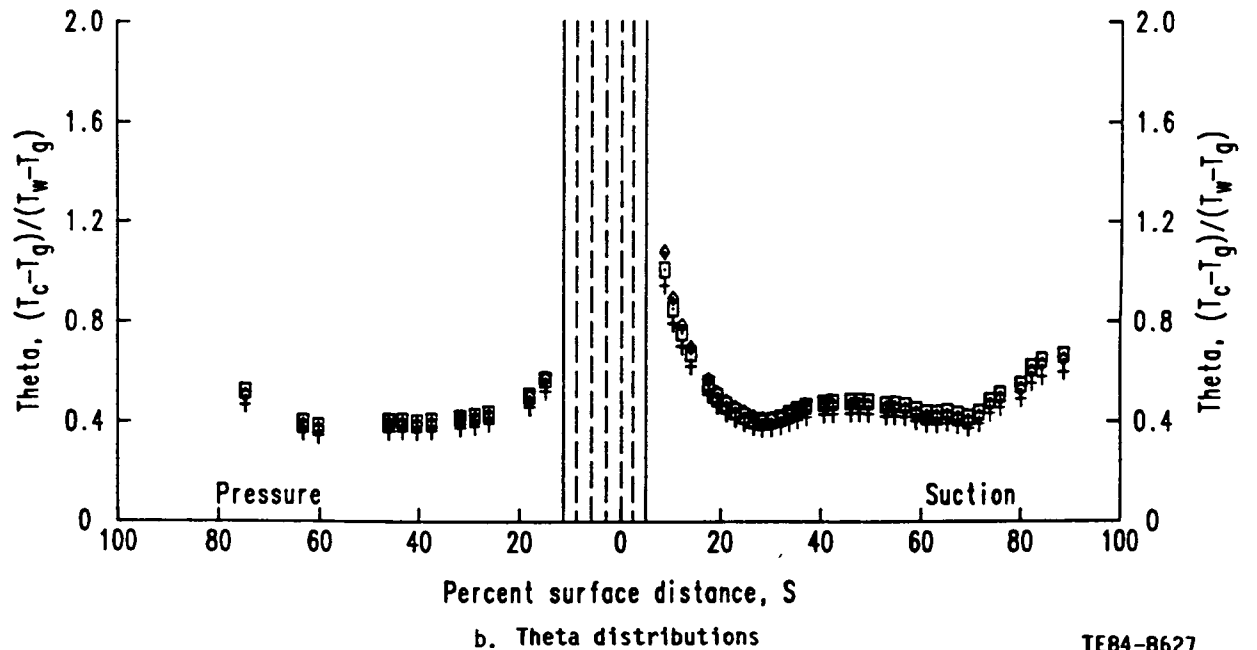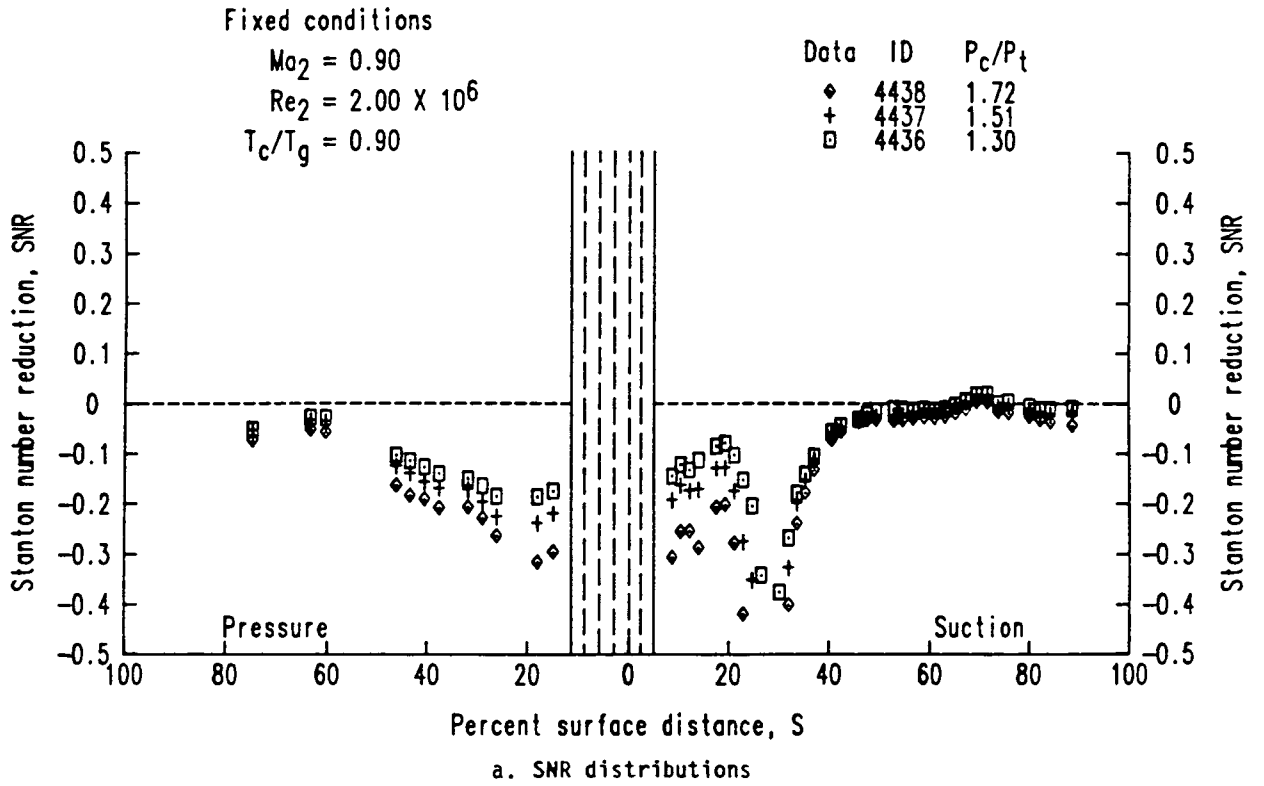
Figure 66. Effects of coolant to free-stream pressure ratio variation--
series 443X (higher blowing strength).
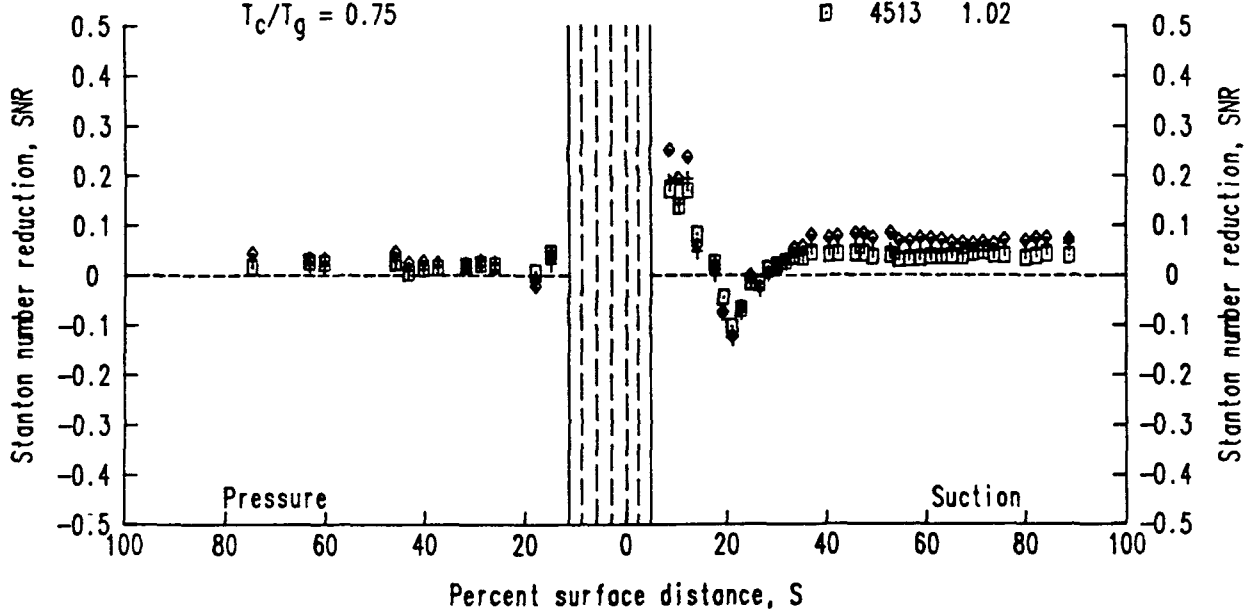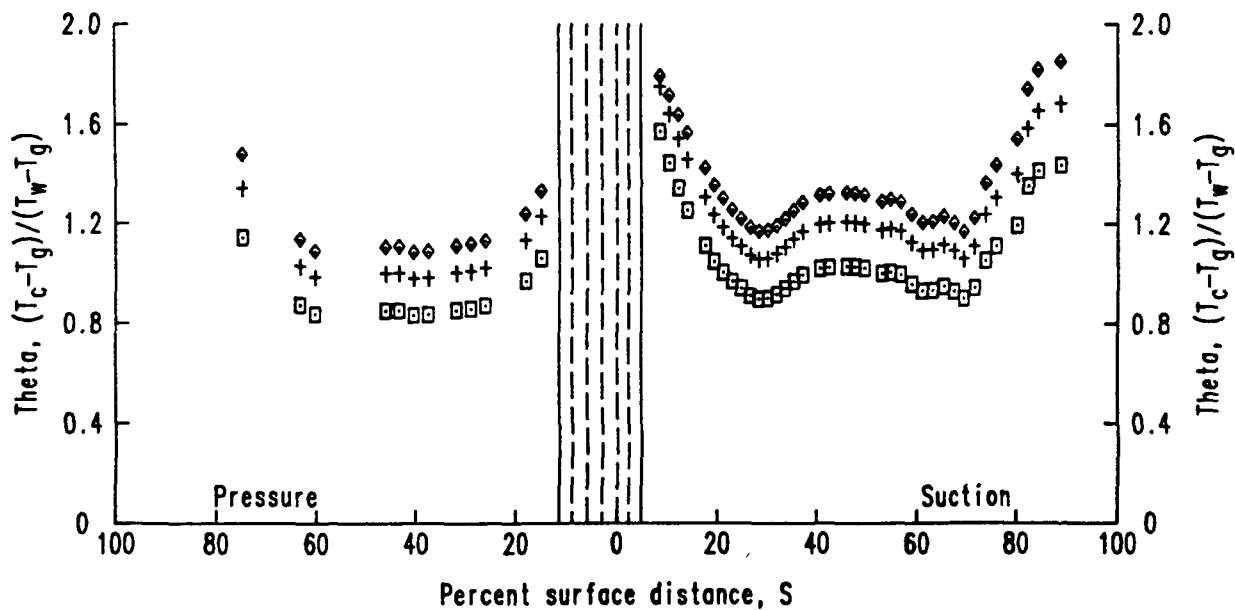
Figure 67. Effects of coolant to free-stream pressure ratio variation--
series 451X.

Fixed conditions
$Ma_2 = 0.89$
$Re_2 = 2.50 \times 10^6$
$T_c/T_g = 0.85$

Data ID P_c/P_t
4533 1.02

a. SNR distributions

b. Theta distributions

TE84-8629

Figure 68. Effects of coolant to free-stream pressure ratio variation—series 453X.

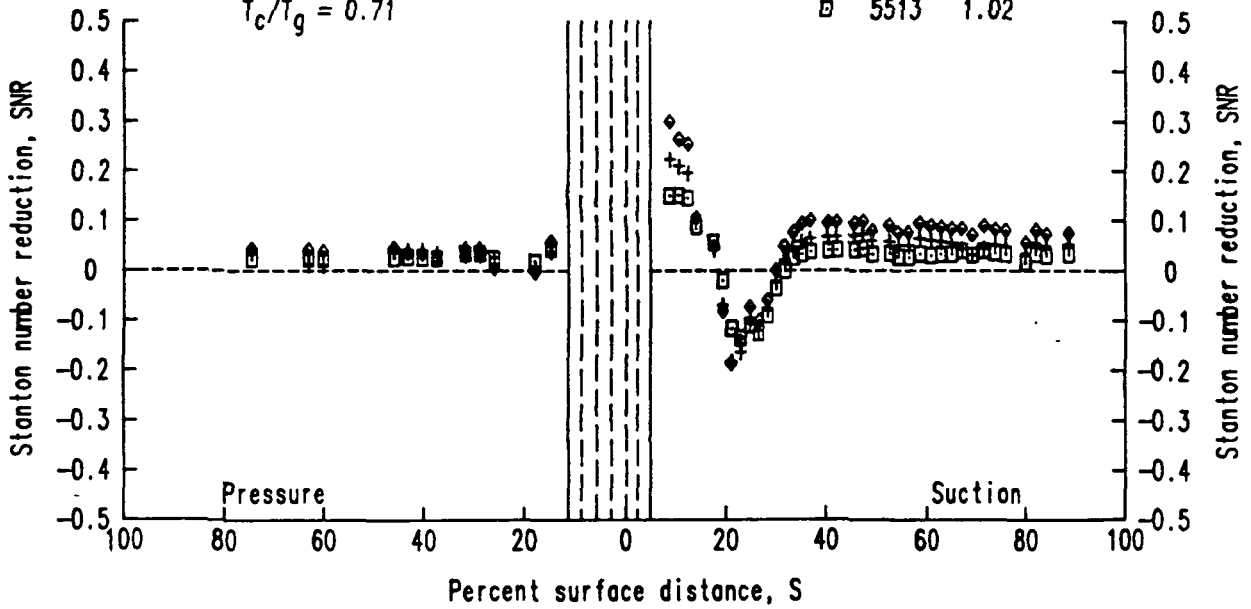Figure 69. Effects of coolant to free-stream pressure ratio variation—
series 541X.

Fixed conditions
$Ma_2 = 1.05$
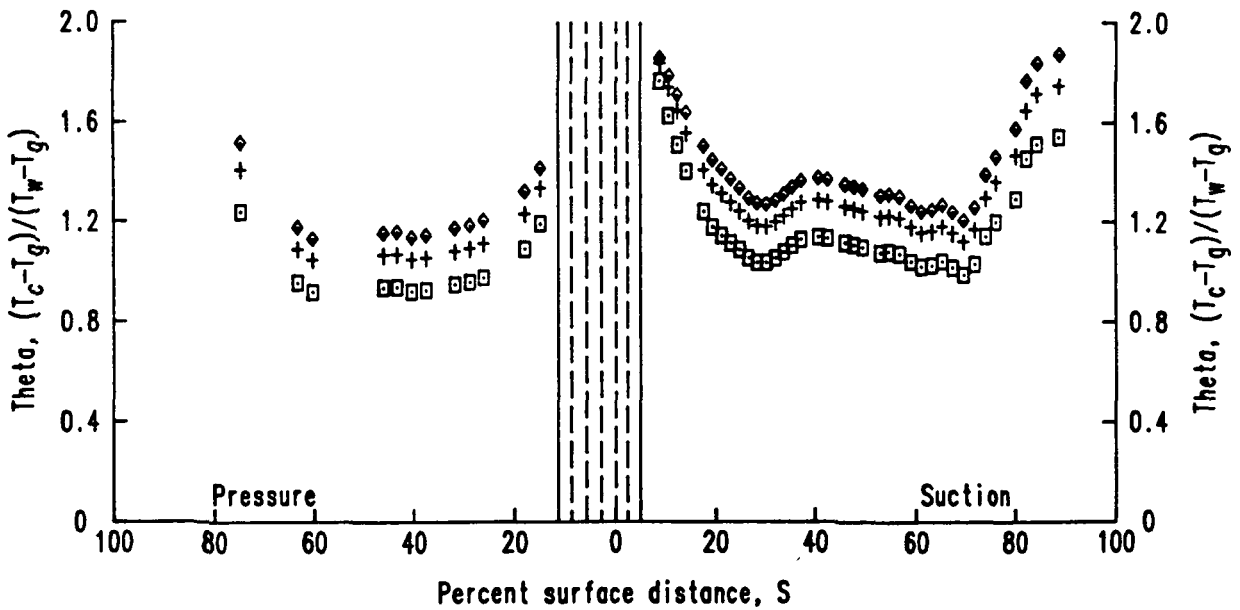$Re_2 = 2.00 \times 10^6$
$T_c/T_g = 0.85$

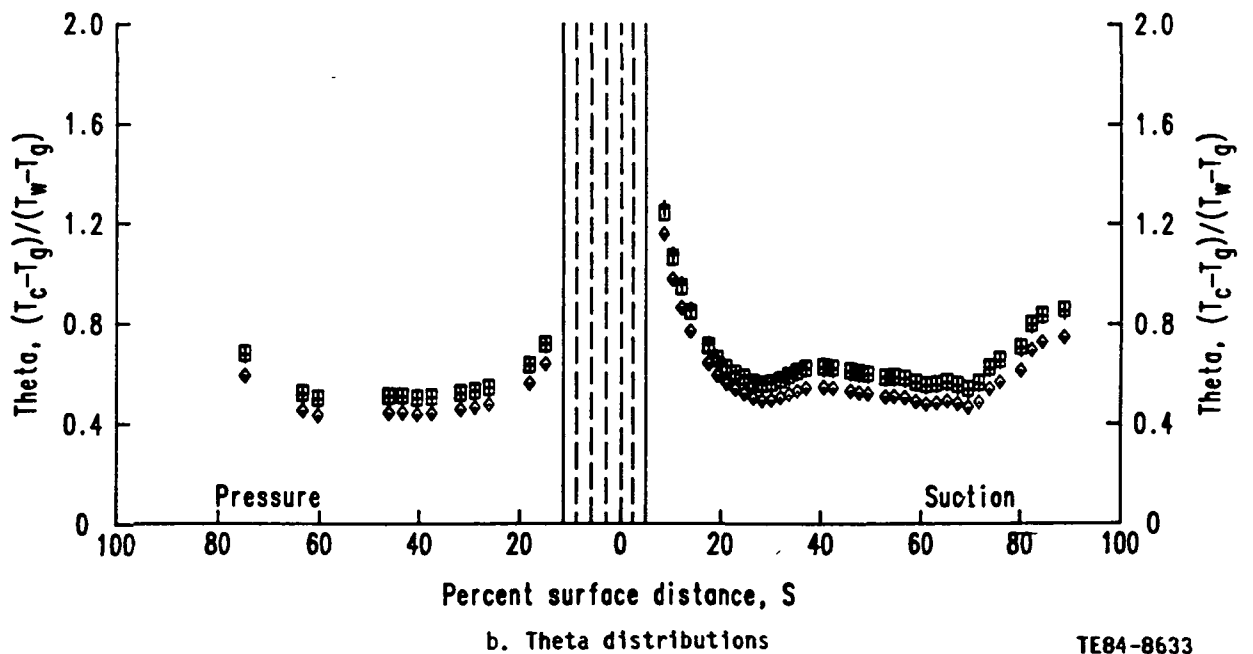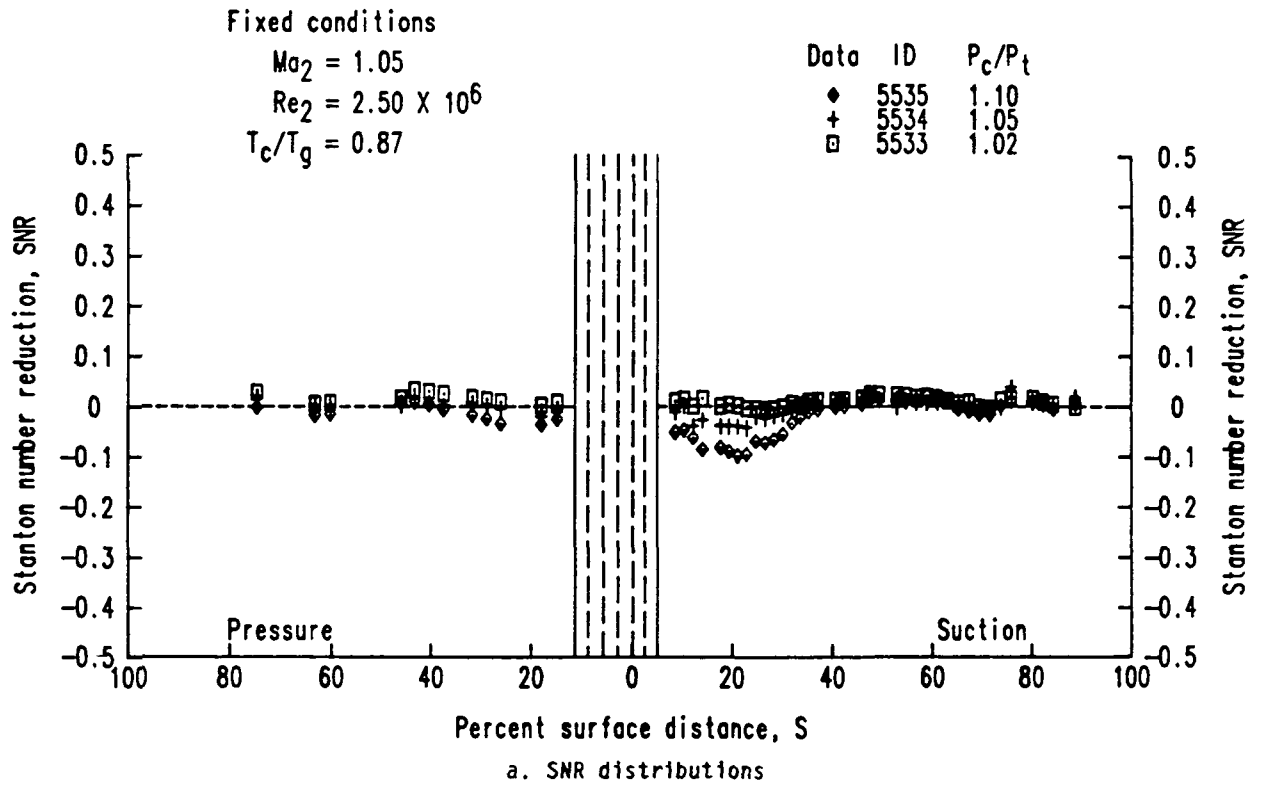| Data	ID	P_c/P_t
◆	5435	1.10
+	5434	1.05
▫	5433	1.02

a. SNR distributions

b. Theta distributions

TE84-8631

Figure 70. Effects of coolant to free-stream pressure ratio variation--
series 543X.

Figure 71. Effects of coolant to free-stream pressure ratio variation—
series 551X.

Figure 72. Effects of coolant to free-stream pressure ratio variation--
series 553X.
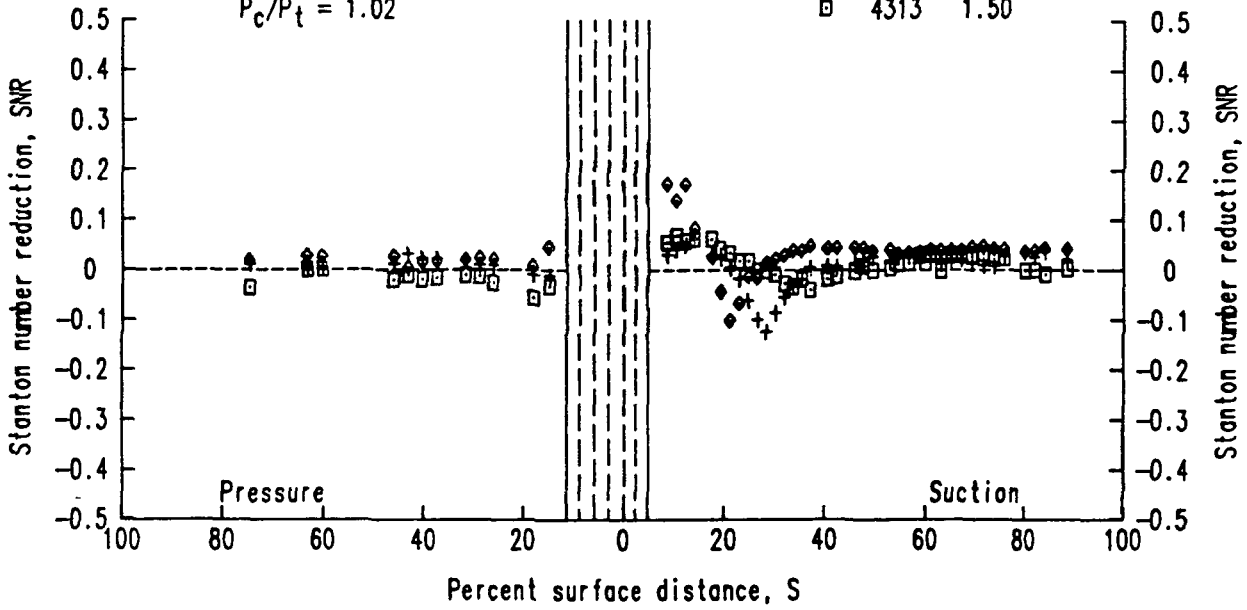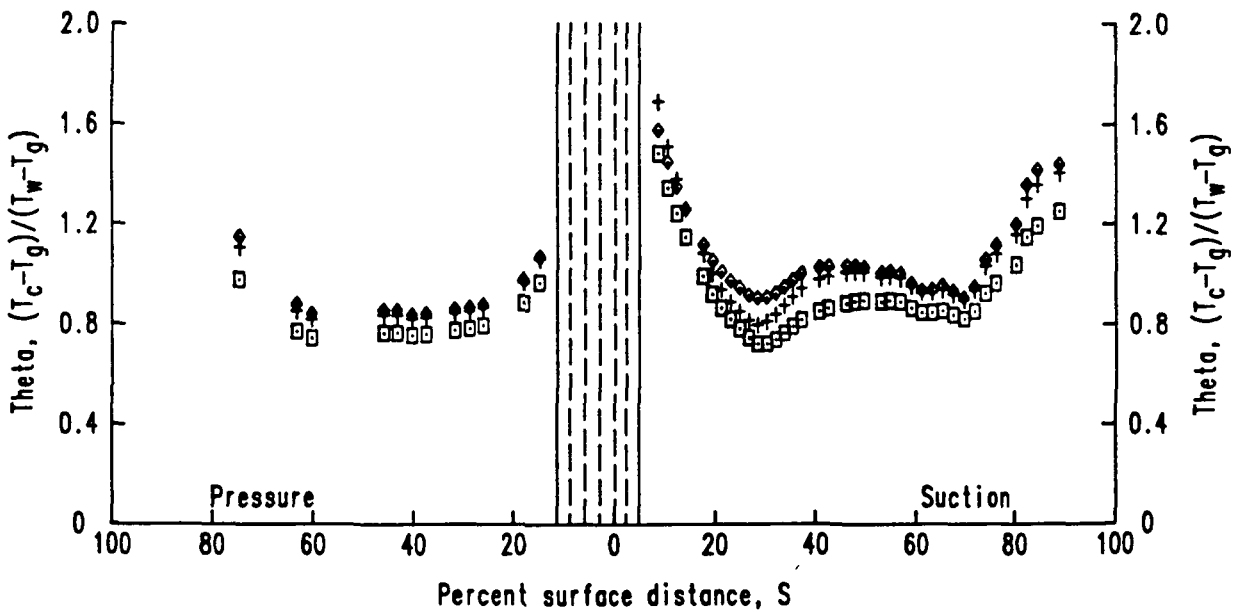
Figure 73. Effects of exit Reynolds number variation--series 4X13.

Fixed conditions

$Ma_2 = 0.89$

$T_c/T_g = 0.73$

$P_c/P_t = 1.05$

Data	ID	$Re_2 \times 10^{-6}$
♦	4514	2.48
+	4414	1.98
▣	4314	1.50

a. SNR distributions

b. Theta distributions

TE84-8635

Figure 74. Effects of exit Reynolds number variation—series 4X14.

162

Figure 75. Effects of exit Reynolds number variation—series 4X15.
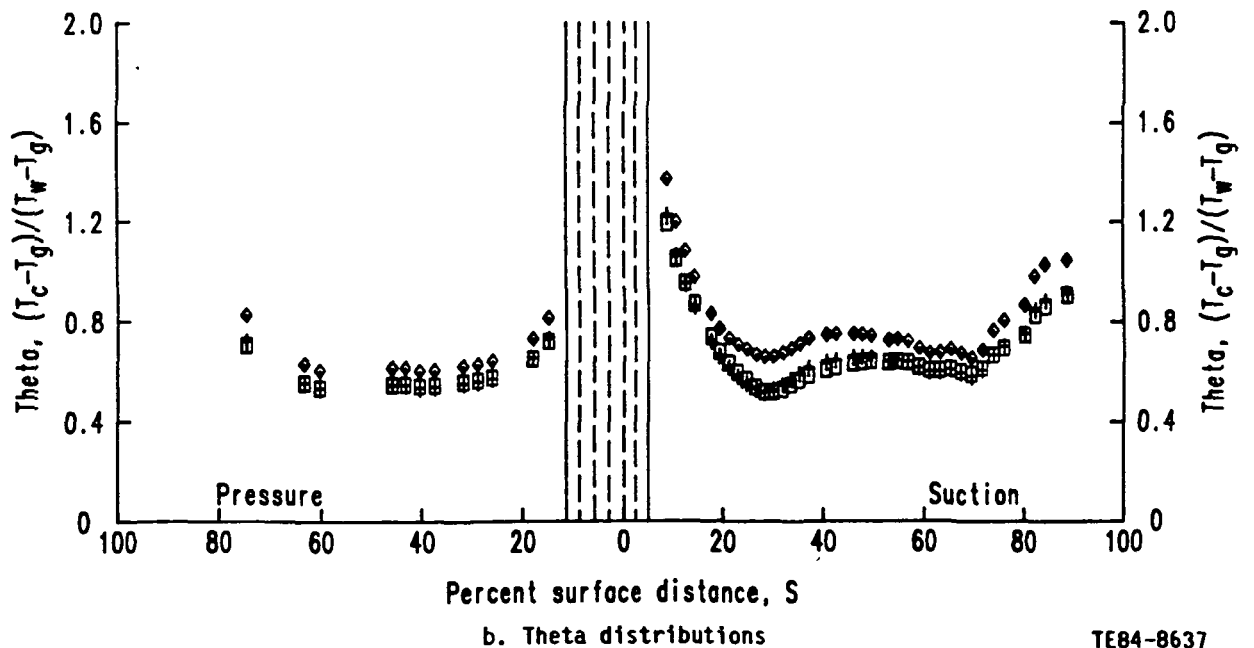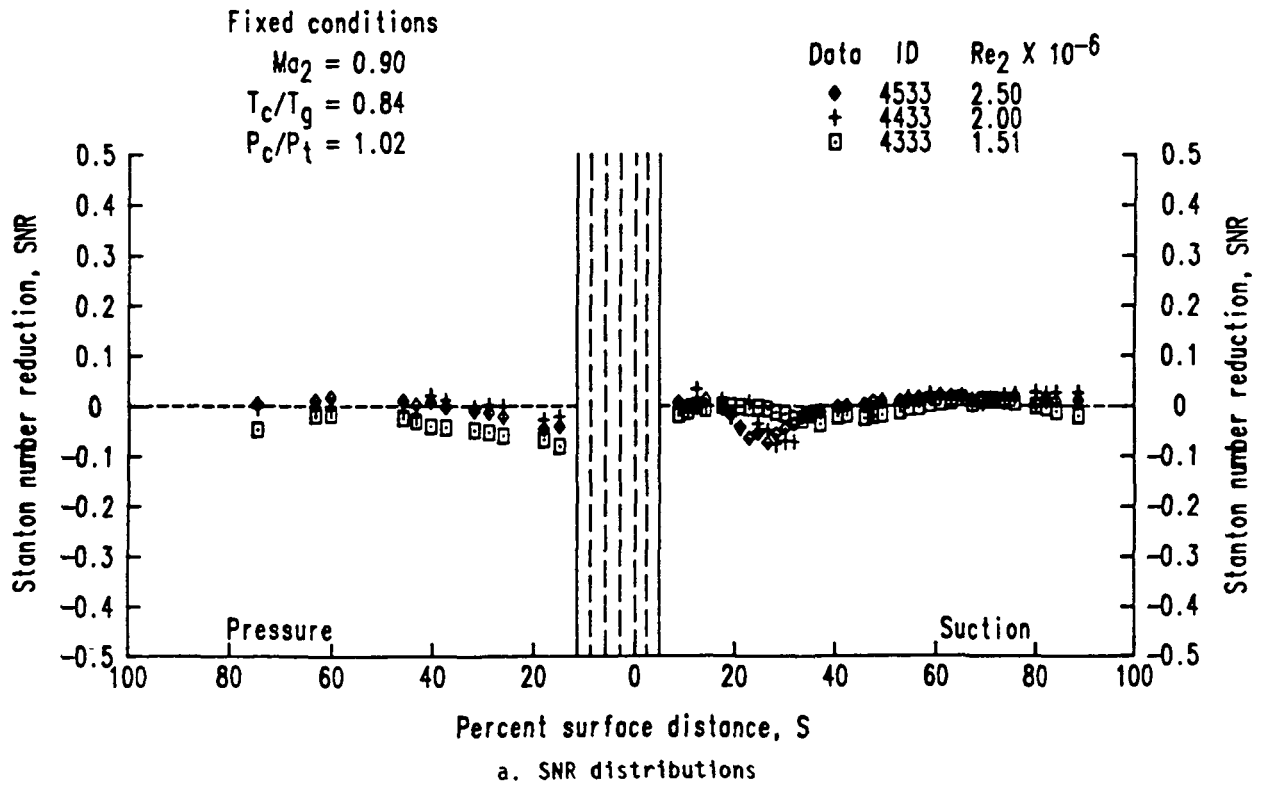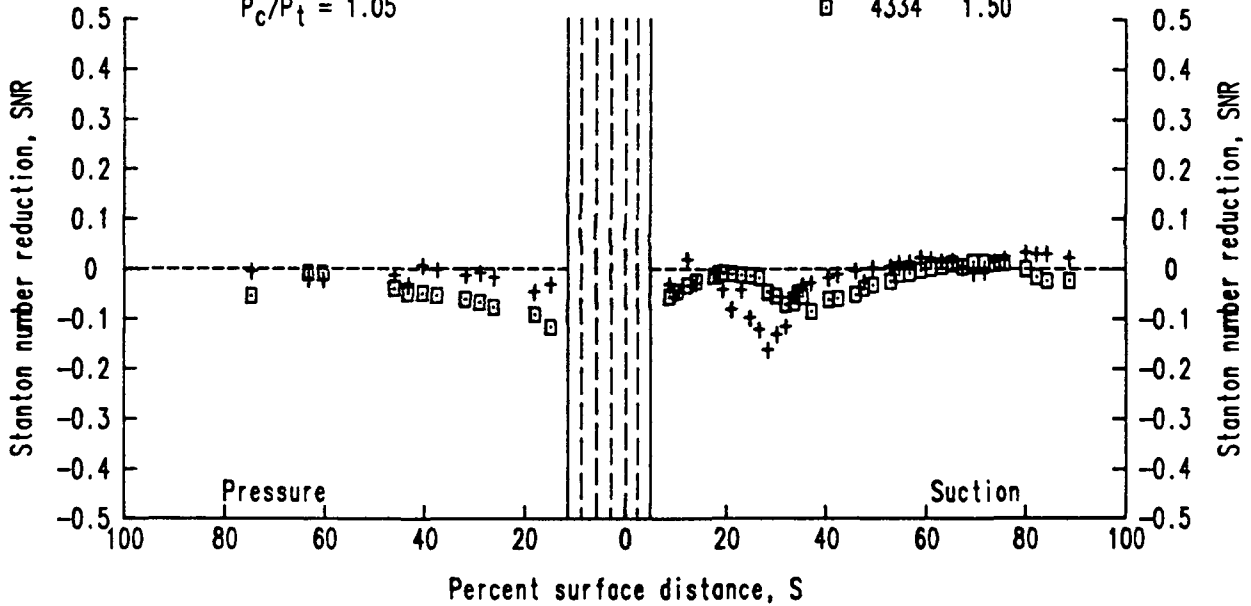
Figure 76. Effects of exit Reynolds number variation—series 4X33.
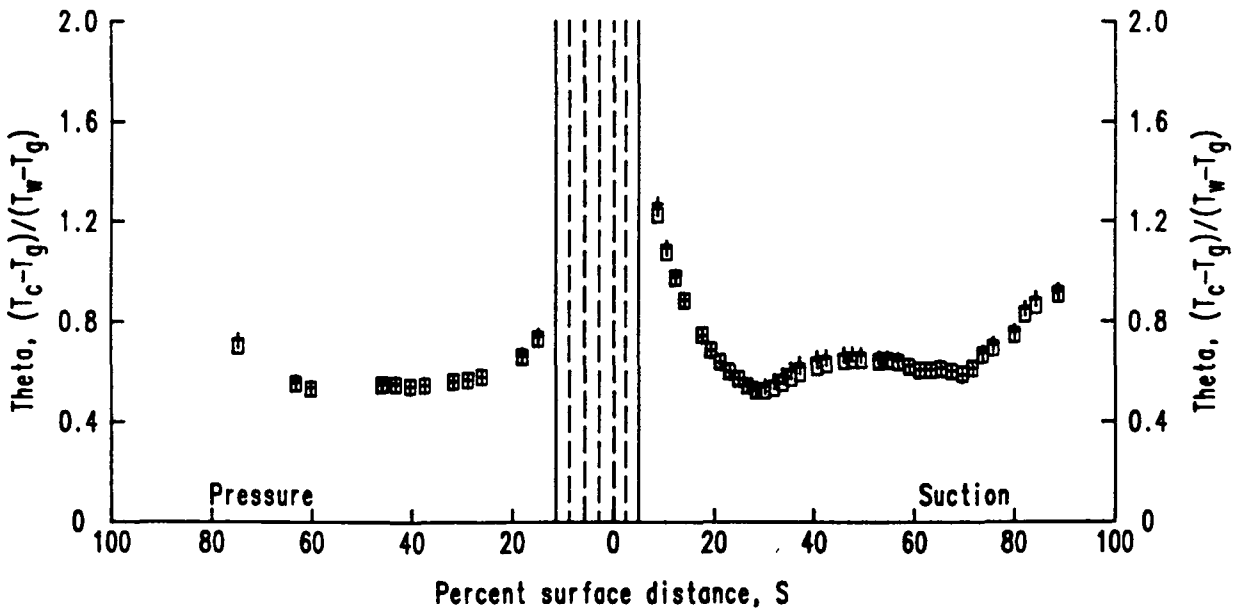
Figure 77. Effects of exit Reynolds number variation—series 4X34.
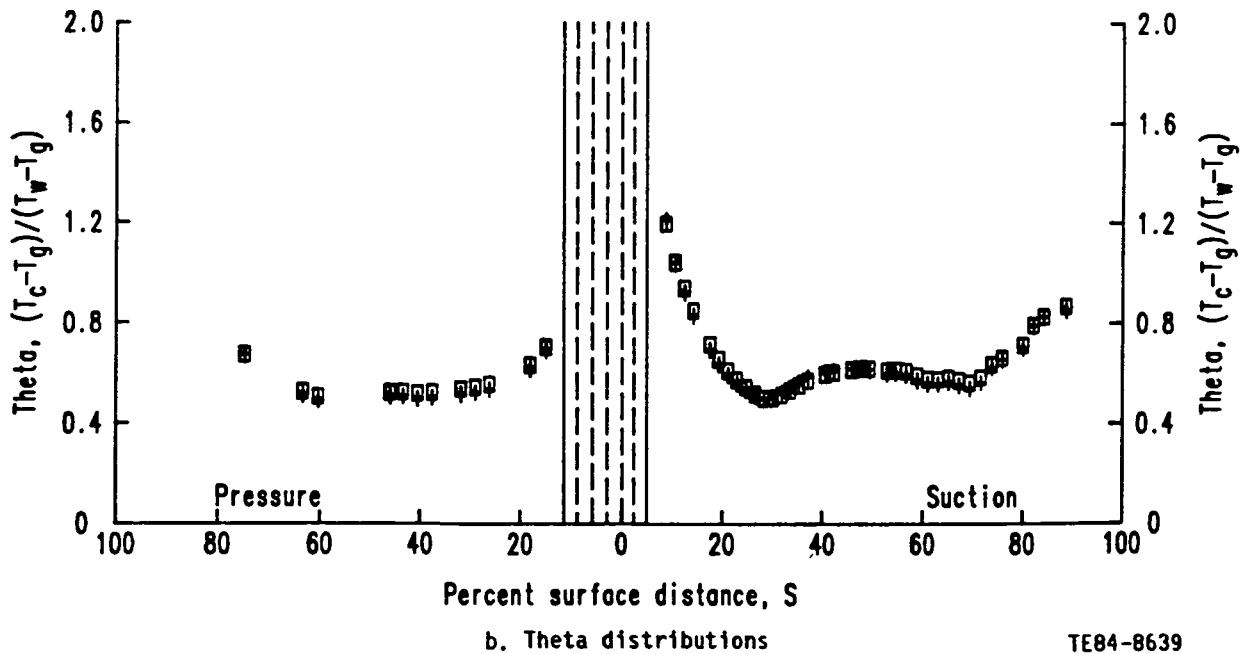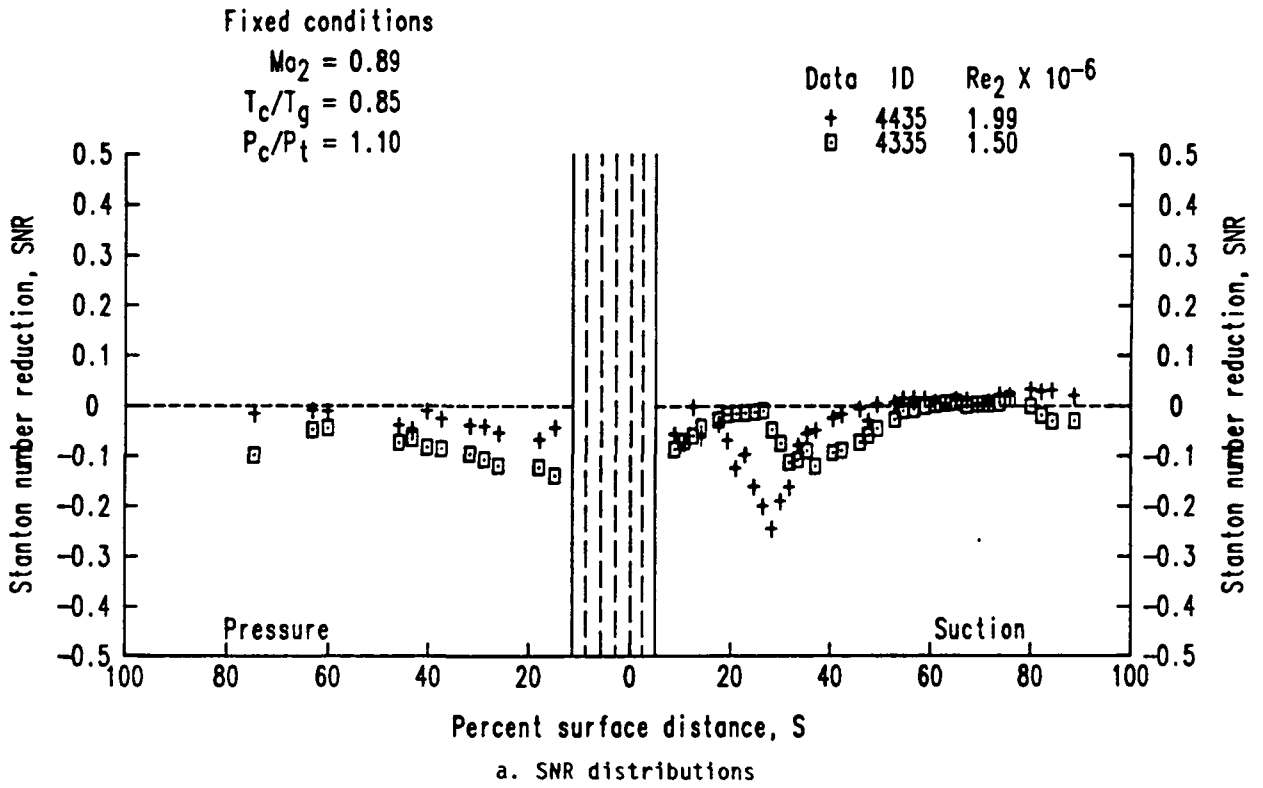
Figure 78.   Effects of exit Reynolds number variation—series 4X35.
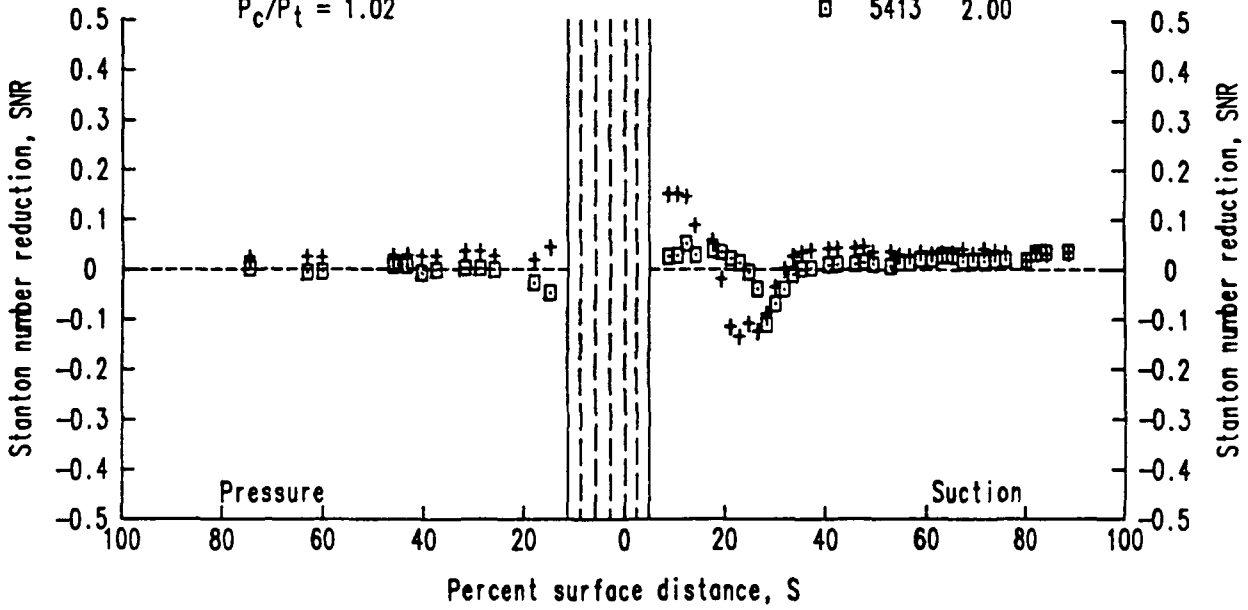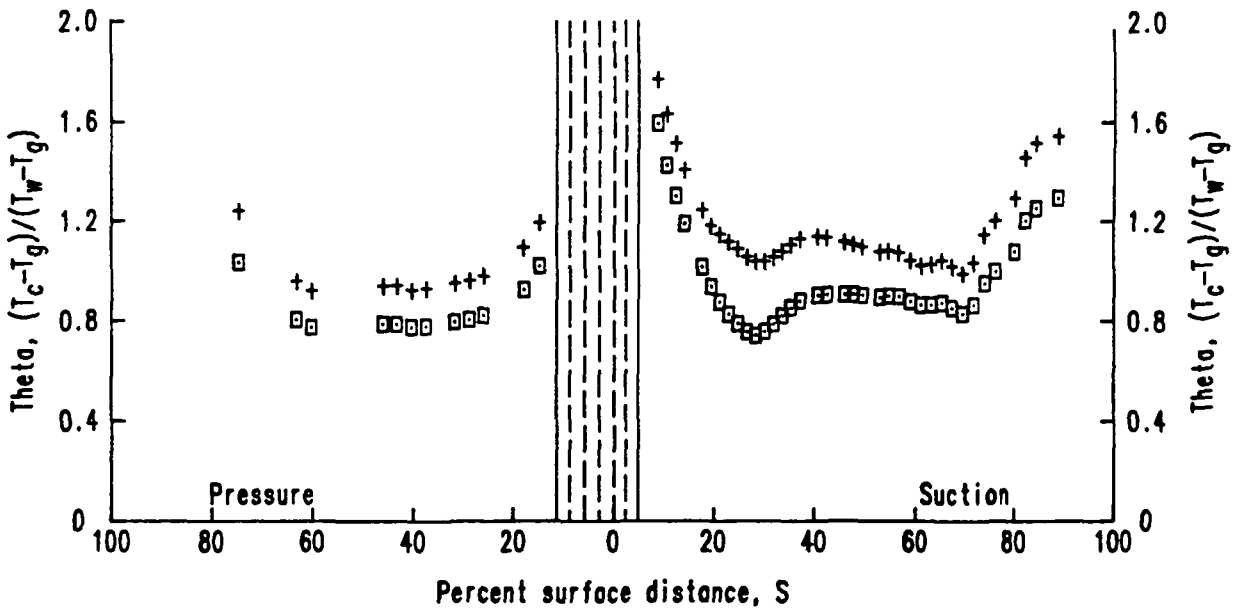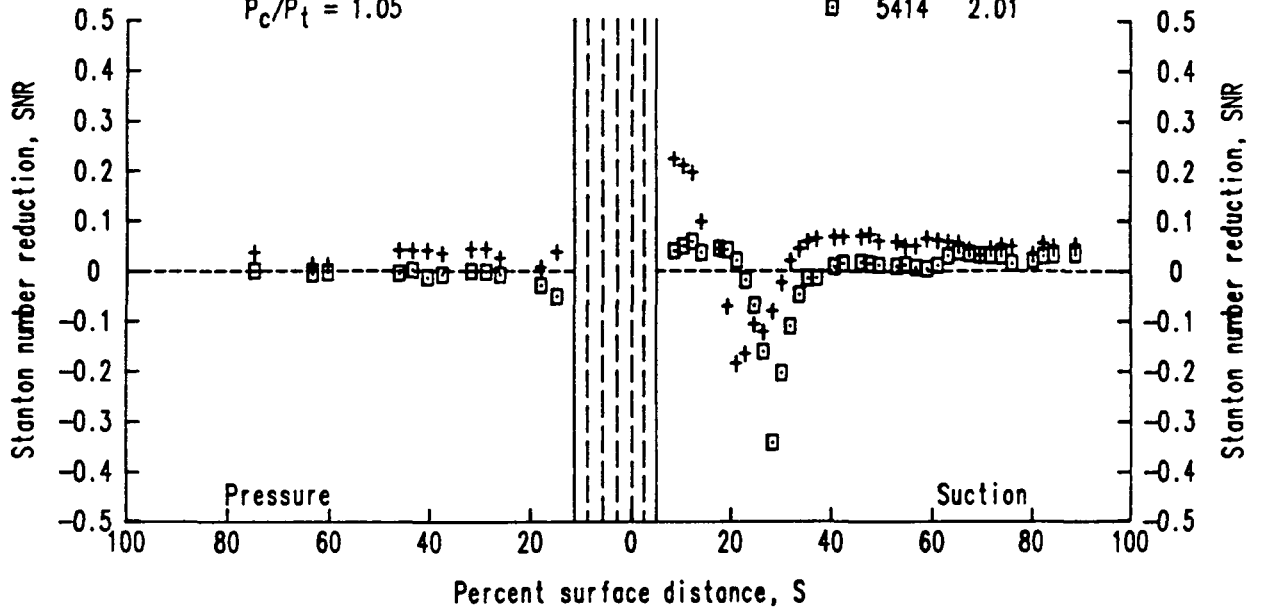
Figure 79.   Effects of exit Reynolds number variation—series 5X13.
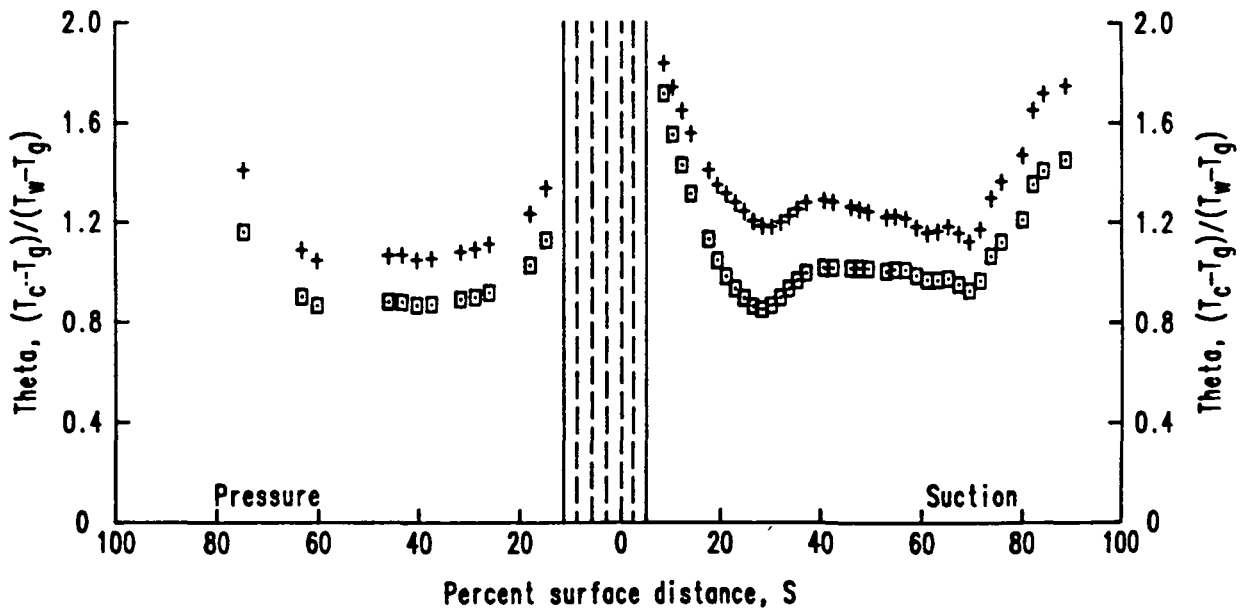
Figure 80. Effects of exit Reynolds number variation—series 5X14.
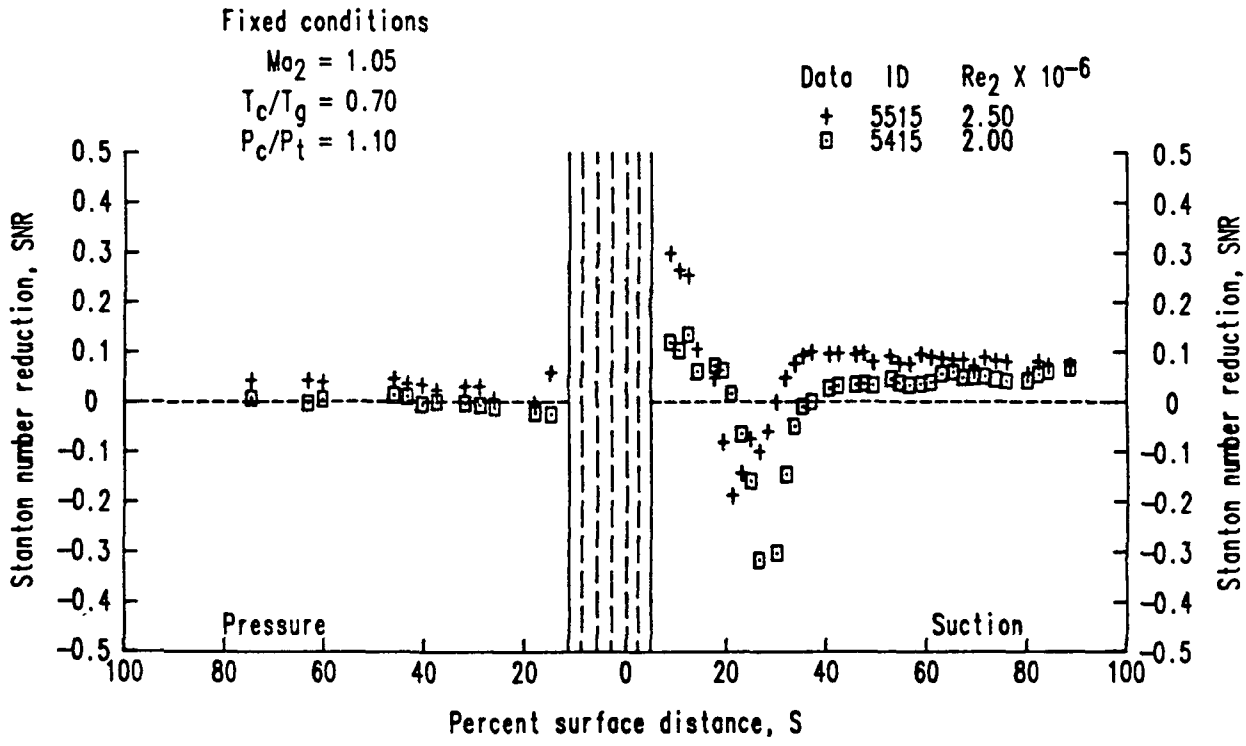
a. SNR distributions
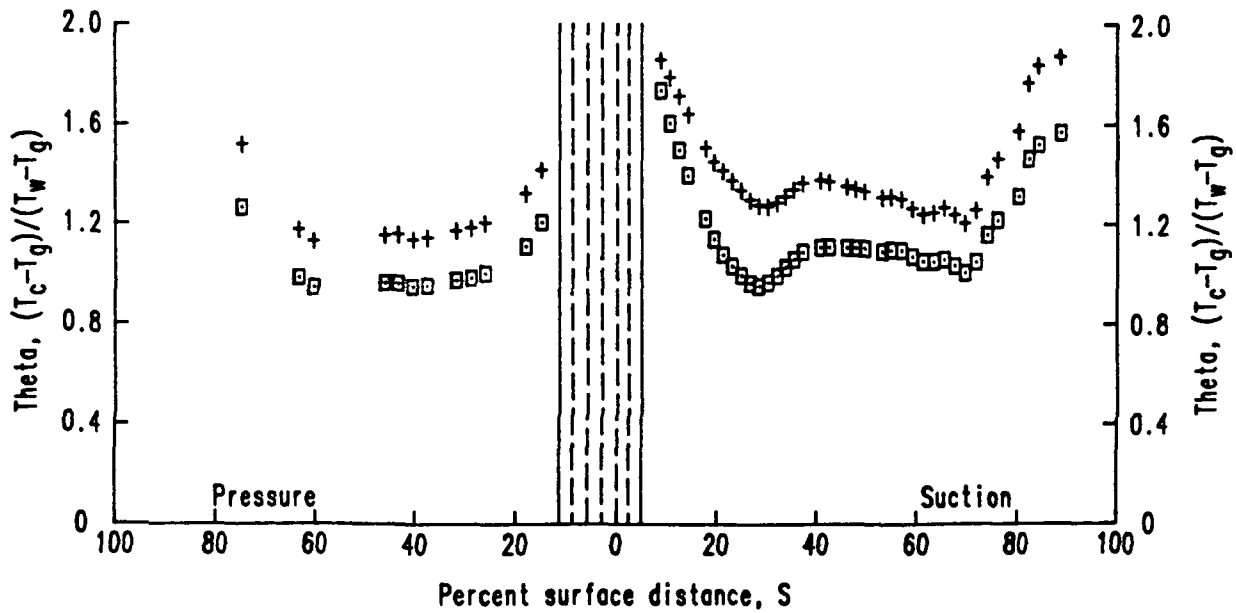
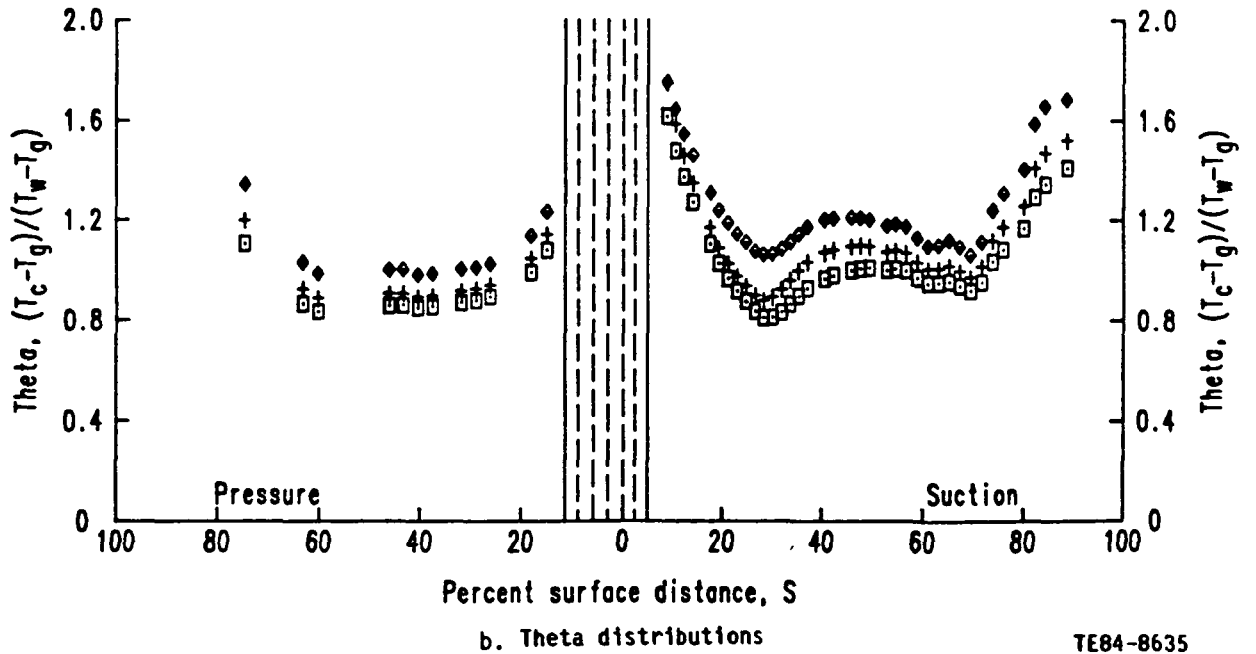b. Theta distributions

TE84-8642

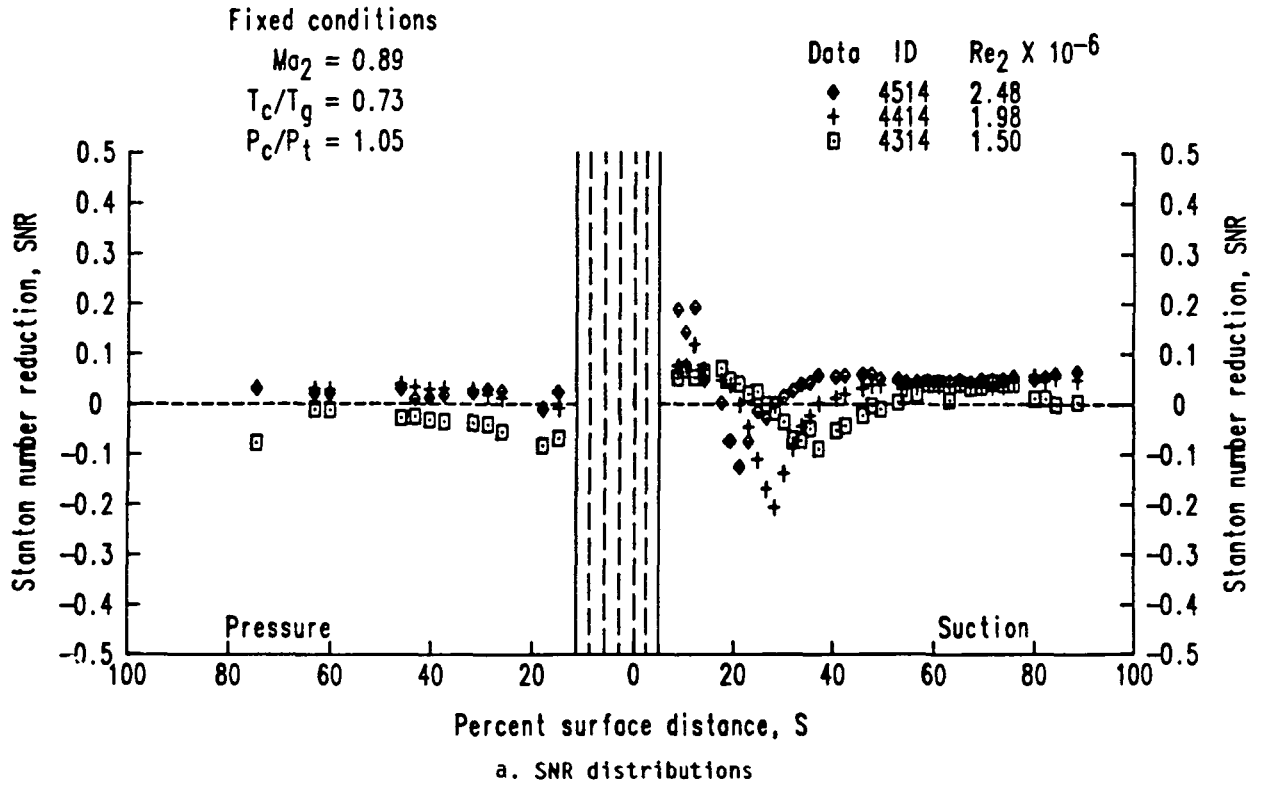Figure 81. Effects of exit Reynolds number variation--series 5X15.

a. SNR distributions

b. Theta distributions
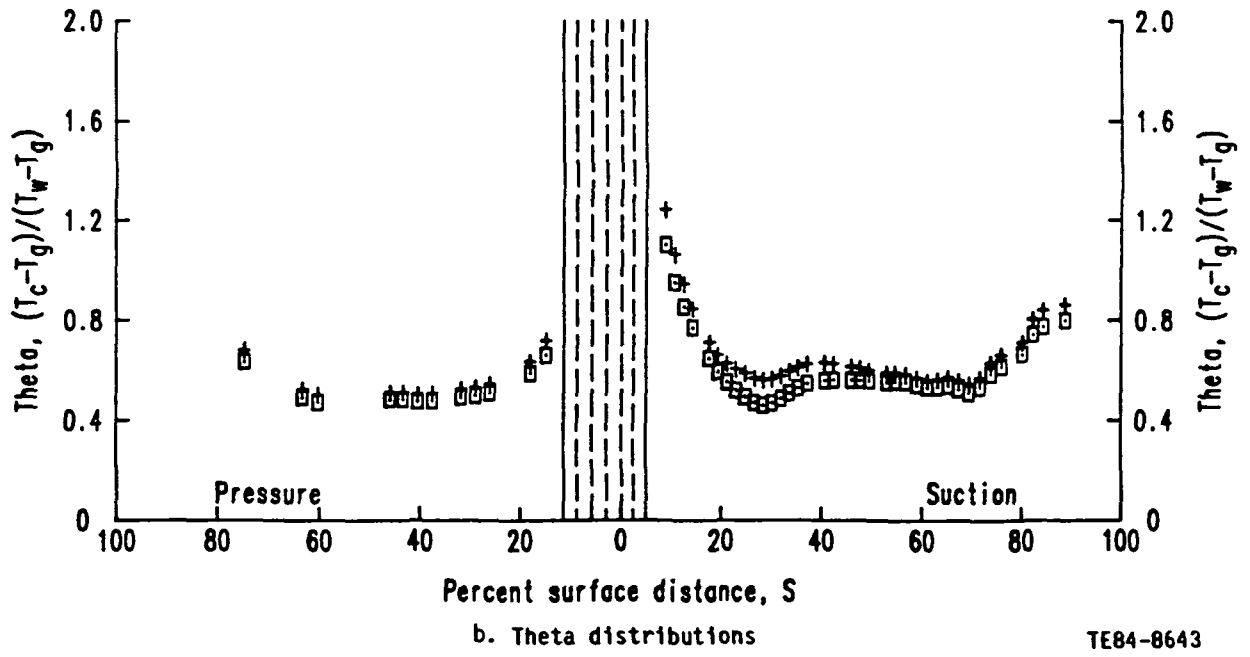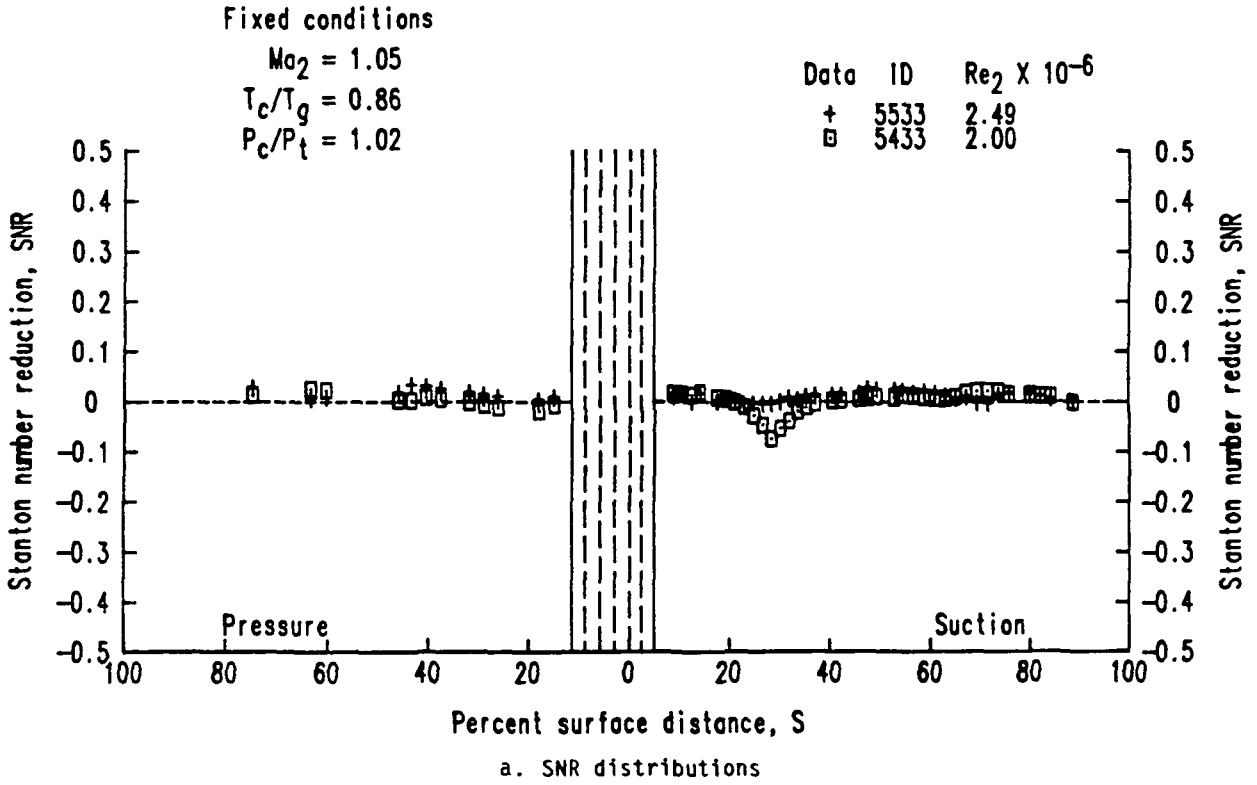
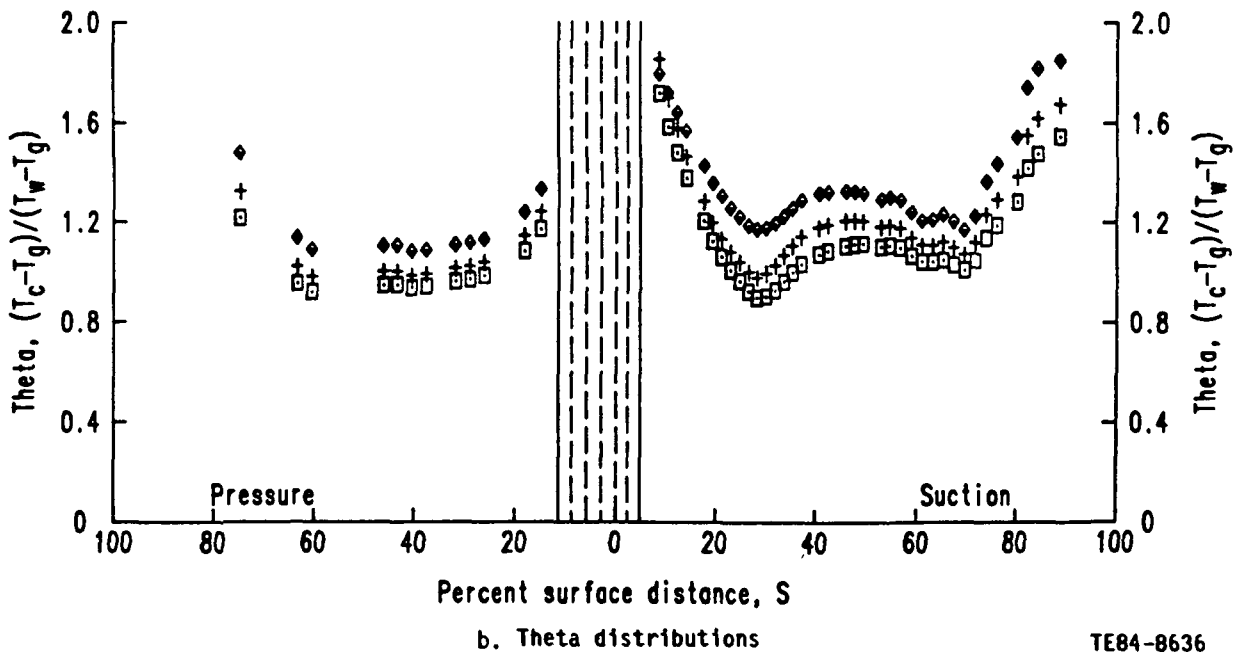TE84-8643

Figure 82. Effects of exit Reynolds number variation--series 5X33.
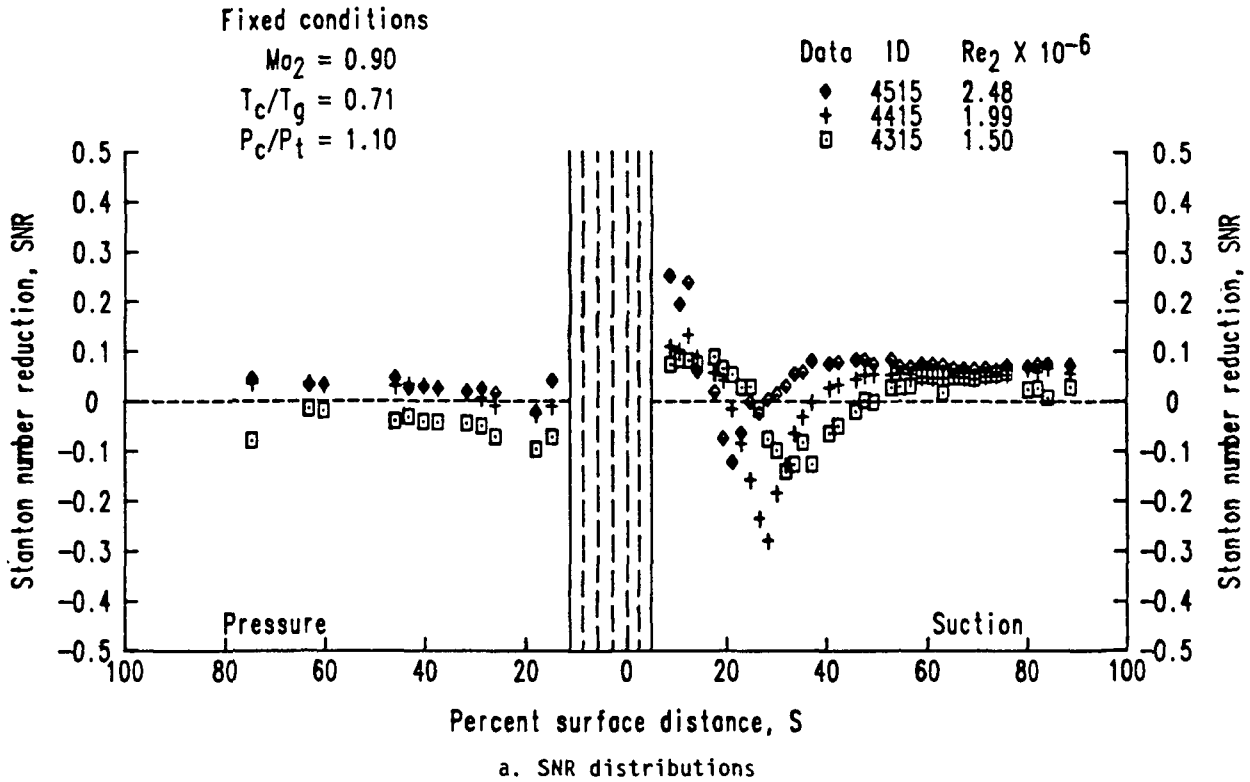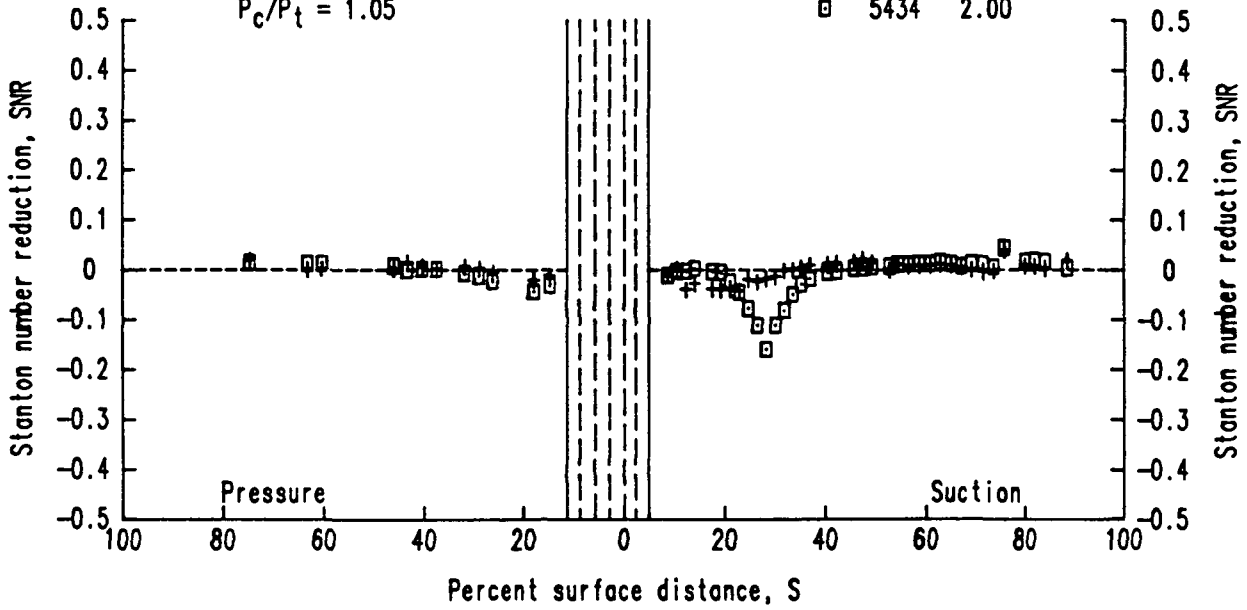
Figure 83. Effects of exit Reynolds number variation—series 5X34.
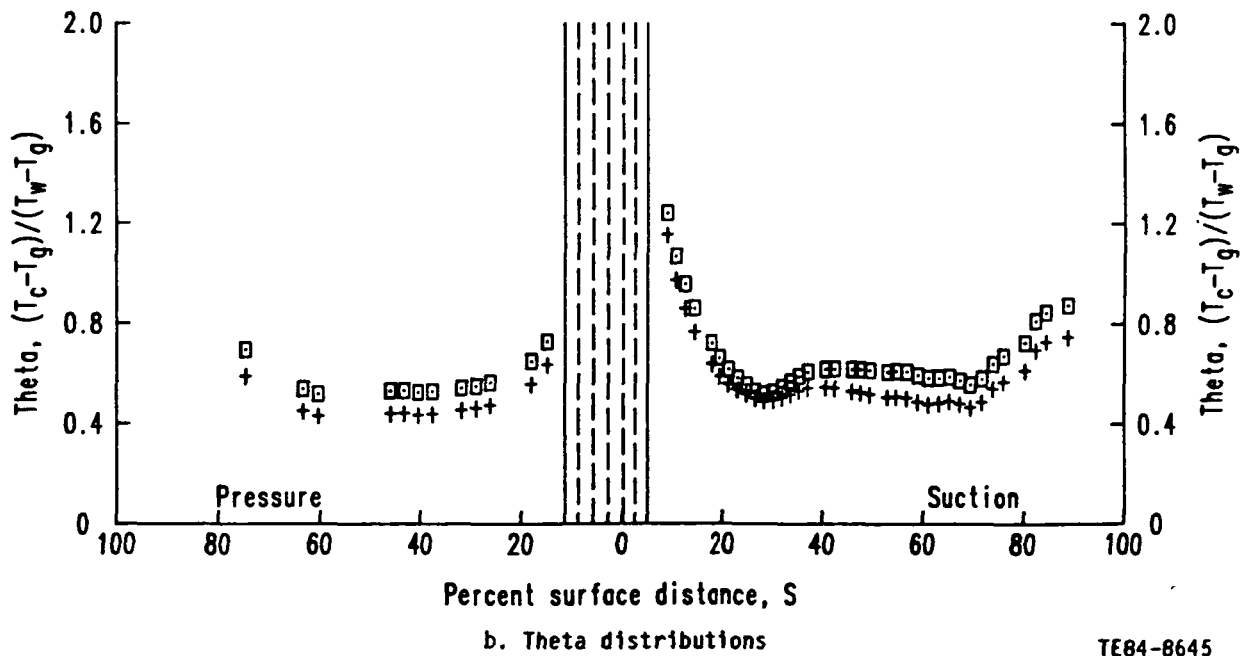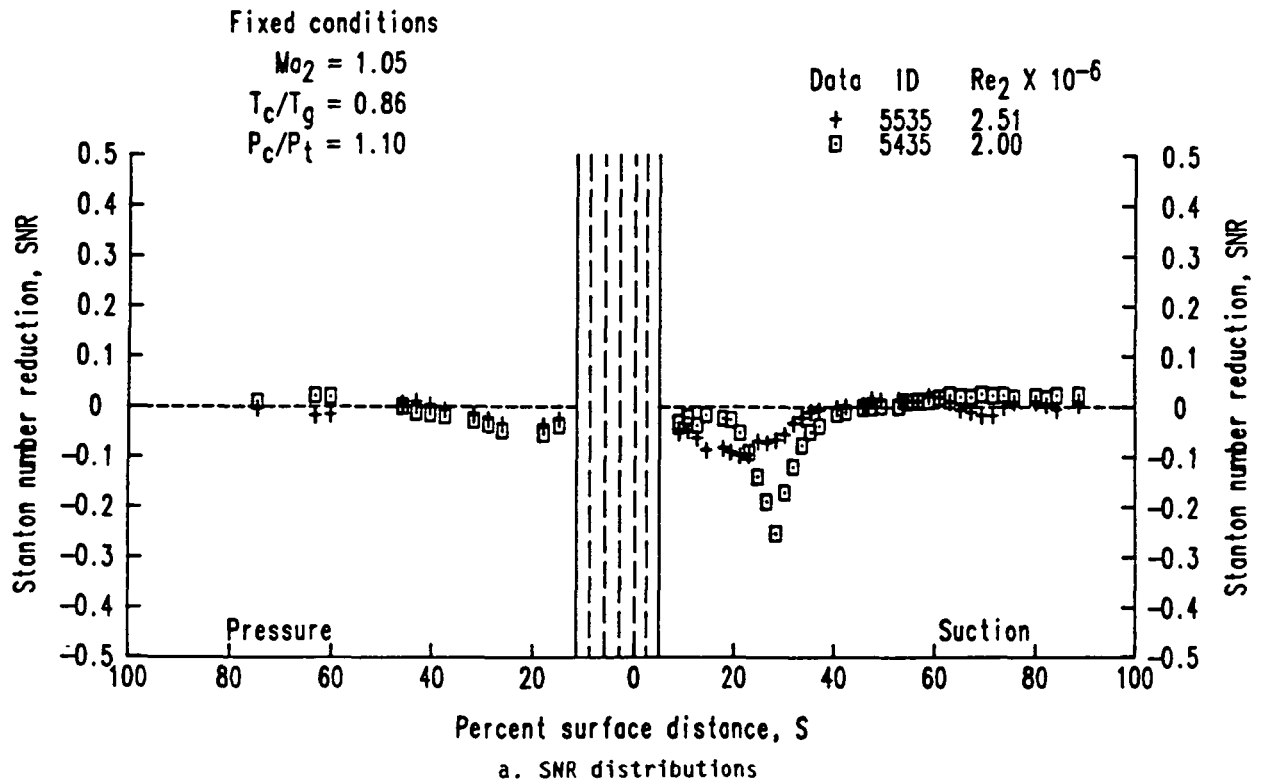
Figure 84.   Effects of exit Reynolds number variation—series 5X35.

Figure 85.   Effects of exit Mach number variation—series X413.
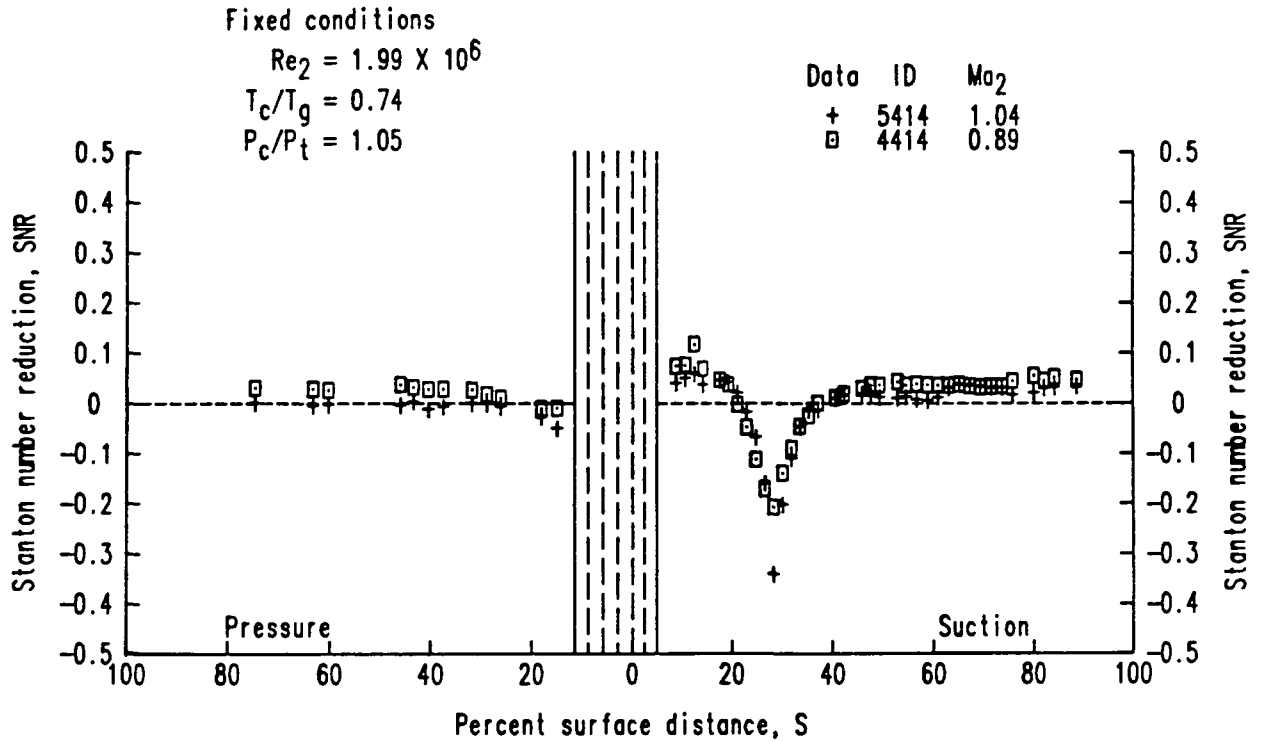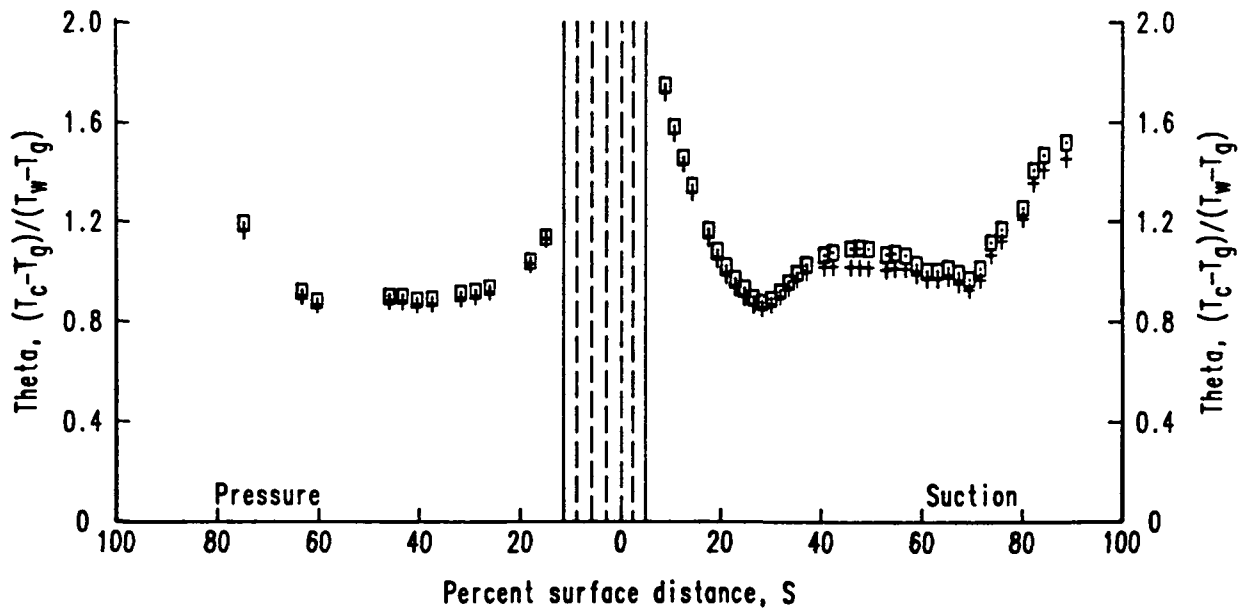
Figure 86. Effects of exit Mach number variation—series X414.

Figure 87. Effects of exit Mach number variation—series X415.

TE84-8648

Fixed conditions
$Re_2 = 2.00 \times 10^6$
$T_c/T_g = 0.85$
$P_c/P_t = 1.02$

Data	ID	Ma_2
+	5433	1.05
□	4433	0.89

a. SNR distributions

b. Theta distributions
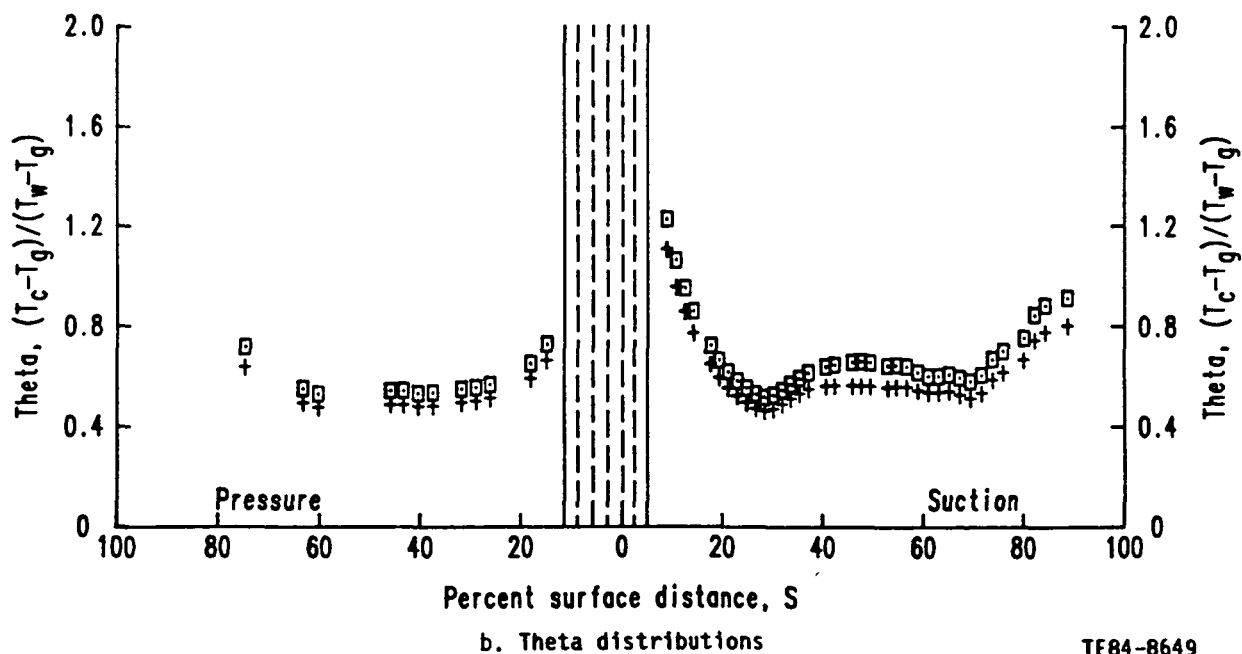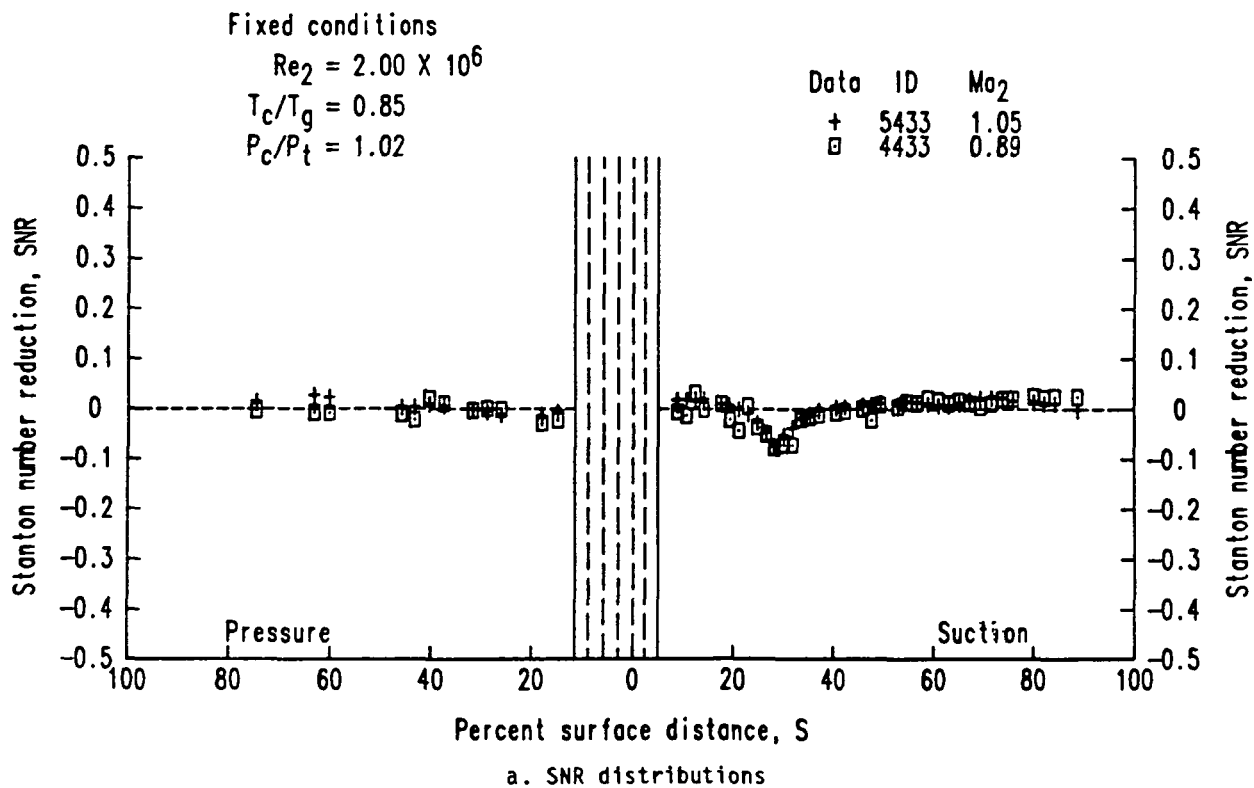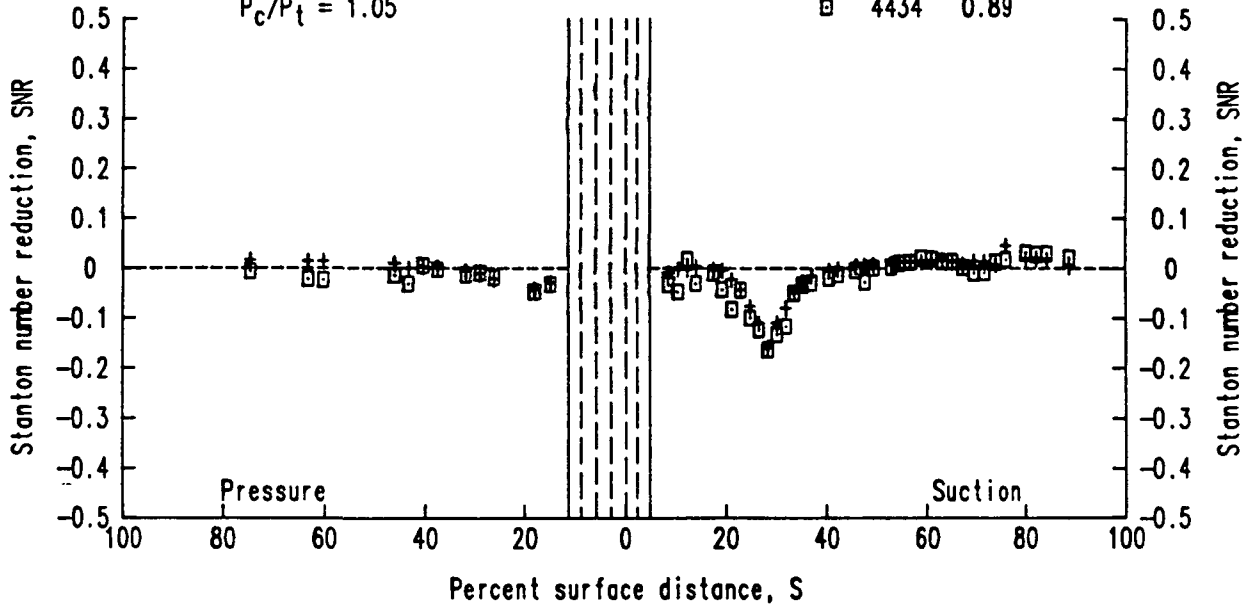
TE84-8649

Figure 88. Effects of exit Mach number variation--series X433.
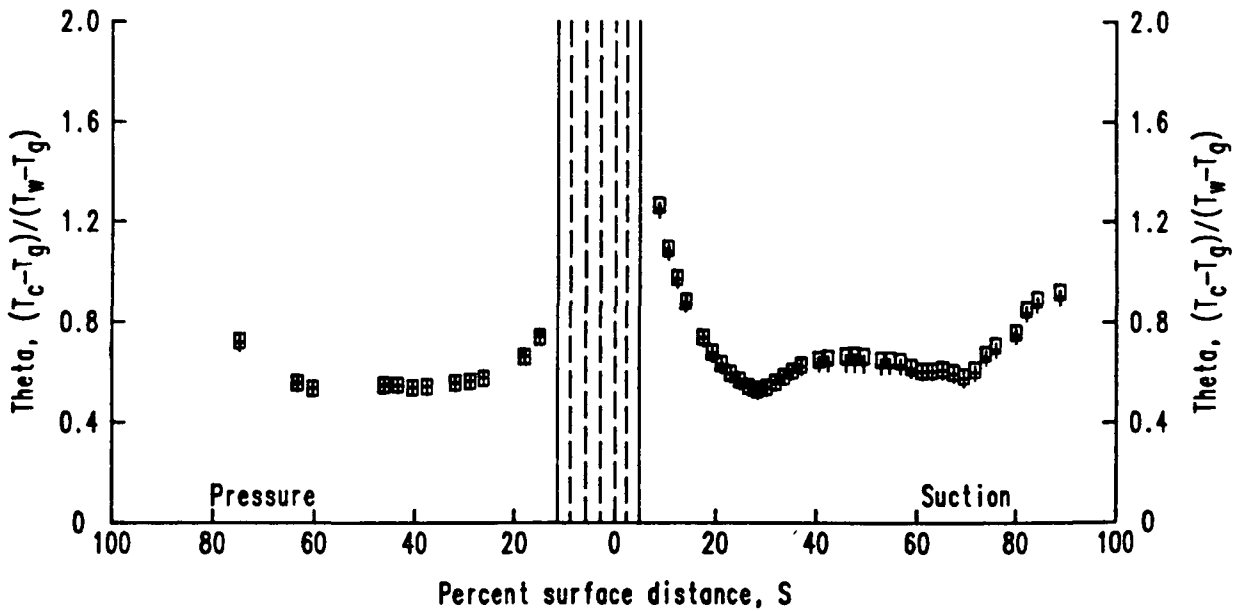
Figure 89. Effects of exit Mach number variation—series X434.
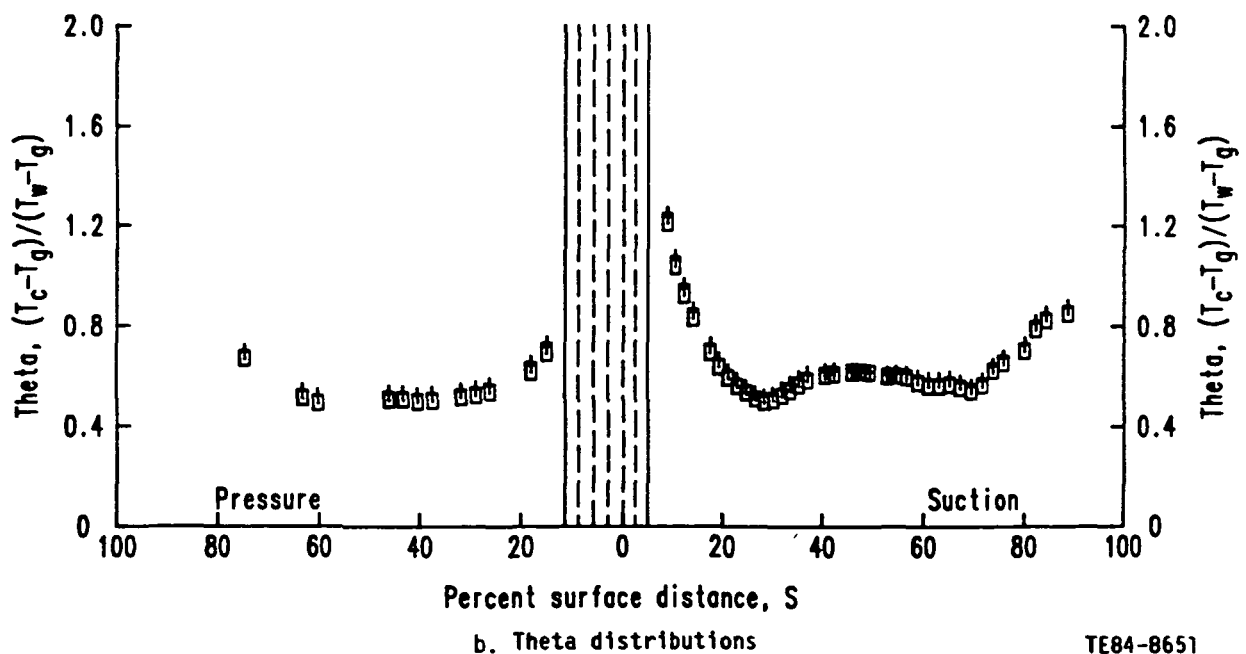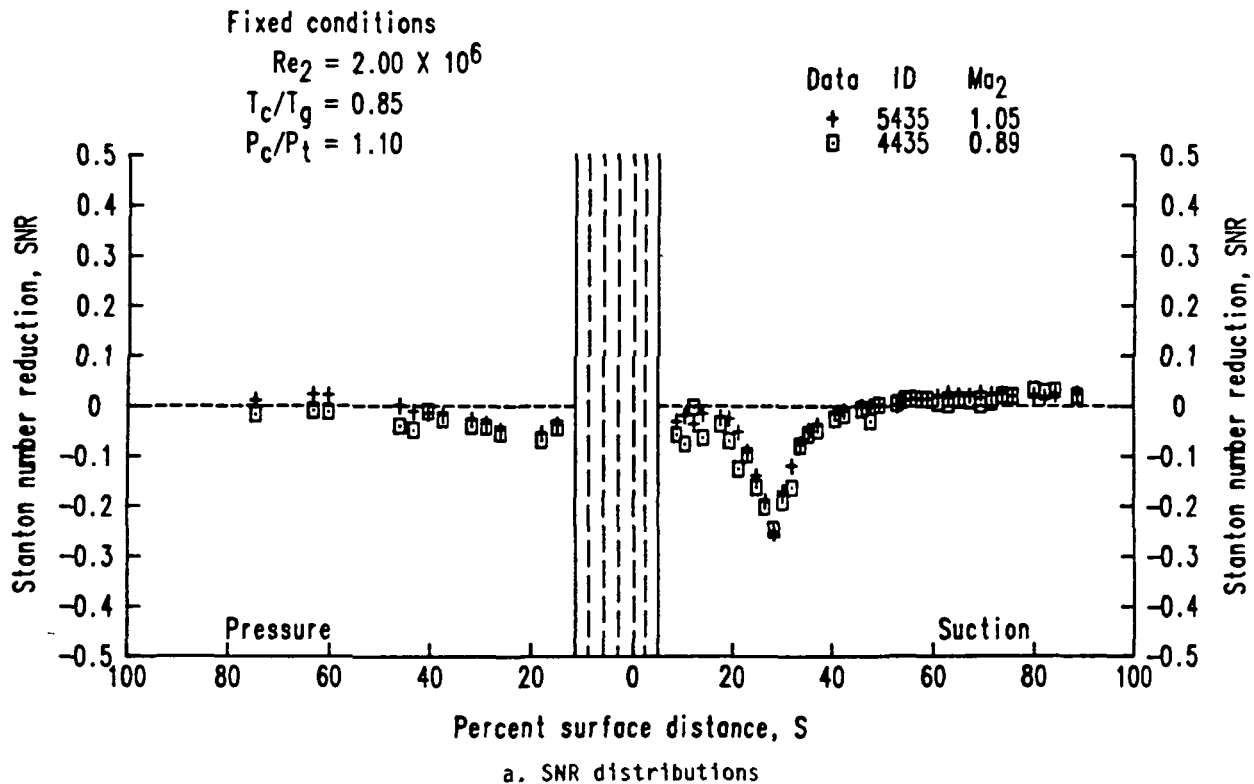
Figure 90. Effects of exit Mach number variation—series X435.
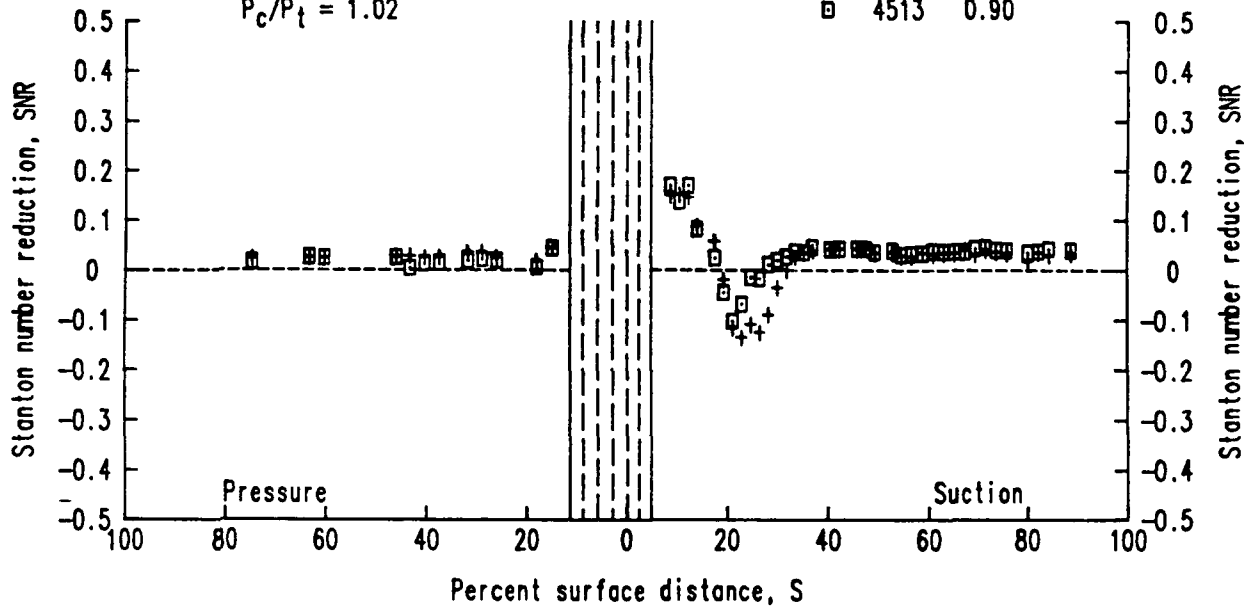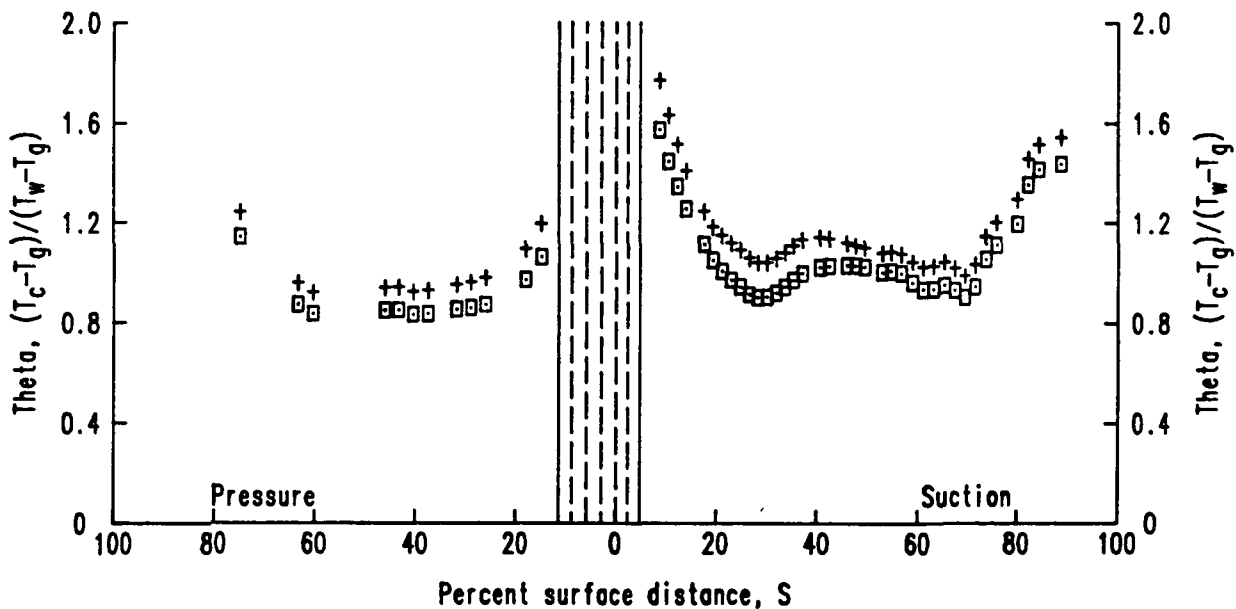
Figure 91. Effects of exit Mach number variation--series X513.
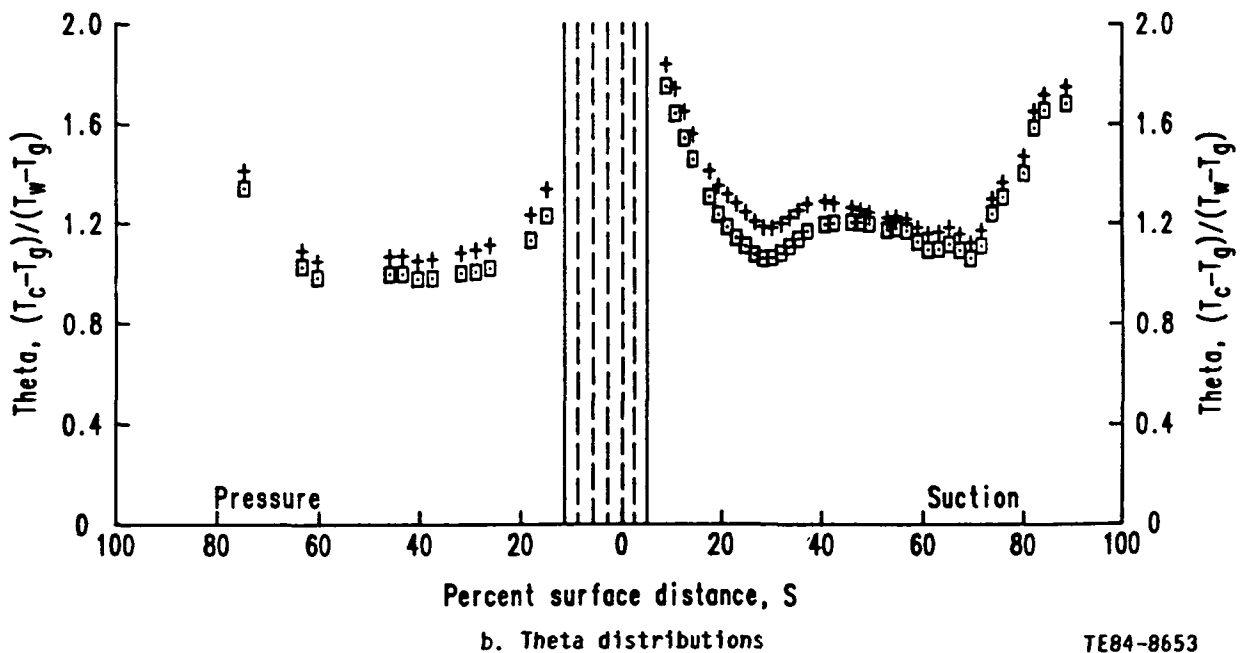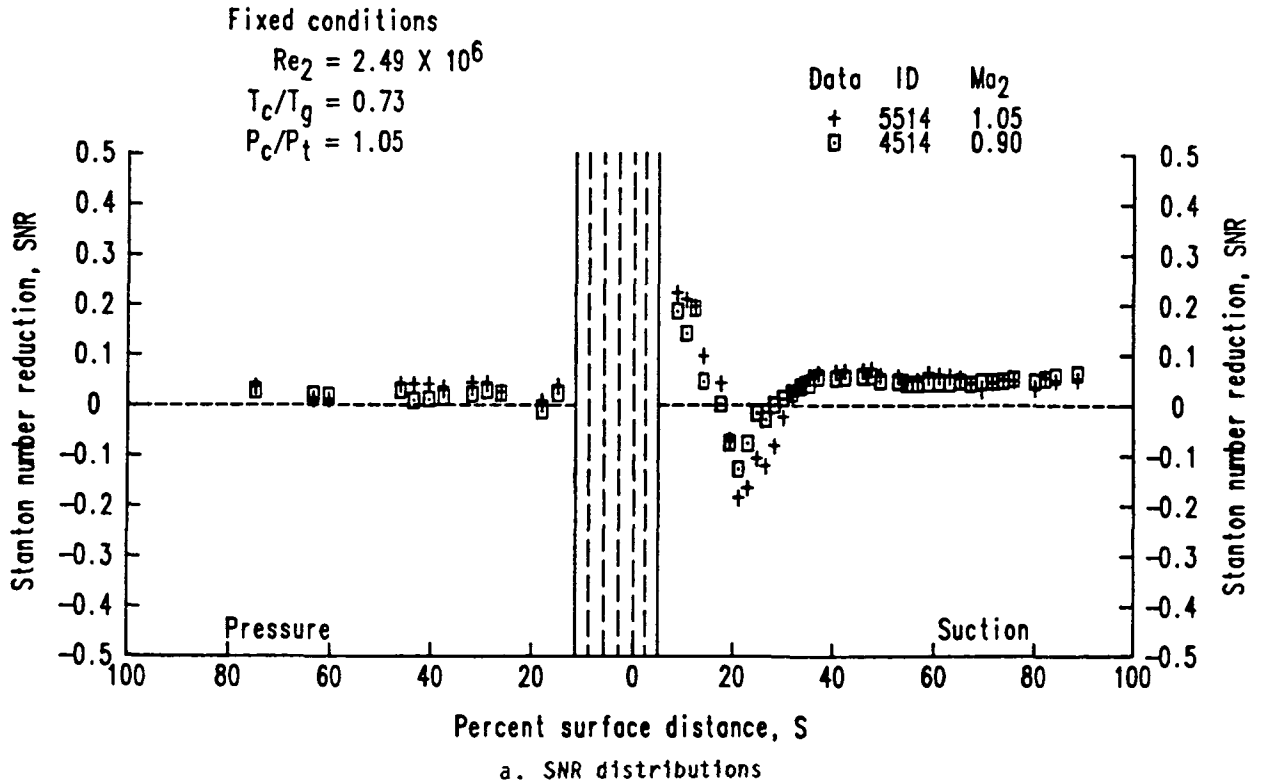
Figure 92. Effects of exit Mach number variation—series X514.
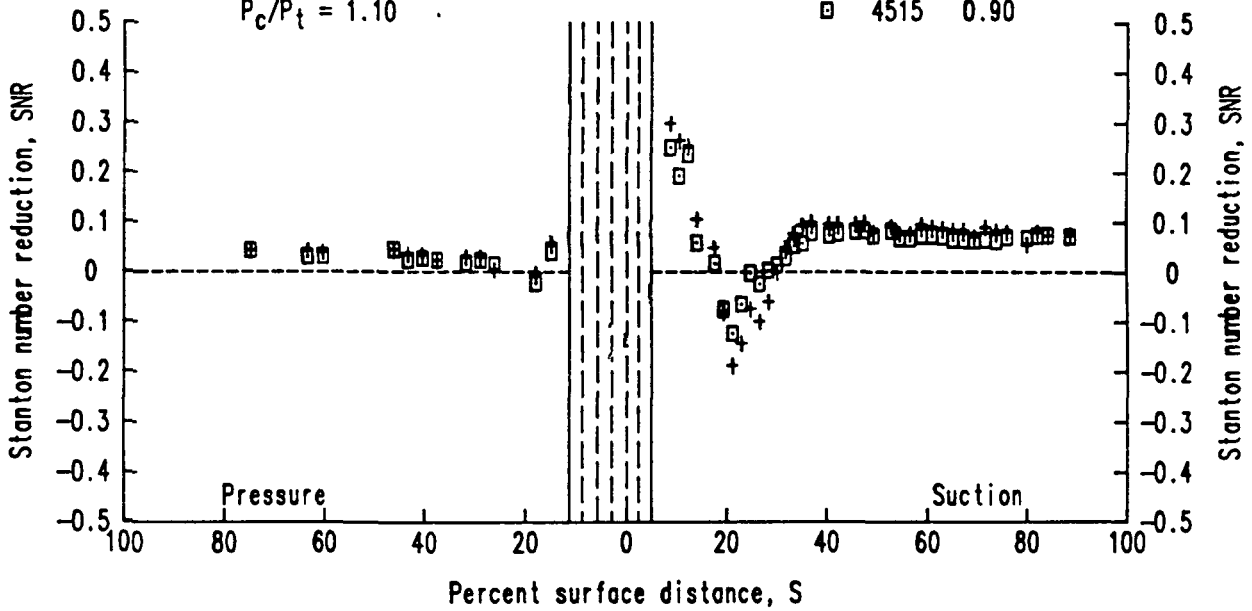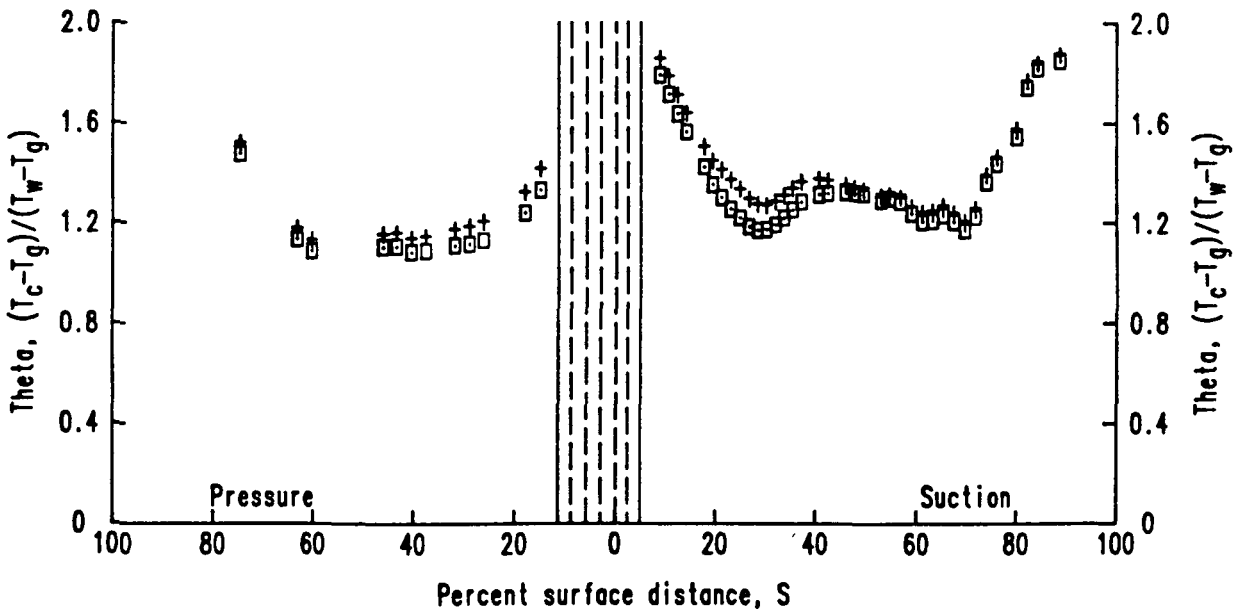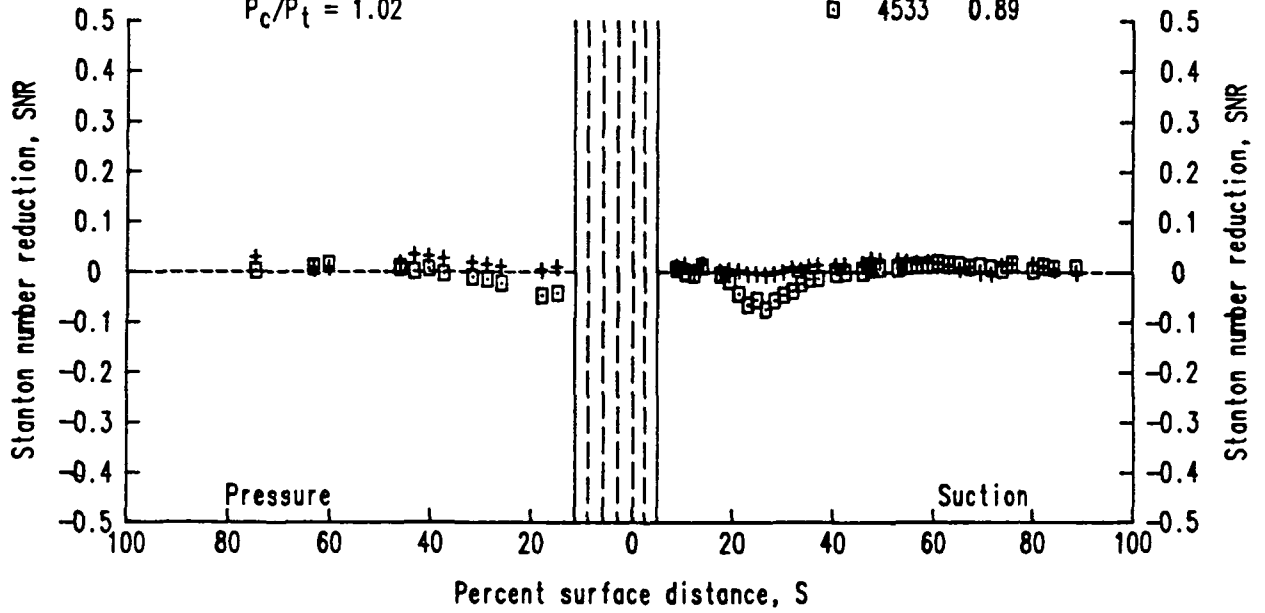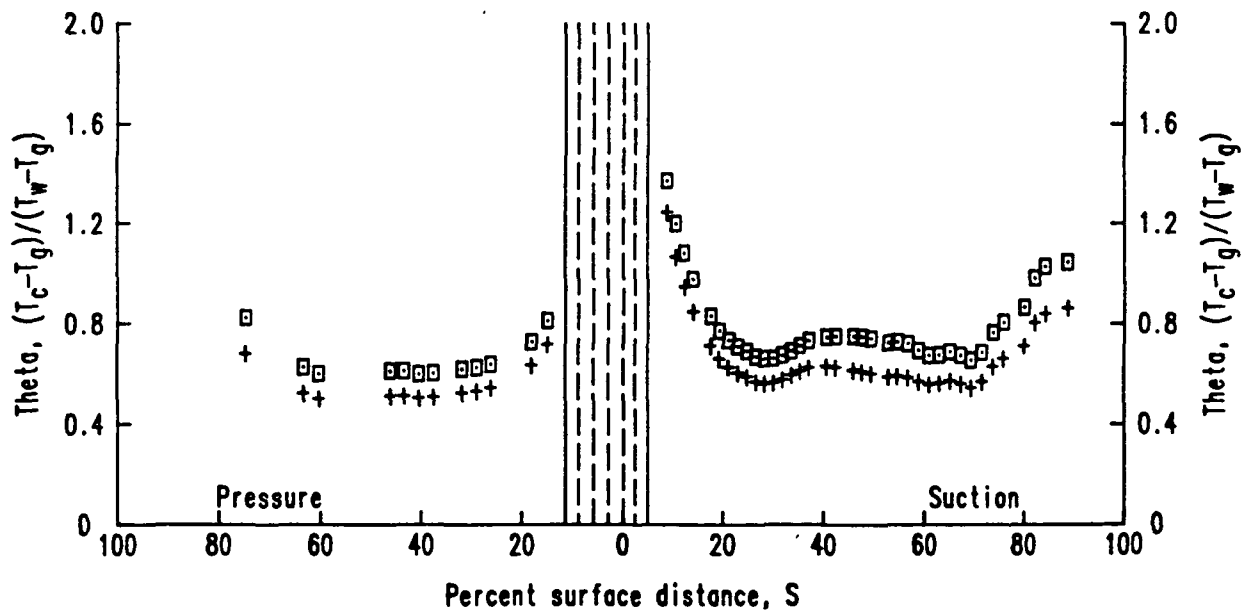
Figure 93.   Effects of exit Mach number variation—series X515.

Figure 94. Effects of exit Mach number variation--series X533.

Figure 95. Effects of coolant to gas absolute temperature ratio variation—series 43X3.

$C-3$
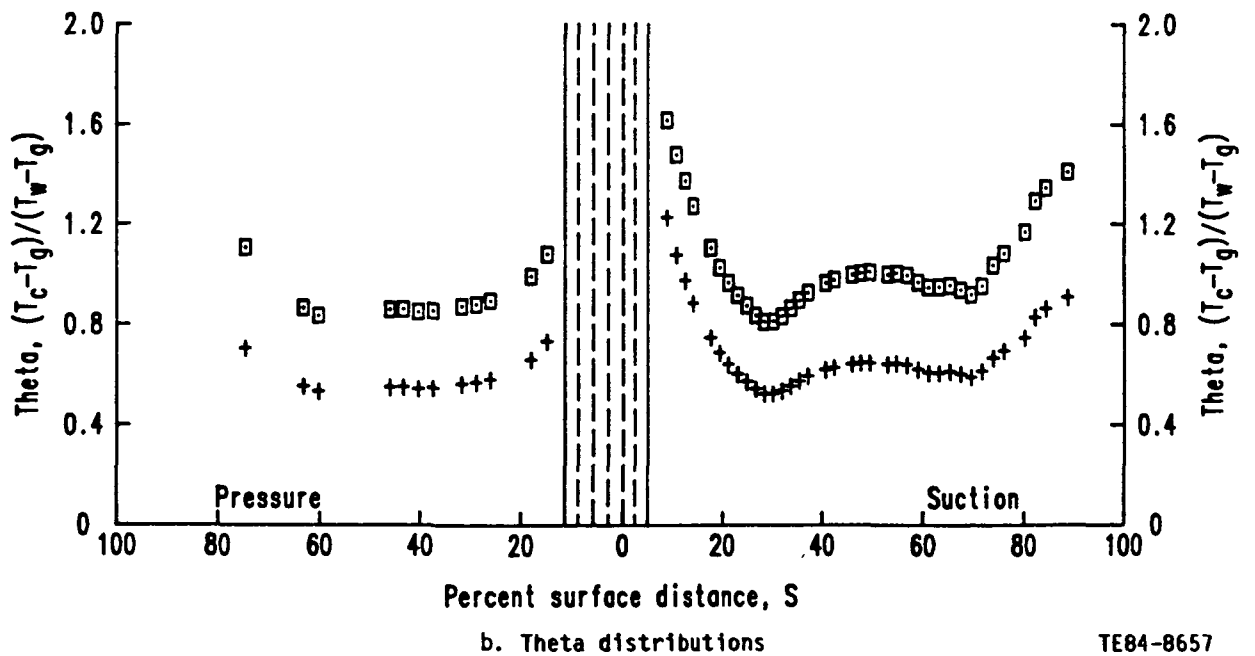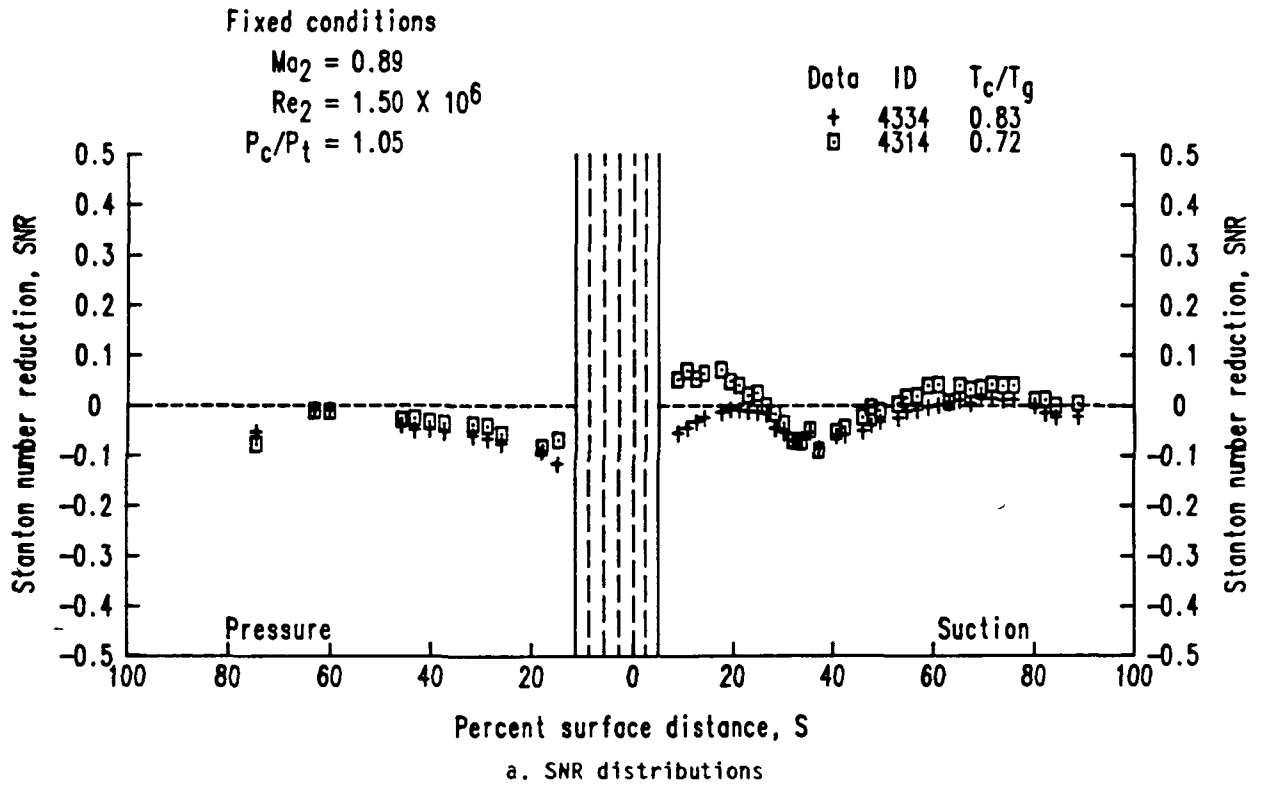
Figure 96. Effects of coolant to gas absolute temperature ratio variation—series 43X4.

184
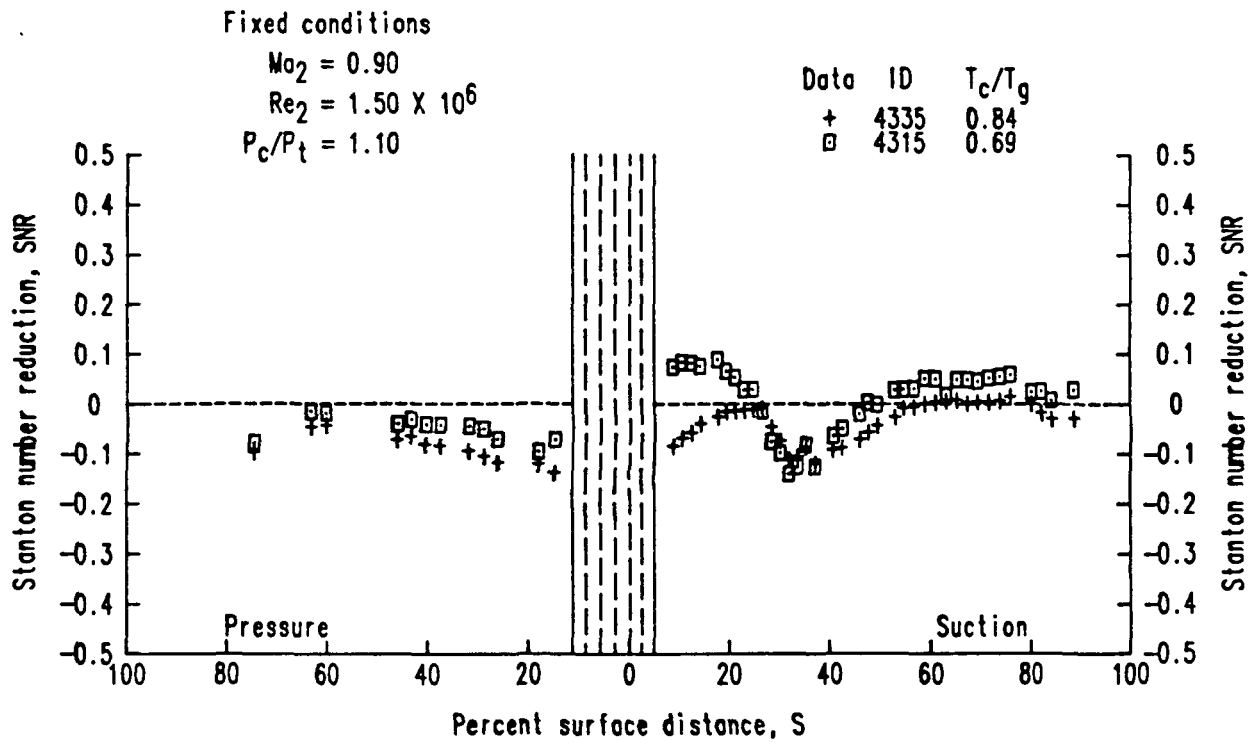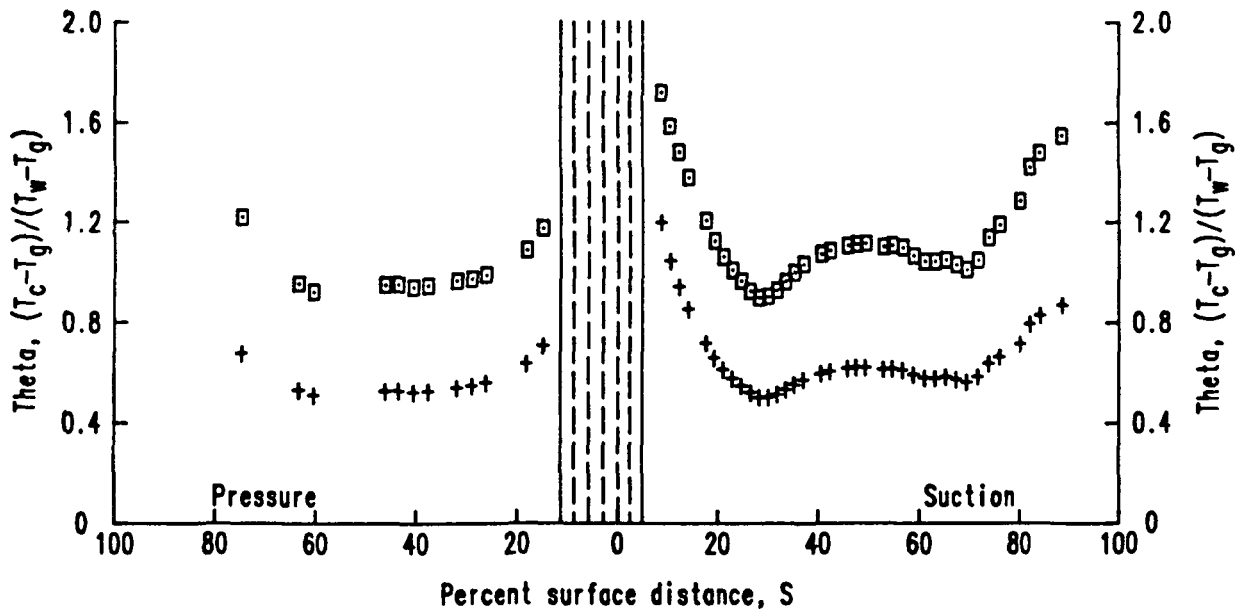
Figure 97. Effects of coolant to gas absolute temperature ratio variation—
series 43X5.

185
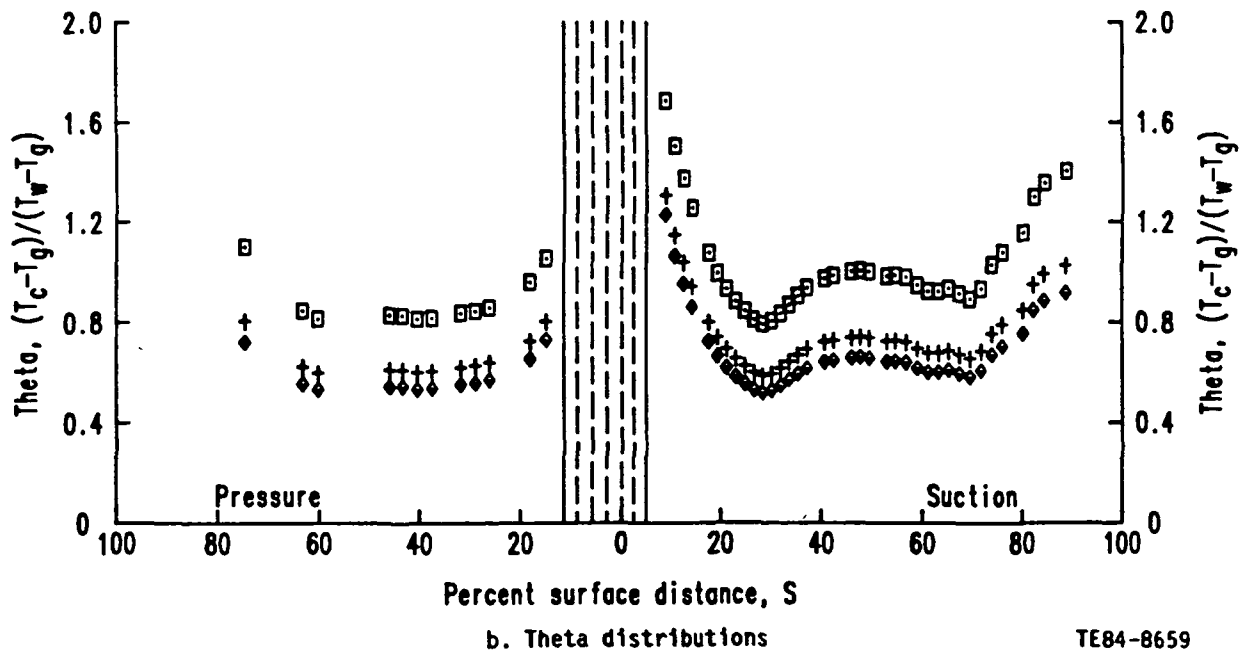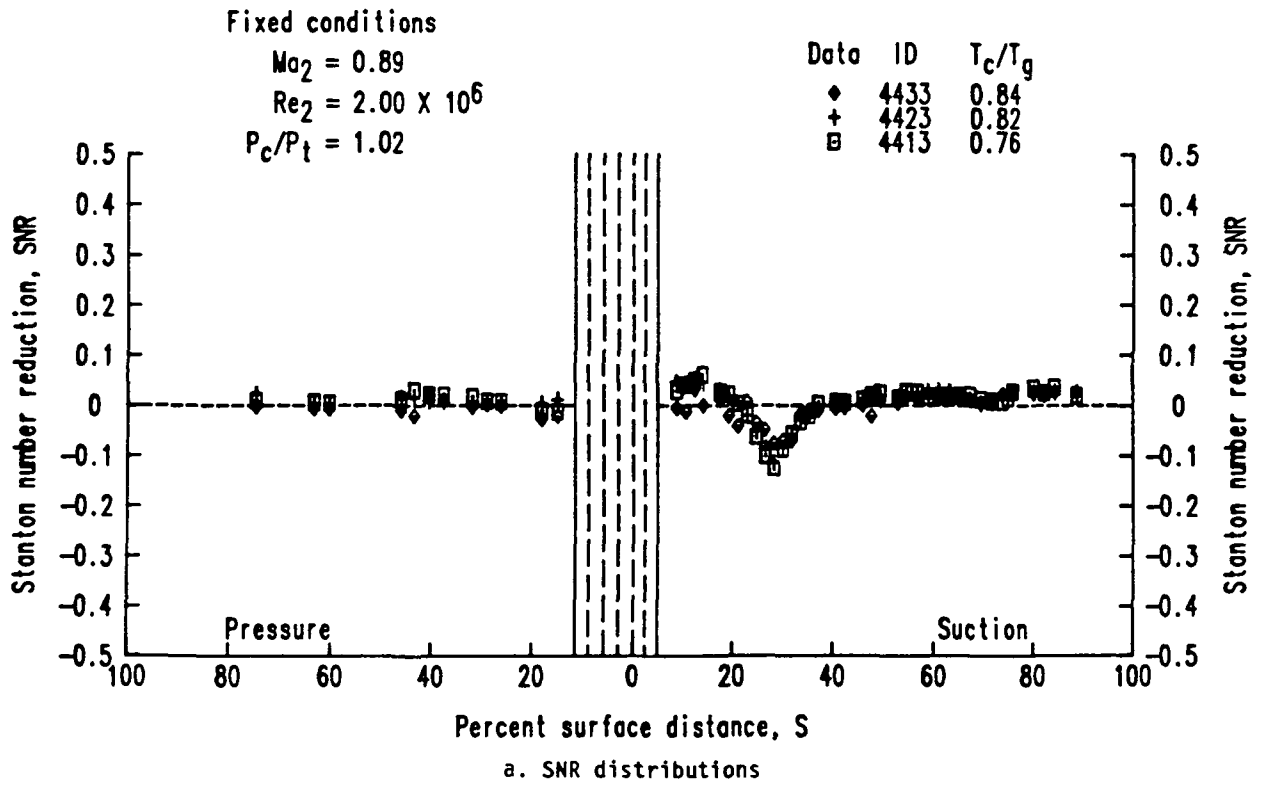
Figure 98. Effects of coolant to gas absolute temperature ratio variation--series 44X3.
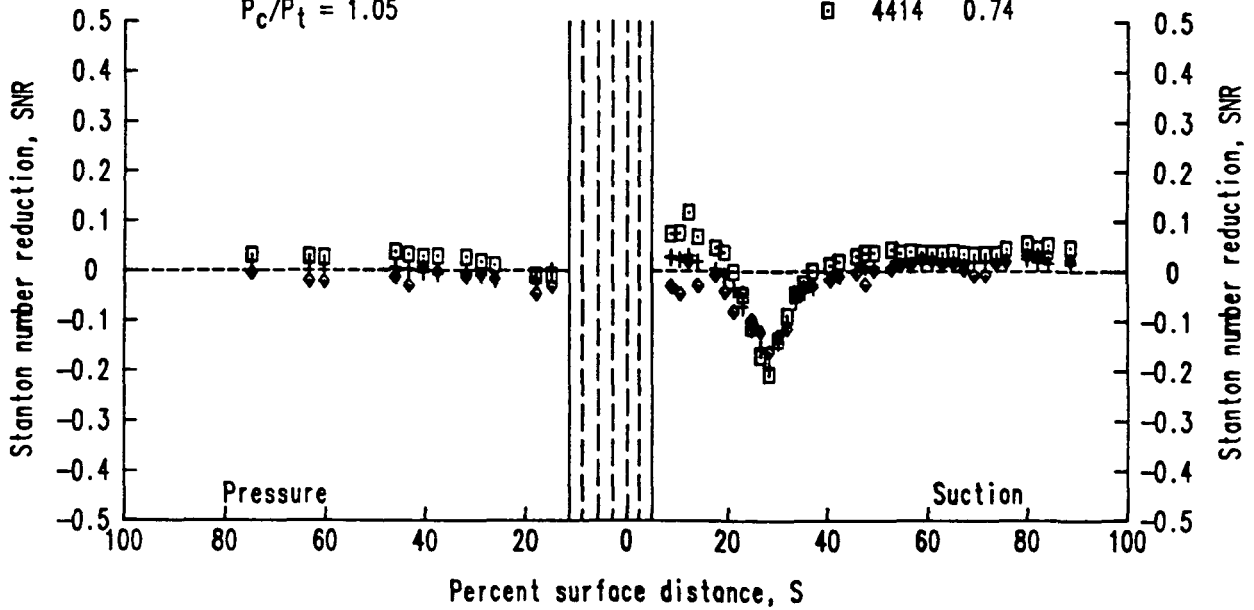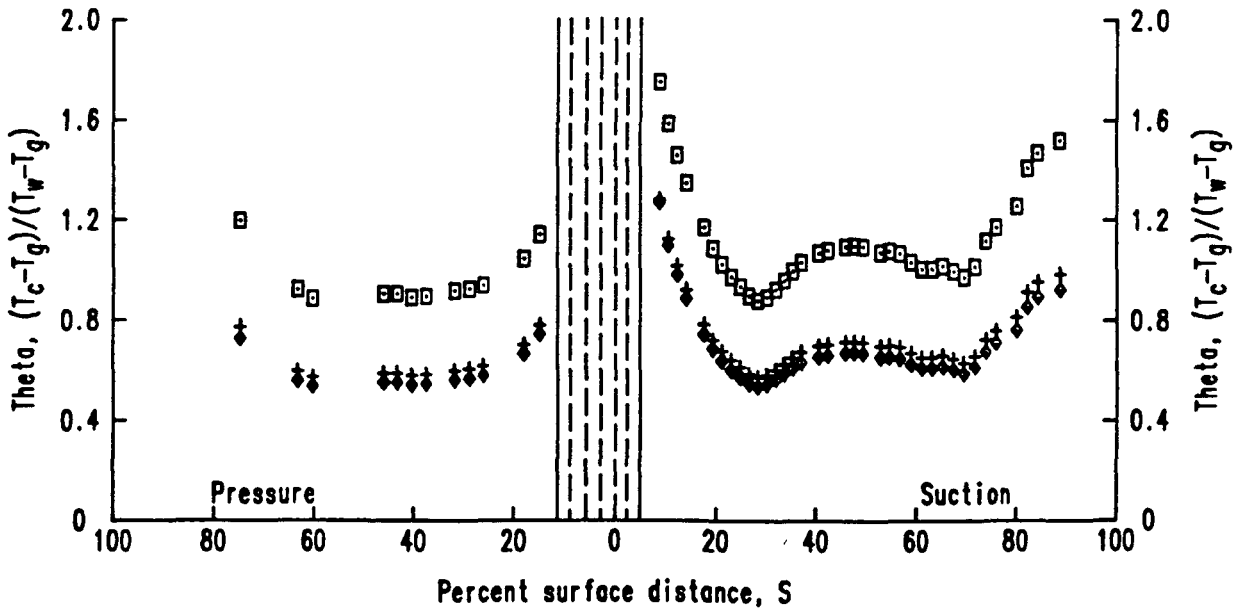
Figure 99. Effects of coolant to gas absolute temperature ratio variation—
series 44X4.
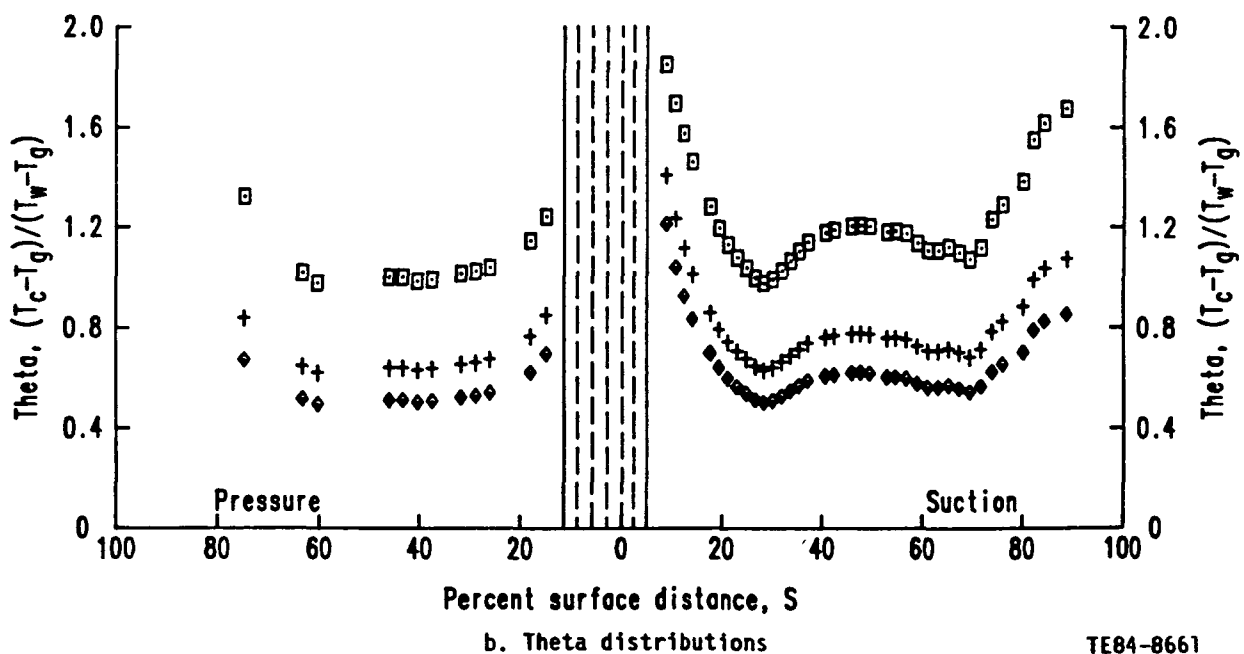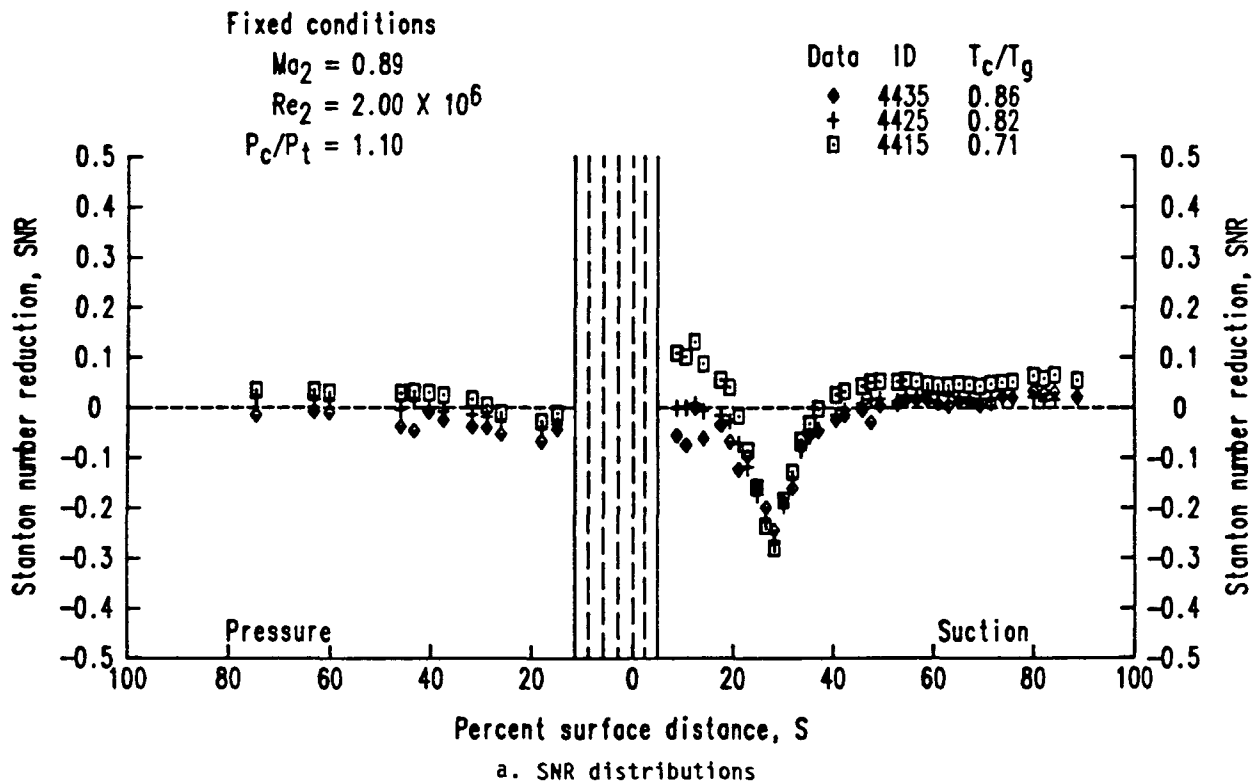
Figure 100. Effects of coolant to gas absolute temperature ratio variation—series 44X5.

Figure 101. Effects of coolant to gas absolute temperature ratio variation--
series 44X6.
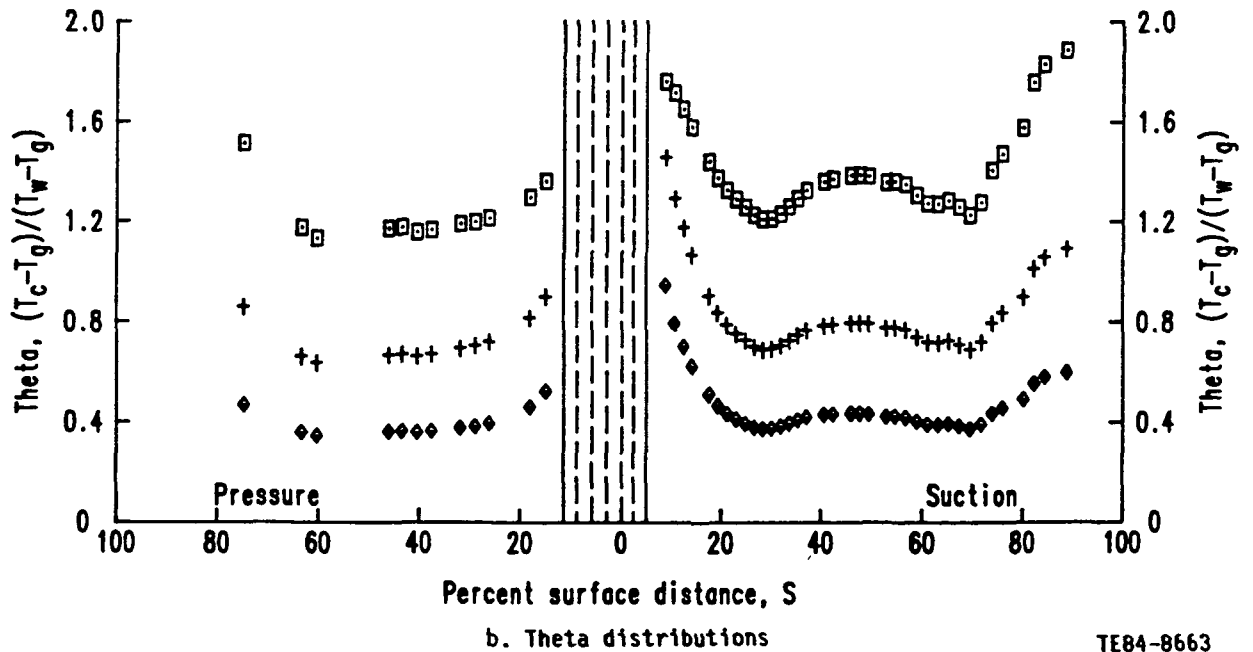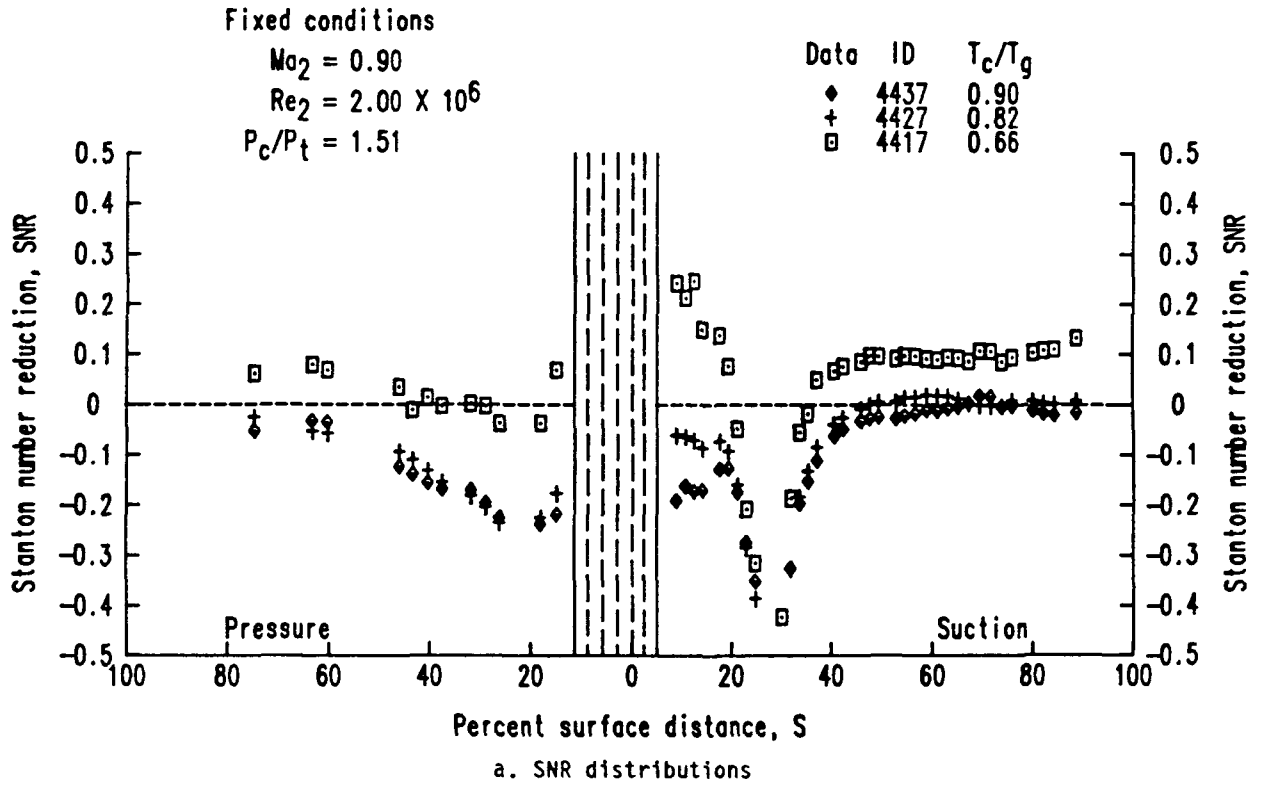
Figure 102. Effects of coolant to gas absolute temperature ratio variation--series 44X7.

Fixed conditions

$M_{a_2} = 0.90$

$Re_2 = 2.00 \times 10^6$

$P_c/P_t = 1.70$

Data	ID	T_c/T_g
◆	4438	0.90
+	4428	0.81
▢	4418	0.65

a. SNR distributions

b. Theta distributions
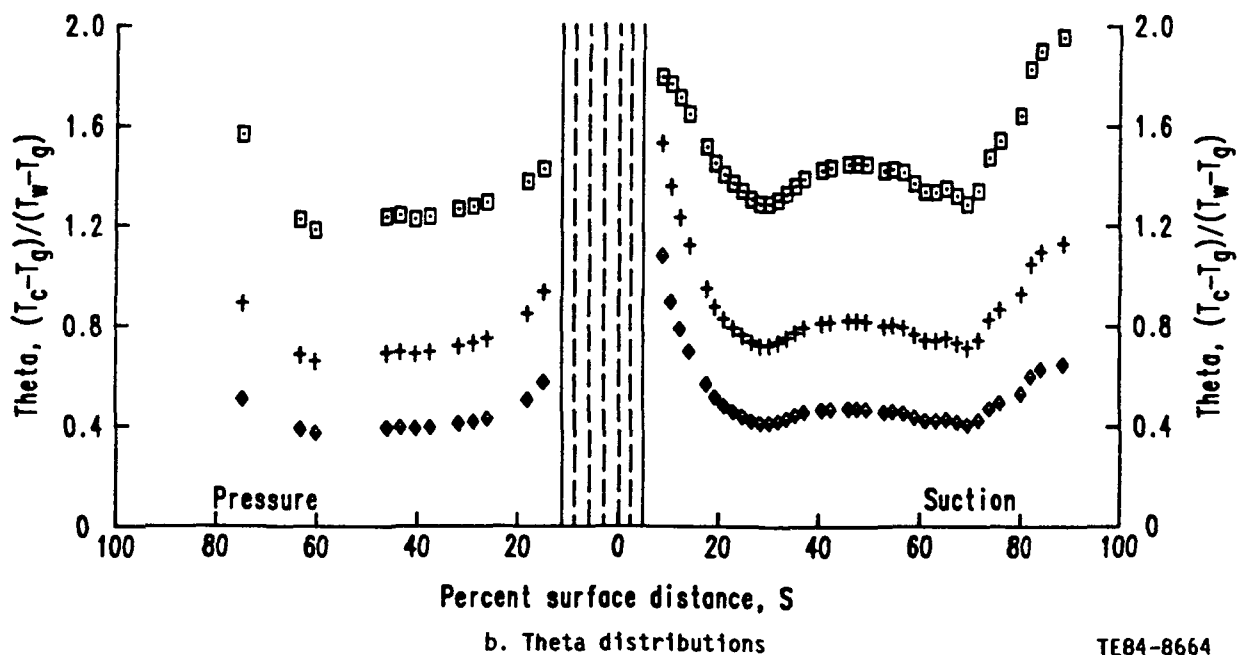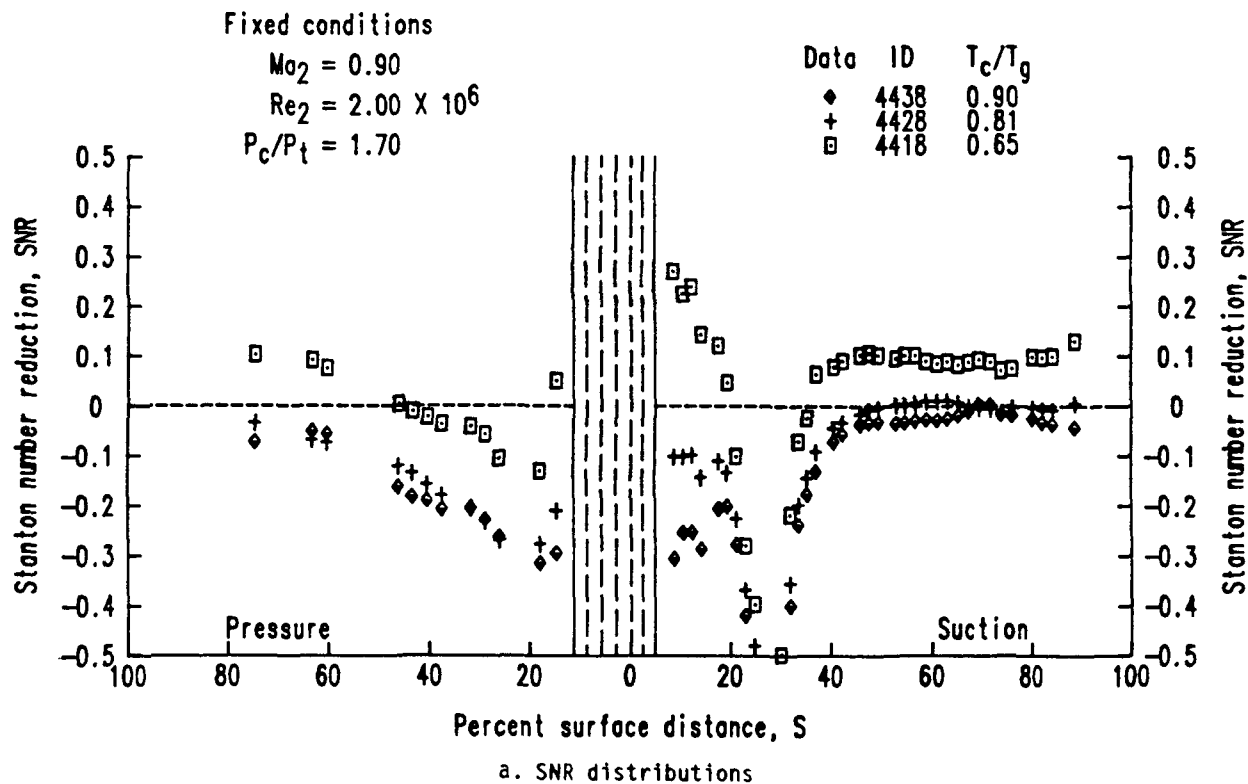
TE84-8664

Figure 103.   Effects of coolant to gas absolute temperature ratio variation--
series 44X8.

191

Fixed conditions

$M_{a2} = 0.90$

$Re_2 = 2.49 \times 10^6$

$P_c/P_t = 1.02$

Data	ID	T_c/T_g
+	4533	0.85
⊡	4513	0.78

Stanton number reduction, SNR

0.5
0.4
0.3
0.2
0.1
0
-0.1
-0.2
-0.3
-0.4
-0.5

100 80 60 40 20 0 20 40 60 80 100

Pressure   Suction

Percent surface distance, S

a. SNR distributions

Theta, $(T_c-T_g)/(T_w-T_g)$

2.0
1.6
1.2
0.8
0.4
0

100 80 60 40 20 0 20 40 60 80 100

Pressure   Suction

Percent surface distance, S
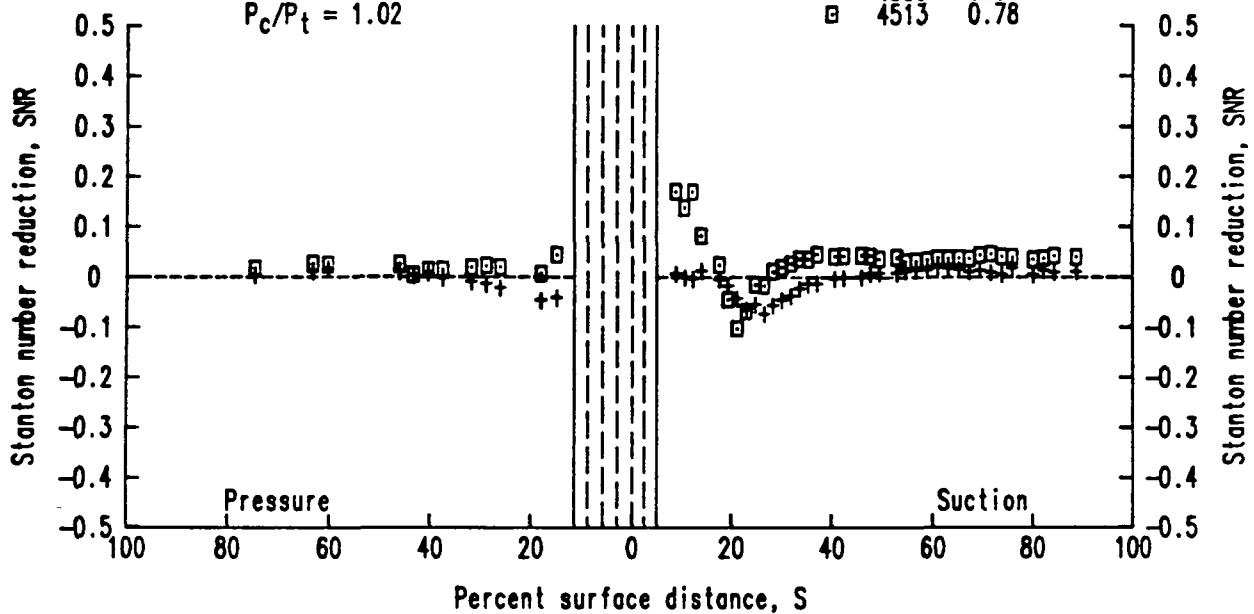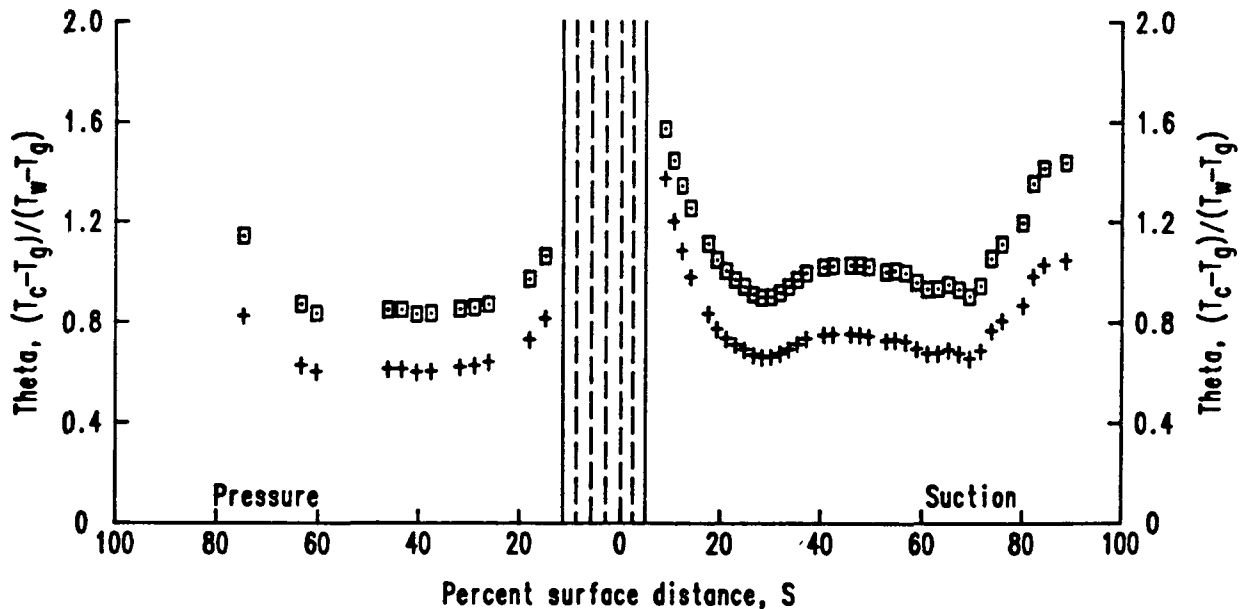
b. Theta distributions

TE84-8665

Figure 104. Effects of coolant to gas absolute temperature ratio variation--series 45X3.

192
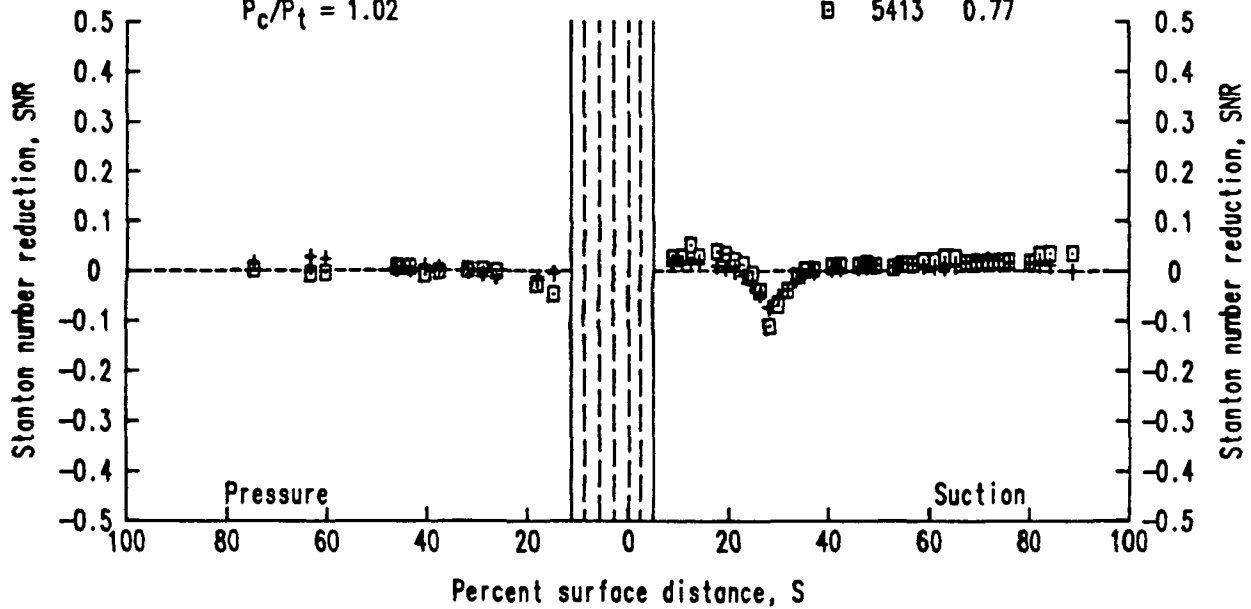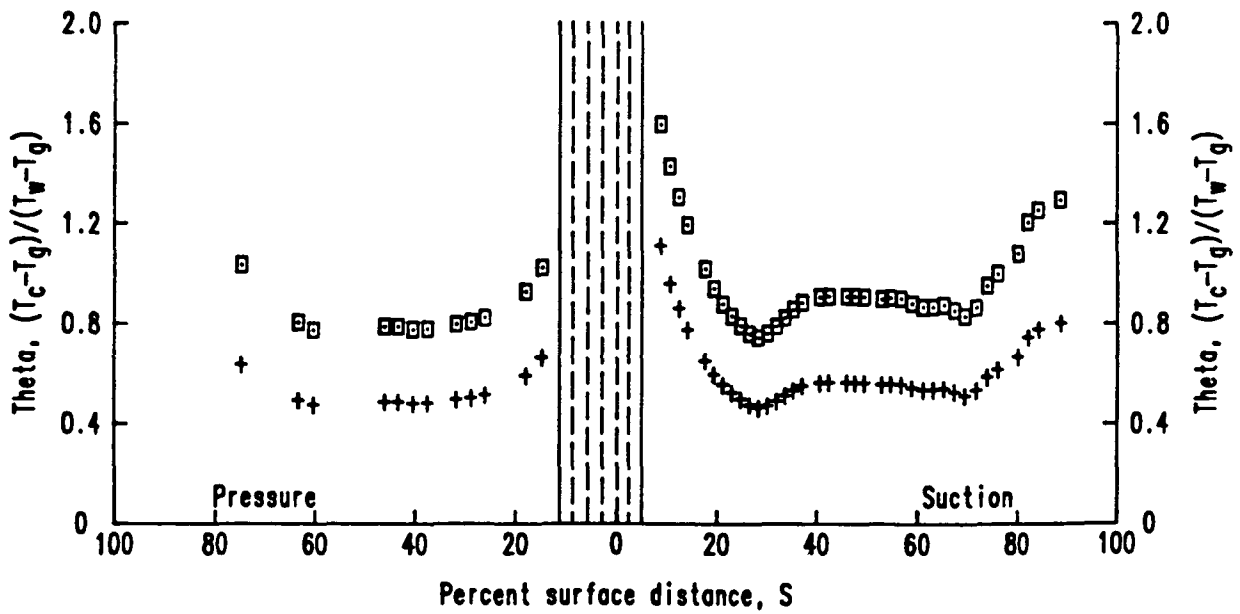
Figure 105. Effects of coolant to gas absolute temperature ratio variation--
series 54X3.
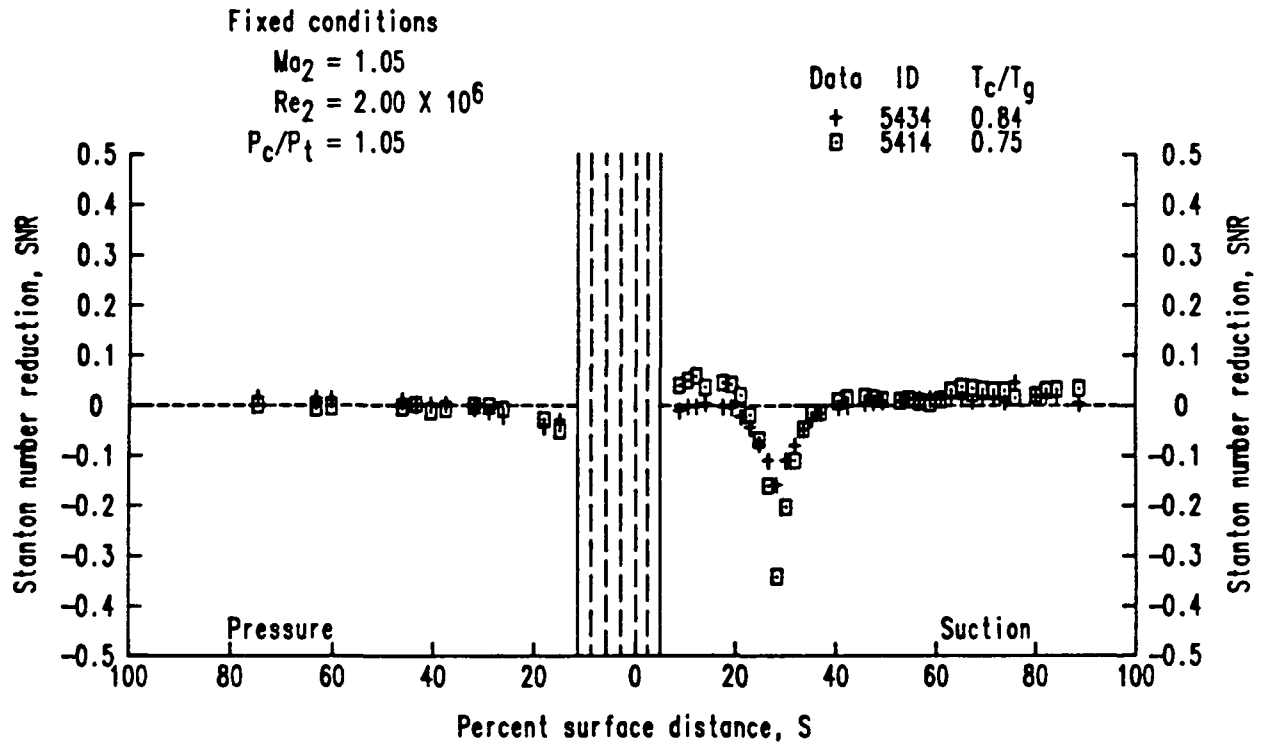
a. SNR distributions
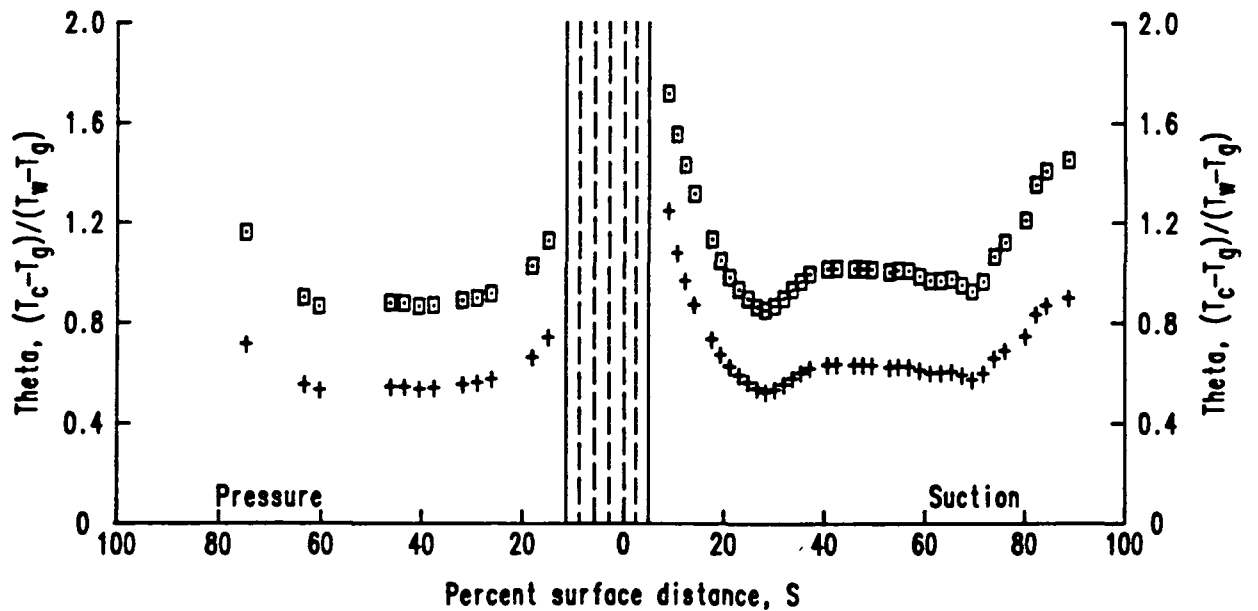
b. Theta distributions

TE84-8667

Figure 106. Effects of coolant to gas absolute temperature ratio variation—series 54X4.

194
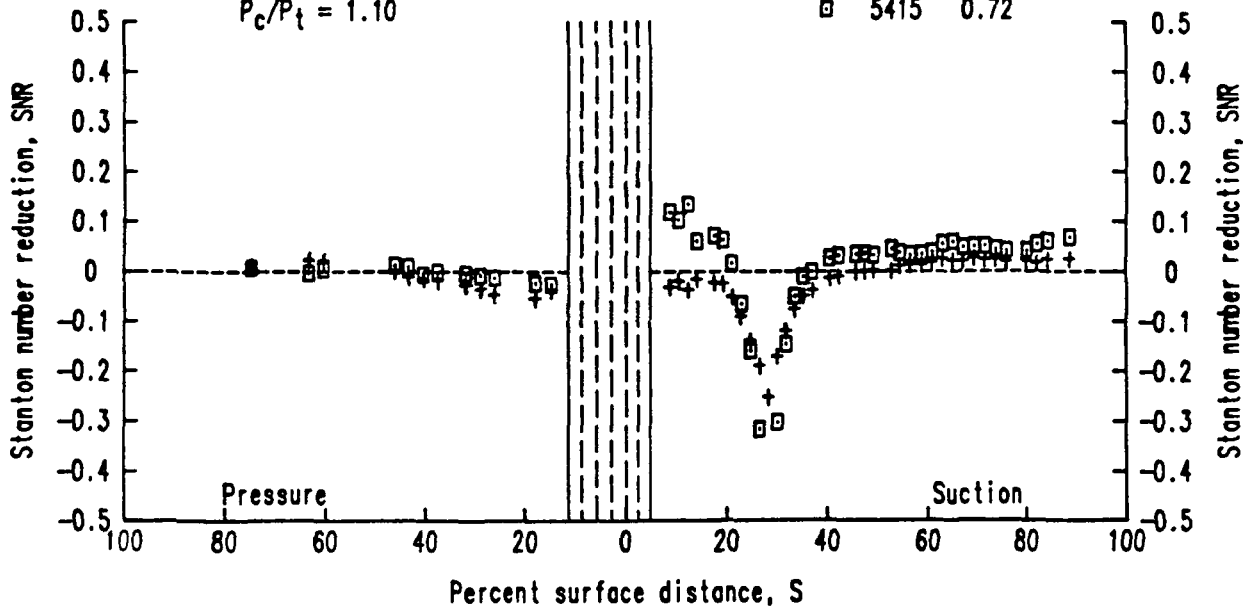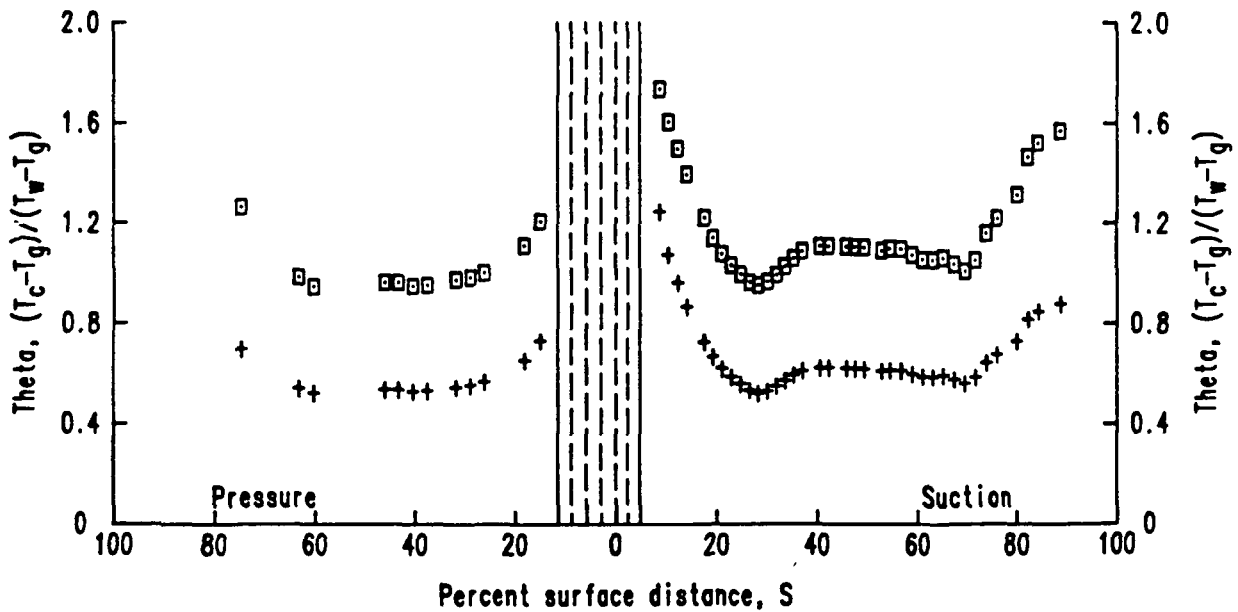
Figure 107. Effects of coolant to gas absolute temperature ratio variation—
series 54X5.
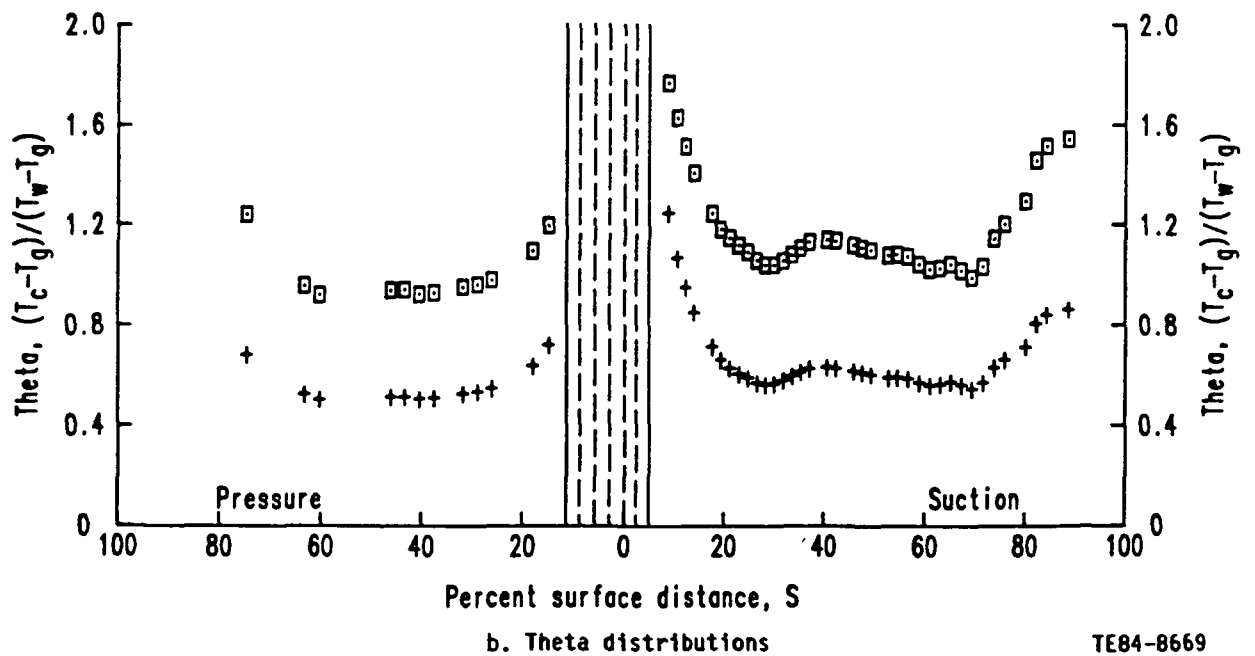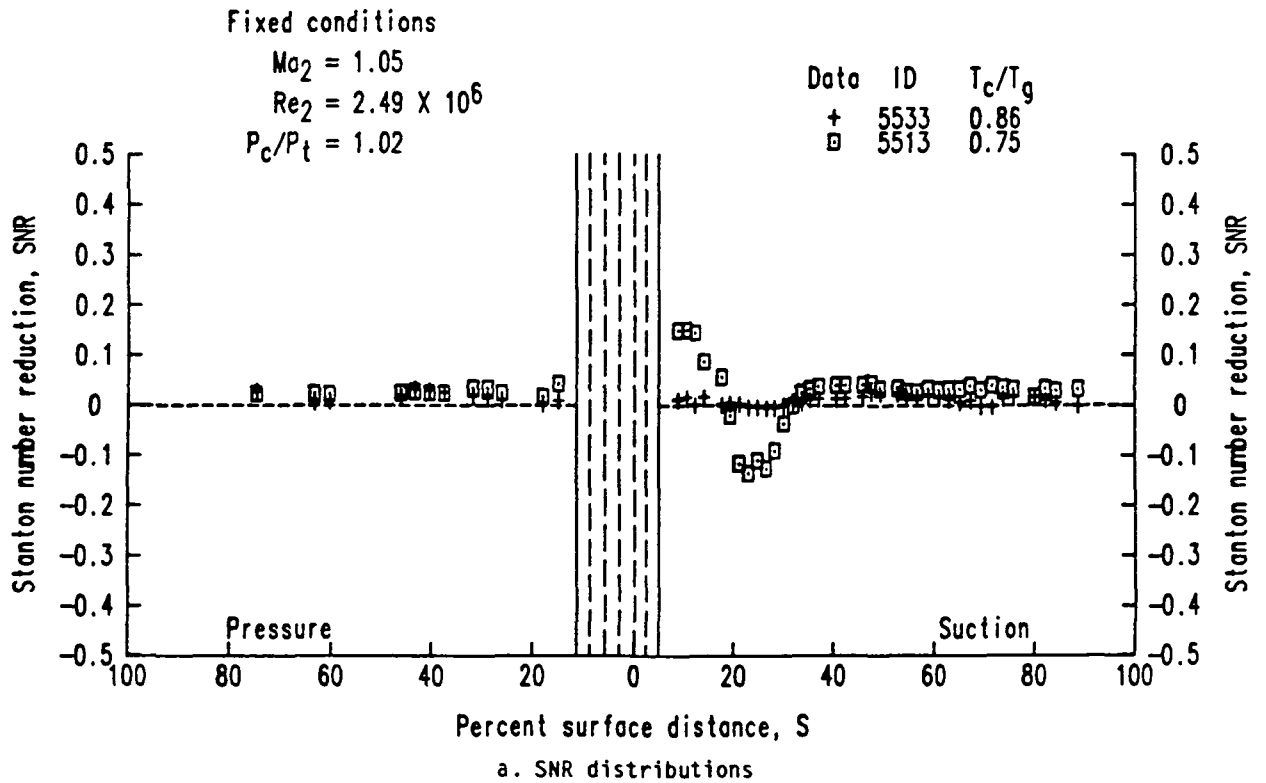
Figure 108. Effects of coolant to gas absolute temperature ratio variation—series 55X3.
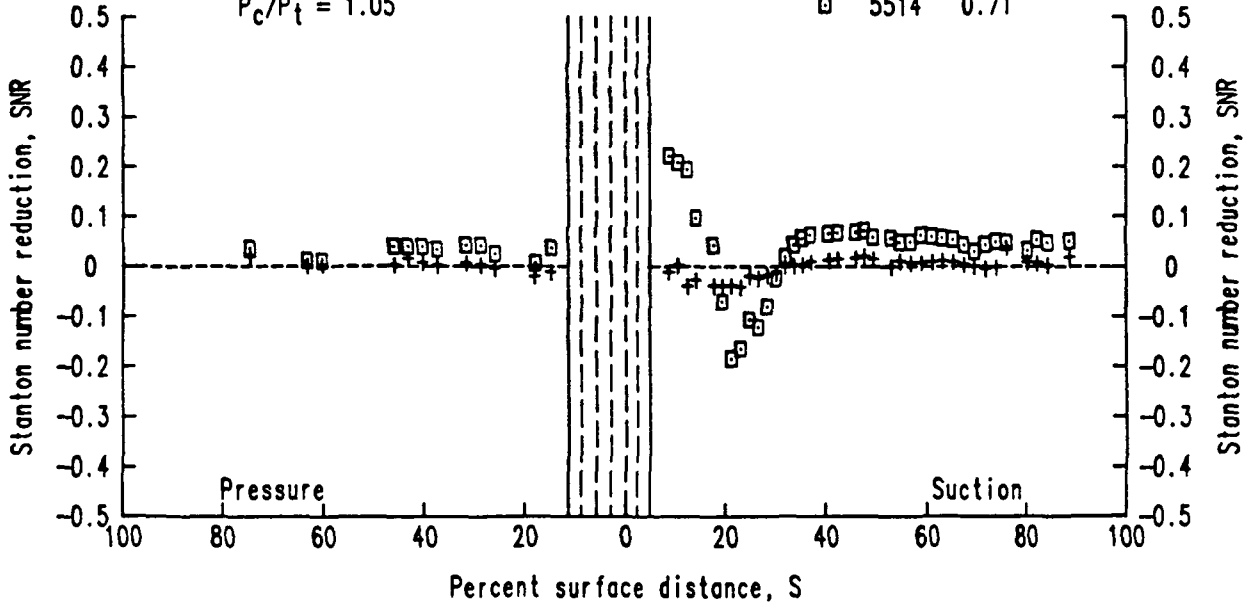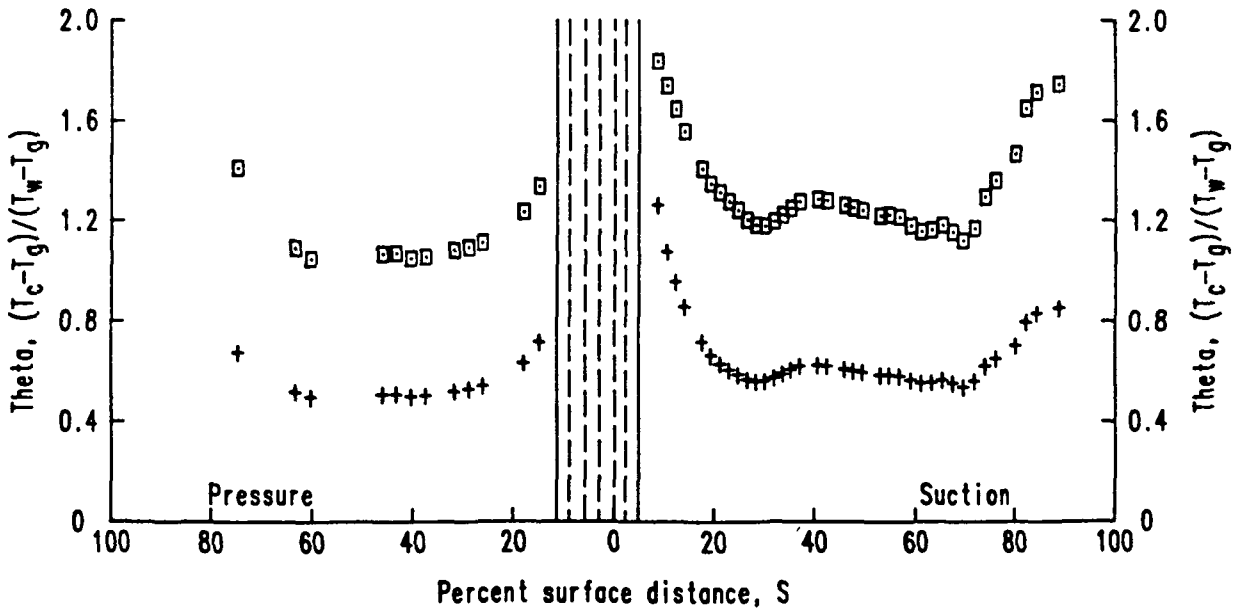
Figure 109. Effects of coolant to gas absolute temperature ratio variation—series 55X4.
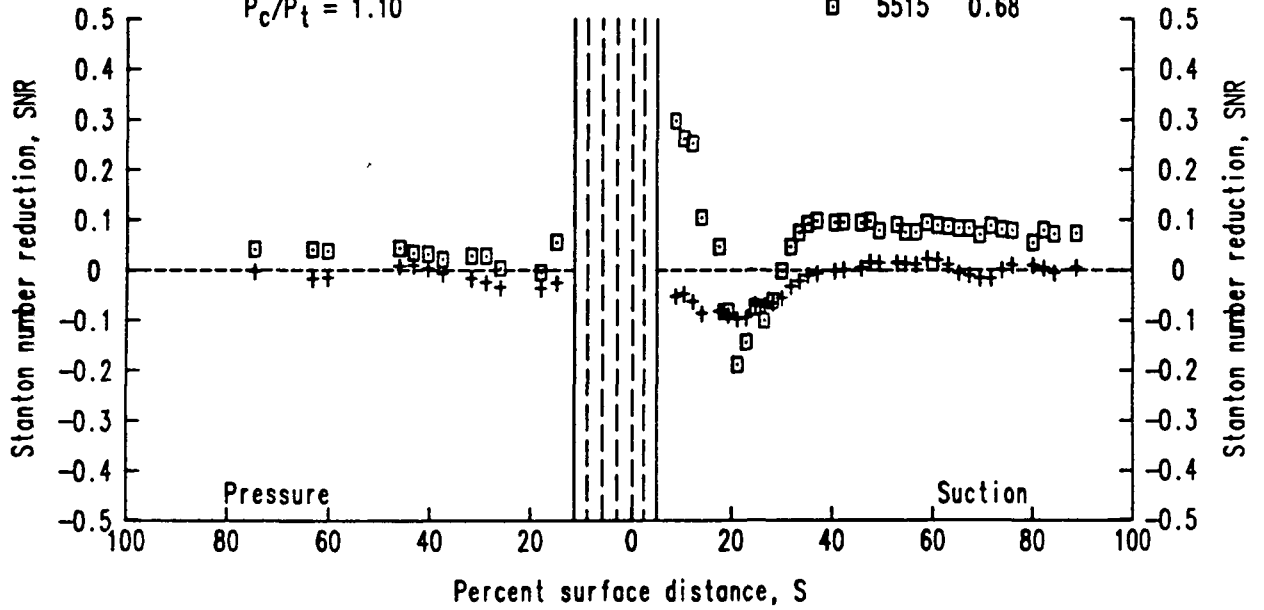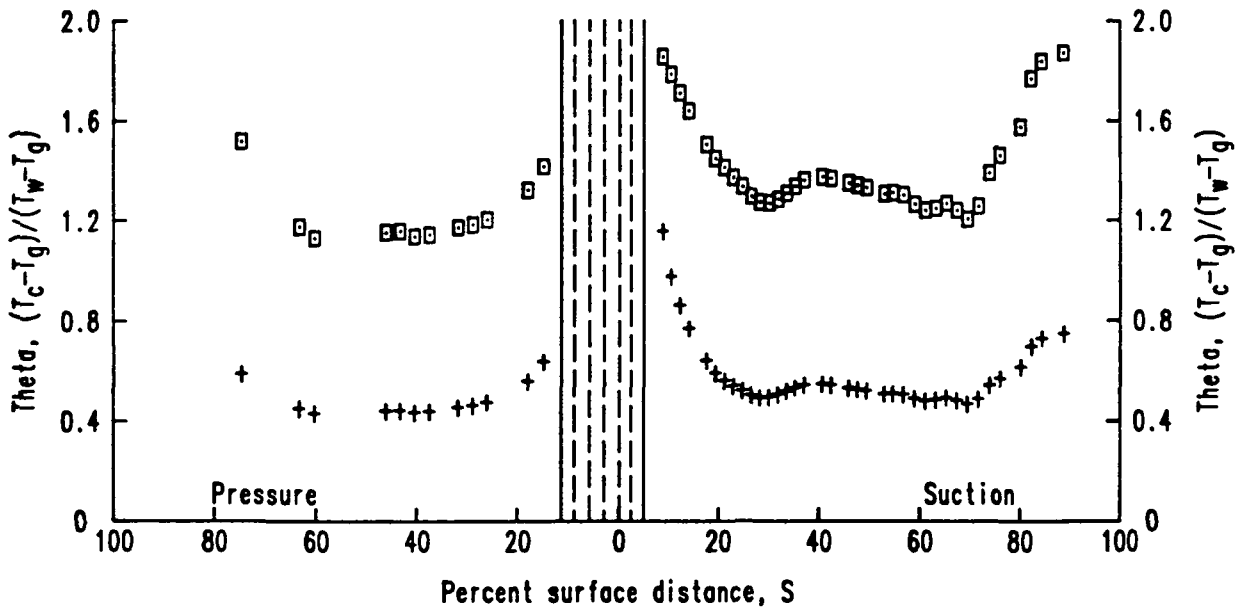
Figure 110. Effects of coolant to gas absolute temperature ratio variation—series 55X5.

APPENDIX C
TURBULENCE MODEL EVALUATION FOR NONFILM-COOLED TURBINE
AIRFOIL APPLICATIONS

One of the primary tasks of Ref 1 was to sort through the numerous turbulence modeling approaches reported in the literature and evaluate their applicability as related to the specific problem of predicting nonfilm-cooled airfoil convective heat transfer in a gas turbine environment. A number of models were selected from initial literature survey studies, coded in the STAN5 numerical framework, and tested against an assembled heat transfer data base.

Although care was taken to develop criteria to ensure that models selected would span the range of turbulence model formulations (zero to two equations) that might be found in a turbine airfoil design tool, a number of approaches that showed promise had to be excluded. One such turbulence model approach studied but not specifically tested was that proposed by McDonald and Fish (Ref 22).

The interesting feature of the McDonald-Fish turbulence model formulation is that transition phenomena associated with free-stream turbulence intensity is directly accounted for using a transport equation, mixing length scale formulation. The merits of this approach as related to the prediction of airfoil surface convective heat transfer were demonstrated and discussed in Ref 22 for the airfoil heat transfer data of Turner (Ref 4). To evaluate the McDonald-Fish approach in this program, the model, as documented in Ref 22, was coded in the STAN5 boundary layer code. After performing necessary benchmark computations to ensure that the model had been properly coded, predictions were made for a number of test condition cases making up the C3X airfoil data base reported in Ref 1. Comparisons between McDonald-Fish predictions, the measured data, other modeling approaches tested previously, and the method described in section 4.3 were made.

Figure 111 shows three experimentally determined heat transfer coefficient distributions obtained in Ref 1 for the nonfilm-cooled C3X airfoil cascade at three exit Reynolds number conditions ($Re_2 = 1.51 \times 10^6$, 1.96×10^6, and

2.49×10^6). As shown in the legend, the exit Mach number (Ma_2) condition for all three cases was approximately 0.90. In addition, the reported free-stream turbulence intensity, measured upstream of the vane row, was 6.5%. The average wall to gas temperature ratio (T_w/T_g) was approximately 0.8. For these conditions boundary layer computations were made using the Crawford et al (Ref 10) mixing length turbulence model contained in the STAN5 code with transition specified by RETRAN = 250. These computations were originally performed in Ref 1 to characterize a so-called unmodified STAN5 mixing length turbulence model approach. The heat transfer coefficient predictions compared with the data presented in Figure 111 are shown in Figure 112.

In addition to the unmodified STAN5 predictions, computations for the same operating conditions were made using the turbulence model formulation developed in Ref 1. These results are shown in Figure 113. Predictions such as the ones shown in Figure 113 were labeled modified STAN5 in Ref 1. In the modeling development work conducted in Ref 1, the unmodified STAN5 results shown in Figure 112 represent the starting point and the modified method predictions shown in Figure 113 represent the end result. These results serve as alternate computations for comparing the McDonald-Fish turbulence model predictions shown in Figures 114 and 115.
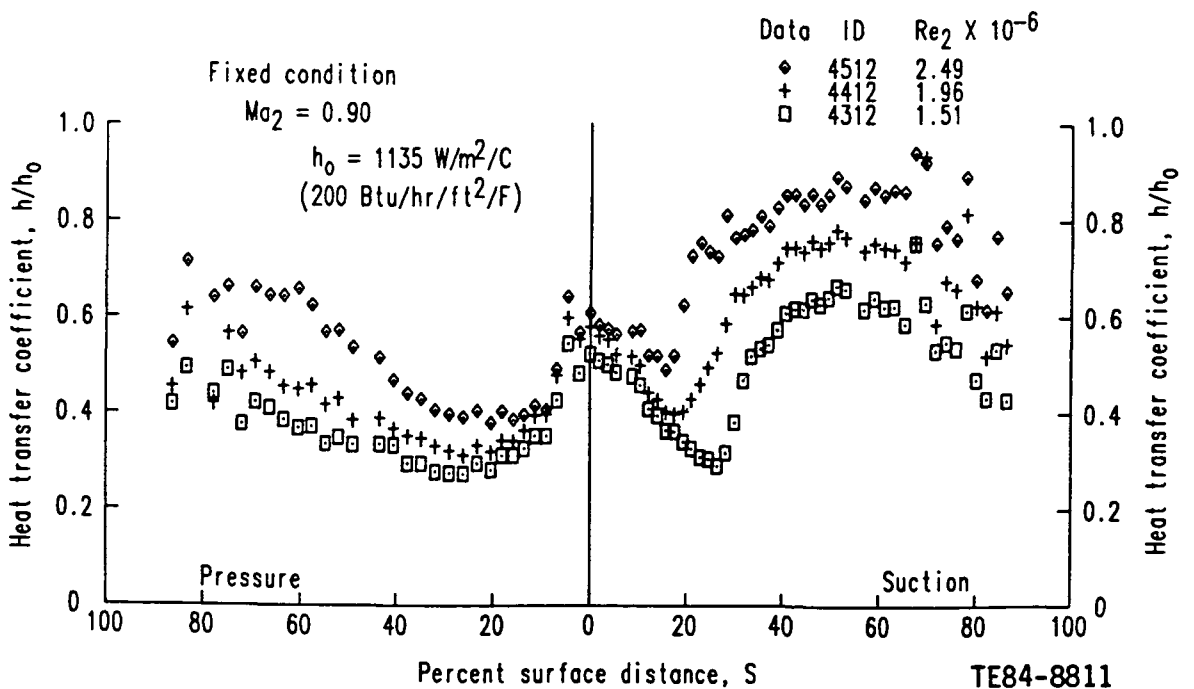
Figure 111. Nonfilm-cooled C3X airfoil surface heat transfer coefficient distribution data obtained at three exit Reynolds number conditions.

200
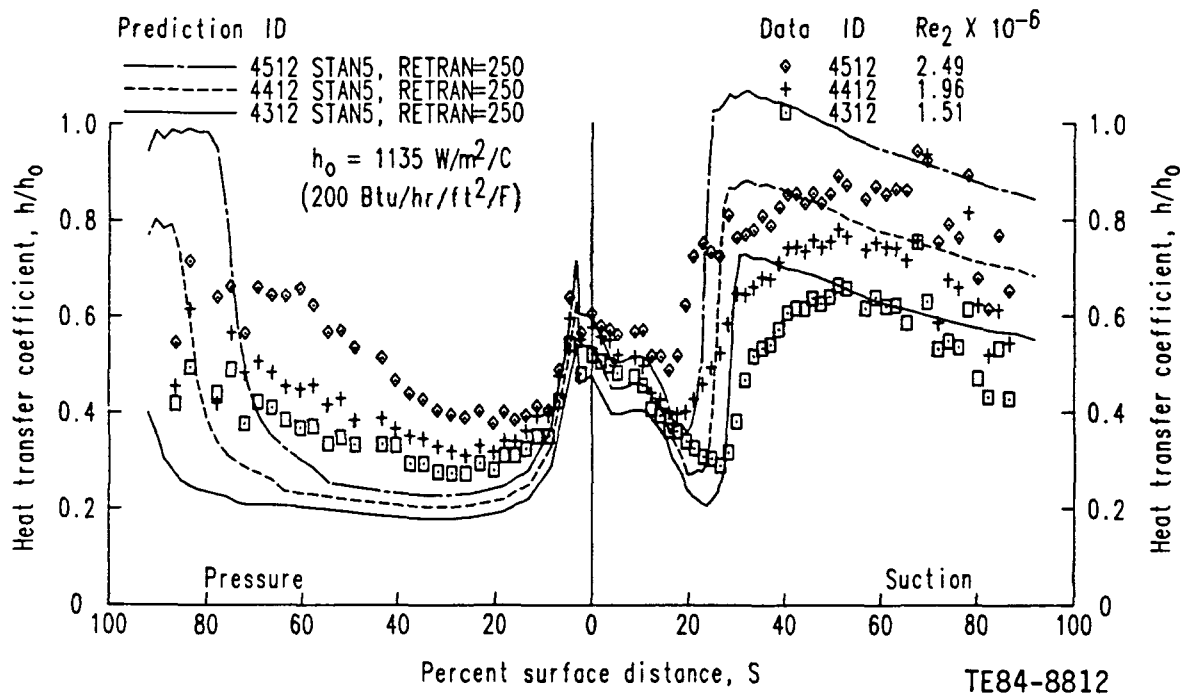
Figure 112. Predicted nonfilm-cooled C3X airfoil heat transfer coefficient distributions obtained using the unmodified, STAN5 computer code and effective viscosity formulation.
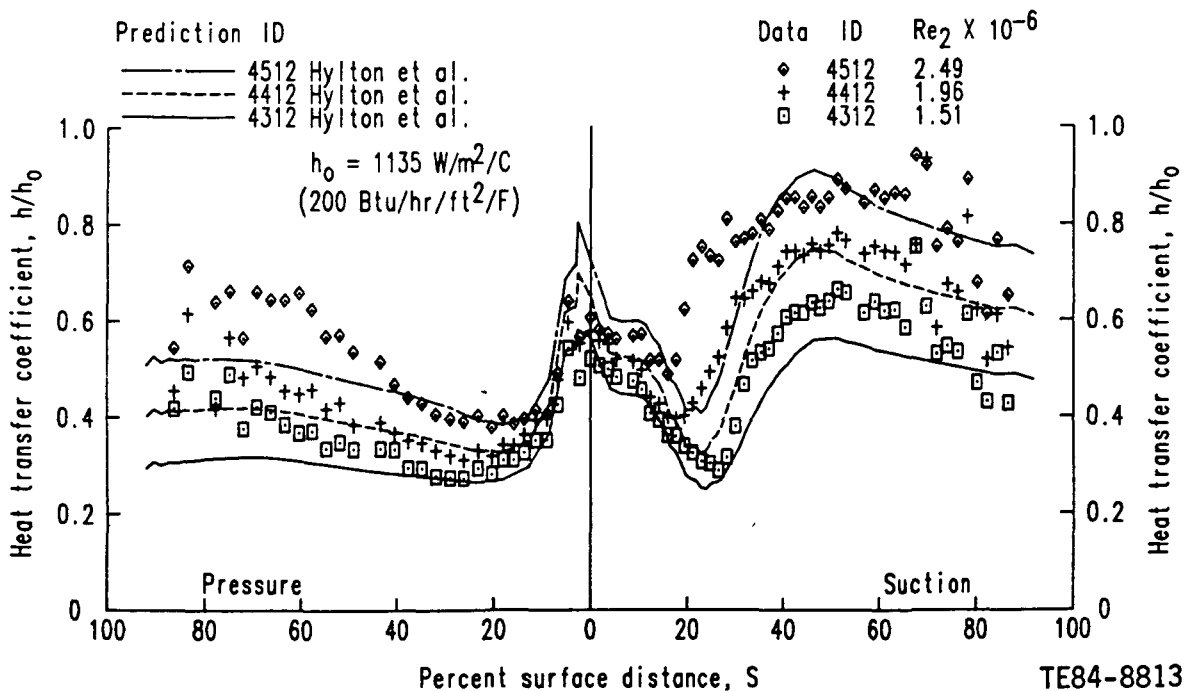
Figure 113. Predicted nonfilm-cooled C3X airfoil heat transfer coefficient distributions obtained using the STAN5 computer code and the Hylton et al effective viscosity formulation.
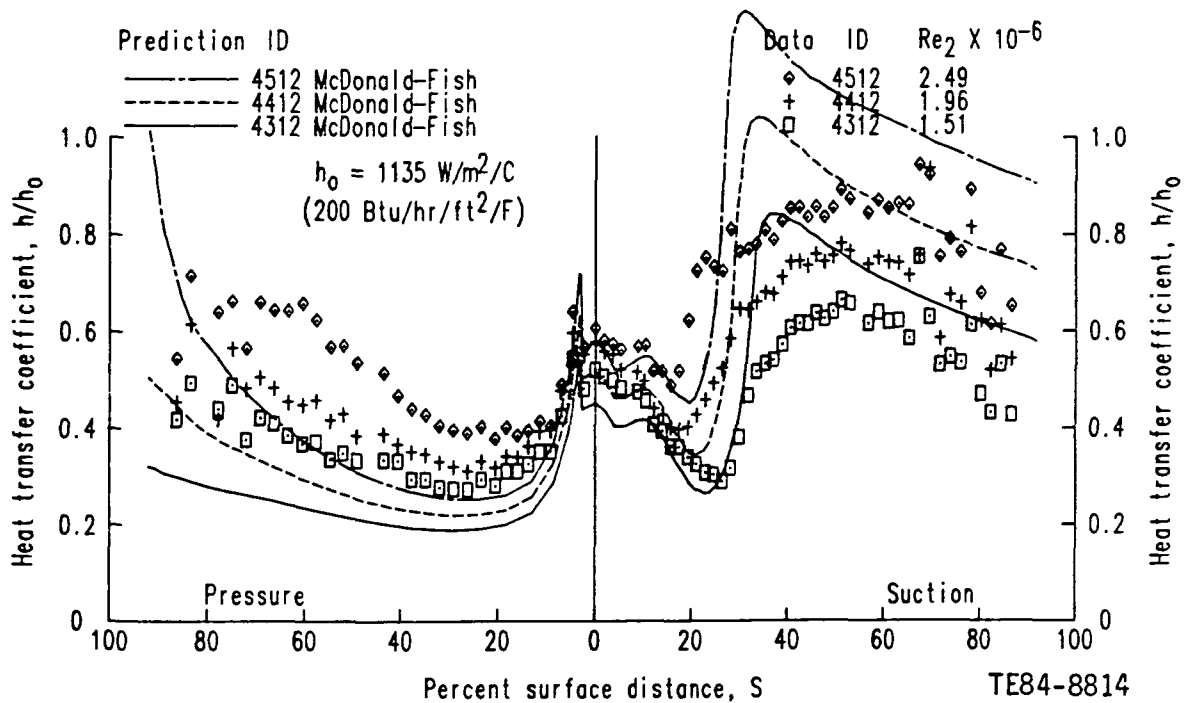
Figure 114. Predicted nonfilm-cooled C3X airfoil heat transfer coefficient distributions obtained using the STAN5 computer code and the McDonald-Fish effective viscosity formulation (constant free-stream turbulence intensity boundary condition).
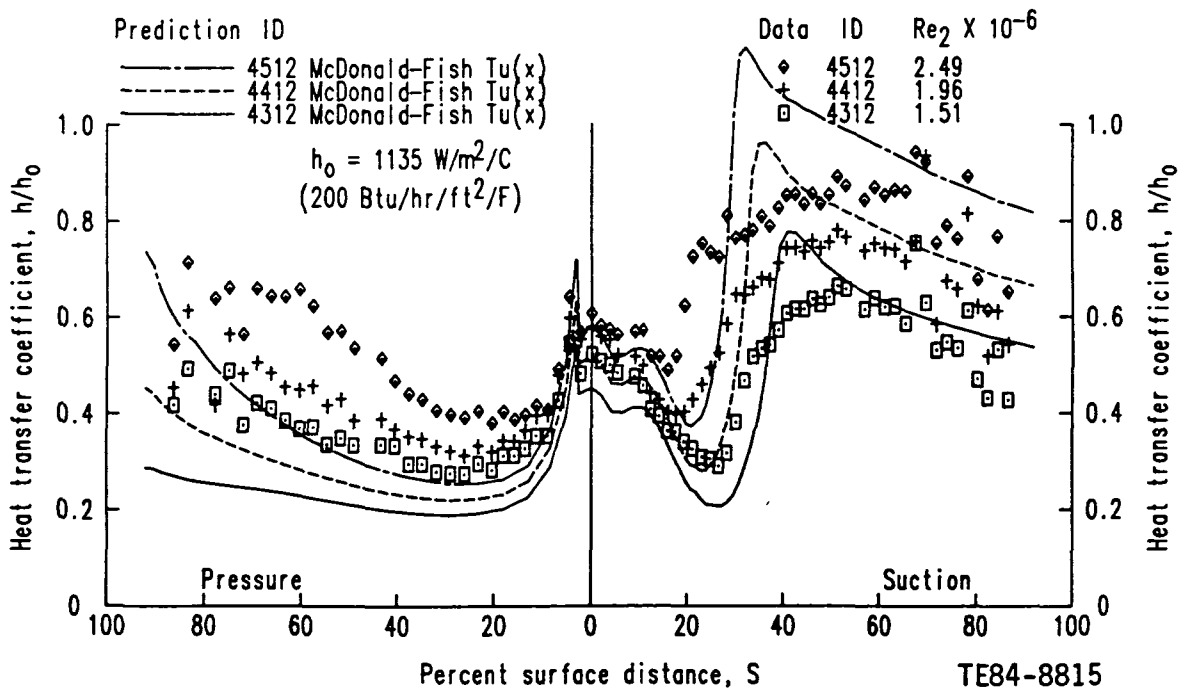
Figure 115. Predicted nonfilm-cooled C3X airfoil heat transfer coefficient distributions obtained using the STAN5 computer code and the McDonald-Fish effective viscosity formulation (variable free-stream turbulence intensity boundary condition).

The McDonald-Fish predictions shown in these figures are distinguished by the fact that for computations shown in Figure 114, the local free-stream turbulence intensity boundary condition was held constant (equal to measured upstream value, 6.5%) and those shown in Figure 115 were computed with a variable turbulence intensity boundary condition [Equation (20)]. The constant turbulence intensity boundary condition is in keeping with the approach discussed in Ref 22 while the variable boundary condition definition is consistent with the approach in Ref 1 used in the formulation discussed in section 4.3. Because the variable boundary condition definition decays (reduces) the turbulence intensity as the Reynolds number increases (as the computation proceeds downstream) the principle difference between the two sets of predictions shown in Figures 114 and 115 is the indicated location of transition occurrence. Beside the implication that transition location can be controlled using the free-stream turbulence intensity boundary condition, both the extended pressure surface and shorter suction surface transition zones indicated by the data are simulated quite well. In modeling transition phenomena as a function of free-stream turbulence, the turbulence model of Ref 22 was better than any of those tested in Ref 1.

The apparent discrepancies between predicted and measured heat transfer levels (especially on the pressure surface) support the idea that for simulating the heat transfer augmentation in nominally laminar zones an effective viscosity formulation that includes a preturbulent flow viscosity term is important. In the general effective viscosity (μ_{eff}) definition given by Equation (10)

$$\mu_{eff} = \mu + \gamma_t \mu_t + \gamma_{Tu} \mu_{Tu} \tag{10}$$

the term $(\gamma_{Tu} \mu_{Tu})$ is included to explicitly model the heat transfer augmentation phenomena in laminar zones where by definition the transition model term (γ_t) would be equal to zero. The importance of including this term in an overall gas turbine environment formulation as related to heat transfer level prediction is illustrated by the results shown in Figures 112 through 114. As originally formulated, both the effective viscosity formulation (Ref 10) used to produce the predictions shown in Figure 112 and the Ref 22 formulation used to produce the predictions shown in Figures 114 and 115 do not contain an explicit model for the term, $\gamma_{Tu} \mu_{Tu}$ (i.e., $\mu_{eff} = \mu + \gamma_t \mu_t$). Although the effective viscosity formulation from Ref 1 used to generate the

predictions shown in Figure 113 contained an explicit model for the $\gamma_{Tu}\mu_{Tu}$ term, $\gamma_t\mu_t$ was not included (i.e., $\mu_{eff} = \mu + \gamma_{Tu}\mu_{Tu}$). On comparing the results shown in Figures 112, 114, and 115 with those shown in Figure 113 in terms of the difference in effective viscosity formulation ($\mu_{eff} = \mu + \gamma_t\mu_t$ versus $\mu_{eff} = \mu + \gamma_{Tu}\mu_{Tu}$), it could be argued that although the first formulation is sufficient for predicting trends, the second formulation gives a better indication of level. Based on results like these, the full effective viscosity formulation [Equation (10)] was adopted in this study to take advantage of both the trend predicting characteristics of the $\gamma_{Tu}\mu_{Tu} = 0$ formulation and the level predicting attributes of the $\gamma_t\mu_t = 0$ formulation. This formulation is defined in section 4.3. Predictions obtained using this model for the same data cases shown in Figures 112 through 115 are shown in Figure 116.

In summary, the McDonald-Fish turbulence model (Ref 22) was an attractive approach for simulating transition phenomena within a single transition/fully turbulent flow formulation. In addition, results shown here indicate that the overall effective viscosity formulation could be improved by including a term to model laminar heat transfer augmentation.
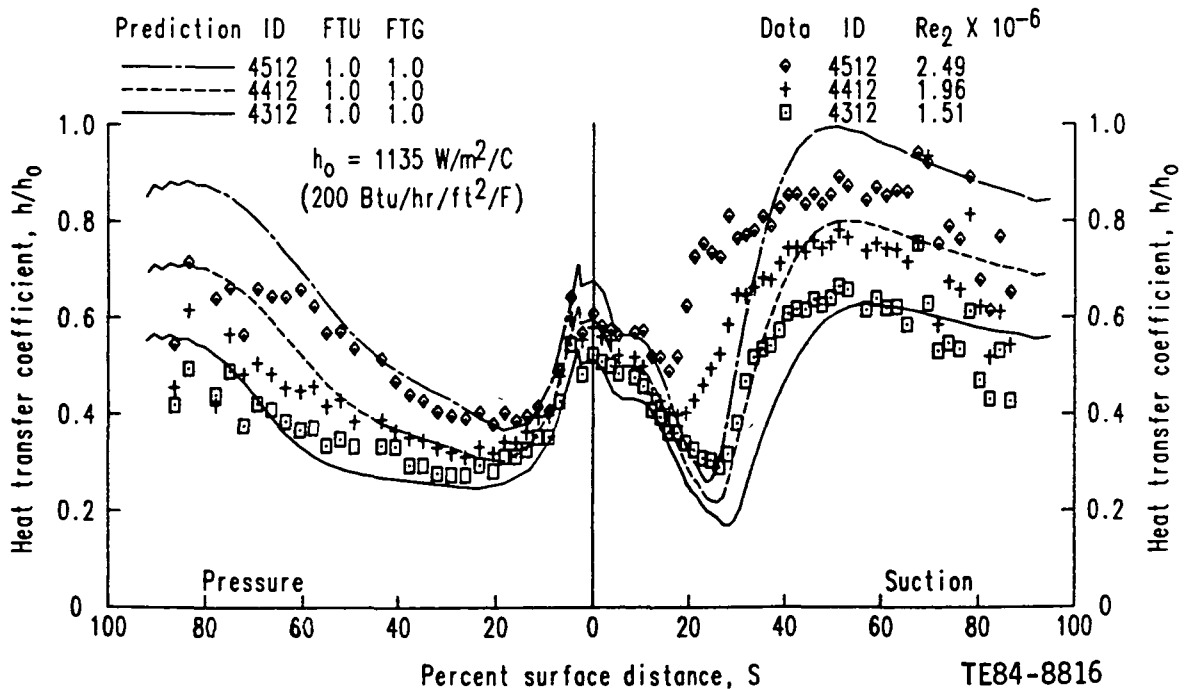
Figure 116. Predicted nonfilm-cooled C3X airfoil heat transfer coefficient distributions obtained using the STAN5 computer code and the proposed leading edge film-cooled method.

APPENDIX D
STAGNATION ZONE SOLUTION INITIATION: STANCOOL EVALUATION

To avoid computing in the actively cooled leading edge region and explicitly modeling coolant jet/boundary layer interaction in the stagnated leading edge region, the approach adopted in this program was to initiate the boundary layer computation in the recovery region and model the recovery region phenomena due to the upstream injection by defining effective free-stream turbulence intensity and gas temperature boundary conditions. In the initial stages of this program, an alternative approach, which initiated the boundary layer computation in the actively cooled leading edge region, was tested. For this approach, the STANCOOL (Ref 7) boundary layer code was used. As documented by Crawford et al (Ref 7), the STANCOOL code is an extension of the STAN5 code containing a model for simulating a discrete site injection process. Because the method is structured to deal with the injection on a row-by-row basis as the computation proceeds downstream, a STANCOOL computation can be initiated in the leading edge region and marched across the injection locations. In a stagnation zone solution initiation approach, the STANCOOL formulation can be applied directly. The purpose of this study was to determine if the STANCOOL coolant jet/boundary layer interaction model was applicable for the stagnated flow injection conditions characteristic of the leading edge film-cooling problem.

To evaluate the method, recovery region Stanton number reduction (SNR) distributions were computed for a number of blowing condition cases comprising the leading edge film-cooled C3X vane data base. The blowing condition case simulated is that identified as run 4415 in Table VI. As the first step in computing the SNR distribution for this case, the no-blowing baseline (4400) heat transfer coefficient (h) or Stanton number (St_{NFC}) distribution was computed. The predicted no-blowing condition heat transfer coefficient distribution compared with measured data is shown in Figure 117.

The suction and pressure surface STANCOOL boundary layer computations performed to produce the results shown in Figure 117 were initiated a small distance downstream of a stagnation point location determined from the results of a non-film-cooled airfoil inviscid blade-to-blade analysis. In Figure 117, the
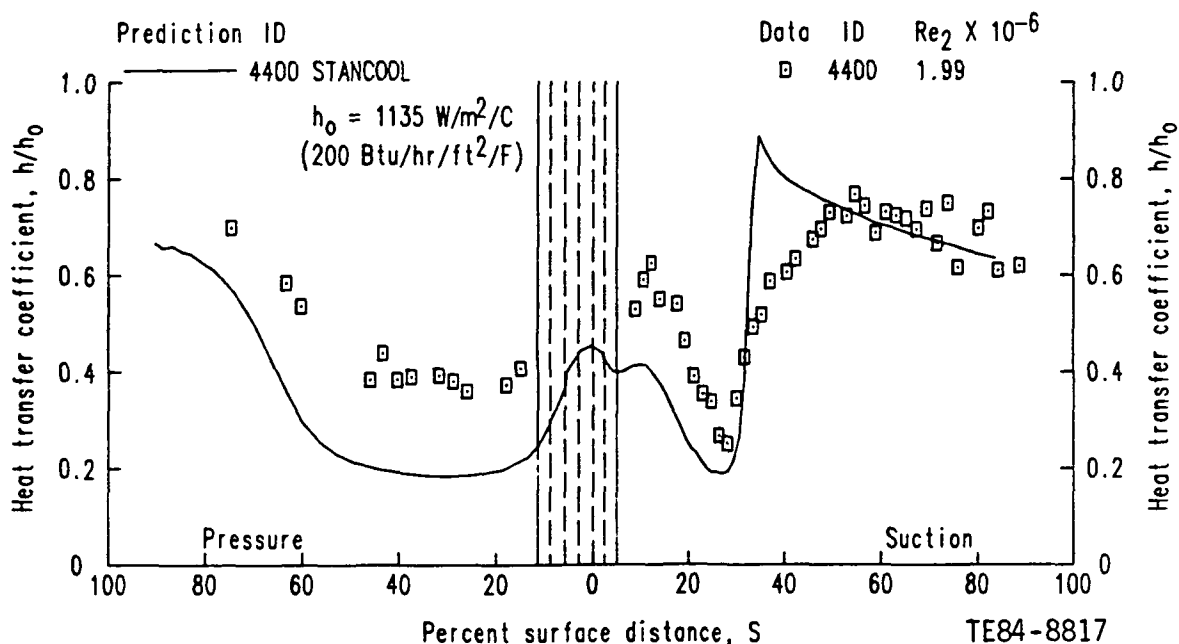
Figure 117. Comparison of predicted and measured no—blowing
heat transfer coefficient distributions using the unmodified STANCOOL
computer code where $T_w/T_g = 0.8$.

stagnation point location corresponds to the surface distance location of the
center row of the five rows of cooling holes (represented by the five vertical
dashed lines drawn around $S = 0$). For the pressure surface computation, the
flow was assumed to be fully turbulent and for the suction surface, the compu-
tation was set up initially to calculate in the laminar mode with transition
defined to start when the momentum thickness Reynolds number reached 350. The
transition and mixing length turbulence model formulations used for the compu-
tation were the unmodified forms contained in STAN5 and/or STANCOOL codes docu-
mented in Ref 7 and 10, respectively. (In STAN5/STANCOOL usage, the pressure
surface computations were performed with MODE = 2 and the suction surface com-
putations with MODE = 1 and RETRAN = 350.) The fully turbulent pressure sur-
face/laminar-transitional-turbulent suction surface simulation follows the
overall approach adopted in this work as discussed in section 4. For all blow-
ing and no-blowing condition computations, the wall temperature was assumed
constant ($T_w/T_g = 0.8$).

For setting up the blowing condition (4415) computations, the experimentally
determined row mass flux ratios [$M = (\rho_w u_w)/(\rho_e/u_e)$] reported in

206

Table IX were used. Because the suction/pressure surface computations were
initiated downstream of the center row of holes (stagnation point location),
this injection location was not considered in the analysis. (This is equiva-
lent to setting M = 0 for the center row.) For both the suction and pressure
surface computations only two rows of cooling holes were specified. Computa-
tions were performed with θ = 1.24 [θ = $(T_c - T_g)/(T_w - T_g)$] to be consistent
with the constant wall temperature assumption. The coolant row location(s) and
values of blowing ratio (M) and film-cooling effectiveness parameter (θ) are
summarized in Table X.

Table X.
Film-cooling parameters (M and θ) for run ID 4415 simulation.

	Suction surface			Pressure surface		
	S (%)	M	θ	S (%)	M	θ
Row 1	0.08	2.08	1.24	5.83	2.34	1.24
Row 2	2.40	1.35	1.24	8.81	1.91	1.24

Besides defining the row film cooling parameters, blowing ratio and film-
cooling effectiveness parameter for the STANCOOL computations, values for the
so-called injection and turbulence augmentation parameters (DELMR and ALAM,
respectively) have to be specified. Crawford et al (Ref 7) developed analyti-
cal expressions for these parameters for the three hole slant angle (α) and
skew angle (β) geometries investigated in the Stanford work (Ref 7). The ALAM
and DELMR expressions as functions of the blowing ratio are reproduced in Fig-
ures 118 and 119, respectively. Because the hole axis geometry (α = 45 deg,
β = 90 deg) and experimental flow conditions for the leading edge film-cooled
C3X vane cascade experiments were significantly different from the Stanford
flat plate experiments (Ref 7), the results shown in Figures 118 and 119 were
used only as a guide for determining values of ALAM and DELMR that were repre-
sentative in order of magnitude.
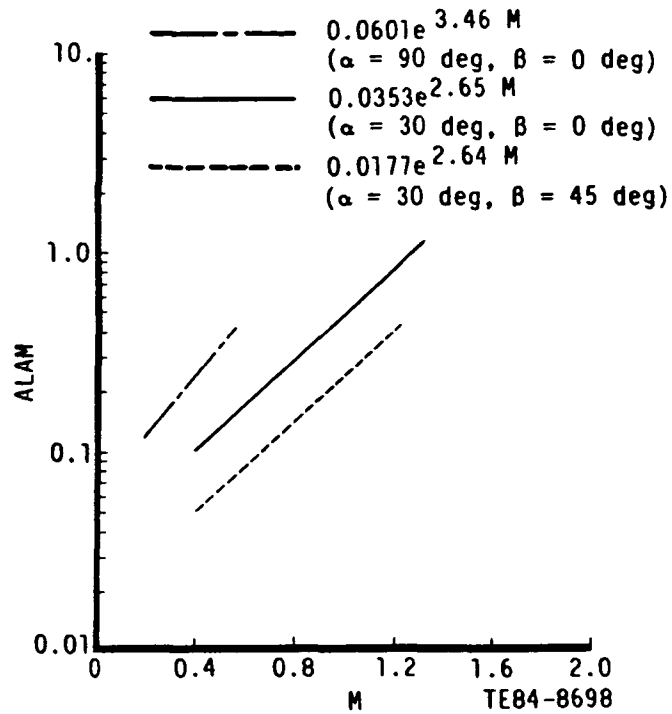
Figure 118.   STANCOOL turbulence augmentation parameter, ALAM.
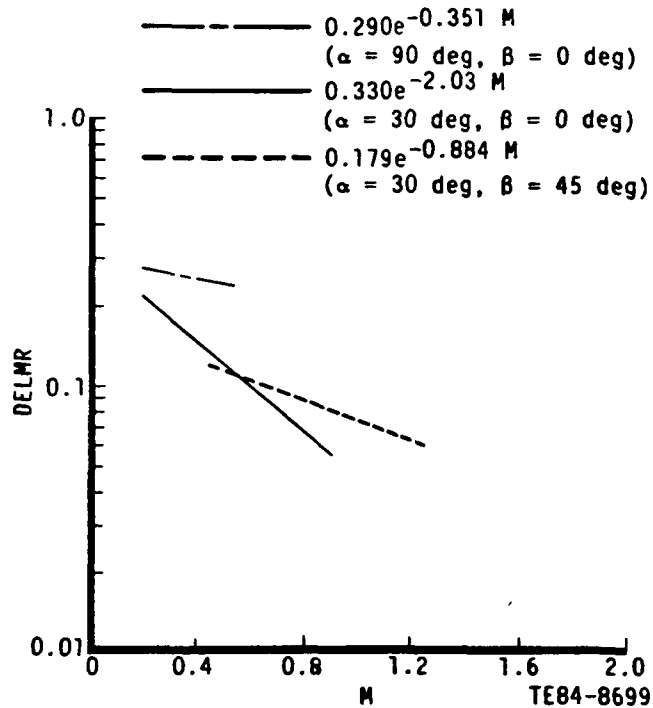
Figure 119.   STANCOOL injection parameter, DELMR.

208
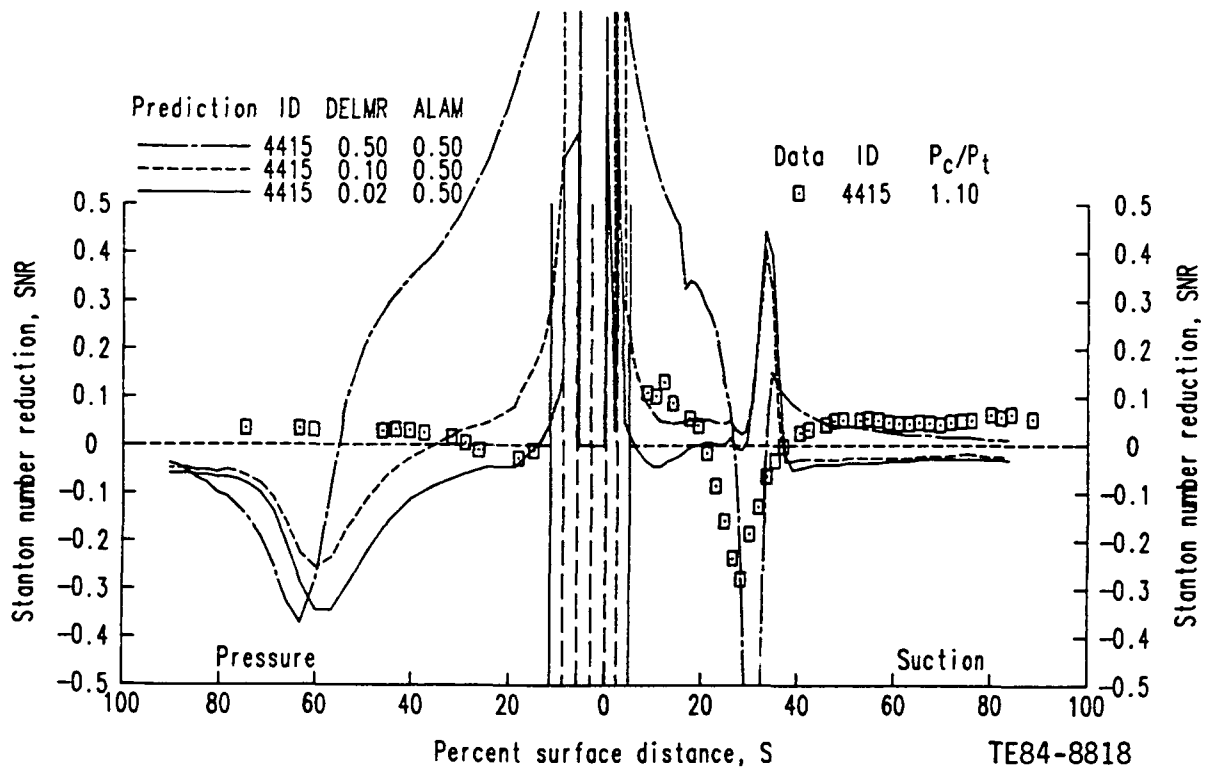
Figure 120. Characteristic STANCOOL predicted Stanton number reduction
distributions and the influence of injection parameter specifications
where $T_w/T_g = 0.8$.

Figure 120 shows three STANCOOL SNR distribution predictions for the 4415 op-
erating conditions compared with the measured distribution. To illustrate that
the computations were initiated within the stagnated flow zone, predicted re-
sults are shown there. However, because measurements were made only in the
recovery region (downstream of the solid vertical lines around S = 0) the
emphasis is placed on only the recovery region result. As the legend indi-
cates, the only difference between the three predicted distributions is the
value of DELMR specified for each computation. As indicated, the result ob-
tained was found to be very sensitive to the value of DELMR. Like Stepka and
Gaugler (Ref 3), coolant was allowed to penetrate the boundary layer and only
the fraction added within the boundary layer at the injection location was
carried in the downstream calculation. The magnitude of the DELMR parameter
controls the amount added; increasing DELMR is equivalent to increased mass
addition. As shown in Figure 120, trapping more coolant significantly reduces
the near downstream recovery region heat transfer level (positive SNR).

For all blowing condition cases tested, the specified value of ALAM was found
to have little or no effect on the overall result as expected because this
parameter controls the magnitude of an augmented mixing length. On the suction

209

surface the flow in the leading edge is initially assumed to be laminar, thus ALAM would have no direct influence unless the boundary layer was transitioned within the array. As for the no-blowing condition simulations, a suction surface momentum thickness Reynolds number transition criterion of RETRAN = 350 was used for the computations shown in Figure 120. For DELMR = 0.50, this value was reached at the second row of holes. Thus, the prediction shown is characteristic of the type of result obtained when simulating early transition due to the injection. Because the pressure surface computations were performed assuming fully turbulent flow, varying the mixing length magnitude by means of ALAM specification had some effect. But because in the STANCOOL formulation the augmented mixing length decayed within two boundary layer thicknesses after the last row of cooling holes, the effect on the downstream recovery region result was negligible.

In addition to changing the magnitude of the two free parameters, ALAM and DELMR, STANCOOL computations were performed using different assumptions regarding boundary layer state at blowing and no-blowing conditions and blowing strength (M) levels. The SNR predictions shown in Figure 120 were based on the assumption that at both blowing (4415) and no-blowing (4400) conditions, the pressure surface boundary layer was fully turbulent and the suction surface boundary layer was initially laminar and began transition when the local momentum thickness Reynolds number reached 350. Also, row M values determined experimentally shown in Table X were specified. In contrast, Figure 121 shows results of STANCOOL computations where, at no-blowing conditions, the fully turbulent pressure surface/transitional suction surface assumption was the same as before, but at blowing conditions, both the suction and pressure surface boundary layers were computed in a fully turbulent mode. The solid curve predictions were obtained using the experimentally determined row M values (Table X; M fraction = 1.0) and the broken curve predictions using half the experimental value (M fraction = 0.5). As the results shown in Figure 121 indicate, the data trend on the suction surface is zonally reproduced but the pressure surface trend is not. These results also show that by adjusting row M values to account for possible experimental errors in measured levels, quantitative agreement can be locally improved but the overall predicted trend remains the same.

Predicted SNR results such as those shown in Figures 120 and 121 for the C3X
at the 4415 blowing condition are characteristic of those obtained at all other
blowing conditions simulated. However, although a number of things were tried
in an attempt to better match SNR data trends and levels, the STANCOOL/stagna-
tion zone solution initiation approach was not fully explored and a serious
developmental effort was not conducted. Although results obtained in this
study were used to partially justify the development of the alternative, re-
covery region solution initiation approach discussed in this report, the re-
sults were not meant to imply that the STANCOOL/stagnation zone solution ini-
tiation approach could not be developed into a useful design tool. The results
do however suggest that a nontrivial developmental effort would be required to
improve the procedure.
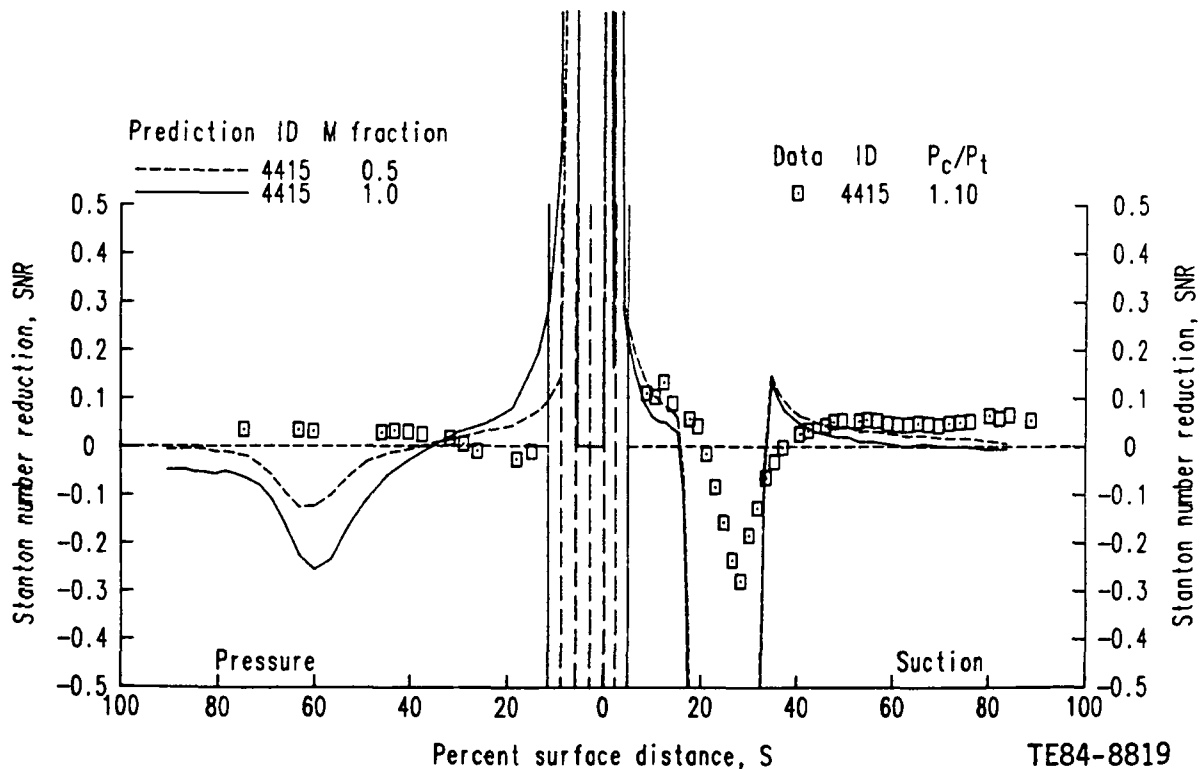
Figure 121. STANCOOL predicted Stanton number reduction distributions
assuming fully turbulent flow and two assumptions regarding row blowing
strength where DELMR = 0.10, ALAM = 0.50, and T_w/T_g = 0.8.

APPENDIX E
SAMPLE STAN5 INPUT DATA

To facilitate an independent evaluation of the overall method developed in this program, STAN5 input decks for one no-blowing condition case and one blowing condition case follow in Tables XI through XIV. The no-blowing condition case corresponds to that identified as ID 4400 in Table VI and the blowing condition case as ID 4415. For each case, separate suction and pressure surface input streams are included.

Figure 122 depicts heat transfer coefficient predictions obtained using ID 4400 input decks and the STAN5 code. These predictions are compared with the experimentally determined distribution obtained at the 4400 operating condition. The prediction labeled unmodified was produced using the original Crawford et al version of STAN5 documented in Ref 10. To reproduce that result, no STAN5 modifications are necessary. In the 4400 suction surface input deck, RETRAN = 350 and MODE = 1. In the pressure surface deck, RETRAN = 350 but MODE = 2. This setup, where the suction surface boundary layer is allowed to transition and the pressure surface boundary layer is assumed to be fully turbulent, is consistent with the proposed approach and is illustrated in both the modified and unmodified results shown in Figure 122.

The prediction labeled modified was generated with the method defined in section 4.3. To assist in implementing the proposed effective viscosity model, the local free-stream turbulence intensity (Tu_e) boundary condition defined using Equation (20) is given in the AUX2 vector [i.e., $AUX2(X) = Tu_e(X)$].

The blowing condition suction and pressure surface input decks for case 4415 are complete in the sense that all boundary condition quantities dependent on FTU and FTG have been modified [e.g., $AUX2(X)_{4415} = 1.2*AUX2(X)_{4400}$ consistent with the definition $Tu_e^* = FTU(Tu_e)$].

Figure 123 illustrates the wall temperature boundary conditions (T_w/T_g curves) contained in the 4400 and 4415 input decks. In keeping with STAN5 usage, these variable wall temperature boundary conditions are given as NXBC local wall enthalpy values in the FJ(1, 1:NXBC) array.
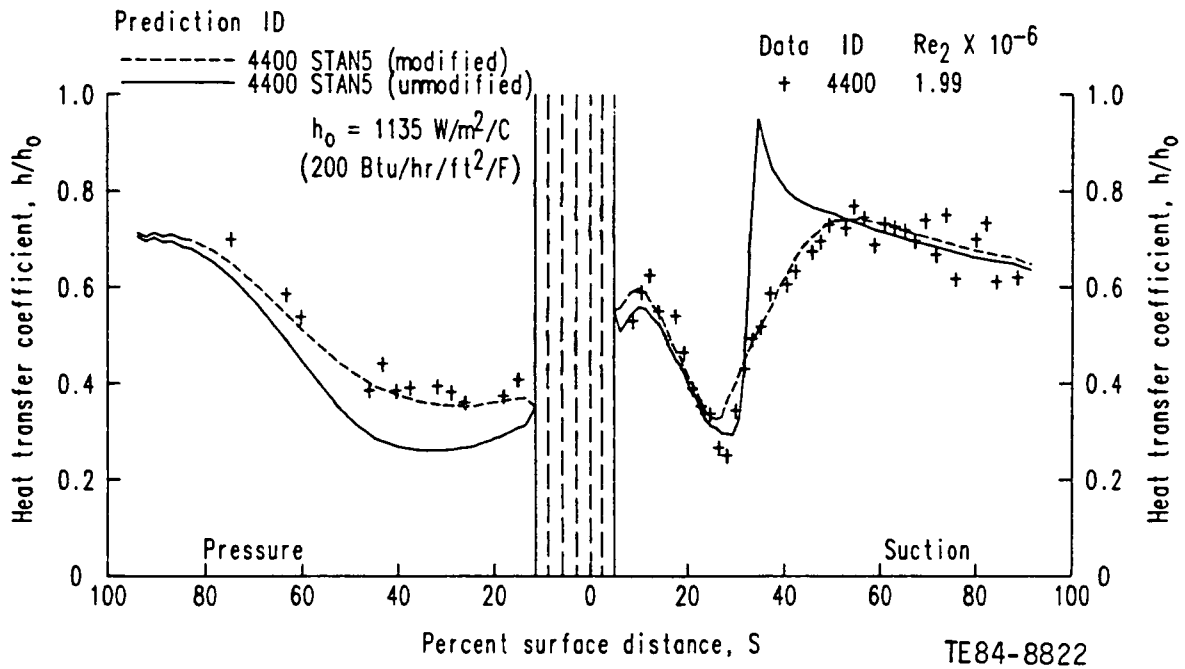
Figure 122. Predicted suction and pressure surface heat transfer coefficient distributions using run 4400 STAN5 input data streams with no-blowing simulation and where FTU = FTG = 1.0.
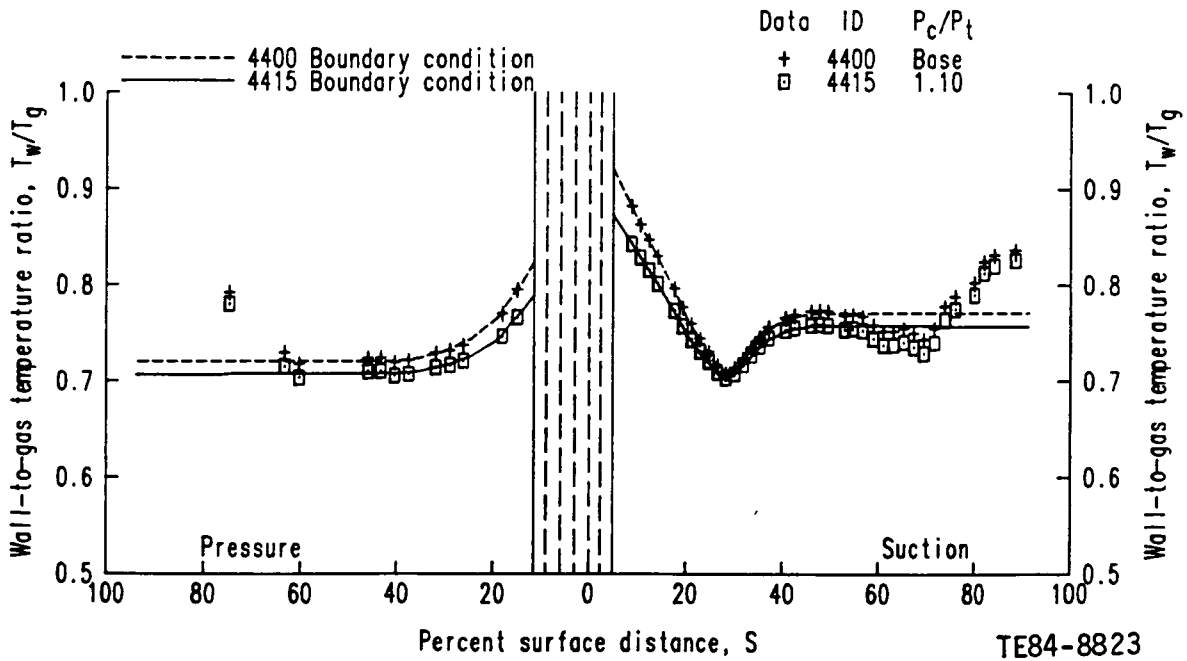
Figure 123. Normalized wall temperature boundary condition distributions used to generate wall enthalpy boundary conditions for STAN5 input streams for runs 4400 and 4415.

Predicted heat transfer coefficient distributions obtained using the method defined in Section IV and the 4400 and 4415 input decks in Table XI are shown in Figure 124 along with the measured data distributions. These no-blowing (4400, FTU = 1.00, FTG = 1.00) and blowing (4415, FTU = 1.20, FTG = 0.94) condition predicted and measured distributions can be used to form Stanton number reduction (SNR) distributions. These distributions are shown in Figure 125.

Finally, although the input format given is STAN5 specific, the decks contain sufficient information (boundary conditions and initial location boundary layer profiles) for executing any other code with a mixing length turbulence model. By reviewing the input format sequence documented by Crawford et al for STAN5 (Ref 10), it should be possible to reformat the following data decks to test the proposed modeling approach using another numerical framework.
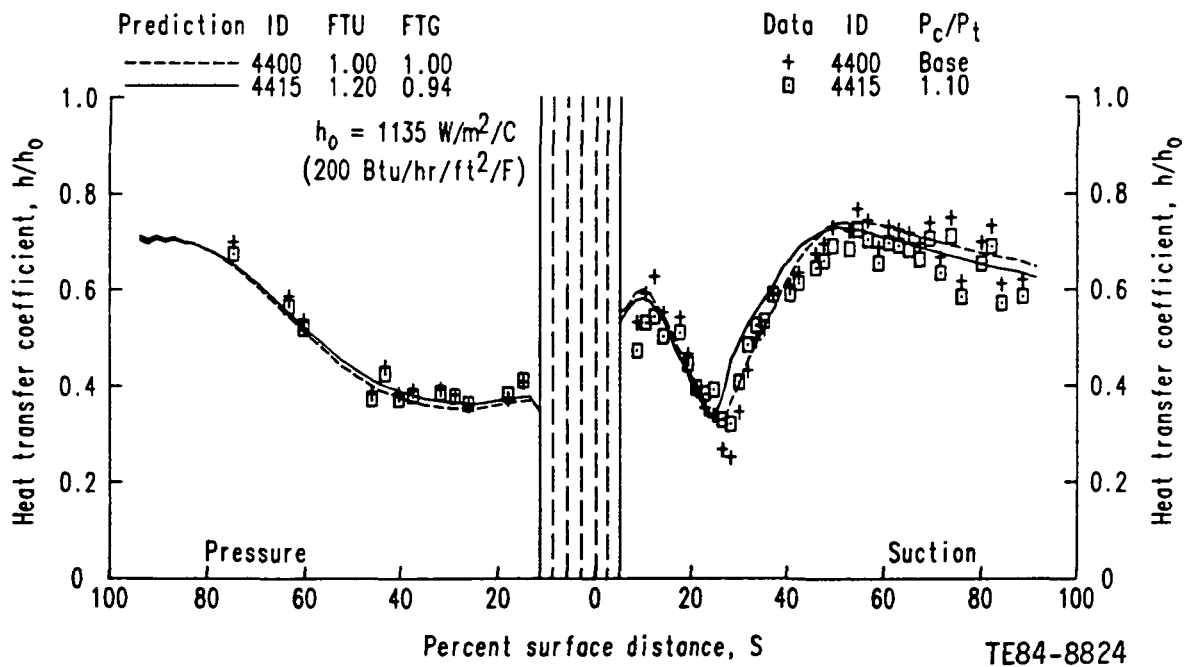
Figure 124. Sample heat transfer coefficient distributions predicted by using input streams and STAN5 code with leading edge film-cooled method modifications for runs 4400 and 4415.
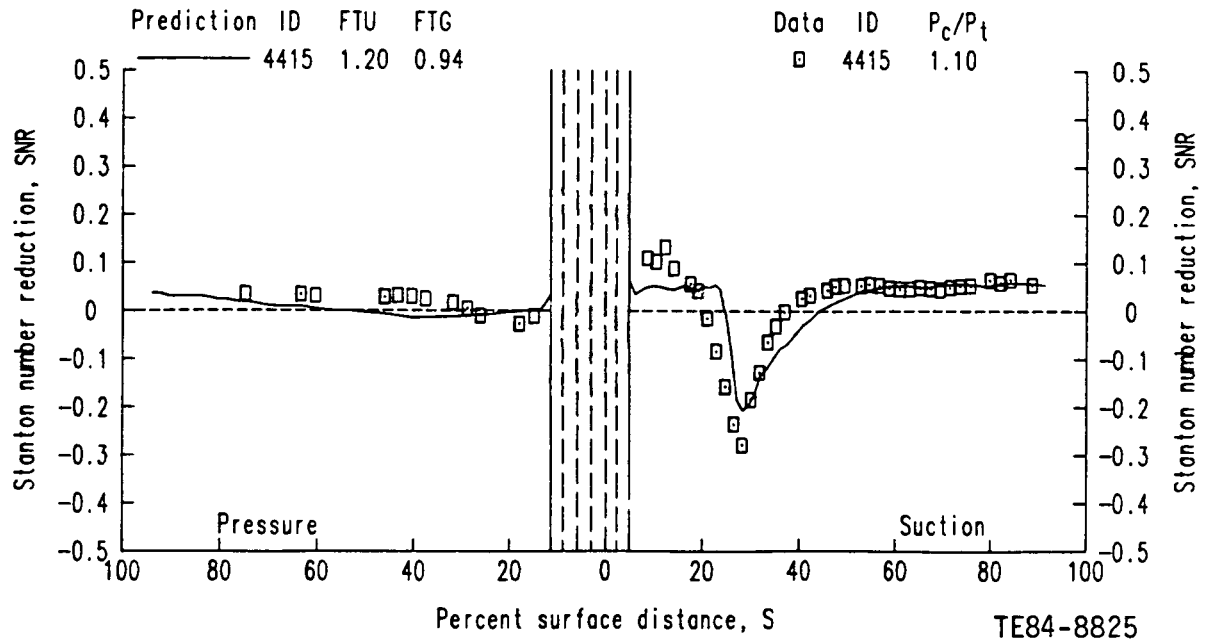
Figure 125. Analytical Stanton number reduction distribution determined
for blowing conditions data using modified STAN5 for run 4415 and
input streams for runs 4400 and 4415.

Table XI.
Suction surface STAN5 input data for run ID 4400.

```
TITLE(1:18)
4400 FTU=1.00 FTG=1.00 (SUCTION)
 GEOM,MODE,FLUID,NEQ,N,KEX,KIN,KENT
    1    1    2    2   39   2   1    1
 XU,XL,DELTAX,RETRAN,FRA,ENFRA,GV
  0.043356  0.596273      1.00     350.00      0.01      0.001      0.0
 BODFOR,SOURCE(1:5)
    0    1    0    0    0
 PO,RHOC,VISOC,PRC(1:5)
  5500.035 0.0842410 0.0000220 0.6837637      0.0       0.0        0.0       0.0
 NXBC,TYPBC(1:5)
   55    1    0    0    0    0
 X(1:NXBC),RW(1:NXBC),AUX1(1:NXBC),AUX2(1:NXBC)
  0.0            1.0            0.0            0.0660
  0.000385       1.0            0.0            0.0660
  0.002639       1.0            0.0            0.0660
  0.014532       1.0            0.0            0.0660
  0.026118       1.0            0.0            0.0660
  0.038602       1.0            0.0            0.0517
  0.043356       1.0            0.0            0.0477
  0.050869       1.0            0.0            0.0424
  0.062166       1.0            0.0            0.0361
  0.072166       1.0            0.0            0.0323
  0.081144       1.0            0.0            0.0295
  0.089225       1.0            0.0            0.0279
  0.096691       1.0            0.0            0.0269
  0.103648       1.0            0.0            0.0261
  0.110283       1.0            0.0            0.0257
  0.116707       1.0            0.0            0.0255
  0.122917       1.0            0.0            0.0252
  0.129064       1.0            0.0            0.0252
  0.135200       1.0            0.0            0.0253
  0.141303       1.0            0.0            0.0252
  0.147439       1.0            0.0            0.0253
  0.153668       1.0            0.0            0.0253
  0.159987       1.0            0.0            0.0253
  0.166410       1.0            0.0            0.0253
  0.172980       1.0            0.0            0.0253
  0.179719       1.0            0.0            0.0253
  0.186625       1.0            0.0            0.0253
  0.193727       1.0            0.0            0.0254
  0.201069       1.0            0.0            0.0254
  0.208640       1.0            0.0            0.0254
  0.216482       1.0            0.0            0.0254
  0.224654       1.0            0.0            0.0254
  0.233132       1.0            0.0            0.0254
  0.242050       1.0            0.0            0.0255
  0.251392       1.0            0.0            0.0255
  0.261313       1.0            0.0            0.0255
  0.271866       1.0            0.0            0.0255
  0.283245       1.0            0.0            0.0256
  0.295542       1.0            0.0            0.0255
  0.309035       1.0            0.0            0.0256
  0.323880       1.0            0.0            0.0255
  0.340328       1.0            0.0            0.0255
  0.358624       1.0            0.0            0.0255
  0.378942       1.0            0.0            0.0255
  0.401333       1.0            0.0            0.0254
  0.425630       1.0            0.0            0.0254
  0.451360       1.0            0.0            0.0254
  0.477673       1.0            0.0            0.0254
  0.503399       1.0            0.0            0.0253
  0.527307       1.0            0.0            0.0254
  0.548386       1.0            0.0            0.0253
  0.565980       1.0            0.0            0.0254
  0.579349       1.0            0.0            0.0253
  0.589556       1.0            0.0            0.0254
  0.596273       1.0            0.0            0.0253
```

Table XI. (cont)

```
UG(1:NXBC),AM(1:NXBC),FJ(1:5,1:NXBC)
     0.0        0.0      289.33        0.0        0.0        0.0        0.0
     3.3155     0.0      289.91        0.0        0.0        0.0        0.0
    25.7815     0.0      291.26        0.0        0.0        0.0        0.0
   151.6731     0.0      285.64        0.0        0.0        0.0        0.0
   266.3811     0.0      280.21        0.0        0.0        0.0        0.0
   361.2339     0.0      276.00        0.0        0.0        0.0        0.0
   398.8586     0.0      276.00        0.0        0.0        0.0        0.0
   463.4282     0.0      271.72        0.0        0.0        0.0        0.0
   589.4739     0.0      265.27        0.0        0.0        0.0        0.0
   714.1738     0.0      259.59        0.0        0.0        0.0        0.0
   854.1877     0.0      255.02        0.0        0.0        0.0        0.0
   976.5437     0.0      251.08        0.0        0.0        0.0        0.0
  1087.8469     0.0      247.16        0.0        0.0        0.0        0.0
  1208.8740     0.0      243.64        0.0        0.0        0.0        0.0
  1296.9946     0.0      240.29        0.0        0.0        0.0        0.0
  1362.6226     0.0      237.06        0.0        0.0        0.0        0.0
  1446.7546     0.0      233.52        0.0        0.0        0.0        0.0
  1503.2920     0.0      230.08        0.0        0.0        0.0        0.0
  1529.7795     0.0      226.98        0.0        0.0        0.0        0.0
  1566.8110     0.0      224.11        0.0        0.0        0.0        0.0
  1597.2537     0.0      221.37        0.0        0.0        0.0        0.0
  1599.9609     0.0      218.85        0.0        0.0        0.0        0.0
  1600.3584     0.0      216.32        0.0        0.0        0.0        0.0
  1603.8132     0.0      213.69        0.0        0.0        0.0        0.0
  1591.4250     0.0      211.62        0.0        0.0        0.0        0.0
  1574.0530     0.0      210.06        0.0        0.0        0.0        0.0
  1561.5911     0.0      211.06        0.0        0.0        0.0        0.0
  1540.9324     0.0      212.67        0.0        0.0        0.0        0.0
  1521.9329     0.0      214.92        0.0        0.0        0.0        0.0
  1504.8792     0.0      217.70        0.0        0.0        0.0        0.0
  1487.6892     0.0      220.20        0.0        0.0        0.0        0.0
  1471.5361     0.0      222.73        0.0        0.0        0.0        0.0
  1460.0193     0.0      224.98        0.0        0.0        0.0        0.0
  1444.8464     0.0      226.22        0.0        0.0        0.0        0.0
  1434.3489     0.0      227.51        0.0        0.0        0.0        0.0
  1420.0120     0.0      228.45        0.0        0.0        0.0        0.0
  1412.0403     0.0      229.04        0.0        0.0        0.0        0.0
  1401.9111     0.0      229.60        0.0        0.0        0.0        0.0
  1402.0046     0.0      229.60        0.0        0.0        0.0        0.0
  1400.3477     0.0      229.60        0.0        0.0        0.0        0.0
  1408.2632     0.0      229.60        0.0        0.0        0.0        0.0
  1412.7051     0.0      229.60        0.0        0.0        0.0        0.0
  1423.2046     0.0      229.60        0.0        0.0        0.0        0.0
  1431.5305     0.0      229.60        0.0        0.0        0.0        0.0
  1444.0496     0.0      229.60        0.0        0.0        0.0        0.0
  1458.0178     0.0      229.60        0.0        0.0        0.0        0.0
  1472.6646     0.0      229.60        0.0        0.0        0.0        0.0
  1489.6809     0.0      229.60        0.0        0.0        0.0        0.0
  1503.6548     0.0      229.60        0.0        0.0        0.0        0.0
  1512.9565     0.0      229.60        0.0        0.0        0.0        0.0
  1524.8584     0.0      229.60        0.0        0.0        0.0        0.0
  1525.8408     0.0      229.60        0.0        0.0        0.0        0.0
  1543.5410     0.0      229.60        0.0        0.0        0.0        0.0
  1600.7864     0.0      229.60        0.0        0.0        0.0        0.0
  1809.6770     0.0      229.60        0.0        0.0        0.0        0.0
Y(1:N+1),U(1:M+1),F(1:5,1:M+1)
 .0            .0      .27600E+03.0            .0          .0          .0
 .38309E-05.12212E+02.27637E+03.0            .0          .0          .0
 .80449E-05.25403E+02.27678E+03.0            .0          .0          .0
 .12680E-04.39600E+02.27724E+03.0            .0          .0          .0
 .17779E-04.54809E+02.27773E+03.0            .0          .0          .0
 .23388E-04.71018E+02.27828E+03.0            .0          .0          .0
 .29558E-04.88183E+02.27888E+03.0            .0          .0          .0
 .36345E-04.10623E+03.27953E+03.0            .0          .0          .0
 .43810E-04.12504E+03.28023E+03.0            .0          .0          .0
 .52022E-04.14444E+03.28099E+03.0            .0          .0          .0
 .61055E-04.16424E+03.28180E+03.0            .0          .0          .0
 .70991E-04.18419E+03.28266E+03.0            .0          .0          .0
 .81921E-04.20401E+03.28356E+03.0            .0          .0          .0
 .93945E-04.22339E+03.28450E+03.0            .0          .0          .0
 .10717E-03.24203E+03.28545E+03.0            .0          .0          .0
 .12172E-03.25966E+03.28642E+03.0            .0          .0          .0
 .13772E-03.27603E+03.28737E+03.0            .0          .0          .0
 .15532E-03.29099E+03.28832E+03.0            .0          .0          .0
```

Table XI. (cont)

```
.17469E-03.30497E+03.28926E+03.0          .0          .0          .0
.19599E-03.31810E+03.29022E+03.0          .0          .0          .0
.21942E-03.33029E+03.29118E+03.0          .0          .0          .0
.24519E-03.34145E+03.29213E+03.0          .0          .0          .0
.27354E-03.35151E+03.29307E+03.0          .0          .0          .0
.30472E-03.36045E+03.29398E+03.0          .0          .0          .0
.33903E-03.36825E+03.29486E+03.0          .0          .0          .0
.37676E-03.37493E+03.29569E+03.0          .0          .0          .0
.41827E-03.38054E+03.29647E+03.0          .0          .0          .0
.46392E-03.38514E+03.29719E+03.0          .0          .0          .0
.51415E-03.38883E+03.29783E+03.0          .0          .0          .0
.56939E-03.39170E+03.29840E+03.0          .0          .0          .0
.63016E-03.39389E+03.29889E+03.0          .0          .0          .0
.69701E-03.39551E+03.29930E+03.0          .0          .0          .0
.77054E-03.39672E+03.29966E+03.0          .0          .0          .0
.85143E-03.39759E+03.29996E+03.0          .0          .0          .0
.94040E-03.39817E+03.30019E+03.0          .0          .0          .0
.10383E-02.39852E+03.30036E+03.0          .0          .0          .0
.11459E-02.39871E+03.30047E+03.0          .0          .0          .0
.12644E-02.39880E+03.30053E+03.0          .0          .0          .0
.13946E-02.39884E+03.30056E+03.0          .0          .0          .0
.15379E-02.39886E+03.30058E+03.0          .0          .0          .0
AK,ALMGG,FR,AQ,BQ,YPMAX,YPMIN
      0.41       0.085       0.010     0.22     0.377     1.0       0.0
APL,BPL,SIGNAL
      25.0       0.0         0.0
PPLAG,PRT(1:5)
      4000.0     0.86        0.0       0.0      0.0       0.0
GC,CJ,AXX,BXX,CXX,DXX,EXX
      32.179     778.0       2.0       0.0      0.0       0.0       0.0
NUMRUN,SPACE,OUTPUT,K1,K2,K3
      1    21    2    0    3    3
```

Table XII.
Pressure surface STAN5 input data for run ID 4400.

```
TITLE(1:18)
4400 FTU=1.00 FTG=1.00 (PRESSURE)
GEOM,MODE,FLUID,NEQ,N,KEX,KIN,KENT
    1    2    2    2   39   2   1    1
XU,XL,DELTAX,RETRAN,FRA,ENFRA,GV
  0.036663  0.452181       1.00     350.00      0.01      0.001      0.0
BODFOR,SOURCE(1:5)
    0    1    0    0    0    0
PO,RHOC,VISOC,PRC(1:5)
  5674.785 0.0861921 0.0000221 0.6840941     0.0       0.0        0.0        0.0
NXBC,TYPBC(1:5)
   42    1    0    0    0    0
X(1:NXBC),RW(1:NXBC),AUX1(1:NXBC),AUX2(1:NXBC)
  0.0            1.0         0.0         0.0660
  0.000385       1.0         0.0         0.0660
  0.010118       1.0         0.0         0.0660
  0.025246       1.0         0.0         0.0660
  0.036663       1.0         0.0         0.0660
  0.046118       1.0         0.0         0.0660
  0.070344       1.0         0.0         0.0660
  0.095639       1.0         0.0         0.0660
  0.120640       1.0         0.0         0.0660
  0.144525       1.0         0.0         0.0595
  0.166880       1.0         0.0         0.0534
  0.187584       1.0         0.0         0.0484
  0.206683       1.0         0.0         0.0444
  0.224296       1.0         0.0         0.0411
  0.240571       1.0         0.0         0.0385
  0.255673       1.0         0.0         0.0363
  0.269750       1.0         0.0         0.0345
  0.282932       1.0         0.0         0.0329
  0.295334       1.0         0.0         0.0316
  0.307069       1.0         0.0         0.0306
  0.318217       1.0         0.0         0.0297
  0.328851       1.0         0.0         0.0289
  0.339029       1.0         0.0         0.0283
  0.348810       1.0         0.0         0.0277
  0.358225       1.0         0.0         0.0273
  0.367296       1.0         0.0         0.0269
  0.376051       1.0         0.0         0.0267
  0.384485       1.0         0.0         0.0263
  0.392599       1.0         0.0         0.0262
  0.400365       1.0         0.0         0.0259
  0.407807       1.0         0.0         0.0259
  0.414765       1.0         0.0         0.0256
  0.421165       1.0         0.0         0.0257
  0.426965       1.0         0.0         0.0251
  0.432119       1.0         0.0         0.0254
  0.436502       1.0         0.0         0.0243
  0.439232       1.0         0.0         0.0270
  0.441602       1.0         0.0         0.0344
  0.443911       1.0         0.0         0.0660
  0.446330       1.0         0.0         0.0443
  0.449008       1.0         0.0         0.0306
  0.452181       1.0         0.0         0.0253
UG(1:NXBC),AM(1:NXBC),FJ(1:5,1:NXBC)
    0.0      0.0      289.33      0.0      0.0      0.0      0.0
    3.3155   0.0      288.75      0.0      0.0      0.0      0.0
   84.0389   0.0      274.29      0.0      0.0      0.0      0.0
  143.9435   0.0      251.98      0.0      0.0      0.0      0.0
  164.3845   0.0      245.28      0.0      0.0      0.0      0.0
  176.7823   0.0      240.04      0.0      0.0      0.0      0.0
  205.7554   0.0      227.72      0.0      0.0      0.0      0.0
  237.6485   0.0      220.70      0.0      0.0      0.0      0.0
  271.1345   0.0      216.71      0.0      0.0      0.0      0.0
  308.2917   0.0      214.78      0.0      0.0      0.0      0.0
  347.9553   0.0      213.90      0.0      0.0      0.0      0.0
  391.0398   0.0      213.90      0.0      0.0      0.0      0.0
```

Table XII. (cont)

436.2356	0.0	213.90	0.0	0.0	0.0	0.0
484.0913	0.0	213.90	0.0	0.0	0.0	0.0
533.4192	0.0	213.90	0.0	0.0	0.0	0.0
584.4189	0.0	213.90	0.0	0.0	0.0	0.0
636.1814	0.0	213.90	0.0	0.0	0.0	0.0
688.9727	0.0	213.90	0.0	0.0	0.0	0.0
741.5681	0.0	213.90	0.0	0.0	0.0	0.0
794.2749	0.0	213.90	0.0	0.0	0.0	0.0
845.7351	0.0	213.90	0.0	0.0	0.0	0.0
896.5459	0.0	213.90	0.0	0.0	0.0	0.0
944.9285	0.0	213.90	0.0	0.0	0.0	0.0
992.5293	0.0	213.90	0.0	0.0	0.0	0.0
1036.3784	0.0	213.90	0.0	0.0	0.0	0.0
1080.0847	0.0	213.90	0.0	0.0	0.0	0.0
1118.3677	0.0	213.90	0.0	0.0	0.0	0.0
1158.6355	0.0	213.90	0.0	0.0	0.0	0.0
1190.7153	0.0	213.90	0.0	0.0	0.0	0.0
1229.1865	0.0	213.90	0.0	0.0	0.0	0.0
1254.9575	0.0	213.90	0.0	0.0	0.0	0.0
1297.4932	0.0	213.90	0.0	0.0	0.0	0.0
1323.2034	0.0	213.90	0.0	0.0	0.0	0.0
1393.6714	0.0	213.90	0.0	0.0	0.0	0.0
1467.1111	0.0	213.90	0.0	0.0	0.0	0.0
1763.7258	0.0	213.90	0.0	0.0	0.0	0.0
1600.3723	0.0	213.90	0.0	0.0	0.0	0.0
990.5823	0.0	213.90	0.0	0.0	0.0	0.0
162.4021	0.0	213.90	0.0	0.0	0.0	0.0
694.2417	0.0	213.90	0.0	0.0	0.0	0.0
1392.1899	0.0	213.90	0.0	0.0	0.0	0.0
1809.6770	0.0	213.90	0.0	0.0	0.0	0.0

Y(1:N+1),U(1:M+1),F(1:5,1:M+1)

.0	.0	.24528E+03.0	.0	.0	.0
.86396E-05	.61580E+01	.24656E+03.0	.0	.0	.0
.18143E-04	.12798E+02	.24796E+03.0	.0	.0	.0
.28597E-04	.19911E+02	.24948E+03.0	.0	.0	.0
.40097E-04	.27477E+02	.25113E+03.0	.0	.0	.0
.52746E-04	.35450E+02	.25291E+03.0	.0	.0	.0
.66660E-04	.43768E+02	.25482E+03.0	.0	.0	.0
.81966E-04	.52342E+02	.25685E+03.0	.0	.0	.0
.98802E-04	.61068E+02	.25899E+03.0	.0	.0	.0
.11732E-03	.69819E+02	.26122E+03.0	.0	.0	.0
.13769E-03	.78464E+02	.26351E+03.0	.0	.0	.0
.16010E-03	.86869E+02	.26585E+03.0	.0	.0	.0
.18475E-03	.94907E+02	.26819E+03.0	.0	.0	.0
.21187E-03	.10247E+03	.27051E+03.0	.0	.0	.0
.24169E-03	.10947E+03	.27277E+03.0	.0	.0	.0
.27450E-03	.11585E+03	.27494E+03.0	.0	.0	.0
.31059E-03	.12158E+03	.27701E+03.0	.0	.0	.0
.35029E-03	.12666E+03	.27894E+03.0	.0	.0	.0
.39396E-03	.13118E+03	.28076E+03.0	.0	.0	.0
.44200E-03	.13538E+03	.28254E+03.0	.0	.0	.0
.49484E-03	.13931E+03	.28430E+03.0	.0	.0	.0
.55296E-03	.14294E+03	.28601E+03.0	.0	.0	.0
.61689E-03	.14626E+03	.28768E+03.0	.0	.0	.0
.68722E-03	.14927E+03	.28927E+03.0	.0	.0	.0
.76459E-03	.15196E+03	.29079E+03.0	.0	.0	.0
.84968E-03	.15432E+03	.29221E+03.0	.0	.0	.0
.94329E-03	.15637E+03	.29353E+03.0	.0	.0	.0
.10463E-02	.15812E+03	.29473E+03.0	.0	.0	.0
.11595E-02	.15958E+03	.29581E+03.0	.0	.0	.0
.12841E-02	.16077E+03	.29676E+03.0	.0	.0	.0
.14212E-02	.16173E+03	.29759E+03.0	.0	.0	.0
.15719E-02	.16248E+03	.29828E+03.0	.0	.0	.0
.17378E-02	.16306E+03	.29886E+03.0	.0	.0	.0
.19202E-02	.16351E+03	.29936E+03.0	.0	.0	.0
.21208E-02	.16385E+03	.29977E+03.0	.0	.0	.0
.23416E-02	.16409E+03	.30008E+03.0	.0	.0	.0
.25844E-02	.16424E+03	.30030E+03.0	.0	.0	.0
.28514E-02	.16432E+03	.30044E+03.0	.0	.0	.0
.31452E-02	.16436E+03	.30052E+03.0	.0	.0	.0
.34684E-02	.16438E+03	.30058E+03.0	.0	.0	.0

AK,ALMGG,FR,AQ,BQ,YPMAX,YPMIN

0.41	0.085	0.010	0.22	0.377	1.0	0.0

APL,BPL,SIGNAL

25.0	0.0	0.0

Table XII. (cont)

```
PPLAG,PRT(1:5)
    4000.0        0.86           0.0        0.0        0.0        0.0
GC,CJ,AXX,BXX,CXX,DXX,EXX
    32.179       778.0           2.0        0.0        0.0        0.0        0.0
NUMRUN,SPACE,OUTPUT,K1,K2,K3
     1    21      2      0     3     3
```

Table XIII.
Suction surface STAN5 input data for run ID 4415.

```
TITLE(1:18)
4415 FTU=1.20 FTG=0.94 (SUCTION)
GEOM,MODE,FLUID,NEQ,N,KEX,KIN,KENT
   1    1    2    2   39    2    1    1
XU,XL,DELTAX,RETRAN,FRA,ENFRA,GV
  0.043356  0.596273    1.00    350.00    0.01    0.001    0.0
BODFOR,SOURCE(1:5)
   0    1    0    0    0
PO,RHOC,VISOC,PRC(1:5)
 5500.023 0.0896279 0.0000211 0.6823527    0.0    0.0    0.0    0.0
NXBC,TYPBC(1:5)
   55    1    0    0    0    0
X(1:NXBC),RW(1:NXBC),AUX1(1:NXBC),AUX2(1:NXBC)
  0.0        1.0        0.0        0.0792
  0.000372   1.0        0.0        0.0792
  0.002639   1.0        0.0        0.0792
  0.014532   1.0        0.0        0.0792
  0.026118   1.0        0.0        0.0792
  0.038602   1.0        0.0        0.0622
  0.043356   1.0        0.0        0.0573
  0.050869   1.0        0.0        0.0510
  0.062166   1.0        0.0        0.0434
  0.072166   1.0        0.0        0.0388
  0.081144   1.0        0.0        0.0355
  0.089225   1.0        0.0        0.0336
  0.096691   1.0        0.0        0.0323
  0.103648   1.0        0.0        0.0313
  0.110283   1.0        0.0        0.0308
  0.116707   1.0        0.0        0.0306
  0.122917   1.0        0.0        0.0303
  0.129064   1.0        0.0        0.0303
  0.135200   1.0        0.0        0.0303
  0.141303   1.0        0.0        0.0302
  0.147439   1.0        0.0        0.0303
  0.153668   1.0        0.0        0.0303
  0.159987   1.0        0.0        0.0303
  0.166410   1.0        0.0        0.0303
  0.172980   1.0        0.0        0.0305
  0.179719   1.0        0.0        0.0305
  0.186625   1.0        0.0        0.0305
  0.193727   1.0        0.0        0.0305
  0.201069   1.0        0.0        0.0305
  0.208640   1.0        0.0        0.0305
  0.216482   1.0        0.0        0.0305
  0.224654   1.0        0.0        0.0306
  0.233132   1.0        0.0        0.0306
  0.242050   1.0        0.0        0.0306
  0.251392   1.0        0.0        0.0306
  0.261313   1.0        0.0        0.0307
  0.271866   1.0        0.0        0.0306
  0.283245   1.0        0.0        0.0307
  0.295542   1.0        0.0        0.0307
  0.309035   1.0        0.0        0.0307
  0.323880   1.0        0.0        0.0306
  0.340328   1.0        0.0        0.0307
  0.358624   1.0        0.0        0.0306
  0.378942   1.0        0.0        0.0306
  0.401333   1.0        0.0        0.0305
  0.425630   1.0        0.0        0.0305
  0.451360   1.0        0.0        0.0305
  0.477673   1.0        0.0        0.0305
  0.503399   1.0        0.0        0.0305
  0.527307   1.0        0.0        0.0305
  0.548386   1.0        0.0        0.0305
  0.565980   1.0        0.0        0.0306
  0.579349   1.0        0.0        0.0303
  0.589556   1.0        0.0        0.0305
  0.596273   1.0        0.0        0.0303
```

Table XIII. (cont)

```
UG(1:NXBC),AM(1:NXBC),FJ(1:5,1:NXBC)
    0.0       0.0     224.44           0.0        0.0        0.0        0.0
    3.1029    0.0     224.31           0.0        0.0        0.0        0.0
   24.9958    0.0     225.01           0.0        0.0        0.0        0.0
  147.0508    0.0     237.99           0.0        0.0        0.0        0.0
  258.2629    0.0     250.77           0.0        0.0        0.0        0.0
  350.2251    0.0     260.71           0.0        0.0        0.0        0.0
  386.7031    0.0     260.71           0.0        0.0        0.0        0.0
  449.3049    0.0     257.55           0.0        0.0        0.0        0.0
  571.5093    0.0     252.80           0.0        0.0        0.0        0.0
  692.4089    0.0     248.60           0.0        0.0        0.0        0.0
  828.1560    0.0     244.99           0.0        0.0        0.0        0.0
  946.7830    0.0     241.74           0.0        0.0        0.0        0.0
 1054.6941    0.0     238.54           0.0        0.0        0.0        0.0
 1172.0330    0.0     235.64           0.0        0.0        0.0        0.0
 1257.4678    0.0     232.88           0.0        0.0        0.0        0.0
 1321.0957    0.0     230.21           0.0        0.0        0.0        0.0
 1402.6638    0.0     227.28           0.0        0.0        0.0        0.0
 1457.4783    0.0     224.43           0.0        0.0        0.0        0.0
 1483.1584    0.0     221.85           0.0        0.0        0.0        0.0
 1519.0615    0.0     219.54           0.0        0.0        0.0        0.0
 1548.5764    0.0     217.39           0.0        0.0        0.0        0.0
 1551.2012    0.0     215.45           0.0        0.0        0.0        0.0
 1551.5864    0.0     213.50           0.0        0.0        0.0        0.0
 1554.9360    0.0     211.34           0.0        0.0        0.0        0.0
 1542.9253    0.0     209.74           0.0        0.0        0.0        0.0
 1526.0828    0.0     208.61           0.0        0.0        0.0        0.0
 1514.0007    0.0     209.48           0.0        0.0        0.0        0.0
 1493.9714    0.0     210.98           0.0        0.0        0.0        0.0
 1475.5510    0.0     213.08           0.0        0.0        0.0        0.0
 1459.0171    0.0     215.41           0.0        0.0        0.0        0.0
 1442.3511    0.0     217.67           0.0        0.0        0.0        0.0
 1426.6902    0.0     219.83           0.0        0.0        0.0        0.0
 1415.5242    0.0     221.64           0.0        0.0        0.0        0.0
 1400.8137    0.0     222.72           0.0        0.0        0.0        0.0
 1390.6362    0.0     223.84           0.0        0.0        0.0        0.0
 1376.7361    0.0     224.54           0.0        0.0        0.0        0.0
 1369.0076    0.0     225.04           0.0        0.0        0.0        0.0
 1359.1870    0.0     225.50           0.0        0.0        0.0        0.0
 1359.2776    0.0     225.50           0.0        0.0        0.0        0.0
 1357.6711    0.0     225.50           0.0        0.0        0.0        0.0
 1365.3455    0.0     225.50           0.0        0.0        0.0        0.0
 1369.6519    0.0     225.50           0.0        0.0        0.0        0.0
 1379.8315    0.0     225.50           0.0        0.0        0.0        0.0
 1387.9038    0.0     225.50           0.0        0.0        0.0        0.0
 1400.0413    0.0     225.50           0.0        0.0        0.0        0.0
 1413.5840    0.0     225.50           0.0        0.0        0.0        0.0
 1427.7842    0.0     225.50           0.0        0.0        0.0        0.0
 1444.2817    0.0     225.50           0.0        0.0        0.0        0.0
 1457.8301    0.0     225.50           0.0        0.0        0.0        0.0
 1466.8481    0.0     225.50           0.0        0.0        0.0        0.0
 1478.3875    0.0     225.50           0.0        0.0        0.0        0.0
 1479.3401    0.0     225.50           0.0        0.0        0.0        0.0
 1496.5005    0.0     225.50           0.0        0.0        0.0        0.0
 1552.0015    0.0     225.50           0.0        0.0        0.0        0.0
 1754.5259    0.0     225.50           0.0        0.0        0.0        0.0
Y(1:N+1),U(1:M+1),F(1:5,1:M+1)
.0         .0      .26071E+03.0              .0         .0         .0
.37017E-05.11847E+02.26102E+03.0             .0         .0         .0
.77736E-05.24644E+02.26138E+03.0             .0         .0         .0
.12253E-04.38419E+02.26176E+03.0             .0         .0         .0
.17180E-04.53178E+02.26219E+03.0             .0         .0         .0
.22599E-04.68909E+02.26266E+03.0             .0         .0         .0
.28561E-04.85570E+02.26317E+03.0             .0         .0         .0
.35119E-04.10309E+03.26373E+03.0             .0         .0         .0
.42332E-04.12134E+03.26434E+03.0             .0         .0         .0
.50267E-04.14018E+03.26499E+03.0             .0         .0         .0
.58996E-04.15940E+03.26569E+03.0             .0         .0         .0
.68597E-04.17876E+03.26643E+03.0             .0         .0         .0
.79158E-04.19799E+03.26720E+03.0             .0         .0         .0
.90776E-04.21679E+03.26800E+03.0             .0         .0         .0
.10356E-03.23487E+03.26882E+03.0             .0         .0         .0
.11761E-03.25196E+03.26965E+03.0             .0         .0         .0
.13308E-03.26781E+03.27047E+03.0             .0         .0         .0
.15008E-03.28230E+03.27127E+03.0             .0         .0         .0
```

Table XIII. (cont)

```
.16879E-03.29581E+03.27208E+03.0          .0          .0          .0
.18938E-03.30851E+03.27290E+03.0          .0          .0          .0
.21202E-03.32030E+03.27371E+03.0          .0          .0          .0
.23692E-03.33109E+03.27452E+03.0          .0          .0          .0
.26431E-03.34082E+03.27532E+03.0          .0          .0          .0
.29445E-03.34947E+03.27609E+03.0          .0          .0          .0
.32759E-03.35701E+03.27683E+03.0          .0          .0          .0
.36405E-03.36348E+03.27754E+03.0          .0          .0          .0
.40416E-03.36891E+03.27819E+03.0          .0          .0          .0
.44828E-03.37336E+03.27879E+03.0          .0          .0          .0
.49681E-03.37694E+03.27934E+03.0          .0          .0          .0
.55019E-03.37973E+03.27982E+03.0          .0          .0          .0
.60891E-03.38185E+03.28023E+03.0          .0          .0          .0
.67350E-03.38343E+03.28058E+03.0          .0          .0          .0
.74455E-03.38461E+03.28089E+03.0          .0          .0          .0
.82271E-03.38545E+03.28114E+03.0          .0          .0          .0
.90868E-03.38602E+03.28134E+03.0          .0          .0          .0
.10033E-02.38637E+03.28148E+03.0          .0          .0          .0
.11073E-02.38656E+03.28157E+03.0          .0          .0          .0
.12217E-02.38665E+03.28163E+03.0          .0          .0          .0
.13476E-02.38669E+03.28166E+03.0          .0          .0          .0
.14860E-02.38670E+03.28168E+03.0          .0          .0          .0
AK,ALMGG,FR,AQ,BQ,YPMAX,YPMIN
      0.41       0.085       0.010      0.22    0.377    1.0       0.0
APL,BPL,SIGNAL
      25.0       0.0         0.0
PPLAG,PRT(1:5)
      4000.0     0.86        0.0        0.0     0.0      0.0
GC,CJ,AXX,BXX,CXX,DXX,EXX
      32.179     778.0       2.0        0.0     0.0      0.0       0.0
NUMRUN,SPACE,OUTPUT,K1,K2,K3
      1    21    2    0    3    3
```

Table XIV.
Pressure surface STAN5 input data for run ID 4415.

```
TITLE(1:18)
4415 FTU=1.20 FTG=0.94 (PRESSURE)
GEOM,MODE,FLUID,NEQ,N,KEX,KIN,KENT
   1     2     2     2    39    2   1     1
XU,XL,DELTAX,RETRAN,FRA,ENFRA,GV
  0.036663  0.452181           1.00      350.00        0.01        0.001        0.0
BODFOR,SOURCE(1:5)
   0     1     0     0     0     0
PO,RHOC,VISOC,PRC(1:5)
  5674.785 0.0916972 0.0000212 0.6822367    0.0         0.0          0.0          0.0
NXBC,TYPBC(1:5)
  42     1     0     0     0     0
X(1:NXBC),RW(1:NXBC),AUX1(1:NXBC),AUX2(1:NXBC)
  0.0               1.0          0.0          0.0792
  0.000372          1.0          0.0          0.0792
  0.010118          1.0          0.0          0.0792
  0.025246          1.0          0.0          0.0792
  0.036663          1.0          0.0          0.0792
  0.046118          1.0          0.0          0.0792
  0.070344          1.0          0.0          0.0792
  0.095639          1.0          0.0          0.0792
  0.120640          1.0          0.0          0.0792
  0.144525          1.0          0.0          0.0715
  0.166880          1.0          0.0          0.0641
  0.187584          1.0          0.0          0.0582
  0.206683          1.0          0.0          0.0533
  0.224296          1.0          0.0          0.0495
  0.240571          1.0          0.0          0.0462
  0.255673          1.0          0.0          0.0435
  0.269750          1.0          0.0          0.0414
  0.282932          1.0          0.0          0.0395
  0.295334          1.0          0.0          0.0381
  0.307069          1.0          0.0          0.0368
  0.318217          1.0          0.0          0.0357
  0.328851          1.0          0.0          0.0347
  0.339029          1.0          0.0          0.0340
  0.348810          1.0          0.0          0.0334
  0.358225          1.0          0.0          0.0328
  0.367296          1.0          0.0          0.0324
  0.376051          1.0          0.0          0.0320
  0.384485          1.0          0.0          0.0317
  0.392599          1.0          0.0          0.0314
  0.400365          1.0          0.0          0.0311
  0.407807          1.0          0.0          0.0311
  0.414765          1.0          0.0          0.0307
  0.421165          1.0          0.0          0.0308
  0.426965          1.0          0.0          0.0302
  0.432119          1.0          0.0          0.0305
  0.436502          1.0          0.0          0.0291
  0.439232          1.0          0.0          0.0324
  0.441602          1.0          0.0          0.0414
  0.443911          1.0          0.0          0.0792
  0.446330          1.0          0.0          0.0532
  0.449008          1.0          0.0          0.0369
  0.452181          1.0          0.0          0.0303
UG(1:NXBC),AM(1:NXBC),FJ(1:5,1:NXBC)
    0.0      0.0      224.44      0.0      0.0      0.0      0.0
    3.1029   0.0      224.56      0.0      0.0      0.0      0.0
   81.4778   0.0      227.90      0.0      0.0      0.0      0.0
  139.5567   0.0      233.08      0.0      0.0      0.0      0.0
  159.3748   0.0      234.64      0.0      0.0      0.0      0.0
  171.3948   0.0      230.59      0.0      0.0      0.0      0.0
  199.4849   0.0      220.97      0.0      0.0      0.0      0.0
  230.4060   0.0      215.45      0.0      0.0      0.0      0.0
  262.8716   0.0      212.26      0.0      0.0      0.0      0.0
  298.8965   0.0      210.58      0.0      0.0      0.0      0.0
  337.3513   0.0      209.79      0.0      0.0      0.0      0.0
  379.1226   0.0      209.79      0.0      0.0      0.0      0.0
```

Table XIV. (cont)

```
 422.9412  0.0   209.79      0.0       0.0       0.0       0.0
 469.3384  0.0   209.79      0.0       0.0       0.0       0.0
 517.1631  0.0   209.79      0.0       0.0       0.0       0.0
 566.6084  0.0   209.79      0.0       0.0       0.0       0.0
 616.7935  0.0   209.79      0.0       0.0       0.0       0.0
 667.9758  0.0   209.79      0.0       0.0       0.0       0.0
 718.9685  0.0   209.79      0.0       0.0       0.0       0.0
 770.0688  0.0   209.79      0.0       0.0       0.0       0.0
 819.9609  0.0   209.79      0.0       0.0       0.0       0.0
 869.2231  0.0   209.79      0.0       0.0       0.0       0.0
 916.1313  0.0   209.79      0.0       0.0       0.0       0.0
 962.2812  0.0   209.79      0.0       0.0       0.0       0.0
1004.7942  0.0   209.79      0.0       0.0       0.0       0.0
1047.1685  0.0   209.79      0.0       0.0       0.0       0.0
1084.2847  0.0   209.79      0.0       0.0       0.0       0.0
1123.3254  0.0   209.79      0.0       0.0       0.0       0.0
1154.4275  0.0   209.79      0.0       0.0       0.0       0.0
1191.7263  0.0   209.79      0.0       0.0       0.0       0.0
1216.7119  0.0   209.79      0.0       0.0       0.0       0.0
1257.9514  0.0   209.79      0.0       0.0       0.0       0.0
1282.8779  0.0   209.79      0.0       0.0       0.0       0.0
1351.1985  0.0   209.79      0.0       0.0       0.0       0.0
1422.3999  0.0   209.79      0.0       0.0       0.0       0.0
1709.9753  0.0   209.79      0.0       0.0       0.0       0.0
1551.5999  0.0   209.79      0.0       0.0       0.0       0.0
 960.3936  0.0   209.79      0.0       0.0       0.0       0.0
 157.4528  0.0   209.79      0.0       0.0       0.0       0.0
 673.0842  0.0   209.79      0.0       0.0       0.0       0.0
1349.7622  0.0   209.79      0.0       0.0       0.0       0.0
1754.5259  0.0   209.79      0.0       0.0       0.0       0.0
Y(1:N+1),U(1:M+1),F(1:5,1:M+1)
.0          .0          .23464E+03.0            .0        .0        .0
.83569E-05.59528E+01.23572E+03.0                .0        .0        .0
.17550E-04.12374E+02.23690E+03.0                .0        .0        .0
.27661E-04.19256E+02.23819E+03.0                .0        .0        .0
.38784E-04.26578E+02.23959E+03.0                .0        .0        .0
.51020E-04.34301E+02.24109E+03.0                .0        .0        .0
.64479E-04.42364E+02.24271E+03.0                .0        .0        .0
.79283E-04.50683E+02.24443E+03.0                .0        .0        .0
.95569E-04.59153E+02.24624E+03.0                .0        .0        .0
.11348E-03.67653E+02.24814E+03.0                .0        .0        .0
.13319E-03.76053E+02.25009E+03.0                .0        .0        .0
.15486E-03.84221E+02.25207E+03.0                .0        .0        .0
.17871E-03.92031E+02.25406E+03.0                .0        .0        .0
.20493E-03.99378E+02.25604E+03.0                .0        .0        .0
.23378E-03.10618E+03.25796E+03.0                .0        .0        .0
.26552E-03.11237E+03.25981E+03.0                .0        .0        .0
.30043E-03.11794E+03.26157E+03.0                .0        .0        .0
.33883E-03.12286E+03.26322E+03.0                .0        .0        .0
.38107E-03.12723E+03.26477E+03.0                .0        .0        .0
.42753E-03.13129E+03.26628E+03.0                .0        .0        .0
.47864E-03.13509E+03.26777E+03.0                .0        .0        .0
.53486E-03.13860E+03.26922E+03.0                .0        .0        .0
.59671E-03.14181E+03.27063E+03.0                .0        .0        .0
.66473E-03.14471E+03.27199E+03.0                .0        .0        .0
.73957E-03.14731E+03.27328E+03.0                .0        .0        .0
.82188E-03.14960E+03.27449E+03.0                .0        .0        .0
.91242E-03.15158E+03.27561E+03.0                .0        .0        .0
.10120E-02.15327E+03.27663E+03.0                .0        .0        .0
.11216E-02.15468E+03.27755E+03.0                .0        .0        .0
.12421E-02.15584E+03.27836E+03.0                .0        .0        .0
.13747E-02.15678E+03.27907E+03.0                .0        .0        .0
.15205E-02.15750E+03.27966E+03.0                .0        .0        .0
.16809E-02.15806E+03.28016E+03.0                .0        .0        .0
.18573E-02.15851E+03.28059E+03.0                .0        .0        .0
.20514E-02.15884E+03.28095E+03.0                .0        .0        .0
.22649E-02.15908E+03.28122E+03.0                .0        .0        .0
.24998E-02.15922E+03.28141E+03.0                .0        .0        .0
.27581E-02.15931E+03.28154E+03.0                .0        .0        .0
.30423E-02.15935E+03.28161E+03.0                .0        .0        .0
.33549E-02.15937E+03.28166E+03.0                .0        .0        .0
AK,ALMGG,FR,AQ,BQ,YPMAX,YPMIN
    0.41       0.085       0.010       0.22    0.377     1.0       0.0
APL,BPL,SIGNAL
    25.0       0.0         0.0
```

Table XIV. (cont)

```
PPLAG,PRT(1:5)
    4000.0        0.86        0.0        0.0        0.0        0.0
GC,CJ,AXX,BXX,CXX,DXX,EXX
    32.179        778.0        2.0        0.0        0.0        0.0        0.0
NUMRUN,SPACE,OUTPUT,K1,K2,K3
    1     21      2      0     3     3
```

APPENDIX F

LIST OF ABBREVIATIONS, ACRONYMS, AND SYMBOLS

A	stagnation region initialization
ACF	Aerothermodynamic Cascade Facility
A/D	analog to digital
ALAM	turbulence augmentation parameter
ASME	American Society of Mechanical Engineers
B	downstream (recovery) region initialization
CA	Chromel-Alumel
CAD/CAM	computer-aided design/computer-aided manufacturing
c_p	specific heat at constant pressure
CPU	central processing unit
Cr	correction factor for thermal entrance region effects
CRT	cathode ray tube
D	cooling hole diameter
DELMR	injection parameter
dT/dn	surface normal temperature gradient
Eu	Euler number
$Eu_{e,d}$	Euler number downstream of the injection site
f	fraction of total
FEM	finite element model
FTG	free-stream total gas temperature factor
FTU	free-stream turbulence intensity factor
h	heat transfer coefficient
h_c	coolant heat transfer coefficient
h_e	external airfoil heat transfer coefficient
h_{FC}	heat transfer coefficient with film cooling
h/h_o	normalized heat transfer coefficient
h_{NFC}	heat transfer coefficient without film cooling
h_o	reference heat transfer coefficient for normalization
HP	Hewlett-Packard
I	total enthalpy
I_e	outer edge total enthalpy
K	kilo
k	thermal conductivity
LDA	laser Doppler anemometer

M	blowing ratio
M	mega
Ma	Mach number
Ma_1	upstream or vane row inlet Mach number
Ma_2	downstream or vane row exit Mach number
m_c	coolant mass
Nu_D	diameter Nusselt number
p	pressure
P_c/P_t	coolant to free-stream pressure ratio (blowing strength)
P/D	hole pitch to diameter ratio
Pr	Prandtl number
Pr_{eff}	effective Prandtl number
Pr_t	turbulent Prandtl number
Pr_{Tu}	laminar augmentation Prandtl number
P_s	surface static pressure
P_s/P_t	static to inlet total pressure ratio
P_t1	cascade inlet total pressure
R	gas constant
Re	Reynolds number
Re_D	diameter Reynolds number
Re_x	surface distance Reynolds number
$Re_{x,e}$	transition endpoint Reynolds number
$Re_{x,o}$	surface distance transition origin Reynolds number
Re_1	upstream or vane row inlet Reynolds number
Re_2	downstream or vane row exit Reynolds number
Re_θ	momentum thickness Reynolds number
$Re_{\theta,o}$	momentum thickness transition origin Reynolds number
R_{LE}	vane leading edge radius
R_{TE}	vane trailing edge radius
S	hole spacing
S	percent surface distance
S/D	hole spacing to diameter ratio
SIAM	Society of Industrial and Applied Mathematics
SNR	Stanton number reduction
S_{po}	pressure surface starting location
S_{so}	airfoil suction surface starting location
St_{FC}	Stanton number with film cooling

St_{NFC}	Stanton number without film cooling
T	temperature
T_c	coolant plenum temperature
T_c/T_g	coolant to gas absolute temperature ratio (cooling strength, thermal dilution strength)
T_g	cascade inlet total temperature
T_g^*	effective gas temperature
$T_{g,d}$	gas temperature downstream of the injection site
$T_{g,u}$	gas temperature upstream of the injection site
$T_{g,\infty}$	total gas temperature
T_s/T_g	static to total temperature ratio
T_s^*/T_g^*	effective static to total temperature ratio
T_t1	cascade inlet free-stream temperature
Tu_e	outer edge free-stream turbulence intensity
Tu_e^*	effective free-stream turbulence intensity
$Tu_{e,d}$	turbulence intensity downstream of the injection site
$Tu_{e,u}$	turbulence intensity upstream of the injection site
Tu_∞	free-stream turbulence intensity
T_w	vane surface temperature
T_w/T_g	vane surface to gas absolute temperature ratio
u	velocity
u_c	coolant velocity
u_e	outer edge free-stream velocity
u_e^*	effective outer edge free-stream velocity
$u_{e,d}$	outer edge velocity downstream of the injection site
$u_{e,u}$	outer edge velocity upstream of the injection site
u_∞	free-stream velocity
x	streamwise coordinate
x_d	streamwise location downstream of the injection site
x_u	streamwise location upstream of the injection site
y	surface normal coordinate
α	hole slant angle
β	hole skew angle
γ_t	transition model term
γ_{Tu}	laminar augmentation intermittency model term
δ_e	boundary layer thickness
$\delta_{e,d}$	boundary layer thickness downstream of the injection site

$\delta_{e,u}$	boundary layer thickness upstream of the injection site
δ_p	jet penetration height
λ	pressure gradient (Pohlhausen) parameter
μ_{eff}	effective viscosity
μ_t	turbulent viscosity
μ_{Tu}	laminar augmentation viscosity
ρ	density
ρ_c	coolant density
$\rho_{e,d}$	density downstream of the injection site
$\rho_{e,u}$	density upstream of the injection site
ρ_∞	free-stream density
θ	film-cooling effectiveness parameter
θ	momentum thickness

REFERENCES

1. L. D. Hylton, M. S. Mihelc, E. R. Turner, D. A. Nealy, and R. E. York, "Analytical and Experimental Evaluation of the Heat Transfer Distribution over the Surfaces of Turbine Vanes," NASA CR-168015, May 1983.

2. K. L. Miller and M. E. Crawford, "Numerical Simulations of Single, Double, and Multiple Row Film-Cooling Effectiveness and Heat Transfer," ASME Paper No. 84-GT-112, 1984.

3. F. S. Stepka and R. E. Gaugler, "Comparison of Predicted and Experimental External Heat Transfer around a Film-Cooled Cylinder in Cross Flow," ASME Paper No. 83-GT-47, 1983.

4. A. B. Turner, "Local Heat Transfer Measurements on a Gas Turbine Blade," Journal of Mechanical Engineering Sciences, Vol 13, pp 1-12, 1971.

5. M. E. Crawford and W. M. Kays, Convective Heat and Mass Transfer, McGraw-Hill, 1980.

6. S. J. Kline and F. A. McClintock, "Describing Uncertainties in Single-Sample Experiments," Mechanical Engineering, January 1953.

7. M. E. Crawford, W. M. Kays, and R. J. Moffat, "Full Coverage Film Cooling on Flat, Isothermal Surfaces: A Summary Report on Data and Predictions," NASA CR-3219, January 1980.

8. D. W. Luckey and M. R. L'Ecuyer, "Stagnation Region Gas Film Cooling—Spanwise Angled Injection from Multiple Rows of Holes," NASA CR-165333, 1981.

9. S. V. Patankar and D. B. Spalding, Heat and Mass Transfer in Boundary Layers, Second Edition, International Textbook Company, Ltd., London, 1970.

10. M. E. Crawford and W. M. Kays, "STAN5—A Program for Numerical Computation of Two-Dimensional Internal and External Boundary Layer Flows," NASA CR-2742, 1976.

11. E. R. G. Eckert and R. M. Drake, Heat and Mass Transfer, McGraw-Hill, 2nd ed, 1959.

12. N. J. Seyb, "The Role of Boundary Layers in Axial Flow Turbomachines and the Prediction of Their Effects," AGARD-AG-164, pp 241-259, 1972.

13. A. Brown and B. W. Martin, "Heat Transfer to Turbine Blades with Special Reference to the Effects of Mainstream Turbulence," ASME Paper No. 79-GT-26, March 1979.

14. A. Brown and R. C. Burton, "The Effects of Free-Stream Turbulence Intensity and Velocity Distribution on Heat Transfer to Curved Surfaces," Journal of Engineering for Power, Vol 100, pp 159-168, 1978.

15. S. Dhawan and R. Narasimha, "Some Properties of Boundary Layer Flow During Transition from Laminar to Turbulent Motion," Journal of Fluid Mechanics, Vol 3, pp 418-436, 1958.

16. J. Dunham, "Predictions of Boundary Layer Transition on Turbomachinery Blades," AGARD-AG-164, 1972.

17. H. Miyazaki and E. M. Sparrow, "Analysis of Effects of Free-Stream Turbulence on Heat Transfer and Skin Friction," Journal of Heat Transfer, Vol 99, pp 614-619, November 1977.

18. R. A. Delaney, "Time-Marching Analysis of Steady Transonic Flow in Turbomachinery Cascades Using the Hopscotch Method," ASME Paper No. 82-GT-152, 1982.

19. O. K. Kwon, E. R. Turner, and Y. M. Kou, "Prediction of Stagnation Flow Heat Transfer on Turbomachinery Airfoils," AIAA Paper No. 83-1173, 1983.

20. J. F. Louis, "Heat Transfer in Turbines," AFWAL-TR-81-2099, 1981.

21. C. Camci and T. Arts, "Experimental Heat Transfer Investigation around the Film-Cooled Leading Edge of a High Pressure Gas Turbine Rotor Blade," ASME Paper No. 85-GT-114, 1985.

22. H. McDonald and R. W. Fish, "Practical Calculations of Transitional Boundary Layers," International Journal of Heat and Mass Transfer, Vol 16, No. 9, 1972.

23. M. F. Blair, "Influence of Free-Stream Turbulence on Boundary Layer Transition in Favorable Pressure Gradients," J. of Engr for Power, Trans of ASME, Vol 104, October 1982, pp 743-750.

24. M. F. Blair, "Influence of Free-Stream Turbulence on Turbulent Boundary Layer Heat Transfer and Mean Profile Development, Part I--Experimental Data," J. of Heat Transfer, Trans of ASME, Vol 105, February 1983, pp 33-40, "Part II--Analysis of Results," pp 41-47.

25. T. Wang, T. W. Simon, J. Buddhavarapu, "Heat Transfer and Fluid Mechanics Measurements in Transitional Boundary Layer Flows," ASME Paper No. 85-GT-113, 1985.

1 Report No NASA CR-174827	2 Government Accession No	3 Recipient's Catalog No
4 Title and Subtitle Turbine Vane External Heat Transfer Volume I. Analytical and Experimental Evaluation of Surface Heat Transfer Distributions with Leading Edge Showerhead Film Cooling		5 Report Date July 1985
		6 Performing Organization Code
7. Author(s) E. R. Turner, M. D. Wilson, L. D. Hylton, R. M. Kaufman		8. Performing Organization Report No EDR 11984, Volume I
9. Performing Organization Name and Address Allison Gas Turbines Division of General Motors Corporation PO Box 420 Indianapolis, Indiana 46206-0420		10. Work Unit No.
		11 Contract or Grant No NAS3-23695
12. Sponsoring Agency Name and Address National Aeronautics and Space Administration Washington, D. C. 20546		13 Type of Report and Period Covered Contractor report
		14 Sponsoring Agency Code

15 Supplementary Notes

Prepared in cooperation with NASA Project Manager H. J. Gladden, NASA-Lewis Research Center, Cleveland, Ohio

16 Abstract

This two-volume report addresses the progress of contract NAS3-23695 to improve the predictive design capabilities for external heat transfer to turbine vanes including the effects of leading edge showerhead film cooling. Volume I describes the analytical and experimental program conducted at Allison Gas Turbines to examine the effect of leading edge showerhead film cooling on downstream heat transfer. This was a combined analytical and experimental program. The experimental study was performed in a two-dimensional linear cascade previously used to obtain vane surface heat transfer distributions on nonfilm-cooled airfoils under NAS3-22761.

The experimental program provided a data base for leading edge showerhead film-cooled turbine vanes to use in developing and evaluating new analytical models.

The analytical effort described in Volume I consists of modifications to the two-dimensional boundary layer model previously developed under NAS3-22761. The results of this effort were the formulation and test of an effective viscosity model capable of predicting heat transfer phenomena downstream of the leading edge film-cooling array on both the suction and pressure surfaces, with and without mass injection. Comparisons of heat transfer calculations made with the model with data taken during the program are presented and indicate good agreement.

17. Key Words (Suggested by Author(s)) Turbine aerodynamics, turbine heat transfer, film cooling, boundary layer heat transfer, Navier-Stokes, turbine cascade analysis	18. Distribution Statement		
19 Security Classif. (of this report) Unclassified	20. Security Classif. (of this page) Unclassified	21. No. of Pages 233	22. Price*